

**INVESTIGATION OF THE MINOR-ELEMENT EFFECTS ON THE OXIDATION  
BEHAVIOR OF  $\gamma$ -NI +  $\gamma'$ -Ni<sub>3</sub>AL ALLOYS**

by

Zhuoqun Li

B.E., Beijing University of Aeronautics and Astronautics, 2003

M.S., Institute of Metal Research, Chinese Academy of Sciences, 2007

Submitted to the Graduate Faculty of  
Swanson School of Engineering in partial fulfillment  
of the requirements for the degree of  
Doctor of Philosophy

University of Pittsburgh

2014

UNIVERSITY OF PITTSBURGH  
SWANSON SCHOOL OF ENGINEERING

This dissertation was presented

by

Zhuoqun Li

It was defended on

March 28, 2014

and approved by

Gerald H Meier, PhD, Professor, Department of Mechanical Engineering and Materials  
Science

Ian Nettleship, PhD, Associate Professor, Department of Mechanical Engineering and  
Materials Science

Lei Li, PhD, Assistant Professor, Department of Chemical and Petroleum Engineering

Dissertation Director: Brian M. Gleeson, PhD, Professor, Department of Mechanical  
Engineering and Materials Science

Copyright © by Zhuoqun Li

2014

# INVESTIGATION OF THE MINOR-ELEMENT EFFECTS ON THE OXIDATION BEHAVIOR OF $\gamma$ -NI + $\gamma'$ -NI<sub>3</sub>AL ALLOYS

Zhuoqun Li, PhD

University of Pittsburgh, 2014

The effects of minor-elements, mainly Hf, Y and Si, on the oxidation behavior of Al<sub>2</sub>O<sub>3</sub>-scale forming  $\gamma$ -Ni +  $\gamma'$ -Ni<sub>3</sub>Al-based alloy and coating compositions were investigated. Firstly, the effects of Si addition on Hf+Y co-doped  $\gamma+\gamma'$  alloys were assessed on both modified-René N5 superalloy and model alloys. It was found that the addition of Si ( $\leq 1$  at. %) decreased the overall weight gain of modified-René N5 superalloy and Ni-20Al-5Cr-0.05Hf-0.05Y (at. %) model alloy under both isothermal (up to 1000 hours) and cyclic (up to 1000 1h cycles) oxidation conditions at 1150°C. Secondly, the effect of Si (1 at. %) addition on the metastable Al<sub>2</sub>O<sub>3</sub>  $\rightarrow$   $\alpha$ -Al<sub>2</sub>O<sub>3</sub> transformation kinetics during the early stage of oxidation was studied on the Ni-20Al-5Cr-0.05Hf-0.05Y model alloy. It was found that the addition of 1 at. % Si delayed the  $\theta \rightarrow \alpha$ -Al<sub>2</sub>O<sub>3</sub> transformation at temperatures above 900°C. In addition, a novel kinetics assessment method was developed to determine the  $\theta \rightarrow \alpha$ -Al<sub>2</sub>O<sub>3</sub> transformation based on analyzing the time dependence of instantaneous time exponent to the weight-gain kinetics (i. e. n-value). This method found success in describing the effect of Si addition in delaying the  $\theta \rightarrow \alpha$ -Al<sub>2</sub>O<sub>3</sub> transformation on Ni-20Al-5Cr-0.05Hf-0.05Y model alloy. Thirdly, the synergistic effect of Si (1 at. %) combined with Hf/Y on the early-stage oxidation behavior of Ni-20Al-5Cr-0.05Hf-0.05Y model alloy was studied by TEM/STEM/EDS. Significantly different microstructures of alumina scale formed on the Si-free and Si-containing alloys after 10 and 30 minutes of oxidation at 1150°C. The alumina scale formed on the Si-free alloy contained a large amount of

Ni-rich particles in the columnar-grained  $\text{Al}_2\text{O}_3$  region close to the scale/metal interface. By contrast, for the Si-containing alloy, a layer of quickly established large-grained  $\text{Al}_2\text{O}_3$ , with much less Ni-rich particles, was observed in the region close to the scale/metal interface. Segregation behavior of Hf and Y was also influenced by the addition of Si. After 2 hours of oxidation at  $1150^\circ\text{C}$ , excessive non-uniform Hf and Y co-segregation was observed at the grain boundaries of alumina scales formed on the Si-free alloy. By contrast, Hf and Y grain-boundary segregations were uniform in the  $\text{Al}_2\text{O}_3$  scale formed on the Si-containing alloy.

## TABLE OF CONTENTS

<b>PREFACE</b> .....	<b>XV</b>
<b>1.0 INTRODUCTION</b> .....	<b>1</b>
<b>2.0 TECHNICAL BACKGROUND</b> .....	<b>3</b>
<b>2.1 FUNDAMENTALS OF HIGH TEMPERATURE OXIDATION OF METALS</b> .....	<b>3</b>
2.1.1 Thermodynamic and kinetic fundamentals of metal oxidation .....	<b>3</b>
2.1.2 Oxidation of alloys .....	<b>9</b>
<b>2.2 ALUMINA-SCALE FORMING ALLOY SYSTEMS</b> .....	<b>11</b>
2.2.1 Aluminum oxide polymorphs and structural relationships .....	<b>12</b>
2.2.2 Kinetics of aluminum oxides phase transformation .....	<b>15</b>
2.2.3 Kinetics of steady-state alumina scale formation.....	<b>18</b>
2.2.4 Transport properties associated with alumina-scale formation.....	<b>21</b>
2.2.5 Compositional effects on the oxidation behavior of alumina scale forming systems .....	<b>24</b>
2.2.5.1 Effects of major alloying elements (Al and Cr) .....	<b>24</b>
2.2.5.2 Effects of reactive elements (REs) .....	<b>29</b>
2.2.5.3 Effects of other minor elements .....	<b>37</b>
<b>2.3 PROTECTIVE COATINGS FOR HIGH TEMPERATURE APPLICATIONS</b> .....	<b>46</b>
2.3.1 Diffusion Coatings.....	<b>46</b>
2.3.2 Overlay Coatings.....	<b>48</b>

2.3.3	Thermal barrier coating system .....	51
2.4	AIMS OF PRESENT STUDY.....	53
3.0	EXPERIMENTAL DETAILS.....	54
3.1	MATERIALS AND SAMPLE PREPARATION FOR OXIDATION TESTING.....	54
3.2	ISOTHERMAL AND CYCLIC OXIDATION TESTING .....	54
3.3	CHARACTERIZATION AND DATA ANALYSIS .....	56
4.0	EFFECT OF SILICON ADDITION ON THE OXIDATION BEHAVIOR OF $\Gamma$ -NI+ $\Gamma'$ -NI <sub>3</sub> AL-BASED ALUMINA SCALE FORMING ALLOYS.....	58
4.1	INTRODUCTION.....	58
4.2	MATERIALS AND EXPERIMENTAL PROCEDURES .....	59
4.3	RESULTS AND DISCUSSION .....	62
4.3.1	Modified René N5 alloys (Group #1).....	62
4.3.2	Ni-20Al-5Cr model alloys (Group #2).....	70
4.3.3	Ni-7.5Cr-13Al-1Ta-1Re-0.12C-0.05Hf-0.05Y alloys (Group #3) .....	76
4.4	SUMMARY AND CONCLUSIONS .....	80
5.0	EFFECTS OF SILICON ADDITION ON THE EARLY STAGE OXIDATION BEHAVIOR OF $\Gamma$ -NI+ $\Gamma'$ -NI <sub>3</sub> AL ALUMINA SCALE FORMING MODEL ALLOYS.....	84
5.1	INTRODUCTION.....	84
5.2	MATERIALS AND EXPERIMENTAL PROCEDURES .....	86
5.3	RESULTS .....	86
5.3.1	Confocal photo-stimulated microspectroscopy (CPSM) characterization .....	86
5.3.2	Semi-quantitative X-ray diffraction characterization.....	92
5.3.3	Construction of Time-Temperature-Transformation (T-T-T) type diagrams.....	98
5.3.4	Mathematical analysis of $\theta \rightarrow \alpha$ -Al <sub>2</sub> O <sub>3</sub> phase transformation kinetics..	104

5.4	DISCUSSION .....	113
5.5	SUMMARY AND CONCLUSIONS .....	119
6.0	TEM CHARACTERIZATION OF THE SCALE/METAL INTERFACE EVOLUTION DURING THE INITIAL OXIDATION STAGE OF $\Gamma$ -Ni+ $\Gamma'$ - Ni <sub>3</sub> Al ALUMINA SCALE FORMING MODEL ALLOYS WITH AND WITHOUT SILICON ADDITION.....	121
6.1	INTRODUCTION.....	121
6.2	MATERIALS AND EXPERIMENTAL PROCEDURES .....	123
6.3	RESULTS .....	124
	6.3.1 Surface morphologies .....	124
	6.3.2 Cross-sectional STEM characterization of the scale/metal interfaces ...	131
6.4	DISCUSSION .....	149
6.5	SUMMARY AND CONCLUSIONS .....	159
7.0	OVERALL CONCLUSIONS.....	161
	BIBLIOGRAPHY.....	164

## LIST OF TABLES

Table 2.1 Summary of parabolic rate constants of some Al <sub>2</sub> O <sub>3</sub> -scale forming alloy compositions .....	20
Table 4.1 Nominal compositions of Al <sub>2</sub> O <sub>3</sub> -scale forming alloys used in this chapter .....	60
Table 4.2 Summary of parabolic rate constants (1150°C) of three groups of alloys studied in this chapter .....	82
Table 4.3 Summary of overall weight gain of three groups of alloys after 1000 one hour cycles of oxidation at 1150°C.....	83
Table 5.1 Nominal composition (at. %) of the two $\gamma+\gamma'$ model alloys studied in this chapter.....	86
Table 5.2 Volume fraction of scale phases (% $\theta$ -Al <sub>2</sub> O <sub>3</sub> and % $\alpha$ -Al <sub>2</sub> O <sub>3</sub> ) of Ni-20Al-5Cr-0.05Hf-0.05Y and Ni-20Al-5Cr-0.05Hf-0.05Y-1Si after oxidized at 1100°C for different time ..	94

## LIST OF FIGURES

Figure 2.1 Ellingham diagram .....	5
Figure 2.2 Simplified model for diffusion-controlled oxidation .....	7
Figure 2.3 Arrhenius diagram for the growth of selected oxides .....	8
Figure 2.4 Schematic diagram of the transition from internal oxidation to external oxidation....	10
Figure 2.5 Crystal structure of $\alpha$ -Al <sub>2</sub> O <sub>3</sub> .....	13
Figure 2.6 The hexagonal unit cell of $\gamma$ -Al <sub>2</sub> O <sub>3</sub> . The oxygen ions are represented by the light-gray spheres and the octahedrally and tetrahedrally coordinated aluminum ions are represented by the big and small dark-gray spheres, respectively .....	13
Figure 2.7 The crystal structure of $\theta$ -Al <sub>2</sub> O <sub>3</sub> . The oxygen ions are represented by blue spheres and the octahedrally and tetrahedrally aluminum ions are represented by red and yellow spheres respectively. Unit cell is shown by lines.....	14
Figure 2.8 Common sequences of phase transformation toward $\alpha$ -Al <sub>2</sub> O <sub>3</sub> .....	15
Figure 2.9 Arrhenius diagrams of log k <sub>p</sub> vs. 1/T for oxidation of pure Ni <sub>50</sub> Al <sub>50</sub> .....	17
Figure 2.10 Arrhenius plot of parabolic rate constant of some Al <sub>2</sub> O <sub>3</sub> -scale forming alloy compositions (see Table 2.1 for references) .....	19
Figure 2.11 Comparison of the apparent parabolic growth constants for Al <sub>2</sub> O <sub>3</sub> with diffusion data .....	23
Figure 2.12 Schematic diagram of the transport process of the growth of Al <sub>2</sub> O <sub>3</sub> scale .....	23
Figure 2.13 Compositional effects on the oxidation of binary Ni-Al system.....	25
Figure 2.14 Isothermal diagram showing the composition limits for the three oxidation mechanisms of Ni-Cr-Al alloys in 0.1 atm of oxygen at 1000°C.....	27
Figure 2.15 Arrhenius diagram for the oxidation of pure NiAl and NiAl-Cr alloys .....	28

Figure 2.16 Typical cyclic oxidation results showing the effect of Y on the adherence of Al <sub>2</sub> O <sub>3</sub> scale formed on FeCrAl alloy at 1200°C in air .....	30
Figure 2.17 Effect of hydrogen annealing on the cyclic oxidation behavior of René N5 (w/o Y) at 1150°C, annealed at 1280°C for 100 hours in 5% H <sub>2</sub> vs. un-annealed control .....	31
Figure 2.18 The effect of Y content on the oxidation weight gain of Co-10Cr-11Al alloy after 100 hours exposure at 1100°C in air.....	32
Figure 2.19 Cyclic oxidation kinetics for several NiCrAl alloys un-doped and single-doped (Hf or Y) with reactive elements exposed at 1100°C.....	34
Figure 2.20 Effect of Hf contents on the overall oxidation weight gain of Co-10Cr-11Al after 100 hours of exposure at 1100°C in air .....	34
Figure 2.21 Effect of Hf and Y contents on the overall oxidation weight gain of CoCrAl and NiAl alloys after 100 hours of exposure at 1100°C.....	35
Figure 2.22 Oxidation kinetics of Ni-22Al-30Pt un-doped and doped with Hf .....	36
Figure 2.23 Cross-section TEM study of Ni-22Al-30Pt un-doped and doped with Hf after 30 minutes of oxidation .....	37
Figure 2.24 Cyclic oxidation kinetics of unmodified and 1 wt. % Si-modified B-1900 superalloys at (a) 1000°C and (b) 1100°C .....	42
Figure 2.25 Effect of silicon concentration of isothermal oxidation kinetics of B-1900 superalloy at 1100°C and 1200°C .....	43
Figure 2.26 Relative oxidation and hot corrosion resistance of high temperature coating systems .....	49
Figure 2.27 Schematic diagram showing the constitution of thermal barrier coating system.....	52
Figure 3.1 Setaram high performance symmetrical TAG system.....	55
Figure 3.2 Schematic diagram of the procedure of cyclic oxidation test.....	56
Figure 4.1 Compositional (Ni-Cr-Al) positions of alloy groups on the oxide map at 1100°C.....	61
Figure 4.2 Isothermal oxidation kinetics of modified-René N5 alloys without and with 0.5 at. % silicon addition at 1150°C.....	63
Figure 4.3 Parabolic plots of weight gain as a function of square root of time of modified-René N5 alloys without and with 0.5 at. % silicon addition at 1150°C.....	64
Figure 4.4 Cross-sectional SEM images of modified-René N5 alloys after 100 hours of isothermal oxidation at 1150°C (a) without Si addition (b) with 0.5 at. % Si addition....	64

Figure 4.5 Cyclic oxidation kinetics of modified-René N5 alloys without and with 0.5 at. % Si addition during 1 hour cycles at 1150°C .....	68
Figure 4.6 Cross-sectional SEM images of modified-René N5 alloys after 1000 1 hour cycles of oxidation at 1150°C (a) without Si addition (b) with 0.5 at. % Si addition.....	68
Figure 4.7 Isothermal oxidation kinetics of Ni-20Al-5Cr-0.05Hf-0.05Y and Ni-20Al-5Cr-0.05Hf-0.05Y-1Si at 1150°C .....	71
Figure 4.8 Parabolic plots of weight gain as a function of square root of time for Ni-20Al-5Cr-0.05Hf-0.05Y and Ni-20Al-5Cr-0.05Hf-0.05Y-1Si at 1150°C .....	71
Figure 4.9 Cross-sectional SEM images of (a) Ni-20Al-5Cr-0.05Hf-0.05Y and (b) Ni-20Al-5Cr-0.05Hf-0.05Y-1Si after 100 hours of oxidation at 1150°C.....	72
Figure 4.10 Cyclic oxidation kinetics of Ni-20Al-5Cr-0.05Hf-0.05Y and Ni-20Al-5Cr-0.05Hf-0.05Y-1Si during 1000 one hour cycles at 1150°C .....	75
Figure 4.11 Cross-sectional SEM images of (a) Ni-20Al-5Cr-0.05Hf-0.05Y and (b) Ni-20Al-5Cr-0.05Hf-0.05Y-1Si after 1000 one hour cycles of oxidation at 1150°C .....	75
Figure 4.12 Isothermal oxidation kinetics of Ni-7.5Cr-13Al-1Ta-1Re-0.12C-0.05Hf-0.05Y-0.5Si and Ni-7.5Cr-13Al-1Ta-1Re-0.12C-0.05Hf-0.05Y-1Si at 1150°C .....	77
Figure 4.13 Parabolic plots of weight gain as a function of square root of time for Ni-7.5Cr-13Al-1Ta-1Re-0.12C-0.05Hf-0.05Y-0.5Si and Ni-7.5Cr-13Al-0.12C-0.05Hf-0.05Y-1Si at 1150°C .....	77
Figure 4.14 Cross-sectional SEM images of (a) Ni-7.5Cr-13Al-1Ta-1Re-0.12C-0.05Hf-0.05Y-1Si and (b) Ni-7.5Cr-13Al-1Ta-1Re-0.12C-0.05Hf-0.05Y-0.5Si after 100 hours of isothermal oxidation at 1150°C .....	78
Figure 4.15 Cyclic oxidation kinetics of Ni-7.5Cr-13Al-1Ta-1Re-0.12C-0.05Hf-0.05Y-0.5Si and Ni-7.5Cr-13Al-1Ta-1Re-0.12C-0.05Hf-0.05Y-1Si during 1 hour cycles at 1150°C .....	79
Figure 4.16 Comparison of parabolic rate constants (1150°C) of three groups of alloy studied in this chapter .....	82
Figure 4.17 Comparison of overall weight gain of three groups of alloys after 1000 one hour cycles of oxidation at 1150°C.....	83
Figure 5.1 Characteristic luminescence spectrum of Cr <sup>3+</sup> -doped $\alpha$ -Al <sub>2</sub> O <sub>3</sub> and $\theta$ -Al <sub>2</sub> O <sub>3</sub> <sup>[140]</sup> .....	87
Figure 5.2 Confocal photo-stimulated microspectroscopy (CPSM) images of thermally grown $\theta$ -Al <sub>2</sub> O <sub>3</sub> and $\alpha$ -Al <sub>2</sub> O <sub>3</sub> formed on Ni-20Al-5Cr-0.05Hf-0.05Y. $\theta$ -Al <sub>2</sub> O <sub>3</sub> is represented by green color and $\alpha$ -Al <sub>2</sub> O <sub>3</sub> is represented by red color. Series images were taken after oxidized for 0.5h, 2h, 6h, 10h, 20h and 50h on Linkam TS1500 hot stage at 1100°C in air. ....	90

Figure 5.3 Confocal photo-stimulated microspectroscopy (CPSM) images of thermally grown $\theta$ - $\text{Al}_2\text{O}_3$ and $\alpha$ - $\text{Al}_2\text{O}_3$ formed on Ni-20Al-5Cr-0.05Hf-0.05Y-1Si. $\theta$ - $\text{Al}_2\text{O}_3$ is represented by green color and $\alpha$ - $\text{Al}_2\text{O}_3$ is represented by red color. Series images were taken after oxidized for 0.5h, 2h, 6h, 10h, 20h and 50h on Linkam TS1500 hot stage at 1100°C in air. ....	91
Figure 5.4 Semi-quantitative approximation of the phase composition of $\theta$ - $\text{Al}_2\text{O}_3$ and $\alpha$ - $\text{Al}_2\text{O}_3$ formed on Ni-20Al-5Cr-0.05Hf-0.05Y and Ni-20Al-5Cr-0.05Hf-0.05Y-1Si alloys as a function of oxidation time at 1100°C .....	95
Figure 5.5 T-T-T type diagram of aluminum oxides formed on Ni-20Al-5Cr-0.05Hf-0.05Y over temperature range 800~1100°C .....	101
Figure 5.6 T-T-T type diagram of aluminum oxides formed on Ni-20Al-5Cr-0.05Hf-0.05Y-1Si over temperature range 800~1100°C .....	102
Figure 5.7 X-ray diffraction spectra of Ni-20Al-5Cr-0.05Hf-0.05Y after 100h oxidation at 800°C (black), 900°C (red), 1000°C (blue) and 1100°C (pink).....	103
Figure 5.8 X-ray diffraction spectra of Ni-20Al-5Cr-0.05Hf-0.05Y-1Si after 100h oxidation at 800°C (red), 900°C (red), 1000°C (blue) and 1100°C (pink).....	103
Figure 5.9 (a) $\Delta m$ vs. $t$ curve of Ni-20Al-5Cr-0.05Hf-0.05Y alloy at 1100°C in air (b) Corresponding $n^i$ vs. $t$ curve of the $\Delta m$ vs. $t$ curve .....	107
Figure 5.10 Schematic of the proposed three-stage $\theta \rightarrow \alpha$ - $\text{Al}_2\text{O}_3$ transformation model during $\text{Al}_2\text{O}_3$ -scale growth .....	108
Figure 5.11 (a) $\Delta m$ vs. $t$ curves of Ni-20Al-5Cr-0.05Hf-0.05Y and Ni-20Al-5Cr-0.05Hf-0.05Y-1Si oxidized at 1100°C in dry air; (b) Corresponding calculated $n^i$ vs. $t$ curves of data shown in (a); (c) Corresponding simulated $f_\alpha$ vs. $t$ curves of data shown in (a) .....	112
Figure 5.12 Comparison of $f_\alpha$ vs. $t$ curves determined by kinetic analysis and obtained by quantitative x-ray diffraction of Ni-20Al-5Cr-0.05Hf-0.05Y alloy oxidized at 1100°C in dry air .....	113
Figure 5.13 (a) Hf-Si phase diagram; (b) Y-Si phase diagram .....	118
Figure 6.1 Surface morphologies of Ni-20Al-5Cr-0.05Hf-0.05Y (a, c, e) and Ni-20Al-5Cr-0.05Hf-0.05Y-1Si (b, d, f) after oxidation at 1150°C for 10 minutes (a – without Si and b – with Si), 0.5 hour (c – without Si and d – with Si) and 2 hours (e – without Si and f – with Si).....	130
Figure 6.2 (a) Cross-sectional STEM images of Ni-20Al-5Cr-0.05Hf-0.05Y after 10 minutes of oxidation at 1150°C (b) Corresponding EDS analysis spectra of selected points .....	133
Figure 6.3 (a) Cross-sectional STEM image of Ni-20Al-5Cr-0.05Hf-0.05Y-1Si after 10 minutes of oxidation at 1150°C (b) Corresponding EDS analysis spectra of selected points.....	134

Figure 6.4 (a) Cross-sectional STEM image of Ni-20Al-5Cr-0.05Hf-0.05Y after 30 minutes of oxidation at 1150°C; (b) and (c) Corresponding EDS analysis spectra of three selected representative areas .....	137
Figure 6.5 (a) Cross-sectional STEM images of Ni-20Al-5Cr-0.05Hf-0.05Y-1Si after 30 minutes of oxidation at 1150°C; (b) and (c) Corresponding EDS analysis spectra of two selected representative areas .....	139
Figure 6.6 Cross-sectional images (a) Ni-20Al-5Cr-0.05Hf-0.05Y and (b) Ni-20Al-5Cr-0.05Hf-0.05Y-1Si after 2 hours of oxidation at 1150°C .....	141
Figure 6.7 EDS line scan analysis of Hf and Y segregation to the grain boundary of Al <sub>2</sub> O <sub>3</sub> scale formed on Ni-20Al-5Cr-0.05Hf-0.05Y alloy after 2 hours of oxidation at 1150°C.....	142
Figure 6.8 TEM selected area diffraction (SAE) pattern of α-Al <sub>2</sub> O <sub>3</sub> [661] taken from the inner layer of the Al <sub>2</sub> O <sub>3</sub> scale formed on Ni-20Al-5Cr-0.05Hf-0.05Y-1Si after 2 hours of oxidation at 1150°C .....	143
Figure 6.9 Semi-quantitative EDS analysis of the Si concentration across from the Al <sub>2</sub> O <sub>3</sub> scale to the alloy substrate for Ni-20Al-5Cr-0.05Hf-0.05Y-1Si after 2 hours of oxidation at 1150°C .....	146
Figure 6.10 Summary of the cross-sectional STEM images of the Al <sub>2</sub> O <sub>3</sub> scale formed on Ni-20Al-5Cr-0.05Hf-0.05Y and Ni-20Al-5Cr-0.05Hf-0.05Y-1Si alloys after 10 minutes, 30 minutes and 2 hours of oxidation at 1150°C.....	148
Figure 6.11 Ni-Al-O phase diagram .....	151
Figure 6.12 (a-d) Schematic of the formation of Ni-rich particles near the scale/metal interface during the early stage of oxidation.....	152
Figure 6.13 Schematics of the transient oxidation of Ni-20Al-5Cr-0.05Hf-0.05Y and Ni-20Al-5Cr-0.05Hf-0.05Y-1Si at 1100°C .....	157
Figure 6.14 (a-d) Elemental maps of Hf and Y obtained by ToF-SIMS after 50 hours of oxidation at 1100°C (a and b) Hf and Y intensity maps in alumina scale formed on the Ni-20Al-5Cr-0.05Hf-0.05Y alloy (c and d) Hf and Y intensity maps in alumina scale formed on the Ni-20Al-5Cr-0.05Hf-0.05Y-1Si alloy.....	158

## PREFACE

Firstly, I would like to truly thank my academic advisor, Professor Brian M. Gleeson, for giving me the opportunity to study with him and for the time and effort that he spent on mentoring, sponsoring and motivating me to pursue my PhD. Definitely, I would have never finished my thesis without Professor Gleeson's help and support.

I would like to thank my committee members: Dr. Gerald H. Meier, Dr. Ian Nettleship and Dr. Lei Li for their invaluable suggestions to improve my thesis.

I would like to thank Dr. Zhihong Tang for his generous assistance in alloy preparation and cyclic oxidation testing.

I would also like to thank Prof. Arthur H. Heuer, Dr. David Hovis and other researchers in the Swagelok Center for Surface Analysis of Materials at Case Western Reserve University for their technical assistance in advanced materials characterization and data analysis.

Special thanks go to Dr. Xiahan Sang for his help in TEM/STEM characterization.

Many thanks go to my colleagues Dr. Wei Zhao, Dr. Xu Liu, Dr. Xiaodan Wu, Dr. Nan Mu and Dr. Juan Manuel Alvarado Orozco. During my stay at Prof. Gleeson's group, I enjoyed our discussion and exchange of ideas very much.

My final acknowledgement goes to my family. Without your love and support, this work would never have been completed.

This work was funded by the Office of Naval Research.

## 1.0 INTRODUCTION

Metallic components used at elevated temperatures usually rely on the formation of a slow-growing, thermally grown oxide (TGO) to protect them against degradation by high-temperature oxidation and hot corrosion. An ideally formed protective TGO should remain stable, dense, planar, continuous and adherent during exposure to service environments. At temperatures above 900°C,  $\alpha$ -Al<sub>2</sub>O<sub>3</sub> is the most desired oxide because of its long-term chemical stability, low oxygen diffusivity and slow growth rate. Thus, a substantial amount of research has been focused on the development of Al<sub>2</sub>O<sub>3</sub>-scale forming alloys and metallic coatings.

There are several factors which determine the establishment of a protective Al<sub>2</sub>O<sub>3</sub> scale; among the most important is the substrate composition. The amount of aluminum in an M-Al (M = base metal) binary alloy necessary for forming external Al<sub>2</sub>O<sub>3</sub> scale depends on such factors as temperature and alloy structure, but the fundamental basis for predicting this amount stems from Wagner's theories <sup>[6]</sup>. A systematic experimental study on the oxidation behavior of the Ni-Al system was firstly reported by Pettit <sup>[7]</sup>. In that work, the oxidation data for binary Ni-Al alloys were presented as a function of temperature and Al contents, and the oxidation behavior was characterized by three regions corresponding to different mechanisms. Subsequently, the influence of a "third element", particularly Cr, was investigated and summarized in the form of oxide maps, which provide general strategies for the design of ternary Al<sub>2</sub>O<sub>3</sub>-scale forming

alloys and coating compositions. A manifestation of the “third element” effect is to facilitate the establishment of an  $\text{Al}_2\text{O}_3$  scale.

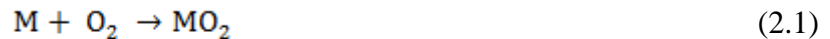
Recently, emphasis has been placed on the influence of minor-element (e.g. Hf, Y, La, Zr, Si, Pt, etc.) additions, which play a significant role in improving the properties and hence performance of  $\text{Al}_2\text{O}_3$  scale<sup>[9-13, 15-17]</sup>. For example, a small amount of Y addition ( $\ll 0.5$  at. %) can remarkably improve scale adhesion<sup>[9, 11]</sup>. Although there have been numerous studies on the mechanism of minor-element effects, this subject is still of considerable interest because there remain many fundamental aspects that are not well understood, particularly with respect to the role of minor-elements on the initial stages of  $\text{Al}_2\text{O}_3$  formation<sup>[14, 17]</sup>. Moreover, recent studies have shown that the addition of two more minor-elements, such as Hf+Y or Hf+Y+Si, has a highly beneficial effect on the formation of protective  $\text{Al}_2\text{O}_3$  scale<sup>[16]</sup>. Indeed more effort is needed to understand the synergistic effects of minor-elements, so that the addition of minor-elements can be optimized to obtain the optimal performance of the  $\text{Al}_2\text{O}_3$  scale.

## 2.0 TECHNICAL BACKGROUND

### 2.1 FUNDAMENTALS OF HIGH TEMPERATURE OXIDATION OF METALS

#### 2.1.1 Thermodynamic and kinetic fundamentals of metal oxidation

Oxidation of metals is a heterogeneous reaction in which metal atoms in solid phase react with oxygen molecules in gas phase to form oxide phase<sup>[2]</sup>. It is not only a chemical reaction but also related to mass transportation between different phases<sup>[3]</sup>. Generally, the oxidation reaction is written as follows<sup>[2]</sup>:



whether the oxidation reaction can thermodynamically occur or not is determined by the Gibbs free energy change of this process. The standard Gibbs free energy of this reaction is calculated by the following equation<sup>[2]</sup>:

$$\Delta G^\circ = -RT \ln \left( \frac{a_{MO_2}}{a_M p_{O_2}} \right) \quad (2.2)$$

where  $a_i$  is the chemical activity of species  $i$ ,  $T$  is the absolute temperature and  $R$  is the gas constant.

If the activity of metal and oxide are taken as unity, the oxygen partial pressure becomes<sup>[2]</sup>:

$$p_{O_2}^{M/MO_2} = e^{\Delta G^{\circ}/RT} \quad (2.3)$$

When the oxygen partial pressure in the environment is greater than this equilibrium partial pressure, oxide is stable to form on a metal surface.

Thermodynamic data are often presented in thermodynamic diagrams, which are useful tools in interpreting the results in oxidation research. There are several kinds of thermodynamic diagrams constructed for different purposes. The Ellingham diagram (Figure 2.1) <sup>[2]</sup>, which is categorized as a standard free energy of formation vs. temperature diagram, is mostly used to determine if an oxide (or sulfide, carbide, etc.) is likely to form under certain conditions. The oxygen partial pressure in equilibrium with oxide can be determined by drawing a straight line from the origin point “O” at the top left corner of the diagram (Figure 2.1 **Ellingham diagram** <sup>[2]</sup>), through the free energy line at the temperature of interest, to intersect with the  $p_{O_2}$  scale on the right side. The value at the intersecting point is the oxygen partial pressure in equilibrium with oxide. Thus, by comparing the oxygen partial pressure in the environment to the oxygen partial pressure in equilibrium with the oxide, the possibility of the formation of this oxide can be ascertained.

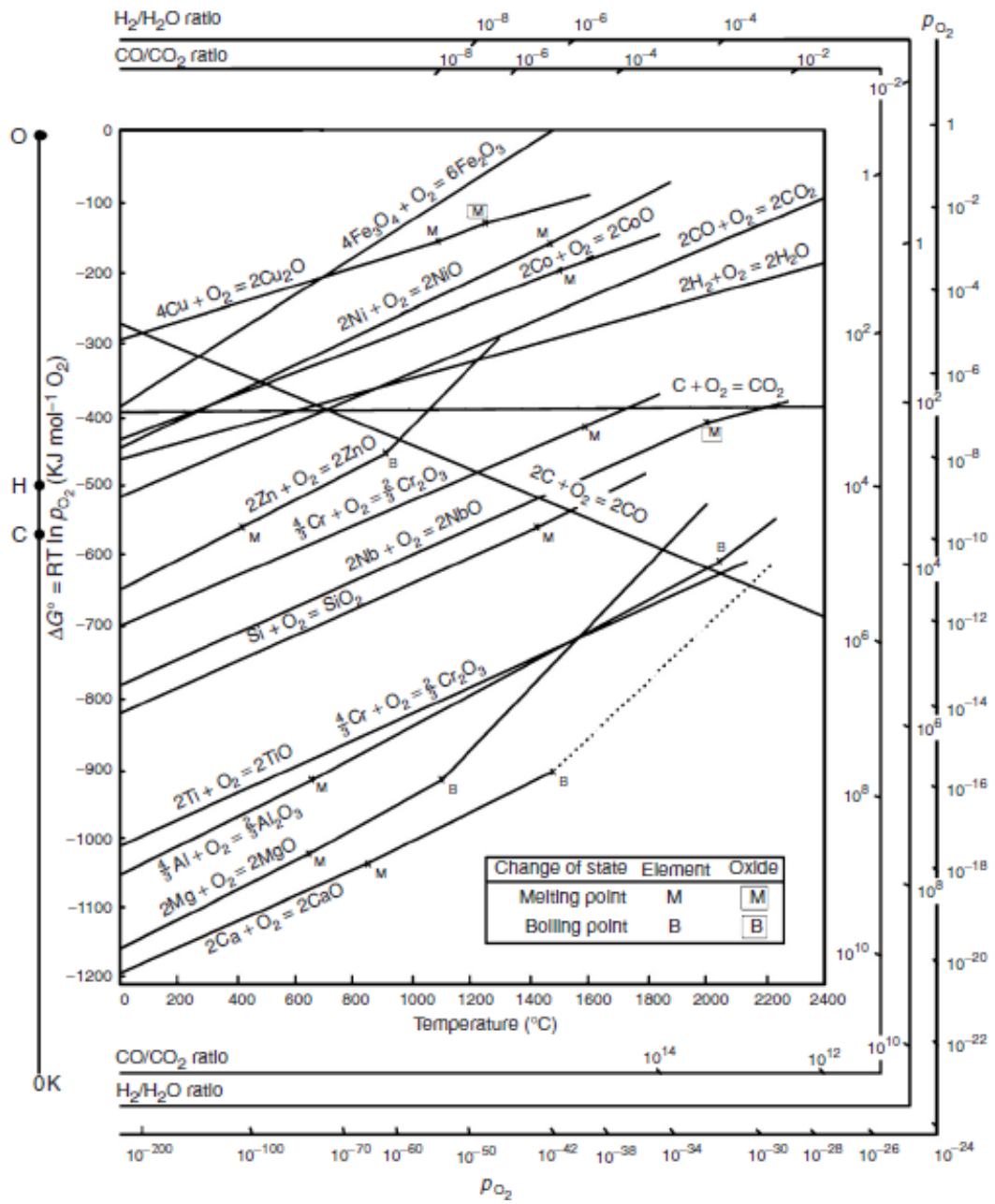


Figure 2.1 Ellingham diagram [2]

Generally, the oxidation rate of metals follows a kinetic rate law that can be defined as:

$$\frac{d\xi}{dt} = f(t) \quad (2.4)$$

where  $\xi$  is a measure of the extent of reaction at time  $t$  [3].

In principle, the oxidation rate of metals can be measured either by the amount of metal or oxygen consumed, or the amount of oxide produced. In practice, the thermogravimetric method is usually used to measure the rate of oxidation by continuously recording the mass gain of the metal or alloy samples as a function of reaction time.

The overall metal oxidation process can be subdivided into several steps [3]: 1) transport of metal to the metal (or alloy)/oxide interface; 2) transport of oxygen to the oxide/gas interface; 3) incorporation of metal or oxygen into the oxide scale; 4) migration of metal and/or oxygen through the oxide scale. Therefore, the overall oxidation rate must be limited by one of these steps. In the case of oxide scale growth, the growth rate is commonly controlled by diffusion of some species through the scale. In such a case, the parabolic rate law (mass gain is proportional to the square root of time) is obeyed, i. e.

$$\Delta m^2 = k_p \cdot t \quad (2.5)$$

where  $\Delta m$  is the mass gain per unit area at time  $t$  and  $k_p$  is the apparent parabolic rate constant.

It should be noted that the parabolic rate law only applies to the stage when a continuous and sufficiently thick oxide scale has been established. It does not apply to the initial stage of oxidation, which is surface-process controlled and too rapid to be observed for most metals.

Figure 2.2<sup>[2]</sup> schematically shows a simplified reaction and transport process for diffusion-controlled oxide growth.

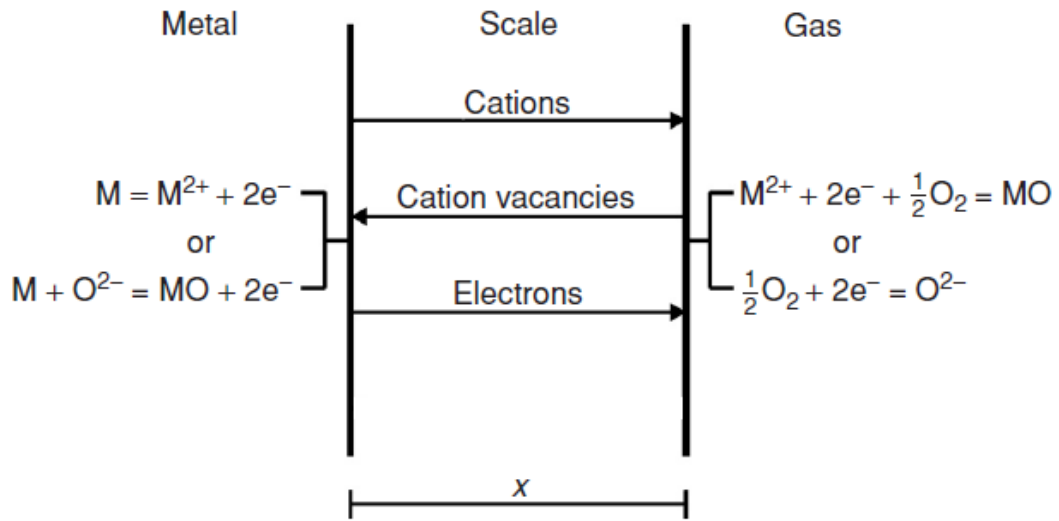


Figure 2.2 Simplified model for diffusion-controlled oxidation<sup>[2]</sup>

In addition to the parabolic rate law, linear and cubic rate laws, together with other empirical combined rate laws can also be obeyed in some conditions<sup>[2]</sup>. For example, oxidation at very high temperature in a dilute oxygen gas mixture may follow the linear rate law because the overall oxidation rate is limited by the transportation of oxygen from bulk gas to oxide/gas interface rather than by diffusion of ions through the scale<sup>[2]</sup>. Another example is the formation of volatile oxides simultaneously with solid oxides. In this situation, a combined rate law containing both parabolic and linear terms is used to describe the oxidation kinetics<sup>[3]</sup>.

Experimental kinetic results for the growth of oxide scale are often presented in the form of apparent parabolic rate constant  $k_p$ . The temperature dependence of  $k_p$  is expressed in an Arrhenius diagram, in which  $k_p$  is plotted as a function of  $1/T$ . Figure 2.3 is the Arrhenius diagram for the growth of some selected oxides<sup>[87]</sup>.

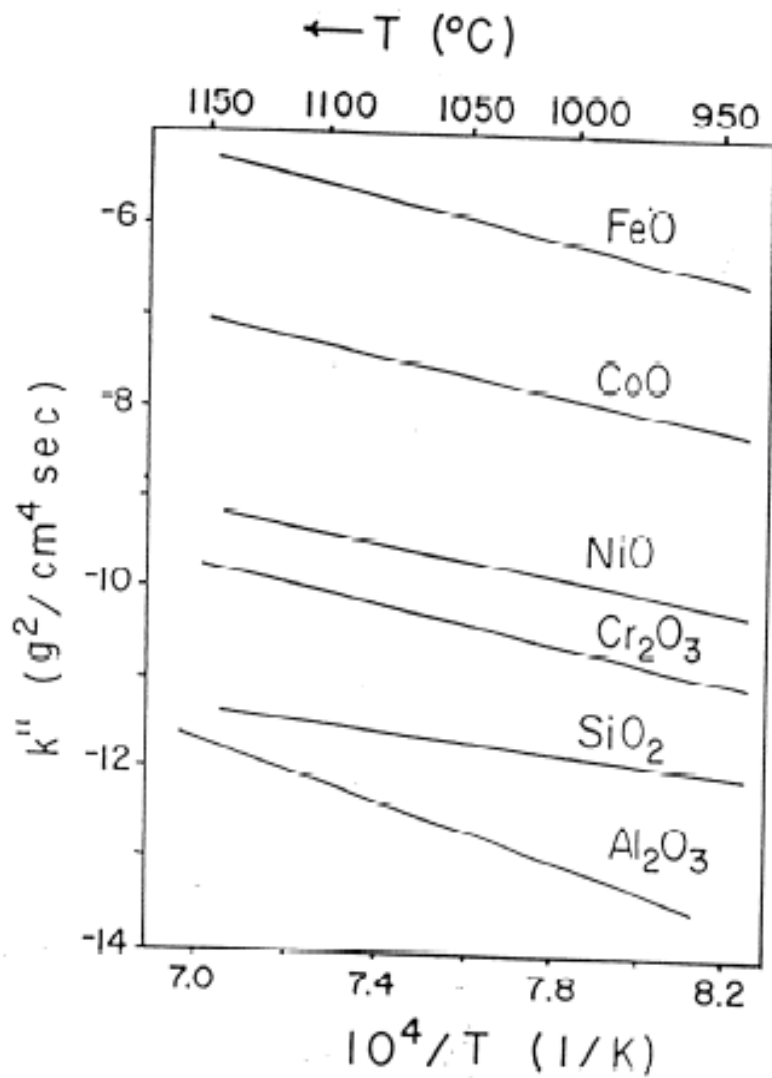


Figure 2.3 Arrhenius diagram for the growth of selected oxides<sup>[87]</sup>

### 2.1.2 Oxidation of alloys

When an alloy is exposed to an oxidizing environment, it can be oxidized in two modes: internally or externally (or occur simultaneously) <sup>[2]</sup>. Internal oxidation is the process in which oxygen molecules dissolve in an alloy, diffuse inward and oxidize one or more elements to form sub-surface precipitates; while external oxidation is the process in which oxidizable alloy elements diffuse outward rapidly and form a continuous layer of oxide scale above the alloy substrate. In practice, internal oxidation is usually undesirable because it may induce corrosion failure by causing embrittlement and dilation of the alloy subsurface region; on the other hand, external oxidation, which is the basis for designing oxidation-resistant of engineering alloys, is often highly desired <sup>[3]</sup>. The crucial factor determining the oxidation mode is the concentration of selectively oxidized solute in alloys. When the solute concentration is relatively low, internal oxidation occurs. As the solute concentration increases to a sufficiently high level, a layer of continuous protective oxide scale forms externally, as depicted schematically in Figure 2.4 <sup>[2]</sup>. Thus, there is a critical solute concentration associated with the transition from internal oxidation to external oxidation.

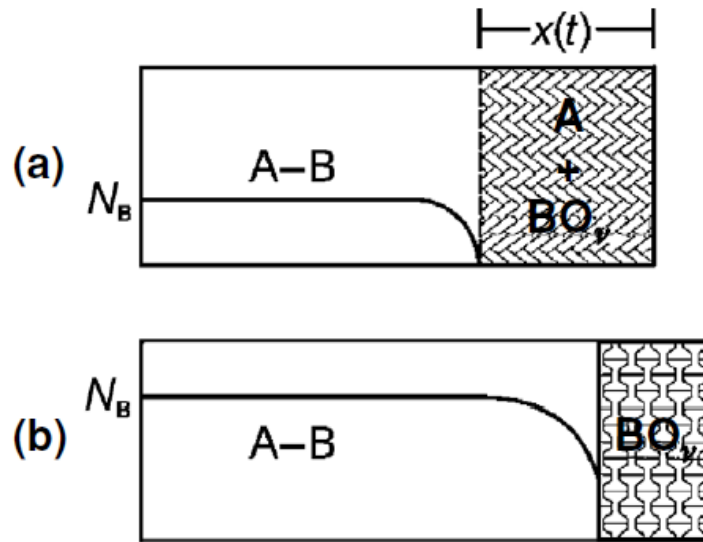


Figure 2.4 Schematic diagram of the transition from internal oxidation to external oxidation <sup>[2]</sup>

Wagner <sup>[6]</sup> proposed an equation for predicting the critical solute concentration. Considering the oxidation reaction of solute B (in solvent A):  $B + \nu O = BO_{\nu}$ , the critical concentration is expressed as follows:

$$N_B^{(o)} = \left[ \frac{\pi g^*}{2\nu} N_O^{(S)} \frac{D_O V_m}{D_B V_{ox}} \right]^{1/2} \quad (2.6)$$

where  $N_B^{(o)}$  is the initial concentration of solute B,  $N_O^{(S)}$  is the oxygen solubility in solvent A,  $D_O$  is the diffusivity of oxygen in solvent A,  $D_B$  is the diffusivity of solute B,  $V_m$  is the molar volume of the solvent A,  $V_{ox}$  is the molar volume of the oxide  $BO_{\nu}$ ,  $\nu$  is the stoichiometric coefficient in the oxidation reaction and  $g^*$  is critical volume fraction of internally precipitated oxide to facilitate the transition.

The mechanism of the transition from internal oxidation to external oxidation was also qualitatively explained by Wagner <sup>[6]</sup>. The internally precipitated oxides, which are usually

impermeable to oxygen, reduce the oxygen inward diffusion. When the oxygen flux is reduced lower than the critical rate for new precipitates nucleation, the outward diffusion of solute B dominates. If the initial solute concentration  $N_B^{(0)}$  is high enough to provide continuous outward flux for the growth of oxides, external oxidation occurs.

## 2.2 ALUMINA-SCALE FORMING ALLOY SYSTEMS

Most engineering alloys used at elevated temperature (e. g. above  $\sim 700^\circ\text{C}$ ) are based on Fe, Co, Ni, which form fast growing, and hence non-protective oxides from the standpoint of long term service. Their oxidation resistance relies on forming a continuous, slow-growing oxide scale by selectively oxidizing some solute (e.g. Cr, Al, Si, etc.)<sup>[1-3]</sup>.

Aluminum is one of the most important alloying elements for high-temperature alloys and metallic coatings. It plays a significant role in providing oxidation resistance by forming continuous and slow-growing  $\alpha\text{-Al}_2\text{O}_3$  scale. The thermodynamically stable  $\alpha\text{-Al}_2\text{O}_3$  scale acts as diffusion barrier, which significantly lowers the metal and oxygen diffusion rate through the oxides. In this way, the oxidation rate is substantially limited to an acceptable low extent.

A great deal of effort has been put on the development of protective  $\alpha\text{-Al}_2\text{O}_3$  scale. There are two key factors determining the protective  $\alpha\text{-Al}_2\text{O}_3$  scale formation<sup>[3]</sup>: temperature and Al content. First of all, the oxidation temperature must be high enough to promote the formation of  $\alpha\text{-Al}_2\text{O}_3$  in preference to those non-protective meta-stable aluminum oxides such as  $\gamma\text{-Al}_2\text{O}_3$  and  $\theta\text{-Al}_2\text{O}_3$ ; secondly, according to Wagner's theory<sup>[6]</sup>, the Al content must be sufficiently high to suppress the internal oxidation and maintain an exclusively external oxidation.

In the following sections, these aspects related to the formation of  $\text{Al}_2\text{O}_3$  scale will be reviewed.

### 2.2.1 Aluminum oxide polymorphs and structural relationships

Aluminum oxide exists in several phases of which  $\alpha$  phase is the most stable thermodynamically. Meta-stable phases, also called transient phases, include  $\gamma$ ,  $\theta$ ,  $\delta$ ,  $\kappa$ ,  $\eta$ ,  $\chi$ ,  $\lambda$   $\beta$  etc., which tend to transform to  $\alpha$  phase after further heating <sup>[18-19]</sup>. The crystal structure of all aluminum oxides can be simply described as a close-packed oxygen sub-lattice with different occupation of tetrahedral and/or octahedral vacancies by aluminum. Depending on the stacking sequence of oxygen layers, aluminum oxides fall into three distinguished groups: ABAB... group ( $\alpha$ - $\text{Al}_2\text{O}_3$ ,  $\kappa$ - $\text{Al}_2\text{O}_3$  and  $\chi$ - $\text{Al}_2\text{O}_3$ ), ABCABC ... group ( $\gamma$ - $\text{Al}_2\text{O}_3$ ,  $\delta$ - $\text{Al}_2\text{O}_3$  and  $\theta$ - $\text{Al}_2\text{O}_3$ ) and ABAC... group ( $\beta$ - $\text{Al}_2\text{O}_3$ ) <sup>[20, 31]</sup>. Among these  $\text{Al}_2\text{O}_3$  polymorphs,  $\gamma$ - $\text{Al}_2\text{O}_3$ ,  $\theta$ - $\text{Al}_2\text{O}_3$  and  $\alpha$ - $\text{Al}_2\text{O}_3$  are the most commonly met in high-temperature oxidation of alloys <sup>[21]</sup>.

$\alpha$ - $\text{Al}_2\text{O}_3$  has a close-packed hexagonal structure in which the oxygen anions constitute an hcp sublattice and aluminum cations occupy 2/3 of the octahedral interstices in an ordered array, shown in Figure 2.5 <sup>[32]</sup>;  $\gamma$ - $\text{Al}_2\text{O}_3$  is commonly described as a cubic defect spinel structure in which the oxygen anions form an fcc sublattice and aluminum cations occupy the octahedrally and tetrahedrally coordinated interstices, see Figure 2.6 <sup>[20]</sup>. Viewing along the [111] direction,  $\text{O}^{2-}$  and  $\text{Al}^{3+}$  layers alternate in  $\alpha$ - $\text{Al}_2\text{O}_3$ , whereas in  $\gamma$ - $\text{Al}_2\text{O}_3$ ,  $\text{Al}^{3+}$  layers arrange in two ways: either layers containing only octahedrally coordinated cations or mixed layers containing both octahedrally and tetrahedrally coordinated cations <sup>[31]</sup>. The lattice structure of  $\theta$ - $\text{Al}_2\text{O}_3$  is monoclinic instead of cubic. It is a structural isomorph of  $\beta$ - $\text{Ga}_2\text{O}_3$ , shown in Figure 2.7 <sup>[32-33]</sup>. Aluminum cations in  $\theta$ - $\text{Al}_2\text{O}_3$  equally distribute over octahedral and tetrahedral interstices.

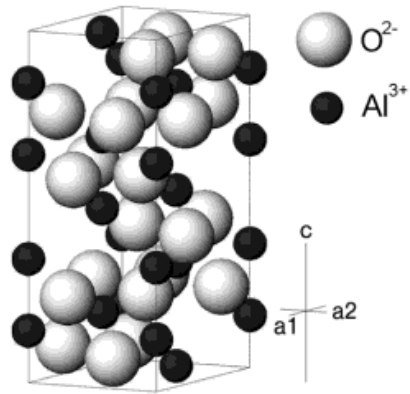


Figure 2.5 Crystal structure of  $\alpha\text{-Al}_2\text{O}_3$  <sup>[32]</sup>

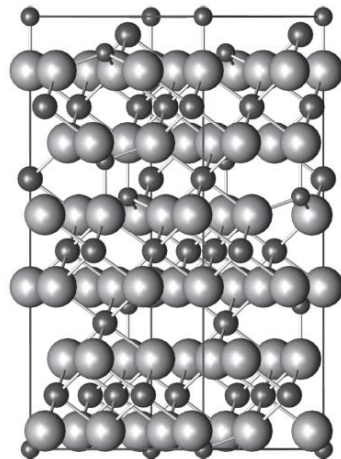


Figure 2.6 The hexagonal unit cell of  $\gamma\text{-Al}_2\text{O}_3$ . The oxygen ions are represented by the light-gray spheres and the octahedrally and tetrahedrally coordinated aluminum ions are represented by the big and small dark-gray spheres, respectively <sup>[20]</sup>

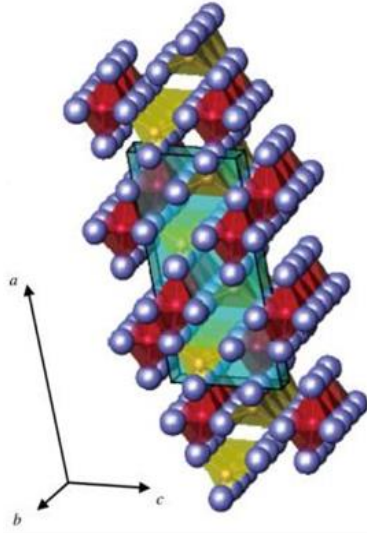


Figure 2.7 The crystal structure of  $\theta$ - $\text{Al}_2\text{O}_3$ . The oxygen ions are represented by blue spheres and the octahedrally and tetrahedrally aluminum ions are represented by red and yellow spheres respectively. Unit cell is shown by lines <sup>[33]</sup>

Rühle *et al.* <sup>[27]</sup> studied the crystallographic orientation relationship between  $\gamma$ - $\text{Al}_2\text{O}_3$  and  $\alpha$ - $\text{Al}_2\text{O}_3$  formed during the transient oxidation stage of  $\gamma'$ - $\text{Ni}_3\text{Al}$  by transmission electron microscopy (TEM). The close-packed planes and close-packed directions of  $\alpha$ - $\text{Al}_2\text{O}_3$  are parallel to the close-packed planes and close-packed directions of  $\gamma$ - $\text{Al}_2\text{O}_3$ , yielding the orientation relationship  $(0001) [1-100]_{\alpha} \parallel (111) [1-10]_{\gamma}$ . Wynnyckyj and Morris <sup>[29]</sup> investigated the kinetics of  $\theta$ - $\text{Al}_2\text{O}_3$  to  $\alpha$ - $\text{Al}_2\text{O}_3$  transformation and proposed a two-stage, diffusional/synchro-shear model. This model involves the formation of critical-sized crystallites and a subsequent rapid non-diffusional shear-type transformation. Moreover, some researchers described the transformation within meta-stable  $\text{Al}_2\text{O}_3$ s and to stable  $\alpha$ - $\text{Al}_2\text{O}_3$  in terms of ordering of cation vacancies, which results in the change of transport properties and growth rate of the scale <sup>[28, 33-34]</sup>.

## 2.2.2 Kinetics of aluminum oxides phase transformation

Ceramists have thoroughly studied the transformation sequences from meta-stable  $\text{Al}_2\text{O}_3$  to stable  $\alpha\text{-Al}_2\text{O}_3$ . The commonly met transformation routes are schematically summarized in Figure 2.8<sup>[19]</sup>. Differences in transformation sequences are ascribed to different precursors.

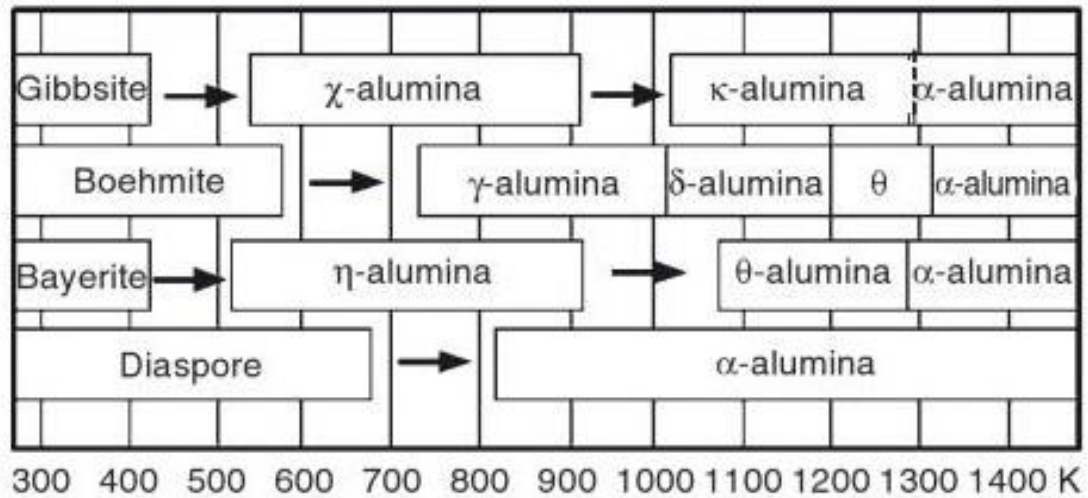


Figure 2.8 Common sequences of phase transformation toward  $\alpha\text{-Al}_2\text{O}_3$ <sup>[19]</sup>

The phase transformation kinetics of  $\text{Al}_2\text{O}_3$  is influenced by many factors, such as temperature, grain size, heating rate, water vapor partial pressure, additives and impurities etc. Among these factors, the influences of temperature and additives are usually paid more attention in the case of  $\text{Al}_2\text{O}_3$ -scale growth<sup>[19, 23-25]</sup>.

At an oxidation temperature below about  $1200^\circ\text{C}$ , nearly all  $\text{Al}_2\text{O}_3$ -scale forming alloys undergo a transient oxidation stage during which meta-stable aluminas (mainly  $\gamma\text{-Al}_2\text{O}_3$  and  $\theta\text{-Al}_2\text{O}_3$ ) form and transform to stable  $\alpha\text{-Al}_2\text{O}_3$ <sup>[3, 14, 17, 20, 21, 28, 35, 37]</sup>. This process plays a significant role in the scale growth behavior and affects the scale performance from two important aspects.

Firstly, the phase transformation from meta-stable aluminas to  $\alpha$ -Al<sub>2</sub>O<sub>3</sub> is accompanied by large volume shrinkage (~10%)<sup>[127]</sup>, because the crystal structure of  $\alpha$ -Al<sub>2</sub>O<sub>3</sub> is more close-packed than that of the meta-stable aluminas<sup>[18, 30-32]</sup>. Stresses developed by such volume contraction will cause cracking, which may deteriorate the scale protection against oxidation and limit the service life of the airfoils<sup>[128-131]</sup>. Secondly, the growth rate of meta-stable aluminas is much higher (1~2 orders of magnitude at the same temperature) than that of  $\alpha$ -Al<sub>2</sub>O<sub>3</sub><sup>[21, 35]</sup>, and the growth of meta-stable Al<sub>2</sub>O<sub>3</sub> is primarily dominated by outward diffusion of aluminum<sup>[14, 48, 132]</sup>. Consequently, the longer the meta-stable aluminas exist, the more aluminum will deplete from the subsurface region of alloy substrate. Overconsumption of aluminum will cause breakaway oxidation when the aluminum level in the alloy substrate is too low to sustain a protective alumina scale<sup>[133]</sup>.

Grabke<sup>[21]</sup> systematically studied the scaling rates of NiAl in the temperature range 700-1400°C and compiled an Arrhenius diagram indicating the Arrhenius lines for  $\gamma$ -Al<sub>2</sub>O<sub>3</sub>,  $\theta$ -Al<sub>2</sub>O<sub>3</sub> and  $\alpha$ -Al<sub>2</sub>O<sub>3</sub>, see Figure 2.9. The hatched regions in this diagram indicated the occurring of phase transformation. In the temperature range 875-925°C, the transformation from  $\gamma$ -Al<sub>2</sub>O<sub>3</sub> to  $\theta$ -Al<sub>2</sub>O<sub>3</sub> caused a slight  $k_p$  increase; in contrast, in the temperature range 950-1050°C, the transformation from  $\theta$ -Al<sub>2</sub>O<sub>3</sub> to  $\alpha$ -Al<sub>2</sub>O<sub>3</sub> results in an abrupt decrease of  $k_p$  by two orders of magnitude. The slow growth rate of  $\alpha$ -Al<sub>2</sub>O<sub>3</sub> is associated with its close packed structure, which makes the transportation of ions difficult through the scale; while the higher growth rate of meta-stable aluminum oxides is related to their relative looser packed structures, which lower the activation energy of lattice diffusion.

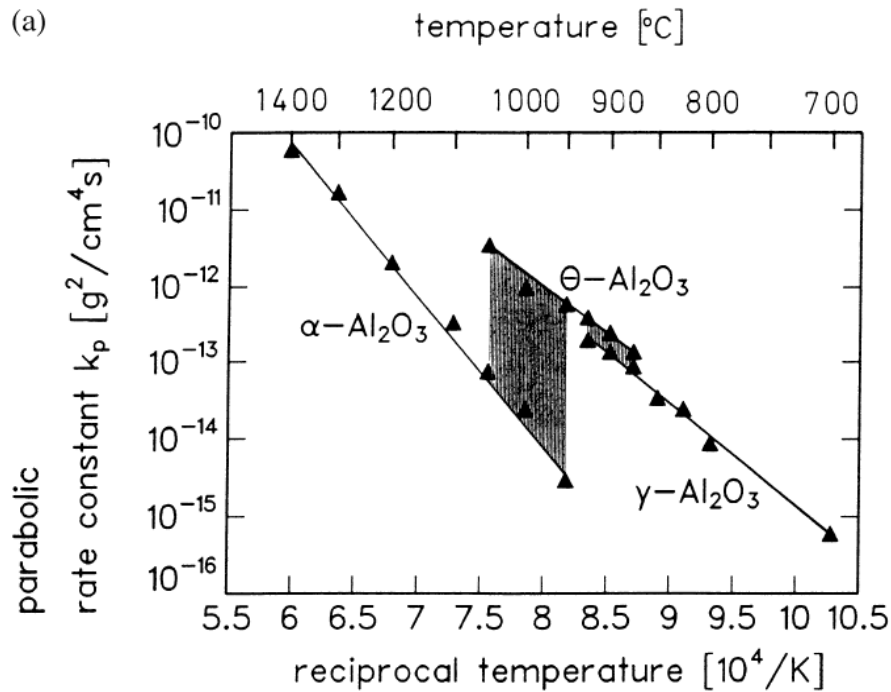


Figure 2.9 Arrhenius diagrams of  $\log k_p$  vs.  $1/T$  for oxidation of pure  $\text{Ni}_{50}\text{Al}_{50}$  [21]

The influences of additives on  $\text{Al}_2\text{O}_3$  phase transformation kinetics have also been studied frequently by ceramists [19, 23, 147, 156-157]. Even though most of those studies were conducted on powders, they can still be used as references for investigating the kinetics of  $\text{Al}_2\text{O}_3$ -scale formation. Pijolat *et al.* [23] studied the effects of  $\text{Zr}^{4+}$  and  $\text{Mg}^{2+}$  on the transformation of meta-stable aluminas to  $\alpha\text{-Al}_2\text{O}_3$ . Their results showed that  $\text{Zr}^{4+}$  inhibits the transformation to  $\alpha\text{-Al}_2\text{O}_3$ , whereas  $\text{Mg}^{2+}$  accelerates this transformation. Vereshagin *et al.* [24] reported that  $\text{Sc}^{3+}$ ,  $\text{Y}^{3+}$  and  $\text{La}^{3+}$  promote the formation of  $\alpha\text{-Al}_2\text{O}_3$ . Simpkin *et al.* [25] studied the influence of Cr and Fe on the formation of  $\alpha\text{-Al}_2\text{O}_3$  from  $\gamma\text{-Al}_2\text{O}_3$ . Their results indicated that 2~5 wt. % addition of Fe promotes the transformation to  $\alpha\text{-Al}_2\text{O}_3$ , whereas 2~4 wt. % Cr retards this transformation. In addition, they noticed that Cr exists as  $\text{Cr}^{6+}$  in  $\gamma\text{-Al}_2\text{O}_3$ , but as  $\text{Cr}^{3+}$  in  $\alpha\text{-Al}_2\text{O}_3$ .

Al<sub>2</sub>O<sub>3</sub>. The compositional effects on phase transformation kinetics in thermally grown Al<sub>2</sub>O<sub>3</sub> will be discussed in more detail in the following sections.

### 2.2.3 Kinetics of steady-state alumina scale formation

The values of parabolic rate constants  $k_p$  for the growth of steady-state Al<sub>2</sub>O<sub>3</sub>-scale can be found in numerous papers [7, 35, 37-47]. Some selective data of un-doped Ni-based Al<sub>2</sub>O<sub>3</sub>-scale forming compositions are summarized in Table 2.1 and presented in an Arrhenius diagram in Figure 2.10. The parabolic rate constants distribute among around one order of magnitude at 1000°C or higher, and the distribution expands wider at temperatures below about 1000°C. There are several reasons for the existence of this dispersion. Firstly, as mentioned in section 2.2.2, the establishment of Al<sub>2</sub>O<sub>3</sub> scale usually experiences a transient stage, during which fast growing meta-stable aluminas form and tend to transform to stable  $\alpha$ -Al<sub>2</sub>O<sub>3</sub>. Since the meta-stable  $\rightarrow$   $\alpha$ -Al<sub>2</sub>O<sub>3</sub> transformation kinetics is influenced by many factors, the contribution of the fast kinetics during transient stage to the overall oxidation kinetics may vary from alloy to alloy. Secondly, since the growth of Al<sub>2</sub>O<sub>3</sub> scale is dominated by both O<sup>2-</sup> inward and Al<sup>3+</sup> outward diffusion through grain boundaries, deviation may exist because of the difference in scale morphologies and microstructures. Thirdly, the impurity level in the alloy substrate also affects the growth kinetics of Al<sub>2</sub>O<sub>3</sub> scale by affecting the transport rate of oxygen and/or aluminum. Finally, different data process methods may result in different  $k_p$  values. For example, Pieraggi [88] proposed that using  $\Delta m$  vs.  $t^{1/2}$  plot is superior to the  $\Delta m^2$  vs.  $t$  plot in determining the steady state parabolic rate constant.

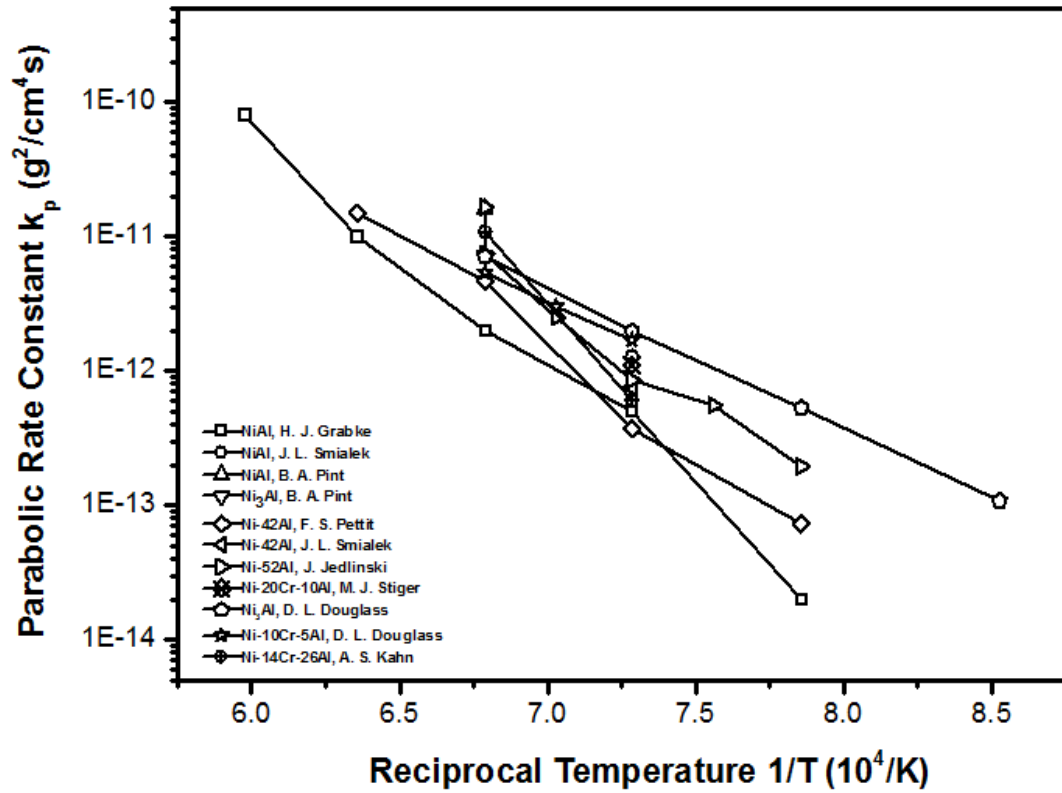


Figure 2.10 Arrhenius plot of parabolic rate constants of some  $\text{Al}_2\text{O}_3$ -scale forming alloy compositions (see Table 2.1 for references)

Table 2.1 Summary of parabolic rate constants of some Al<sub>2</sub>O<sub>3</sub>-scale forming alloy compositions

Code	Alloy (at. %)	Atmosphere	Time (hr)	Temperature (°C)	k <sub>p</sub> (g <sup>2</sup> /cm <sup>4</sup> •s)	Reference
A	NiAl	Dry He-O <sub>2</sub>	N/A	900(θ)	~2×10 <sup>-13</sup>	[35]
				1000	~2×10 <sup>-14</sup>	
				1100	~5×10 <sup>-13</sup>	
				1200	~2×10 <sup>-12</sup>	
				1300	~1×10 <sup>-11</sup>	
				1400	~8×10 <sup>-11</sup>	
B	NiAl	1 atm air	100	1100	1.28×10 <sup>-12</sup>	[37]
C	NiAl	1 atm air		1200	~1.6×10 <sup>-11</sup>	[39]
D	Ni <sub>3</sub> Al	1 atm air		1200	7.1×10 <sup>-12</sup>	[40]
E	Ni-42Al	0.1 atm air		1000	7.28×10 <sup>-14</sup>	[7]
				1100	3.72×10 <sup>-13</sup>	
				1200	4.67×10 <sup>-12</sup>	
				1300	1.49×10 <sup>-11</sup>	
F	Ni-42Al	1 atm air	100	1100	7.5×10 <sup>-13</sup>	[41]
G	Ni-52Al	1 atm air	200	1000	1.95×10 <sup>-13</sup>	[42]
				1050	5.53×10 <sup>-13</sup>	
				1100	8.58×10 <sup>-13</sup>	
				1150	2.51×10 <sup>-12</sup>	
				1200	7.42×10 <sup>-12</sup>	
				1300	1.65×10 <sup>-11</sup>	
H	Ni-20Cr-10Al	1 atm air		1100	1.1×10 <sup>-12</sup>	[43]
I	Ni <sub>3</sub> Al	1 atm air	50	1200	7.1×10 <sup>-12</sup>	[44]
				1100	1.97×10 <sup>-12</sup>	
				1000	5.3×10 <sup>-13</sup>	
				900	1.08×10 <sup>-13</sup>	
J	Ni-10Cr-5Al	1 atm air	60	1200	5.4×10 <sup>-12</sup>	[45]
				1150	3.0×10 <sup>-12</sup>	
				1100	1.7×10 <sup>-12</sup>	
K	Ni-14Cr-26Al	1 atm air	30.5	1200	1.08×10 <sup>-11</sup>	[46]
				1100	6.03×10 <sup>-13</sup>	
L	Ni-42Al	1 atm air	100	900	4.61×10 <sup>-14</sup>	[47]
	Ni-50Al			2.31×10 <sup>-13</sup>		
	Ni-55Al			6.0×10 <sup>-13</sup>		

## 2.2.4 Transport properties associated with alumina-scale formation

There has been a great deal of studies on the transport processes in  $\alpha$ -Al<sub>2</sub>O<sub>3</sub> in order to gain a better understanding of the growth mechanism of the scale [48-56]. However, the mechanism is not always straightforward because the transport properties in alumina scales are sensitive to many factors, such as substrate chemical compositions (e.g. impurities and reactive elements), scale phase compositions (meta-stable Al<sub>2</sub>O<sub>3</sub> vs.  $\alpha$ -Al<sub>2</sub>O<sub>3</sub>), and scale microstructure (fine-grained vs. coarse-grained Al<sub>2</sub>O<sub>3</sub>) etc. Previously, an inert-marker method was widely used to determine the transport mechanism, but recent studies have shown that results obtained by this method are not always reliable [4]. Nowadays, investigation of transport mechanism mainly relies on the isotopic tracer method [48-49]. The two-stage-oxidation experiment, in which a sample was firstly oxidized in <sup>16</sup>O<sub>2</sub> atmosphere and subsequently in an <sup>18</sup>O<sub>2</sub> enriched atmosphere, is often conducted. By interpreting the in-depth concentration of <sup>18</sup>O, the transport mode can be ascertained.

Young and de Wit [48] initially studied the oxidation mechanism of NiAl by <sup>18</sup>O tracer and Rutherford backscattering spectrometry at the temperature range between 1170K and 1420K. Their results indicated that Al<sup>3+</sup> outward diffusion is the predominant transport process. Jedlinski and Borchardt [49] also studied the oxidation mechanism of  $\beta$ -NiAl by two-stage oxidation method using isotope <sup>18</sup>O tracer. It was found that the Al<sub>2</sub>O<sub>3</sub> scale formed mainly by Al<sup>3+</sup> outward diffusion. Furthermore, the contribution of the O<sup>2-</sup> inward diffusion increased with the increasing of temperature and oxidation time. Later work by Pint *et al.* [50] on  $\beta$ -NiAl and FeCrAl alloys showed that at 1200°C the un-doped  $\alpha$ -Al<sub>2</sub>O<sub>3</sub> was grown by simultaneous Al<sup>3+</sup> and O<sup>2-</sup> transports.

The transport properties of meta-stable Al<sub>2</sub>O<sub>3</sub> have not been studied as thoroughly as that of  $\alpha$ -Al<sub>2</sub>O<sub>3</sub>. Pint *et al.* [50] investigated the growth mechanism of  $\theta$ -Al<sub>2</sub>O<sub>3</sub> formed on FeCrAl

alloys. It was shown that  $\theta$ -Al<sub>2</sub>O<sub>3</sub> grew primarily by Al<sup>3+</sup> outward diffusions. Graham *et al.* [51] studied the oxidation of Fe-8Al alloy at 850°C. Their results indicated that Al<sup>3+</sup> outward diffusion is predominant during the growth of  $\gamma$ -Al<sub>2</sub>O<sub>3</sub>.

The measurements of diffusion coefficients of Al<sup>3+</sup> and O<sup>2-</sup> in Al<sub>2</sub>O<sub>3</sub> have been carried out by many workers. The diffusion coefficients of oxygen in both single crystalline and polycrystalline aluminum oxides were also measured in order to determine the effect of grain boundaries [52-54]. Hindam and Whittle [55] compiled a diagram comparing the effective diffusion coefficients ( $D_{\text{eff}}$ ) of Al<sup>3+</sup> and O<sup>2-</sup> with apparent parabolic growth constants for Al<sub>2</sub>O<sub>3</sub>, see Figure 2.11. A reasonable conclusion has been drawn that grain boundary diffusion is responsible for the growth of Al<sub>2</sub>O<sub>3</sub> scale.

So far, it is generally accepted that the growth of Al<sub>2</sub>O<sub>3</sub> scale is dominated by both Al<sup>3+</sup> outward and O<sup>2-</sup> inward diffusion through Al<sub>2</sub>O<sub>3</sub> grain boundaries, schematically shown in Figure 2.12 [137].

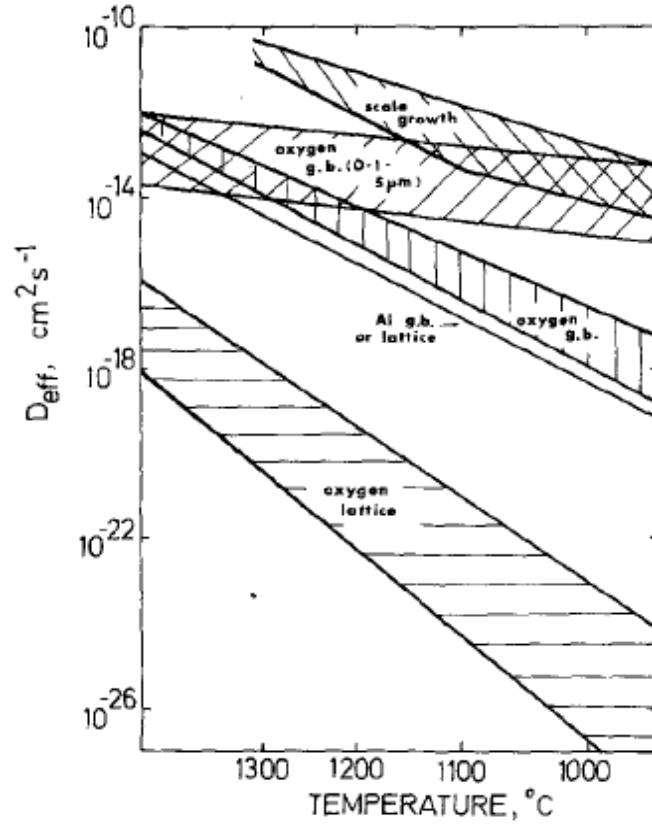


Figure 2.11 Comparison of the apparent parabolic growth constants for  $\text{Al}_2\text{O}_3$  with diffusion data <sup>[55]</sup>

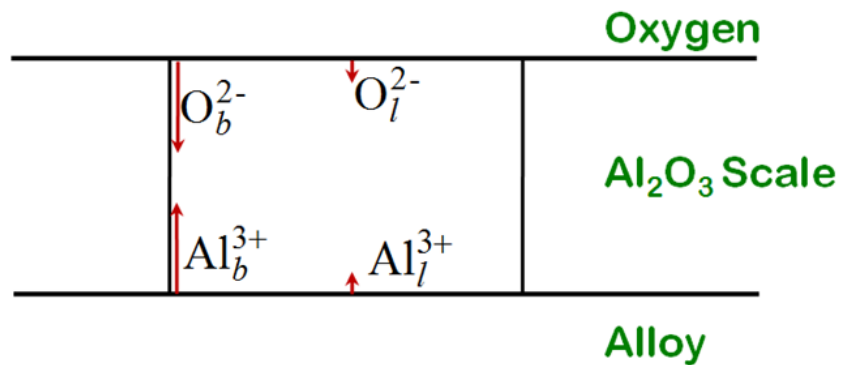


Figure 2.12 Schematic diagram of the transport process of the growth of  $\text{Al}_2\text{O}_3$  scale <sup>[137]</sup>

## **2.2.5 Compositional effects on the oxidation behavior of alumina scale forming systems**

Alloying elements play an important role in the oxidation behavior of  $\text{Al}_2\text{O}_3$ -scale forming alloys and metallic coatings. Effects of major alloying elements, Al and Cr, are of primary concern because they are added to almost all superalloys in order to improve not only environmental resistances but also mechanical properties <sup>[7-8]</sup>. In addition to Al and Cr, effects of minor elements, especially reactive elements (REs), are often taken into account because of their beneficial effects on improving scale performance <sup>[9-11]</sup>. In the following sections, the effects of both major and minor alloying elements on the oxidation behavior of  $\text{Al}_2\text{O}_3$ -scale forming alloys will be introduced in more detail.

### **2.2.5.1 Effects of major alloying elements (Al and Cr)**

One of the most important factors determining the formation of protective  $\text{Al}_2\text{O}_3$  scale is the Al content. According to Wagner's <sup>[6]</sup> theory introduced in section 2.1.2, the Al content must be high enough to suppress the internal oxidation and maintain an exclusively external formation of  $\text{Al}_2\text{O}_3$  scale. The effects of Al content on the oxidation behavior of Ni-Al and Fe-Al binary systems, which are the base composition of diffusion coatings for gas turbine engines, were studied extensively. Pettit <sup>[7]</sup> systematically studied the effect of Al content of the oxidation behavior of Ni-Al binary system in pure oxygen environment at 0.1 atm. The oxidation results were presented in a diagram as a function of temperature and composition, see Figure 2.13. This diagram is characterized by three regions corresponding to different oxidation mechanisms. In region I, external NiO and internal  $\text{Al}_2\text{O}_3$  formed at all temperatures investigated; in region II, external  $\text{Al}_2\text{O}_3$  formed initially, but subsequently it was overtaken by rapidly growing NiO and spinel due to inadequate supply of Al; in region III, steady-state external  $\text{Al}_2\text{O}_3$  formed

exclusively because of either increasing temperature or Al supply. This diagram can be used as a reference when designing the composition of alloys and metallic coatings, which need the formation of  $\text{Al}_2\text{O}_3$  scale for oxidation protection.

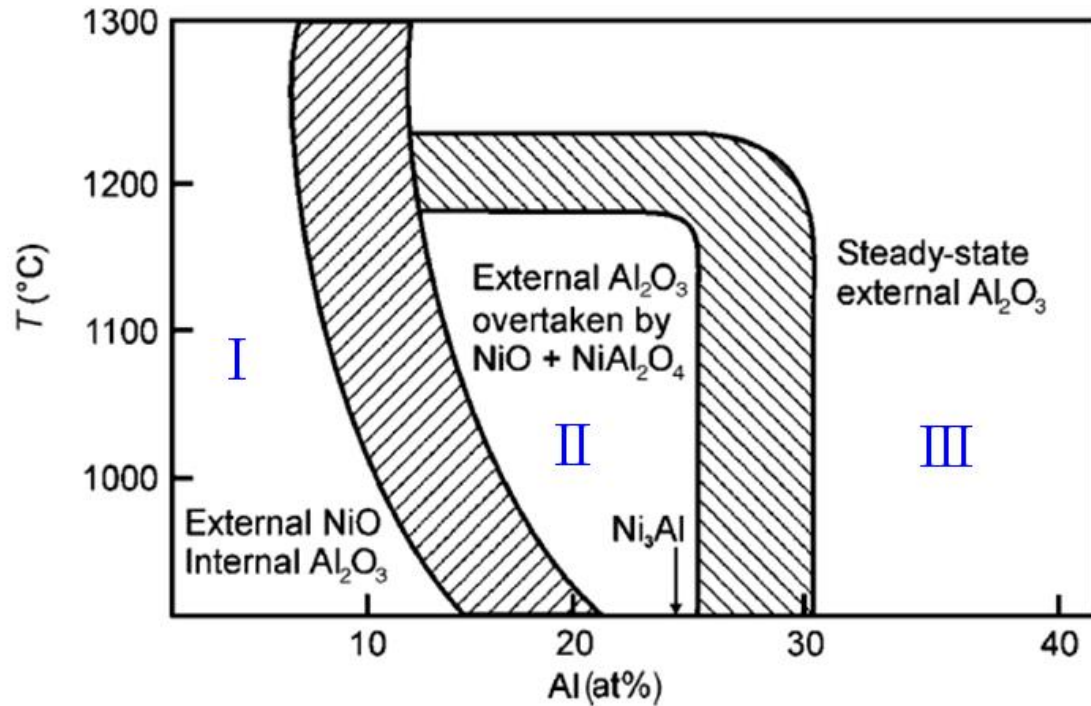


Figure 2.13 Compositional effects on the oxidation of binary Ni-Al system <sup>[7]</sup>

The oxidation behavior of the Fe-Al system is similar to that of Ni-Al system <sup>[92-93]</sup>. The minimum amount of Al required forming protective  $\text{Al}_2\text{O}_3$  scale has also been investigated. At 800°C, the experiment value of the critical Al content is approximately 13.3 at. % <sup>[92]</sup>. A more carefully study estimates this value around 14 at. % at temperature range 800-1000°C <sup>[93]</sup>.

The compositional effects of Cr were also studied thoroughly by a number of investigators because it strongly affects the oxidation and hot corrosion resistance as well as mechanical properties <sup>[8, 91]</sup>. With respect to the oxidation resistance of  $\text{Al}_2\text{O}_3$ -scale forming alloy

system, the primary effect of Cr is that it reduces the critical Al content required for establishing an external  $\text{Al}_2\text{O}_3$  scale. Giggins and Pettit initially investigated the oxidation behavior of Ni-Cr-Al alloys between  $1000^\circ\text{C}$  and  $1200^\circ\text{C}$ , and constructed an “oxide map” in which the experimental oxidation results were superposed on the isothermal ternary composition triangle, as shown in Figure 2.14. This empirical diagram fell into three regions corresponding to three different oxidation mechanisms. In region I, external NiO scale and internal  $\text{Al}_2\text{O}_3/\text{Cr}_2\text{O}_3$  subscale formed; in region II, external  $\text{Cr}_2\text{O}_3$  scale and internal  $\text{Al}_2\text{O}_3$  subscale formed; in region III, only external  $\text{Al}_2\text{O}_3$  scale formed. Here, it should be noted that the oxide map was constructed based on kinetic processes rather than thermodynamic results even it looks similar to ternary phase diagram. From this oxide map, it can be seen that the addition of 10 wt. % Cr can reduce the critical Al content for external  $\text{Al}_2\text{O}_3$  formation to as low as 5 wt. %, while this critical values is around 17 wt. % for Ni-Al binary system without Cr addition. The proposed mechanism of Cr in promoting external  $\text{Al}_2\text{O}_3$  scale formation at much less lower Al content was that Cr limited the oxygen inward diffusion so that the internal oxidation of Al was suppressed. The reduction of Al content by adding Cr is of technological importance because it allowed the improvement of ductility of alloys and metallic coatings.

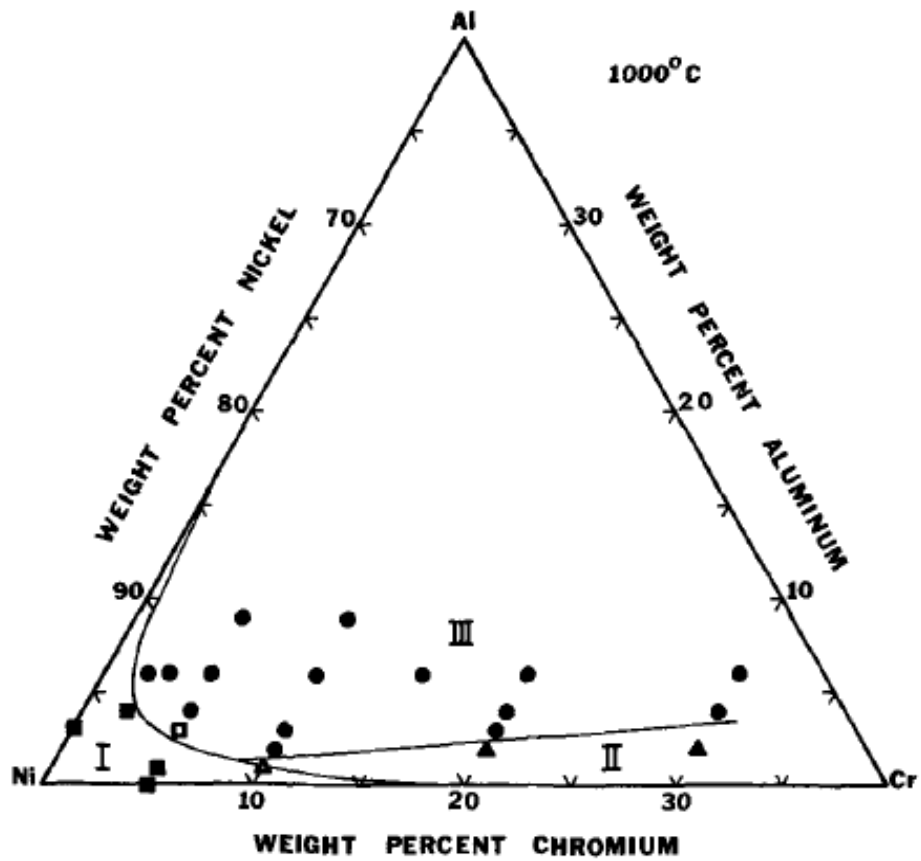


Figure 2.14 Isothermal diagram showing the composition limits for the three oxidation mechanisms of Ni-Cr-Al alloys in 0.1 atm of oxygen at 1000°C [8]

Another effect of Cr was that it stabilized  $\alpha$ - $\text{Al}_2\text{O}_3$  in preference to meta-stable  $\text{Al}_2\text{O}_3$  during the transient stage of oxidation. Brumm and Grabke <sup>[21]</sup> investigated the Cr effect on the initial oxidation stage of  $\beta$ -NiAl in the temperature range 700-1400°C. The Arrhenius diagram, which compared the datum of pure NiAl and NiAl alloyed with different concentration of Cr, is shown in Figure 2.15. At a temperature 1000°C for instance, the transformation of  $\theta \rightarrow \alpha$ - $\text{Al}_2\text{O}_3$  was faster for NiAl-Cr alloys than pure NiAl. It was postulated that the initial formation of  $\text{Cr}_2\text{O}_3$  favored the nucleation of  $\alpha$ - $\text{Al}_2\text{O}_3$  and therefore accelerated the meta-stable  $\rightarrow \alpha$ - $\text{Al}_2\text{O}_3$  transformation.

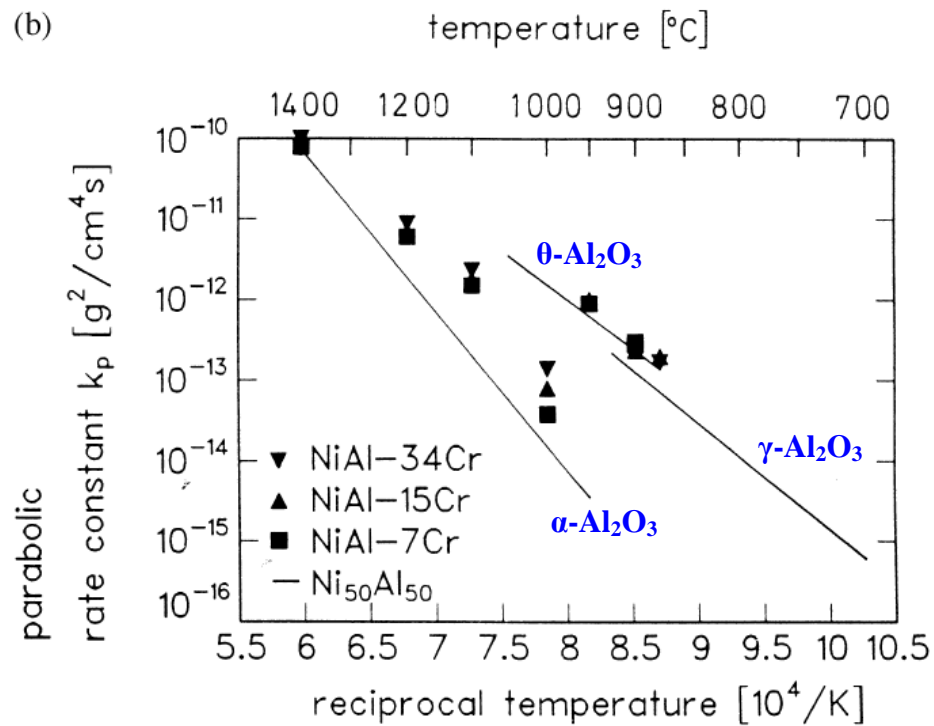


Figure 2.15 Arrhenius diagram for the oxidation of pure NiAl and NiAl-Cr alloys <sup>[21]</sup>

### 2.2.5.2 Effects of reactive elements (REs)

The study of the effects of reactive elements on the oxidation behavior began as early as 1937<sup>[9]</sup>. Since then, a significant amount of research has been conducted in order to understand the role of reactive elements in improving the oxidation resistance of alloys and metallic coatings using at elevated temperatures. Recently, substantial progresses in advanced characterization techniques made it possible to investigate the effects of reactive elements even at atomic level, giving a better insight into this subject.

Generally, reactive elements affect the oxidation behavior of alloys and metallic coatings in three ways <sup>[9-11]</sup>: 1) promote selective oxidation of the element (Al or Cr), which forms continuous protective oxide scale; 2) decrease the scale growth rate, but this effect is limited on Al<sub>2</sub>O<sub>3</sub>-scale forming alloys than on Cr<sub>2</sub>O<sub>3</sub>-scale forming alloys; 3) improve scale adhesion and inhibit scale failure. A number of mechanisms were proposed to explain the beneficial effects of reactive elements. Most of these mechanisms concern the role of reactive elements in changing the transport properties of diffusing species (Al<sup>3+</sup> and O<sup>2-</sup>). For instance, Y has been reported to segregate at oxide grain boundaries and change the growth mechanism of  $\alpha$ -Al<sub>2</sub>O<sub>3</sub> from combination of Al and O transportation to predominantly O diffusion <sup>[12]</sup>. While some other mechanisms paid attention to the influence of reactive elements on mechanical properties of Al<sub>2</sub>O<sub>3</sub> scale <sup>[61]</sup>. In the following sections, the effects of the mostly used reactive elements (Y and Hf) and their mechanism will be introduced in more detail.

#### *a) Effect of Yttrium*

Yttrium is the most frequently studied among these reactive elements adding to Al<sub>2</sub>O<sub>3</sub>-scale forming alloys, because it significantly improved the scale adhesion. Figure 2.16 is a typical cyclic oxidation results <sup>[92]</sup>, showing the improvement of Al<sub>2</sub>O<sub>3</sub> scale adherence by

addition of Y. There were several mechanisms proposed to explain the role of Y in improving  $\text{Al}_2\text{O}_3$  scale adherence. In 1980, Whittle and Stringer<sup>[9]</sup> summarized them as follows: 1) scale plasticity enhancement, 2) graded seal mechanism, 3) growth process modification, 4) chemical bonding, 5) vacancy sink mechanism and 6) oxide pegging. There were strong evidences supporting some of these hypotheses, but controversies still exist. For example, the “oxide pegging” mechanism was once widely recognized because oxide pegs was believed to provide mechanical keying for the scale by protruding into the alloy substrate. However, this mechanism does not always apply because good adherence can also be obtained by adding reactive elements in the absence of pegs<sup>[11]</sup>.

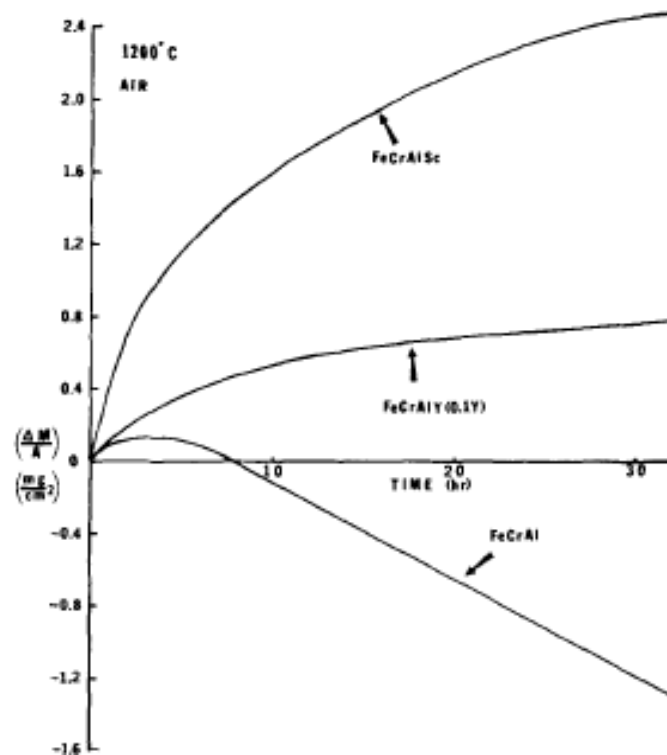


Figure 2.16 Typical cyclic oxidation results showing the effect of Y on the adherence of  $\text{Al}_2\text{O}_3$  scale formed on FeCrAl alloy at 1200°C in air<sup>[92]</sup>

The most recent breakthrough in understanding scale adhesion was the role of impurities, sulfur, in particular. By annealing alloys in H<sub>2</sub> atmosphere for desulfurization, scale adhesion was significantly improved, see Figure 2.17. Proper addition of Y was believed to neutralize the detrimental effect of S by a gettering effect, thereby enhancing scale adherence <sup>[94]</sup>. However, some studies suggested that S segregation may not be the only factor causing scale spallation <sup>[63]</sup>.

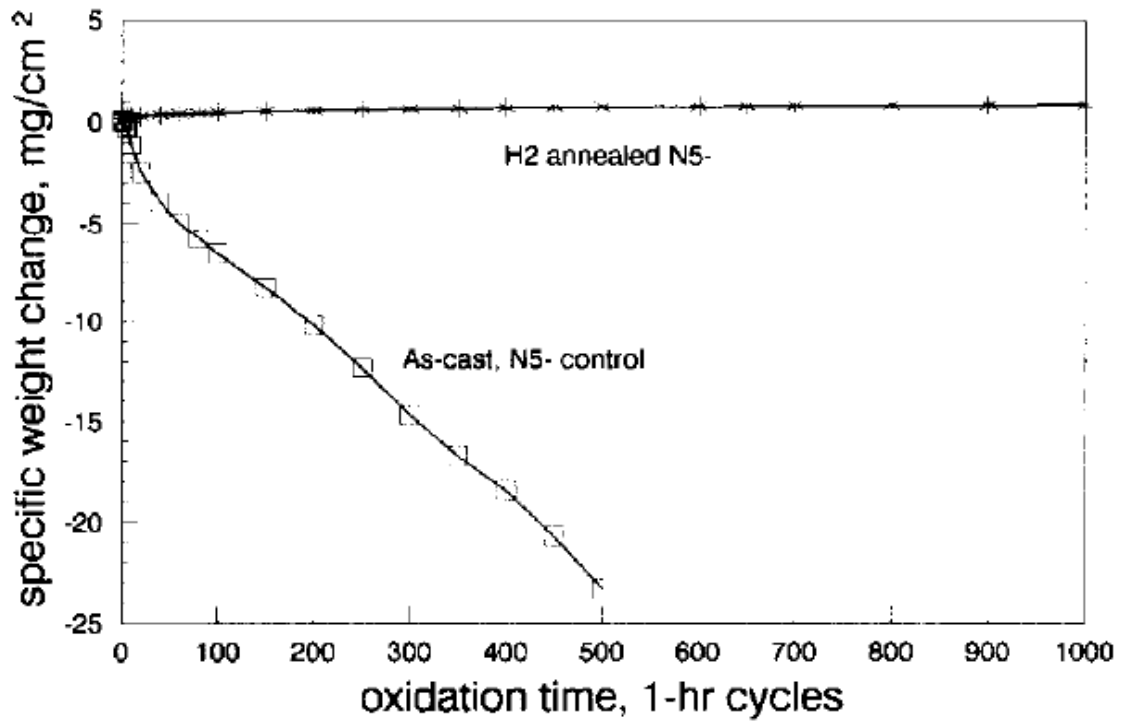


Figure 2.17 Effect of hydrogen annealing on the cyclic oxidation behavior of René N5 (w/o Y) at 1150°C, annealed at 1280°C for 100 hours in 5% H<sub>2</sub> vs. un-annealed control <sup>[79]</sup>

Yttrium addition was also reported to decrease the scale growth rate, but this effect was limited on Al<sub>2</sub>O<sub>3</sub>-scale forming alloy systems. Stringer and Whittle <sup>[59]</sup> systematically studied the relationship between Y content and isothermal oxidation rate of Co-Cr-Al alloys at 1100°C.

Their results indicated that the overall oxidation weight gain was decreased with the increasing of Y content, see Figure 2.18. These authors ascribed this effect to that Y decreased the length of the initial transient period before the establishment of steady state kinetics.

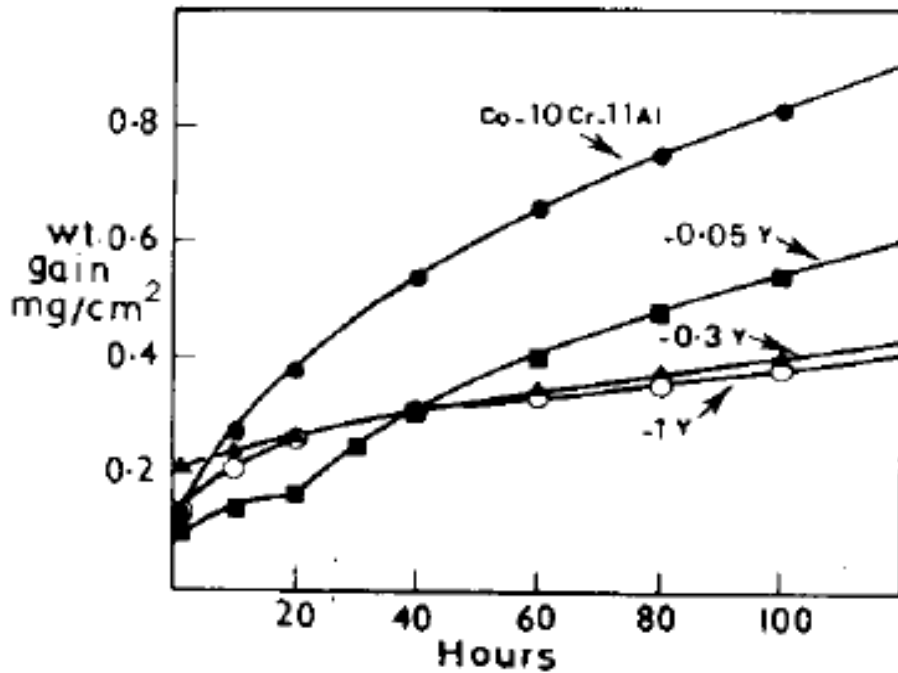


Figure 2.18 The effect of Y content on the oxidation weight gain of Co-10Cr-11Al alloy after 100 hours exposure at 1100°C in air <sup>[59]</sup>

Yttrium addition is also believed to affect the transient stage of  $\text{Al}_2\text{O}_3$  scale growth, particularly the meta-stable  $\rightarrow \alpha\text{-Al}_2\text{O}_3$  transformation kinetics. Since the meta-stable  $\text{Al}_2\text{O}_3$  is less protective than  $\alpha\text{-Al}_2\text{O}_3$ , the effect of Y is of significant concern from the standpoint of engineering. Previously, Y was believed to promote the protective  $\alpha\text{-Al}_2\text{O}_3$  scale formation <sup>[10]</sup>. The proposed mechanism for this effect was that yttrium oxides formed on the alloy surface facilitated the nucleation of  $\text{Al}_2\text{O}_3$  by acting as heterogeneous nucleation sites, thereby decreased the time required for developing a complete layer of  $\alpha\text{-Al}_2\text{O}_3$  scale. However, a later study <sup>[42]</sup>

showed that the addition of Y retarded the  $\theta \rightarrow \alpha\text{-Al}_2\text{O}_3$  transformation. Jelinski *et al.* [42] used a model of defect structure to explain the effect of Y on the meta-stable  $\rightarrow \alpha\text{-Al}_2\text{O}_3$  transformation. The occurrence of the phase transformation from meta-stable  $\text{Al}_2\text{O}_3$  ( $\gamma$ ,  $\eta$  or  $\theta$ ) to  $\alpha\text{-Al}_2\text{O}_3$  required a source of anion vacancies. When Y was doped into the alloy, it occupied the divalent vacant sites of meta-stable  $\text{Al}_2\text{O}_3$ . With the increase of Y doping concentration, the amount of anion vacancies decreased. Thus, the meta-stable  $\rightarrow \alpha\text{-Al}_2\text{O}_3$  transformation was inhibited due to the lacking of anion vacancies. Pint *et al.* [14] proposed that Y entered into the relatively open  $\theta\text{-Al}_2\text{O}_3$  lattice, inhibiting the martensitic-type  $\theta \rightarrow \alpha\text{-Al}_2\text{O}_3$  transformation. Both Jedlinski and Pint pointed out that the effect of Y addition on the formation of  $\alpha\text{-Al}_2\text{O}_3$  should be separated from its effect on the meta-stable  $\rightarrow \alpha\text{-Al}_2\text{O}_3$  transformation kinetics.

### ***b) Effect of Hafnium***

Hafnium is another commonly used reactive elements in  $\text{Al}_2\text{O}_3$ -scale forming alloys. It has similar effects as Y in some aspects [9-11]. In terms of improving scale adherence, Hf is effective in some cases but not as universal as Y. Figure 2.19 shows a comparison of the cyclic oxidation behavior of various NiCrAl alloys doped (Hf or Y) and un-doped with reactive elements at  $1100^\circ\text{C}$  [43].

Hafnium addition was also able to decrease the overall oxidation weight gain of  $\text{Al}_2\text{O}_3$ -scale forming alloys. Stringer and Whittle [59] systematically studied the isothermal oxidation kinetics of Co-Cr-Al alloy as a function of Hf contents at  $1100^\circ\text{C}$ , see Figure 2.20. It was shown that the overall weight gain was minimized at a substantial low Hf content. Higher addition Hf increased the overall weight gain. Whittle [59] and Pint [16] summarized the relationship between Hf/Y contents and the overall oxidation weight gain of some representative  $\text{Al}_2\text{O}_3$ -scale forming alloys, shown in Figure 2.21. The effect of Hf showed similar trend on Co-Cr-Al and NiAl alloys.

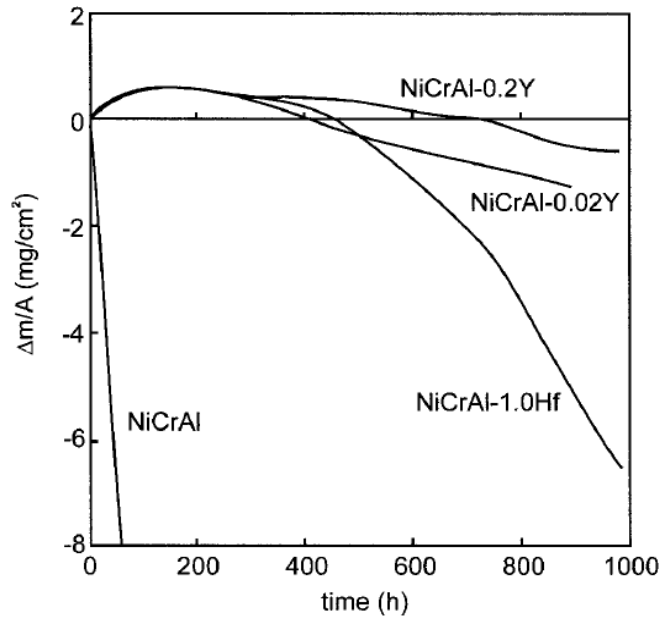


Figure 2.19 Cyclic oxidation kinetics for several NiCrAl alloys un-doped and single-doped (Hf or Y) with reactive elements exposed at 1100°C [43]

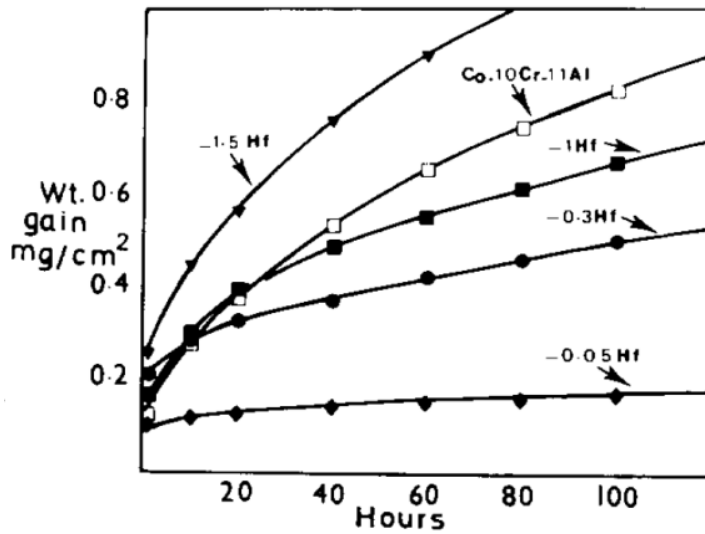


Figure 2.20 Effect of Hf contents on the overall oxidation weight gain of Co-10Cr-11Al after 100 hours of exposure at 1100°C in air [59]

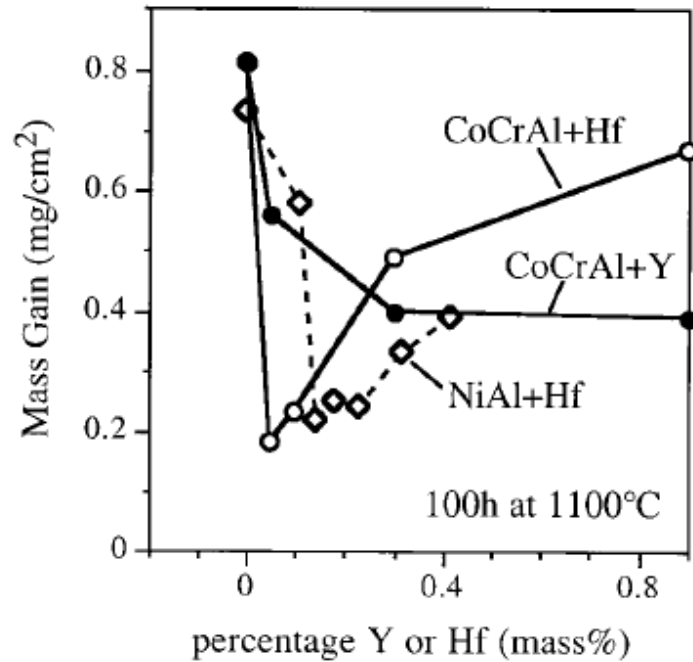


Figure 2.21 Effect of Hf and Y contents on the overall oxidation weight gain of CoCrAl and NiAl alloys after 100 hours of exposure at 1100°C<sup>[16]</sup>

The Hf effect on the early-stage oxidation behavior of Al<sub>2</sub>O<sub>3</sub>-scale forming alloys was studied by several authors. Pint<sup>[62]</sup> examined the effect of HfO<sub>2</sub> dispersion on the phase composition and morphology of Al<sub>2</sub>O<sub>3</sub> scale grown on β-NiAl and found that Hf slowed the θ → α-Al<sub>2</sub>O<sub>3</sub> phase transformation. It was suggested that the larger Hf<sup>4+</sup> radii in the relative open crystal structure of θ-Al<sub>2</sub>O<sub>3</sub> inhibited the diffusionless, martensitic- or shear-type transformation from cubic to hexagonal Al<sub>2</sub>O<sub>3</sub>. Subsequently, Hayashi and Gleeson<sup>[17]</sup> studied the effect of Hf addition on the early-stage oxidation behavior of Pt-modified γ-Ni<sub>3</sub>Al base alloys. Their results also indicated that Hf delayed the meta-stable → α-Al<sub>2</sub>O<sub>3</sub> transformation. The oxidation kinetics of Ni-22Al-30Pt with and without Hf is shown in Figure 2.22. The Hf-containing alloy gained more weight than the Hf-free alloy during the very initial 30 minutes, but it quickly slowed down

with further exposure; whereas Hf-free alloy had a slower oxidation rate at the beginning, but it increased continuously as the oxidation proceeded, resulting a crossover with the Hf-containing alloy at around 8 hours. After 30 minutes of oxidation, cross-sectional TEM images (see Figure 2.23) showed that the meta-stable  $\text{Al}_2\text{O}_3$  formed on the Hf-free alloy had completely transformed to  $\alpha\text{-Al}_2\text{O}_3$ ; while almost no  $\alpha\text{-Al}_2\text{O}_3$  was observed in the alumina scale formed on the Hf-containing alloy. The authors ascribed the initial faster weight gain of the Hf-containing alloy to the relatively slow meta-stable  $\rightarrow \alpha\text{-Al}_2\text{O}_3$  transformation. Since the parabolic rate constants of meta-stable aluminas is 1~2 orders of magnitude than that of  $\alpha\text{-Al}_2\text{O}_3$ , longer existence of meta-stable aluminas will in turn cause higher weight gain. The relatively lower steady state oxidation rate of the Hf-containing alloy was because of the Hf segregation to the oxide grain boundaries, which inhibited the  $\text{Al}^{3+}$  outward diffusion.

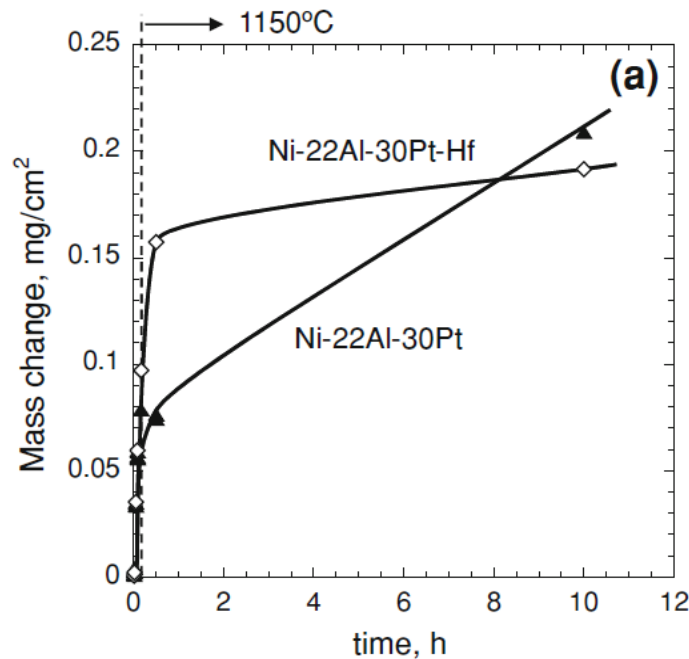


Figure 2.22 Oxidation kinetics of Ni-22Al-30Pt un-doped and doped with Hf <sup>[17]</sup>

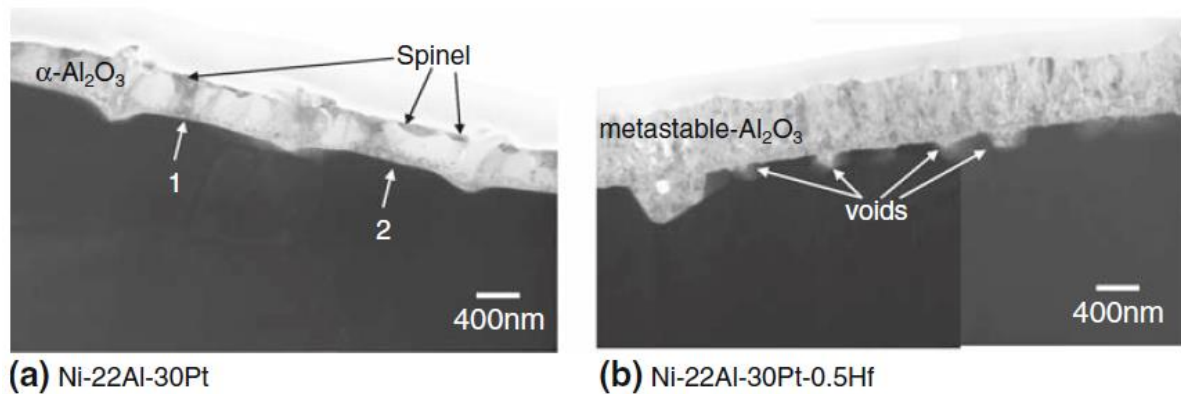


Figure 2.23 Cross-section TEM study of Ni-22Al-30Pt un-doped and doped with Hf after 30 minutes of oxidation <sup>[17]</sup>

Recently, Hou *et al.* <sup>[77]</sup> studied the effect of Hf addition on the S segregation at Al<sub>2</sub>O<sub>3</sub>-scale/metal interfaces by scanning Auger microscopy. It was found that Hf eliminated the S segregation to Al<sub>2</sub>O<sub>3</sub>-scale/metal interfaces due to its strong sulfide forming tendency. Since the S segregation to Al<sub>2</sub>O<sub>3</sub>-scale/metal interfaces is extremely detrimental to scale adhesion, the addition of Hf enhanced the scale adherence by tying up S. In addition to S, Hf was also reported to tie up other impurities, such as C, which may also plays an important role in determining scale adherence. A recent study by Pint <sup>[11]</sup> showed that scale adherence increased with the increasing of Hf/C ratio.

### 2.2.5.3 Effects of other minor elements

Besides reactive elements, other minor alloying elements are often present in Al<sub>2</sub>O<sub>3</sub>-scale forming alloy and coating compositions. These elements are either deliberately added to improve scale performances or contaminated from manufacture processes. In this section, the effects of

some minor alloying elements, which are focused on or related to this research, on the oxidation behavior of Al<sub>2</sub>O<sub>3</sub>-scale forming alloys will be reviewed respectively.

### *a) Effects of Silicon*

Silicon is not a commonly met element in Ni-based superalloys. It is generally considered as a deleterious impurity whose concentration must be controlled at a very low level through careful melting practices. This is because Si is believed to promote the precipitation of brittle phases which might increase the tendency of grain-boundary cracking <sup>[1, 112, 115-116]</sup>. Miner <sup>[115]</sup> investigated the microstructural effect of Si on IN-713C Ni-based superalloy, and found that the addition of 1 wt. % Si promoted the formation of an embrittling Laves phase, essentially Mo(Ni, Si)<sub>2</sub>. Another reason to avoid the significant presence of Si in a Ni-based superalloy is that Si is a potent melting point depressant. A high concentration of Si may cause incipient melting, which often occur in grain boundaries with high segregation tendencies, thereby accelerating the degradation of superalloy components <sup>[1, 121-122]</sup>. Therefore, even though SiO<sub>2</sub>, in principle, is capable to provide protection against high-temperature oxidation because it is thermodynamically stable at elevated temperature, similar to Al<sub>2</sub>O<sub>3</sub>, there have been few studies on the development of SiO<sub>2</sub>-scale forming alloy and coating compositions. Smialek <sup>[84]</sup> tried to develop fused silicon-rich coatings, which were expected to provide oxidation resistance by forming SiO<sub>2</sub> or other silicates, for superalloys. Slurry compositions of Ni-67Al, Al-20Si, Al-40Si, Al-60Si and Al-80Si (in at. %) were used to form fully dense coatings with a high remelt temperature. Unfortunately, even a considerable amount of Si were used in the slurry mixture, the resultant coatings were still composed of Ni-Al phases and the protection of none of these coatings was derived from SiO<sub>2</sub> formation. Moreover, the diffusion of Si from coating material

into superalloy substrate was also a matter of concern, because Si tends to decrease the melting point of nickel by forming low-melting eutectics.

The effects of Si, as a minor alloying element, on the oxidation behavior of Cr<sub>2</sub>O<sub>3</sub>-scale forming systems, particularly stainless steel, have been studied by several workers. Evans and co-workers<sup>[86]</sup> systematically studied the relationship between Si content (ranging from 0.05 ~ 0.25 wt. %) and the oxidation resistance of nitride 20Cr-25Ni stainless steel in a CO<sub>2</sub>-based atmosphere at 1123K. Their results indicated that the optimum oxidation resistance was obtained at intermediate Si content ~ 0.9 wt. %. These authors ascribed this to the establishment of a SiO<sub>2</sub> layer, which was believed to act as diffusion barrier between Cr<sub>2</sub>O<sub>3</sub> scale and alloy substrate. Later, Landkopf *et al.*<sup>[95]</sup> studied the influence of Si in the oxidation behavior of Y-containing AISI-204 type stainless steel at 1000°C. It was found that with the presence of Y, Si increased the oxidation resistance and the scale adherence. This result was then confirmed by Riffard and co-workers<sup>[66]</sup>, who have worked on Y-coated and ion-implanted stainless steel. Significant Si enrichment was observed along the scale/metal interface compared to Y-free blank sample. Y was believed to promote the continuous SiO<sub>2</sub> layer formation at scale/metal interface. A more recent study on the effects of Si and reactive elements on the oxidation behavior of conventional austenitic stainless steel also showed that reactive elements enhanced the SiO<sub>2</sub> layer formation<sup>[85]</sup>.

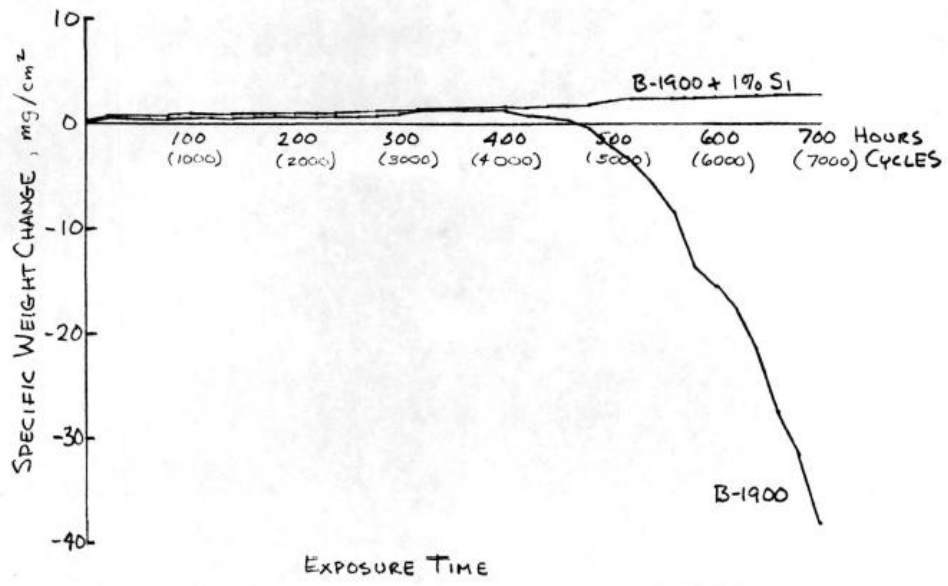
Even though Si was deliberately added to Al<sub>2</sub>O<sub>3</sub>-scale forming coatings, such as diffusion aluminide coatings, to enhance their protection to high temperature oxidation and hot corrosion for superalloy substrates, systematic investigations on the role of Si on the oxidation behavior of Al<sub>2</sub>O<sub>3</sub>-scale forming alloys has been quite limited<sup>[82, 84, 114, 117-120]</sup>.

In the early 1970s, Lowell *et al.* <sup>[81-83]</sup> published a series NASA technical note, which initially reported the beneficial effects of Si addition on the isothermal and cyclic oxidation resistance of the commercial Ni-based high-fraction-gamma-prime superalloy B-1900. Prior to studying the effect of Si on oxidation behavior of B-1900 superalloy, Lowell and co-workers firstly did a survey study of the addition of Si on cyclic oxidation behavior of  $\gamma'$ -Ni<sub>3</sub>Al and  $\beta$ -NiAl as model alloys <sup>[82]</sup>. It was found that Si markedly improved the oxidation resistance of  $\gamma'$ , but the oxidation resistance of  $\beta$  was not affected by Si addition. The cyclic oxidation kinetics (at 1000°C and 1100°C) of unmodified and 1 wt. % Si-modified B-1900 superalloy is shown in Figure 2.24. At both temperatures, the Si-modified B-1900 superalloy slowly increased weight gain. In contrast, the unmodified B-1900 superalloy initially gained weight for several hours (400 hours at 1000°C and 90 hours at 1100°C), but it was followed by a gradually increased weight loss until the end of the test. Moreover, the unmodified B-1900 showed marked spallation as the sample began to lose weight, while the Si-modified B-1900 only produced very slight spallation. The effect of Si concentration on the isothermal oxidation kinetics (at 1100°C and 1200°C) of B-1900 superalloy is shown in Figure 2.25 <sup>[83]</sup>. At both temperatures (1100°C and 1200°C), the oxidation rate decreased as the increase of Si concentration. The high-gas-velocity oxidation resistance of 0.6 wt. % Si-modified B-1900 superalloy was almost comparable to that of the unmodified B-1900 superalloy with a commercial aluminide coating. The authors believed that the beneficial effect of Si on the oxidation resistance was associated with the increase fraction of Al<sub>2</sub>O<sub>3</sub> in the scale, because Si restrained the formation of less protective NiO and spinel. The similar effect of Si in reducing the growth rate of NiO was also observed in Cr<sub>2</sub>O<sub>3</sub>-scale forming Ni-20Cr alloy and NiO-forming Ni-Si alloy. It is noteworthy that the crystallized or layer of SiO<sub>2</sub> was never found in those studies, which is different from the finding in Evan's

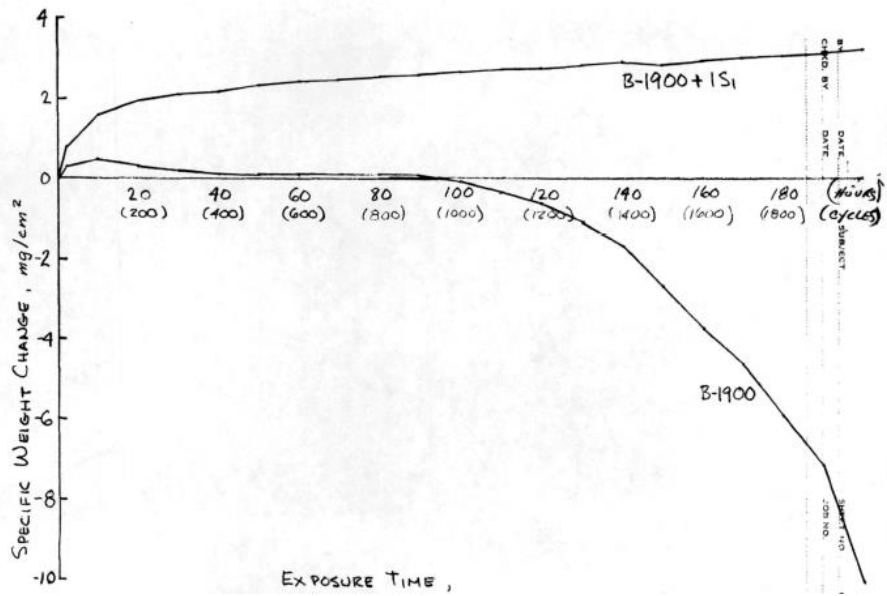
work on stainless steel. In addition, Lowell and co-workers also found that the addition of silicon to B-1900 superalloy caused much of the  $\gamma'$  phase to precipitate as large nodules during solidification. A laves phased  $\text{Mo}(\text{Ni}, \text{Si})_2$  was also found in Si-modified alloys.

Tamari<sup>[140]</sup> did some research on the effects of Si on the oxidation resistance of diffusion aluminide coatings and overlay coatings. Similarly beneficial effect of Si was observed by these researchers. They ascribed the mechanism of the beneficial effect of Si to the fact that Si partially substitutes ions of aluminum and increase the density of  $\alpha\text{-Al}_2\text{O}_3$ . In addition to these studies done by Lowell *et al.* and Tamari, Quadackers *et al.*<sup>[100]</sup> also mentioned in a paper that 0.95 wt. % Si addition moderately improved the cyclic oxidation resistance of an  $\text{Al}_2\text{O}_3$ -scale forming ODS Ni-Cr-Al alloy after 1000 hours of cyclic oxidation at 1050°C.

Recently, Gleeson and co-workers<sup>[137]</sup> found the beneficial effect of Si on co-doped Hf+Y-modified  $\gamma+\gamma'$  alloy. A small amount of Si addition, normally less than 1 at. %, to these alloys not only reduced the overall oxidation weight gain, but also improved scale adhesion in comparison to the Si-free counterpart. The mechanism of the synergistic role of Si in the growth behavior of  $\text{Al}_2\text{O}_3$  scale with the presence of Hf and/or Y was not clear yet. But it should be different from that on the  $\text{Cr}_2\text{O}_3$ -scale forming system, since no  $\text{SiO}_2$  layer was observed underneath  $\text{Al}_2\text{O}_3$  scale. Thus, more attention may need to be paid on the role of Si in affecting the oxidation behavior via altering microstructure or other properties of alloy substrate.



(a)



(b)

Figure 2.24 Cyclic oxidation kinetics of unmodified and 1 wt. % Si-modified B-1900 superalloys at (a) 1000°C and (b) 1100°C [82]

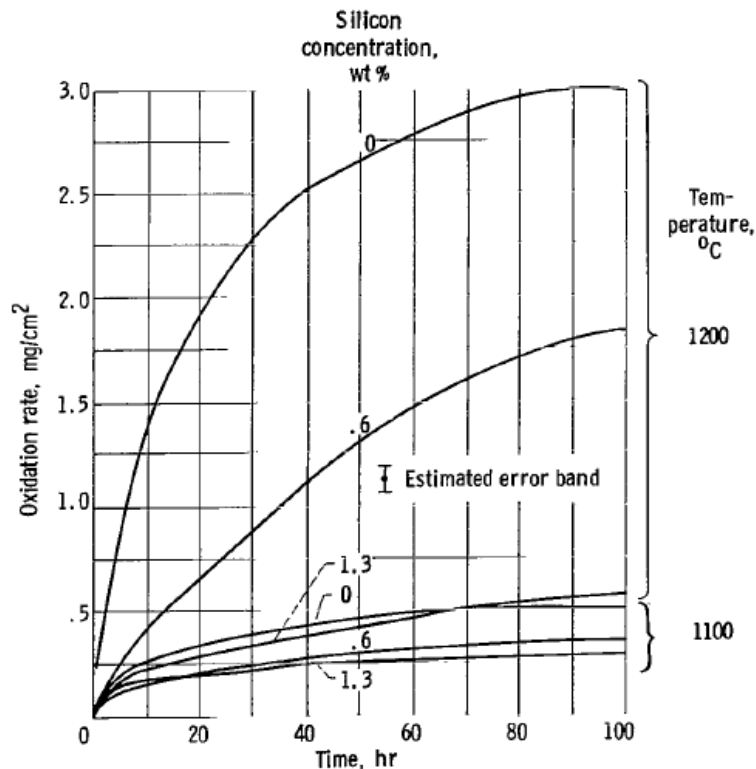


Figure 2.25 Effect of silicon concentration of isothermal oxidation kinetics of B-1900 superalloy at 1100°C and 1200°C [83]

### ***b) Effects of Platinum***

Platinum is an inactive element, which does not form stable oxide under normal conditions. It is commonly used to modify  $\text{Al}_2\text{O}_3$ -scale forming metallic coatings in order to improve both high-temperature oxidation and hot corrosion resistance. One of the most significant application of Pt is the addition of Pt to aluminide coatings, resulting single-phased ((Ni, Pt) Al) or dual-phased (may contain  $\text{PtAl}_2$ ,  $\text{Pt}_2\text{Al}_3$  or  $\text{PtAl}_3$  intermetallic phases) microstructures [69].

Earlier studies generally believed that Pt promoted the selective oxidation of aluminum by excluding the outward diffusion of refractory elements (such as Mo, W and Ta) from superalloy substrate to the coating<sup>[96]</sup>. Recently, emphasis was placed on the role of Pt in improving scale adhesion. It is widely believed that Pt inhibits S segregation which is detrimental to scale adherence<sup>[73]</sup>. Zhang *et al.*<sup>[71]</sup> investigated the cyclic oxidation behavior of a  $\beta$ -(Ni, Pt)Al coating. It was found that Pt improved the  $\alpha$ -Al<sub>2</sub>O<sub>3</sub> scale adherence even at a relatively higher S content compared with the low-S Pt-free sample. A more recent study of the Pt effect on novel  $\gamma$ -Ni+ $\gamma'$ -Ni<sub>3</sub>Al bond coat also showed that Pt addition mitigated the detrimental effect of S by inhibiting S segregation to scale/metal interface<sup>[77]</sup>. The mechanism by which Pt inhibits S segregation is still not clear. One hypothesis was that Pt segregated to scale/metal interface and competed with the segregation of S. Gleeson and co-workers<sup>[98]</sup> studied the segregation behavior of Pt on free clean (Pt, Ni)<sub>3</sub>Al(111) surface by both experiment and first principle calculation. It was concluded that Pt segregation was energetically favored. However, Pt segregation was not always observed at scale/metal interface. In the case of Al<sub>2</sub>O<sub>3</sub>/ $\gamma$ -Ni+ $\gamma'$ -Ni<sub>3</sub>Al, the segregation behavior of Pt was similar to that on free surfaces, whereas no platinum interface segregation was found in the case of Al<sub>2</sub>O<sub>3</sub>/ $\beta$ -NiAl. Another possible mechanism by which Pt improves scale adhesion is that Pt inhibited void formation at the scale/metal interface by changing the diffusivity in the substrate<sup>[99]</sup>.

Besides the segregation behavior of Pt, another interesting point which needs to be clarified is the effect of Pt with the presence of reactive elements (Hf and/or Y). Although both reactive elements and Pt reduce the detrimental effect of S, the mechanism may be totally different because reactive elements have high affinities with S whereas platinum sulfide is less

stable. Hence, the influence of reactive elements should be taken into account when studying the role of Pt.

### ***c) Effects of Titanium***

Titanium is often present in Ni-based superalloys. It acts as  $\gamma'$  former to achieve the desired volume fraction of strengthening  $\gamma'$  phase. Titanium is also a common commercial addition to ferritic stainless steel to improve corrosion resistance. In terms of the Ti effects on the high-temperature oxidation resistance of  $\text{Al}_2\text{O}_3$ -scale forming alloys, both beneficial and detrimental effects were reported.

In 1972, Lowell and Santoro<sup>[81]</sup> investigated the effects of Ti on cyclic oxidation behavior of  $\gamma'$ -Ni<sub>3</sub>Al and  $\beta$ -NiAl model alloys. Their results showed that Ti had little effect on the oxidation resistance of  $\gamma'$ -Ni<sub>3</sub>Al and slightly beneficial effect on  $\beta$ -NiAl. In 1997, Pint *et al.*<sup>[62]</sup> reported the effect of TiO<sub>2</sub> oxide dispersion on the phase composition and morphology of  $\text{Al}_2\text{O}_3$  scale growth on  $\beta$ -NiAl. It was found that Ti accelerated the transformation from  $\theta \rightarrow \alpha$ - $\text{Al}_2\text{O}_3$ . Same results were obtained by Quadackers and co-workers<sup>[100]</sup>. A recent study by Tawancy *et al.*<sup>[101]</sup> indicated that Ti degrades the adherence of  $\text{Al}_2\text{O}_3$  scale. In their study, the effects of Ti were examined by comparing the performances of thermal barrier coating system on two single crystal superalloys, containing “high-Ti (1.0 wt. %)” and “low-Ti (0.3 wt. %)”. It was seen that the average coating life on the “high-Ti” alloy substrate is significantly shorter than that on the “low-Ti” alloy substrate. These authors ascribed the degradation of coating performance on “high-Ti” alloy substrate to the formation of Ti-rich oxide particles near the scale/metal interface. Quadackers *et al.*<sup>[102]</sup> examined the role of Ti in the distribution and transport of Y in  $\text{Al}_2\text{O}_3$  scale on Fe-based ODS alloys. Ti was found to segregate to alumina grain boundaries as YTi-based oxide particles, which modified the growth mechanism of the oxide scale from nearly

exclusively oxygen inward diffusion to a combination of oxygen inward diffusion and a limited Y and Ti outward diffusion.

## **2.3 PROTECTIVE COATINGS FOR HIGH TEMPERATURE APPLICATIONS**

### **2.3.1 Diffusion Coatings**

The deposition of diffusion coating involves an interdiffusion process between the coating material and the base metal, resulting chemical and microstructural change of the metal surface. The deposition techniques of diffusion coatings include slurry cementation, powder pack cementation and chemical vapor deposition (CVD).

Diffusion aluminide coating is the most widely used protective coating for superalloys. During the deposition processes, aluminum is released from gaseous aluminum halides at elevated temperature and it in turn reacts with the superalloy substrate to form the coatings. Goward and Boone<sup>[108]</sup> classified the aluminide diffusion coating on nickel-based superalloys as either “outward diffusion” type or “inward diffusion” type based on the coating microstructures and compositions. “Inward diffusion” coating is formed by predominant inward motion of aluminum from the coating media, while “outward diffusion” coating is formed by predominant outward diffusion of nickel from the substrate alloy. The microstructure of “inward diffusion” coating is  $\delta$ -Ni<sub>2</sub>Al<sub>3</sub> phase and/or aluminum-rich  $\beta$ -NiAl phase and subsequently heat-treated to form nickel-rich  $\beta$ -NiAl phase. The microstructure of “outward diffusion” coating is  $\beta$ -NiAl phase with a nickel deficient interdiffusion zone developed below due to the outward diffusion of nickel.

Diffusion aluminide coating can be modified by adding other elements such as Cr, Si, Pt and reactive elements (REs) to improve their performance in some aspects <sup>[109-111]</sup>. For example, Cr-modified aluminide diffusion coatings have better resistance to hot corrosion attack and RE-modified aluminide diffusion coatings showed generally lower oxidation rate than RE-free aluminide diffusion coatings. Platinum was proved to be the most effective element to improve both high-temperature oxidation and hot corrosion resistance of diffusion aluminide coatings. Platinum is normally introduced into the aluminide diffusion coating by electroplating 5~10  $\mu\text{m}$  platinum followed by a heat-treatment process at elevated temperature prior to the aluminizing processes. Depending on the relative activity of aluminum during coating processes, the microstructure of Pt-modified diffusion aluminide coating can be divided into two types: external single-phase  $\beta\text{-(Pt, Ni)Al}$  and external two-phase  $\text{PtAl}_2+\beta\text{-NiAl}$ . The beneficial effects of the addition of platinum include: 1) improve the high temperature oxidation resistance by promoting the formation of protective  $\alpha\text{-Al}_2\text{O}_3$  scale for longer periods of time, 2) improve the adherence of the protective  $\alpha\text{-Al}_2\text{O}_3$  scale; 3) significantly improve the high temperature hot corrosion resistance and also improve the low temperature hot corrosion resistance in some degree.

Recently, Pt-modified  $\gamma+\gamma'$  phase structure coatings were developed by several groups (Richerby and Wing, 1999; Rickerby *et al.*, 1999; Adesanva *et al.*, 20001; Nicolls, 2003 and Gleeson *et al.* 2004). The  $\gamma+\gamma'$  coating microstructure has better compatibility with the superalloy substrate which also has  $\gamma+\gamma'$  microstructure. There are two attractive advantages of using this type of  $\gamma+\gamma'$  coating for superalloys. Firstly, since the  $\gamma+\gamma'$  microstructure has higher creep strength than that of  $\beta\text{-NiAl}$ , this type of  $\gamma+\gamma'$  aluminide coating is able to resist creep-induced “ramping” failure. Secondly, the  $\gamma+\gamma'$  microstructure eliminates the formation of detrimental topological packed (TCP) phases in the interdiffusion zone. Comparing with the

tradition  $\beta$ -(Pt, Ni)Al platinum-modified diffusion aluminide coating, the Pt-modified  $\gamma+\gamma'$  aluminide coating has satisfactory high temperature oxidation and hot corrosion resistance despite that the Al content is significantly lower.

### 2.3.2 Overlay Coatings

Diffusion aluminide coatings have significant resistance to high temperature oxidation because the Al content in the coating is much higher than the critical Al content required for forming protective  $\alpha$ -Al<sub>2</sub>O<sub>3</sub> scale. However, there are several disadvantages limiting the performance of diffusion aluminide coating. For example, traditional diffusion-based aluminide coatings have rather poor high temperature hot corrosion resistance because of the absence or low content of Cr. Moreover, diffusion coatings based on  $\beta$ -NiAl phase has poor solubility of other minor elements that limits the flexibility for the modification of coating compositions. Furthermore, the thermal stability of coating microstructure after extended periods of exposure at high temperature is also a factor that needs to be considered. One degradation mode of  $\beta$ -NiAl aluminide coating is that the  $\gamma'$ -Ni<sub>3</sub>Al network forms inside the  $\beta$ -NiAl phase due to the consumption of Al and interdiffusion of Ni and Al. The  $\gamma'$ -Ni<sub>3</sub>Al network acts as short-circuit corrosion paths leading to the rapid failure of the coating. Therefore, in order to combat these disadvantages of diffusion aluminide coatings, overlay coatings have been developed with minimal dependence and affection on substrate compositions.

The commonly met composition of overlay coating is M-Cr-Al-X, where M represents Ni, Co or a combination and X stands for oxygen-reactive elements such as Hf, Y or Si [112-113]. This composition has higher Cr content which is essential for maintaining good hot corrosion resistance. The ductility of the coating has also been improved because the addition of Cr

significantly reduces the critical Al content required for forming protective  $\alpha$ -Al<sub>2</sub>O<sub>3</sub> scale. The addition of reactive elements (REs) helps to improve the alumina scale adherence and decrease oxidation rate. It is generally agreed that the M-Cr-Al-X composition found a good balance between high temperature oxidation resistance, hot corrosion resistance and coating ductility. The relative oxidation and hot corrosion resistance of high temperature coating systems (diffusion and overlay coatings) is schematically summarized in Figure 2.26.

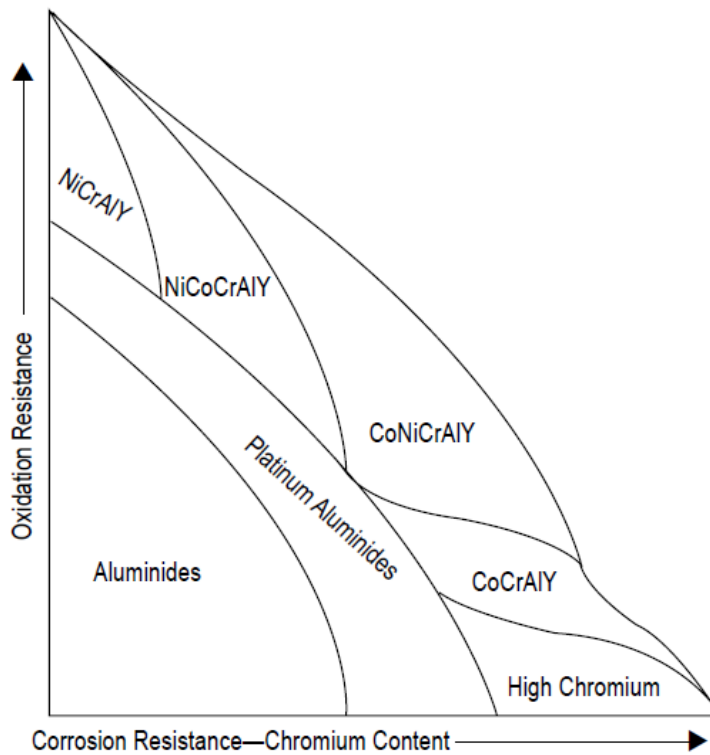


Figure 2.26 Relative oxidation and hot corrosion resistance of high temperature coating systems

[113]

The phase composition of M-Cr-Al-X overlay coatings varies with its chemical composition. Overlay coatings based on Co-Cr-Al system is normally composed of  $\beta$ -CoAl phase and ductile  $\gamma$ -Co-based ductile matrix. With the increase of Al and Cr contents,  $\sigma$ -CoCr

phase appears in the alloy. The phase composition of coatings based on Ni-Cr-Al and Ni-Co-Cr-Al systems are relatively complicated than that of Co-Cr-Al system. The major phases in Ni-Cr-Al system include:  $\gamma$ -Ni-based phase,  $\gamma'$ -Ni<sub>3</sub>Al phase,  $\beta$ -NiAl phase and  $\alpha$ -Cr-based phase; while in Ni-Co-Cr-Al system, the main phase constitutes are  $\gamma$ -Ni-based phase,  $\beta$ -(Ni, Co)Al phase,  $\gamma'$ -(Ni, Co)<sub>3</sub>Al phase and  $\alpha$ -Cr-based phase. The number of phases in these two systems depends on the alloy chemical compositions. The amount of  $\beta$  phase is controlled by the content of aluminum.  $\gamma \leftrightarrow \gamma'$  phase transformation and phase reaction  $\beta + \gamma \leftrightarrow \gamma' + \alpha$  were observed for several alloy compositions in some temperature range.

Electron beam plasma vapor deposition (EB-PVD) and plasma spray (PS) are the two primary techniques for overlay coating deposition. The EB-PVD process involves vaporization of pre-alloyed coating materials ingots by focused electron beam in a vacuum environment. The vaporized coating materials fill the vacuum chamber and condense on the superalloy substrates. While PS is performed by injecting pre-alloyed powder into high temperature plasma inert gas and these melted particles in turn impact, adhere and agglomerate on the superalloy substrates to form a coating. Comparing with EB-PVD technique, PS has its own advantage of being able to provide more compositional flexibility even the vapor pressure of elements in coating materials are widely different from each other. As can be seen in Figure 2.26, the oxidation and hot corrosion resistance of overlay coatings are generally better than diffusion coatings. However, since both EB-PVD and PS are “light-of-sight” deposition processes, uniform coating thickness is difficult to ensure, especially for components with complex shapes. More recently, “smart overlay coating” has been developed based on the concept that a single coating can respond to different forms of corrosion attack – high temperature oxidation, high temperature (Type I) and low temperature (Type II) hot corrosion – by forming appropriate protective scales (chromia and

alumina). In order to meet these joint requirements, a chemically graded coating structure, with enrichment of aluminum and chromium, has been designed. It is expected that the “smart overlay coating” is able to respond to its environment in a pseudo-intelligent manner.

### **2.3.3 Thermal barrier coating system**

In 1980s, the application of thermal barrier coating system (TBCs) to gas turbine blades became one of the trends for improving engine efficiencies. TBCs significantly reduce the exposure temperature of superalloy substrate, and meanwhile allow the increasing of operating temperature in conjunction with active film cooling <sup>[178]</sup>.

Thermal barrier coating system is composed of three primary layers from top to bottom: thermally insulating ceramic top coat, thermally grown oxide (TGO) and oxidation-resistance metallic bond coat. In this system, each layer has its specific function and property. Figure 2.27 is a schematic diagram showing the constitution of thermal barrier coating system. The thermally insulating ceramic top coat acts as thermal insulator, which maximizes the temperature drop across the thickness of the coating and lowers the exposure temperature of superalloy substrate. The chemical composition of this ceramic top coat is normally written as  $Y_2O_3$  (7-8 wt. %) – stabilized  $ZrO_2$ .  $Y_2O_3$  is added to combat the monoclinic to tetragonal transformation of  $ZrO_2$  at the temperature of 1180°C. The  $Y_2O_3$ -stabilized  $ZrO_2$  is deposited either by air plasma spray (APS) or electron beam physical vapor deposition (EB-PVD). The ceramic coat deposited by EB-PVD has its unique columnar structure, which helps to accommodate stresses caused by ceramic/metal thermal expansion mismatch. The thermally grown oxide (TGO) is a thin layer of oxide ( $\alpha-Al_2O_3$ ) slowly grown from the underneath metallic bond coat. Since the  $Y_2O_3$ -stabilized  $ZrO_2$  top coat is oxygen transparent, the TGO serves as diffusion barrier, preventing the metallic

bond coat from further oxidation. In state-of-the-art TBCS, the oxidation-resistance metallic bond coat is either platinum diffusion aluminide coating or MCrAlY overlay coating, the characteristics of which have been introduced in the previous two sections.

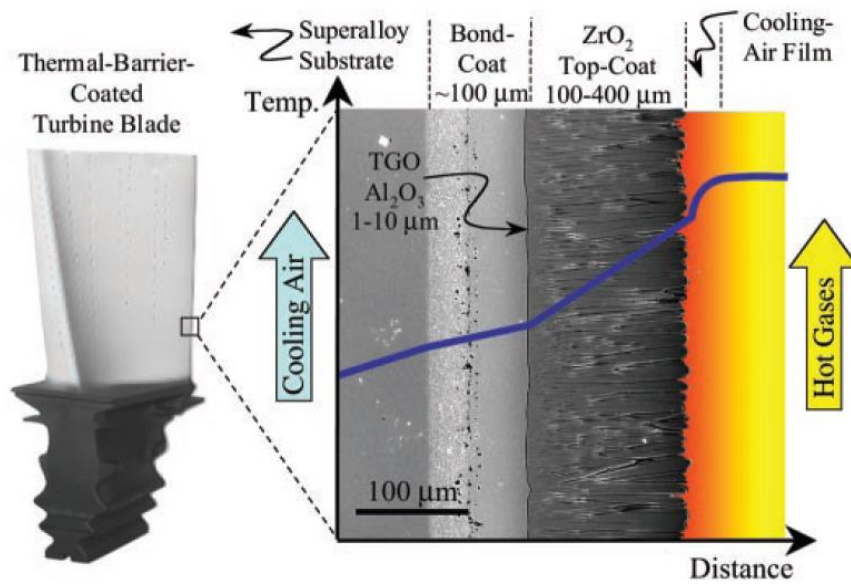


Figure 2.27 Schematic diagram showing the constitution of thermal barrier coating system <sup>[178]</sup>

## 2.4 AIMS OF PRESENT STUDY

Based on the literature review presented, the primary aim of this study is to gain a fundamental understanding of the role of minor additions, mainly Hf, Y and Si, in affecting the oxidation behavior of  $\gamma$ -Ni +  $\gamma'$ -Ni<sub>3</sub>Al Al<sub>2</sub>O<sub>3</sub>-scale forming alloy and metallic coating compositions. Four specific goals of this research are as follows:

1) Systematically assess the effects of minor additions of Hf, Y and Si, particularly in some combinations, on the oxidation behavior of  $\gamma$ -Ni +  $\gamma'$ -Ni<sub>3</sub>Al Al<sub>2</sub>O<sub>3</sub>-scale forming alloy and metallic coating compositions, including both commercial and model compositions;

2) Understand the role of minor additions in affecting the establishment of a stable  $\alpha$ -Al<sub>2</sub>O<sub>3</sub> with particular focus on the meta-stable  $\rightarrow \alpha$ -Al<sub>2</sub>O<sub>3</sub> transformation kinetics;

3) Gain a better understanding of the influence of minor additions during the very initial stage of oxidation, with particular emphasis on their effects on the nano-to-submicron Al<sub>2</sub>O<sub>3</sub>-scale structure in the regions near the scale/meta interface;

4) Obtain a more complete understanding of the synergistic effects of Hf, Y and Si on the oxidation behavior of  $\gamma$ -Ni +  $\gamma'$ -Ni<sub>3</sub>Al Al<sub>2</sub>O<sub>3</sub>-scale forming alloy and metallic coating compositions.

Achieving these goals will be of both fundamental and practical significance. The fundamental significance is related to understanding the complex interplay of scaling behavior and alloy/coating composition. The practical significance is related to guiding design of alloys and coatings for high-temperature service in aggressive atmosphere.

### **3.0 EXPERIMENTAL DETAILS**

#### **3.1 MATERIALS AND SAMPLE PREPARATION FOR OXIDATION TESTING**

All alloy ingots used in this study were prepared by Ar-arc melting followed by drop casting at the Materials Preparation Center, Ames Laboratory<sup>[184]</sup>. The subsequent heat-treatments were then conducted at Iowa State University. More details of the alloy composition and heat-treatment procedures will be provided in each results chapter.

For high-temperature oxidation testing, approximately 1mm thick and 10mm diameter coupon samples were cut from the heat-treatment ingots and grounded to 1200-grit finish using SiC abrasive paper. The samples were then ultrasonic cleaned with acetone and isopropyl and dried immediately before testing. Prior to cleaning, the dimensions of samples were measured by digital caliper for calculating the surface area.

#### **3.2 ISOTHERMAL AND CYCLIC OXIDATION TESTING**

Isothermal oxidation tests were conducted using Setaram High Performance Symmetrical TAG system (see Figure 3.1) in flowing dry air at temperatures interested in. Samples were hung on a sapphire hook at room temperature and then placed into the vertical furnace. Both of the heating and cooling steps were done inside the furnace and the heating and cooling rates were program

controllable. In order to keep the results consistent, the heating and cooling rates used in this study were set as  $99^{\circ}\text{C}/\text{s}$  for all samples tested. The weight change of each sample was continuously recorded by the program and plotted as a function of time. Before and after a given TGA test, the weight of the sample was measured by an analytical balance as a check of the values recorded by the TGA system.



Figure 3.1 Setaram high performance symmetrical TAG system

Cyclic oxidation tests were carried out at Iowa State University. Each cycle consisted of one hour at 1150°C followed by 30 minutes at ~75°C, schematically shown in Figure 3.2. Sample weight change was measured using analytical balance after every two cycles for the first twenty cycles and then intermittently thereafter.

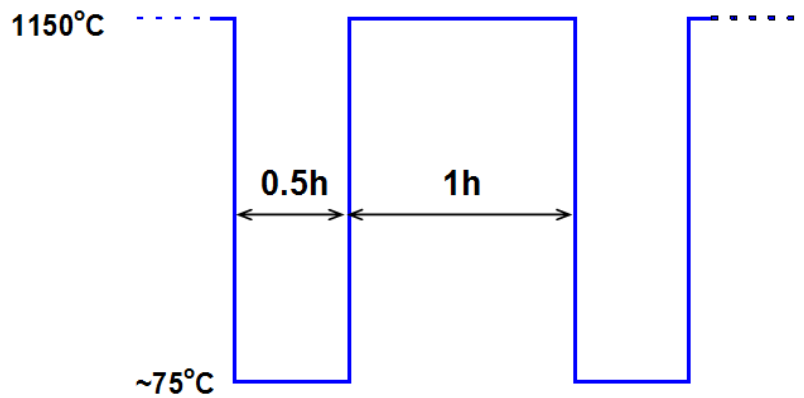


Figure 3.2 Schematic diagram of the procedure of cyclic oxidation test

### 3.3 CHARACTERIZATION AND DATA ANALYSIS

The characterization techniques used in this study include: scanning electron microscopy (SEM), transmission electron microscopy (TEM), scanning transmission electron microscopy (STEM), energy dispersive X-ray spectroscopy (EDS), X-ray diffraction (XRD) and confocal photo-stimulated microscopy (CPSM). In the following chapters, additional information of some specific characterization methods will be provided before presenting the results, in order to

elucidate their necessities or advantages in obtaining the results. The softwares used in this study for data analysis are Excel and OriginPro Student Version.

## 4.0 EFFECT OF SILICON ADDITION ON THE OXIDATION BEHAVIOR OF $\gamma$ - NI+ $\gamma'$ - $\text{Ni}_3\text{Al}$ -BASED ALUMINA SCALE FORMING ALLOYS

### 4.1 INTRODUCTION

From the standpoint of superalloy design, silicon is generally considered as a deleterious impurity in nickel-base superalloys and its concentration must be controlled to a very low level for two main reasons: 1) silicon may promote the precipitation of brittle phases which could increase the tendency of grain-boundary cracking <sup>[1, 112, 115-116]</sup>; and 2) silicon is a potent melting-point depressant <sup>[1, 121-122]</sup>; But, in terms of the influence of silicon on the oxidation resistance of nickel-based  $\text{Al}_2\text{O}_3$ -scale forming alloys, beneficial effects were reported by several groups <sup>[81-83, 100, 117-120, 137]</sup>. However, even though silicon was demonstrated to improve both isothermal and cyclic oxidation resistance of  $\text{Al}_2\text{O}_3$ -scale forming B-1900 nickel-based superalloy as early as 1970s <sup>[82]</sup>, systematic investigations on the role of silicon on the oxidation behavior of  $\text{Al}_2\text{O}_3$ -scale forming alloys are still quite limited <sup>[84, 100, 114, 117-120]</sup>.

The primary objective of the study in this chapter was to systematically evaluate the influence of silicon addition on the isothermal and cyclic oxidation kinetics of three  $\text{Al}_2\text{O}_3$ -scale forming alloys, and demonstrate to what extent if any the silicon addition can benefit the oxidation resistance of these alloys. A secondary objective was to select an optimum alloy for

further studies to advance the understanding of the silicon effect on the early stage of oxidation, particularly the metastable  $\rightarrow \alpha\text{-Al}_2\text{O}_3$  transformation.

## 4.2 MATERIALS AND EXPERIMENTAL PROCEDURES

The  $\text{Al}_2\text{O}_3$ -scale forming alloys used in the present study fall into three major groups: one group of modified commercial superalloy (#1) and two groups of model  $\gamma\text{-Ni}+\gamma'\text{-Ni}_3\text{Al}$ -base alloys (#2 & #3). The nominal compositions of the various alloys studied are given in Table 4.1. The modified commercial superalloy was designed based on the composition of René N5<sup>[1]</sup> and, accordingly it was co-doped with Hf and Y. The two groups of model  $\gamma\text{-Ni}+\gamma'\text{-Ni}_3\text{Al}$ -based alloys (#2 & #3) used in this study were also co-doped with Hf and Y. The purpose for choosing co-doped base alloy compositions is that the addition of two or more reactive elements (REs) was recently shown to be a promising strategy for optimizing the beneficial effects of reactive elements and further improving the oxidation resistance<sup>[16]</sup>. Figure 4.1 shows the compositional (Ni-Cr-Al) positions of the three groups of alloys on the oxide map (1100°C) published by Giggins and Pettit<sup>[8]</sup>. It seems that all of these alloys should be  $\text{Al}_2\text{O}_3$ -scale forming at 1100°C.

All alloys were prepared as drop-cast rods at the Materials Preparation Center, Ames Laboratory<sup>[184]</sup>. Solutionizing heat-treatment of modified-René N5 was conducted in the following manner: 1277°C/4hrs  $\rightarrow$  1287°C/2hrs  $\rightarrow$  1296°C/3hrs  $\rightarrow$  1313°C/2hrs  $\rightarrow$  1316°C/2hrs  $\rightarrow$  1318°C/2hrs  $\rightarrow$  water quench to room temperature. Ingots of the two groups of model  $\gamma+\gamma'$ -based  $\text{Al}_2\text{O}_3$ -scale forming alloys were homogenized at 1200°C for 6 hours followed by 1150°C for 48 hours in vacuum. For each alloy composition, two identical samples were prepared and

oxidized to confirm the results of each testing run, but results from one representative single run will be presented in the following section.

Table 4.1 Nominal compositions of Al<sub>2</sub>O<sub>3</sub>-scale forming alloys used in this chapter

<b>Alloy Group</b>	<b>Base Composition (at. %)</b>	<b>Hf</b>	<b>Y</b>	<b>Si</b>
<b>1</b>	<b>Ni-13.79Al-8.08Cr-7.64Co-</b>	0.08	0.02	0.5
	<b>0.95Mo-1.63W-0.97Re-2.16Ta</b>	0.08	0.02	0
<b>2</b>	<b>Ni-20Al-5Cr</b>	0.05	0.05	1
		0.05	0.05	0
<b>3</b>	<b>Ni-7.5Cr-13Al-1Ta-1Re-0.12C</b>	0.05	0.05	1
		0.05	0.05	0.5

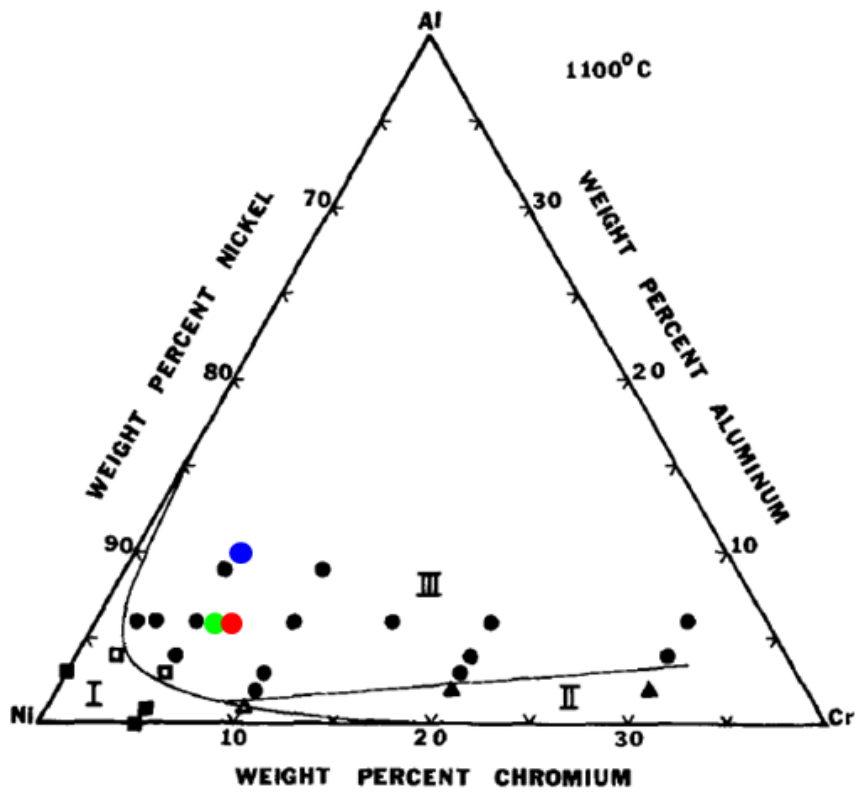


Figure 4.1 Compositional (Ni-Cr-Al) positions of alloy groups on the oxide map at 1100°C

#1 (Red, modified René N5 superalloy), #2 (Blue, Ni-20Al-5Cr-0.05Hf-0.05Y) and #3 (Green, Ni-7.5Cr-13Al-1Ta-1Re-0.12C-0.05Hf-0.05Y) <sup>[8]</sup>

## 4.3 RESULTS AND DISCUSSION

### 4.3.1 Modified René N5 alloys (Group #1)

Figure 4.2 shows the isothermal oxidation kinetics at 1150°C of the modified-René N5 alloys without and with 0.5 at. % silicon addition. The overall weight gains appear to be moderately decreased by the addition of silicon. The weight-gain curves plotted as a function of square root of time are shown in Figure 4.3. Generally, the results have a trend similar to what has been reported in other studies of Al<sub>2</sub>O<sub>3</sub>-scale forming alloys, where the oxidation rate is relatively high at the initial stage of oxidation, but then gradually reduced after about 1 ~ 2 hours [37, 40, 62]. Fitting straight lines through data at times greater than ~4 hours allowed for determination of the parabolic rate constant,  $k_p$ , which is  $8.8 \times 10^{-13} \text{ g}^2/\text{cm}^4 \cdot \text{s}$  for the Si-free alloy and  $7.8 \times 10^{-13} \text{ g}^2/\text{cm}^4 \cdot \text{s}$  for the Si-containing alloy at 1150°C. The parabolic plots in Figure 4.3 also show that the decrease in the overall weight gain (after 100 hours of oxidation) by the addition of silicon is mainly due to the influence of silicon during the initial stage of oxidation.

Figure 4.4 (a) and (b) show representative cross-sectional SEM images of modified-René N5 alloys after 100 hours of oxidation at 1150°C. The oxide scale on the Si-free alloy is mainly Al<sub>2</sub>O<sub>3</sub> with a very thin layer of NiO and/or NiAl<sub>2</sub>O<sub>4</sub> on the surface. Randomly distributed HfO<sub>2</sub> particles, which were mostly round-shaped, with diameter ranging from 0.2 ~ 0.5 μm, were observed at the scale/alloy interface and also inside the scale. The phases in the oxide scale were identified based on EDS compositional analysis. By contrast, the oxide scale on the Si-containing alloy was solely Al<sub>2</sub>O<sub>3</sub> without an obvious layer of NiO or NiAl<sub>2</sub>O<sub>4</sub> on the surface. Relatively large (>1μm) rounded and elongated HfO<sub>2</sub> particles were present inside the Al<sub>2</sub>O<sub>3</sub> scale, with some even running through the entire scale. In addition, the scale/metal interface of

the Si-free alloy was relatively planar, while it became non-planar with the addition of silicon. No Si-bearing oxides were found in the scale formed on the Si-containing alloy.

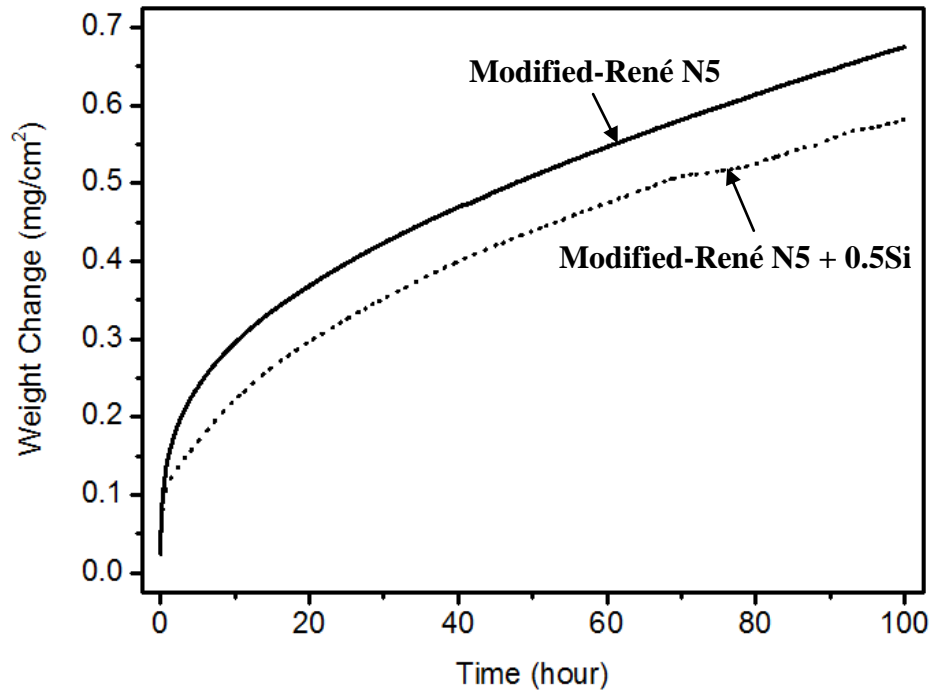


Figure 4.2 Isothermal oxidation kinetics of modified-René N5 alloys without and with 0.5 at. % silicon addition at 1150°C

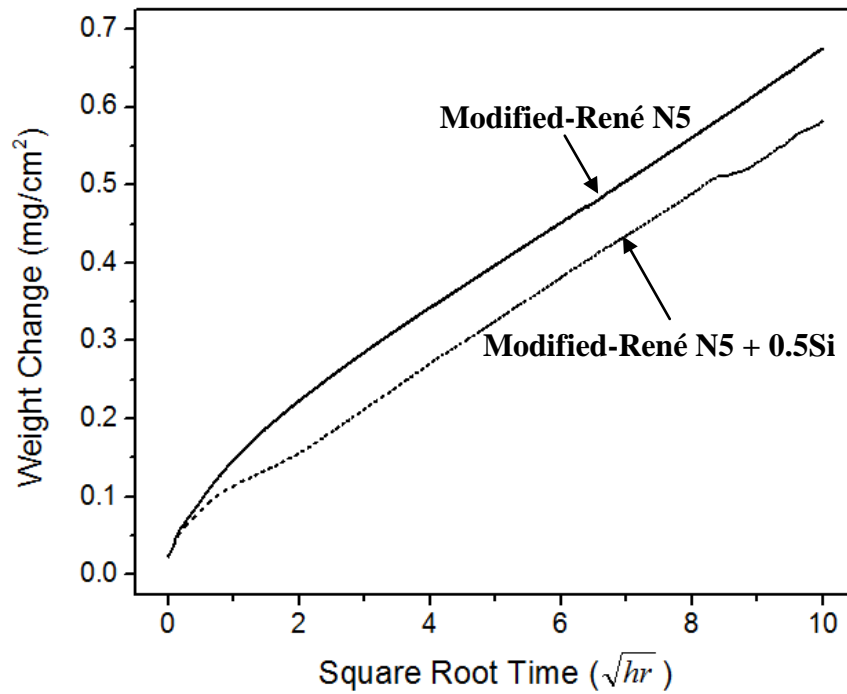


Figure 4.3 Parabolic plots of weight gain as a function of square root of time of modified-René N5 alloys without and with 0.5 at. % silicon addition at 1150°C

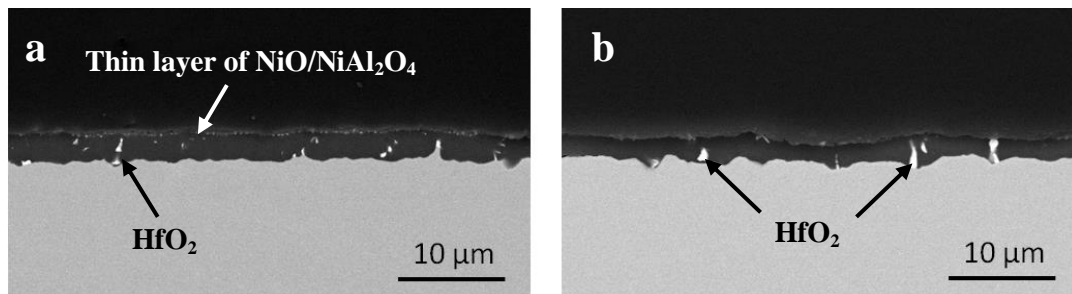


Figure 4.4 Cross-sectional SEM images of modified-René N5 alloys after 100 hours of isothermal oxidation at 1150°C (a) without Si addition (b) with 0.5 at. % Si addition

Comparing the current results with the work reported by Lowell *et al.* [82, 83] and Gao [167], two agreements were found: 1) no Si-bearing oxides were observed in the alumina scale formed on the Si-containing alloy; and 2) the addition of Si suppressed the surface formation of NiO and/or NiAl<sub>2</sub>O<sub>4</sub>.

The reason for the nonexistence of Si-bearing oxides can be explained from both thermodynamic and kinetic points of view. Thermodynamically, Al<sub>2</sub>O<sub>3</sub> is more stable than SiO<sub>2</sub> at 1150°C [2]. Thus, when the Si-containing alloy preferentially established a complete layer of Al<sub>2</sub>O<sub>3</sub>, the oxygen partial pressure at the scale/metal interface became too low to stabilize SiO<sub>2</sub> formation. Kinetically, in order for the Si to be oxidized externally and form a significant volume of SiO<sub>2</sub>, the concentration of Si in the alloy substrate must be sufficiently high to make the outward flux of Si greater than the inward flux of O; however, in this study, the Si level is only 0.5 at. %, which is too low for SiO<sub>2</sub> to form externally. Therefore, it is reasonable that Si-bearing oxides were not found in the alumina scale.

Next, the role of Si in suppressing the formation of NiO and/or NiAl<sub>2</sub>O<sub>4</sub> is so far not conclusive, even though this phenomenon has been intermittently reported since 1970s [81-83, 167, 183]. It could be inferred to be due to several possible mechanisms. One possible interpretation is that Si suppressed the growth of NiO and/or NiAl<sub>2</sub>O<sub>4</sub> through promoting the selective oxidation of Al whose oxide  $\alpha$ -Al<sub>2</sub>O<sub>3</sub> has low diffusivity. This speculated mechanism could be similar as the proposed mechanism of the frequently reported beneficial effect of reactive elements (e.g. Y and Hf) in promoting selective oxidation of Al (or Cr) [9-11]. Reactive elements that have high affinity for oxygen could be oxidized very quickly during the very initial stage of oxidation. In the subsequent stages of oxidation, oxides of reactive elements could facilitate the nucleation of Al<sub>2</sub>O<sub>3</sub> by acting as heterogeneous nucleation sites and decrease the time required for developing

a complete layer of  $\alpha$ -Al<sub>2</sub>O<sub>3</sub> scale <sup>[10]</sup>. The full establishment of  $\alpha$ -Al<sub>2</sub>O<sub>3</sub> will significantly suppress the outward diffusion of Ni to form NiO and/or NiAl<sub>2</sub>O<sub>4</sub> because of its low diffusivity <sup>[55]</sup>. In addition, reactive elements usually segregate to Al<sub>2</sub>O<sub>3</sub> grain boundaries, making the diffusion of Ni and O through Al<sub>2</sub>O<sub>3</sub> grain boundaries even more difficult <sup>[9, 11]</sup>. The mechanism proposed for reactive elements could be applied to interpret the effect of Si in suppressing the formation of NiO and/or NiAl<sub>2</sub>O<sub>4</sub>, but the heterogeneous nucleation sites may not be SiO<sub>2</sub>, since this oxide is unlikely to form from both thermodynamic and kinetic points of view, as discussed above. It is possible that Si reacted with reactive elements, either Hf or Y, and formed some new phases (such as Hf<sub>x</sub>Si<sub>y</sub> or Y<sub>x</sub>Si<sub>y</sub> <sup>[59, 78]</sup>) acting as heterogeneous nucleation sites and promoting the selective oxidation of Al. This topic will be discussed in the next chapter in combination with further results. Another possible interpretation is that Si segregated to the initially grown NiO grain boundaries and suppressed the growth of NiO and/or NiAl<sub>2</sub>O<sub>4</sub> through inhibiting the outward diffusion of Ni. This speculation could be supported by the results reported by Atkinson *et al.* <sup>[176]</sup>. It is known that the growth of NiO is dominated by outward diffusion of Ni<sup>2+</sup> through NiO grain boundaries <sup>[2]</sup>. Atkinson *et al.* <sup>[176]</sup> investigated the self-diffusion of Ni in NiO bicrystal and found that extensive segregation of Si to the NiO grain boundaries suppressed the outward grain-boundary diffusion of Ni. Thus, once the outward diffusion of Ni is inhibited, the growth of NiO could be suppressed to a significantly low level.

The cyclic oxidation kinetics of modified-René N5 alloys without and with 0.5 at. % Si addition during one hour cycles at 1150°C is shown in Figure 4.5. Figure 4.6 (a) and (b) are the cross-sectional SEM images of these two alloys after 1000 one hour cycles of oxidation at 1150°C. The overall mass gain after 1000 one hour cycles for the Si-free alloy was 1.24 mg/cm<sup>2</sup>, but only 0.99 mg/cm<sup>2</sup> for the Si-containing alloy, indicating that the addition of 0.5 at. % Si

considerably decreased the overall oxidation rate. Even though this trend is similar to that of isothermal oxidation kinetics at 1150°C, no obvious layer of NiO or NiAl<sub>2</sub>O<sub>4</sub> was observed on the scale surface of either the Si-free or the Si-containing alloy after cyclic oxidation. This means that the above discussed effect of silicon addition in restraining the formation of NiO and/or NiAl<sub>2</sub>O<sub>4</sub> is not responsible for decreasing the overall weight gain. One possible mechanism is that the addition of silicon reduced the Al and O grain-boundary diffusion, which dominates the Al<sub>2</sub>O<sub>3</sub> scale growth<sup>[137]</sup>. Direct evidence of Si in changing transport properties of Al<sub>2</sub>O<sub>3</sub> has not been reported, but effects of reactive elements (e. g. Hf and Y) on modifying the transport processes through Al<sub>2</sub>O<sub>3</sub> grain boundaries have been discussed frequently<sup>[9, 11, 16, 40, 50, 62]</sup>. If the addition of Si could help reactive elements to distribute along Al<sub>2</sub>O<sub>3</sub> grain boundaries in a more efficient manner, the phenomenon that Si addition decreasing the overall oxidation rate could be rationally explained. However, the current results are not enough to determine whether and how Si could help the distribution behavior of reactive elements. In the next two chapters, this speculation will be discussed with more results.

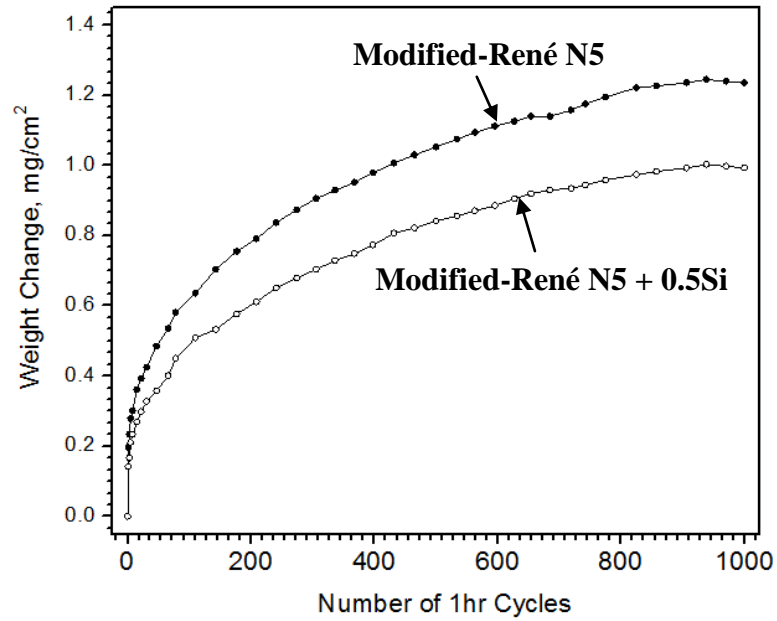


Figure 4.5 Cyclic oxidation kinetics of modified-René N5 alloys without and with 0.5 at. % Si addition during 1 hour cycles at 1150°C

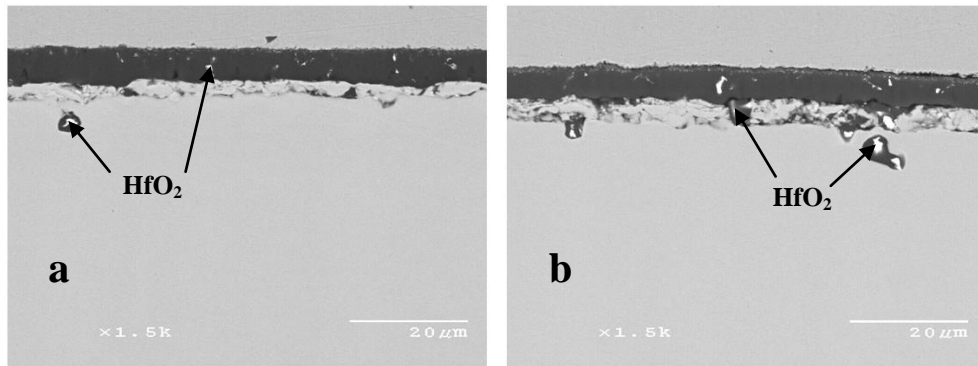


Figure 4.6 Cross-sectional SEM images of modified-René N5 alloys after 1000 1 hour cycles of oxidation at 1150°C (a) without Si addition (b) with 0.5 at. % Si addition

Generally, both the Si-containing and the Si-free modified-René N5 alloys exhibited good oxidation resistance throughout the 1000 cycles, with no obvious scale spallation. A rather non-uniform but distinct layer was observed beneath the  $\text{Al}_2\text{O}_3$  scale on both the Si-free and the Si-containing alloys. This layer appeared more non-uniform for the Si-containing alloy (Figure 4.6 b). It is possible that this non-uniform layer was formed during sample preparation processes, but the root cause is not clear in this study. Interfacial cavities or vacancies generated by excessive outward cation diffusion may be responsible for poor adhesion<sup>[167, 183]</sup>. Oxide particles formed by heavy elements (e.g. Hf, Y, Mo, Ta etc.) were observed either embedded in the scale or sparsely enveloped by  $\text{Al}_2\text{O}_3$  in the subsurface zone beneath the scale for both the Si-containing and the Si-free alloy.

### 4.3.2 Ni-20Al-5Cr model alloys (Group #2)

Figure 4.7 shows the isothermal oxidation kinetics of Ni-20Al-5Cr-0.05Hf-0.05Y and Ni-20Al-5Cr-0.05Hf-0.05Y-1Si alloys exposed for 100 hours at 1150°C. Generally, the overall weight gain of the Si-containing alloy is lower than that of the Si-free counterpart. One noticeable feature of the kinetic curves is that they crossover at ~40 hours. Before this crossover, the oxide scale on the Si-containing alloy grew relatively fast, but it was then exceeded by the Si-free alloy after this crossover point. Thus the overall weight gain for the Si-free alloy eventually became larger than that for the Si-containing alloy. Figure 4.8 shows the parabolic plots of weight gain as a function of square root of time for both of the Si-free and Si-containing alloys. These two plots give a better perspective of the change of growth rate with exposure time. It is shown that both scales formed on the Si-free and Si-containing alloys experienced an initial fast-growing stage and a subsequent slow-growing stage. This kind of change has also been reported in other Al<sub>2</sub>O<sub>3</sub>-scale forming alloy systems and is usually believed to be caused by transformation from the metastable  $\theta$ -Al<sub>2</sub>O<sub>3</sub> to stable structure of  $\alpha$ -Al<sub>2</sub>O<sub>3</sub> [17, 62]. Fitting the straight lines after ~4 hours gave  $k_p$  values of  $7 \times 10^{-13}$  g<sup>2</sup>/cm<sup>4</sup>·s for the Si-free alloy and  $5 \times 10^{-13}$  g<sup>2</sup>/cm<sup>4</sup>·s for the Si-containing alloy. For the Si-containing alloy, the initial oxidation rate (<1 h) is higher than that of the Si-free alloy, but it slowed to a comparatively lower oxidation rate with continued exposure. This further elucidates the occurrence of the crossover on the kinetic curves. It is thus reasonable to speculate that the effect of silicon in reducing the overall weight gain is mainly due to its effect on the initial oxidation kinetics.

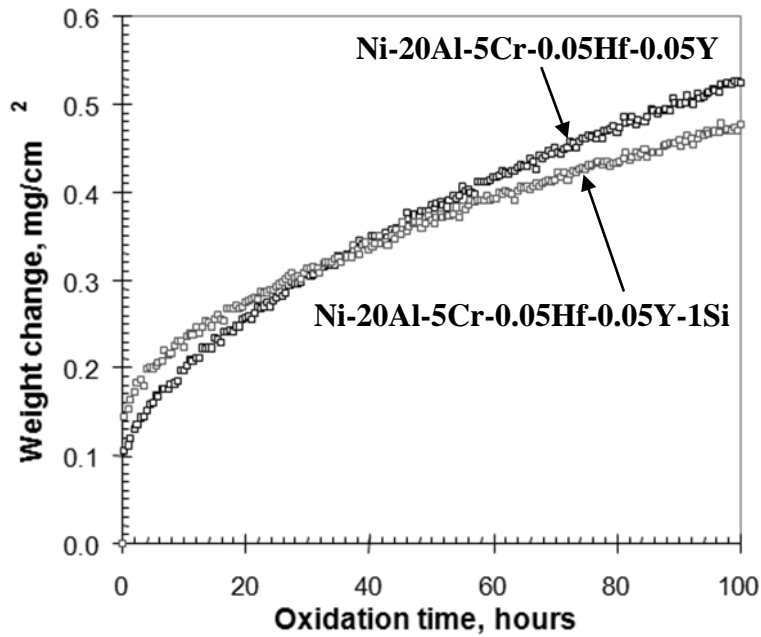


Figure 4.7 Isothermal oxidation kinetics of Ni-20Al-5Cr-0.05Hf-0.05Y and Ni-20Al-5Cr-0.05Hf-0.05Y-1Si at 1150°C

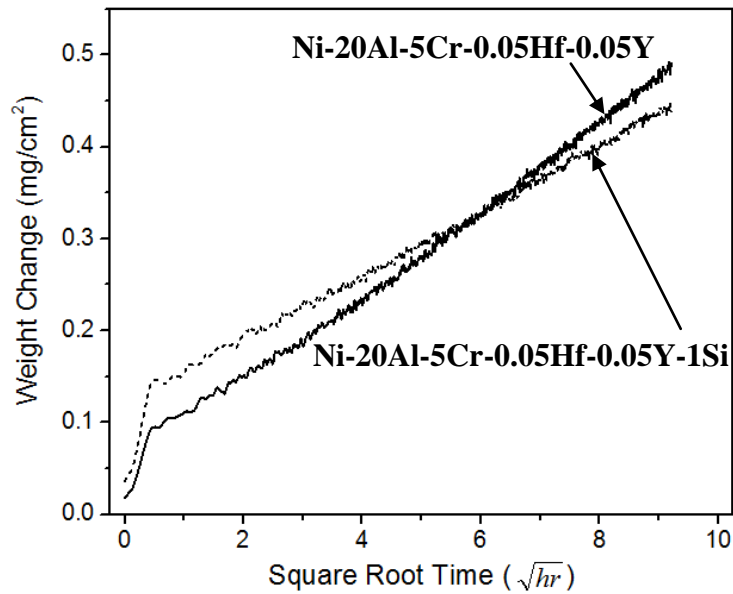


Figure 4.8 Parabolic plots of weight gain as a function of square root of time for Ni-20Al-5Cr-0.05Hf-0.05Y and Ni-20Al-5Cr-0.05Hf-0.05Y-1Si at 1150°C

Cross-sectional SEM images of the Si-free and Si-containing alloys after 100 hours of oxidation at 1150°C are shown in Figure 4.9 (a) and (b), respectively. Both the Si-free and the Si-containing alloys form an exclusive  $\text{Al}_2\text{O}_3$  scale with very few  $\text{HfO}_2$  and/or  $\text{Y}_2\text{O}_3$  particles dispersed inside the scale. These particles have relatively bright contrast compared to the dark  $\text{Al}_2\text{O}_3$  scale background. No  $\text{HfO}_2$  and/or  $\text{Y}_2\text{O}_3$  particles were observed either along the scale/metal interface or in the subsurface zone underneath the scale. The scale/metal interface of the Si-containing alloy is relatively non-planar compared to that of the Si-free alloy. Some areas of the  $\text{Al}_2\text{O}_3$  scale on the Si-containing alloy were extremely thin, as indicated by the arrow in Figure 4.9 (b). Compared with the Si-free alloy, the average scale thickness of the Si-containing alloy is slightly lower, but the scale thickness varies over a larger range.

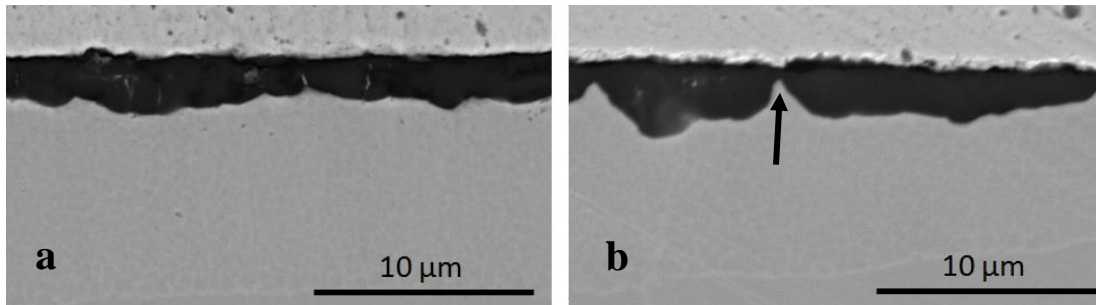


Figure 4.9 Cross-sectional SEM images of (a) Ni-20Al-5Cr-0.05Hf-0.05Y and (b) Ni-20Al-5Cr-0.05Hf-0.05Y-1Si after 100 hours of oxidation at 1150°C

Several mechanisms have been suggested to explain the development of non-planar scale/metal interface [13, 41, 124-125]. Hindam and Smeltzer [124] proposed that a localized thin area (such as that arrowed in Figure 4.9) acted as an impingement site with aluminum lateral diffusion occurring from this impingement site to the vicinity area to resulting thickening the neighboring scale. The mechanism of the formation of the impingement sites on the alloy (Ni-6 wt. % Al)

used by Hindam and Smeltzer was believed due to the connection of internal rod shaped  $\text{Al}_2\text{O}_3$  at the front, which decreased the Al and O fluxes at the connection/impingement sites. It is agreed that the non-planar scale/metal interface could be caused by some impingement sites, but the impingement sites should form by a totally different mechanism, because in this study the alloy (Ni-20Al-5Cr-0.05Hf-0.05Y at.%) composition sits in the region where only external oxidation is expected to occur<sup>[8]</sup>. It is possible that the addition of Si facilitates the reactive elements (Hf and/or Y) to form excessive segregation sites at some  $\text{Al}_2\text{O}_3$  grain boundaries. These excessive segregation sites will significantly decrease the O inward diffusion and Al outward diffusion, and in turn act as impingements to promote aluminum lateral diffusion, in accordance with that Hindam and Smeltzer proposed<sup>[124]</sup>. Another possible explanation to the formation of non-planar scale/metal interface is that the localized thickening is caused by some rapid diffusion paths for aluminum or oxygen or both species<sup>[13]</sup>. The so-called fast diffusion paths could be  $\text{Al}_2\text{O}_3$  grain boundaries that have much less reactive elements (Hf and/or Y) segregation than its neighboring ones, as it is mentioned above that excessive segregation of reactive elements to  $\text{Al}_2\text{O}_3$  grain boundaries will significantly decrease the Al and O diffusion rate through the alumina scale. So if the above speculation that Si facilitated excessive segregation of Hf and/or Y at some particular grain boundaries is the case, then it is very possible that some  $\text{Al}_2\text{O}_3$  grain boundaries without Hf and/or Y segregation will act as fast diffusion path and cause localized thickening of the scale. However, since no direct evidence in support of the speculation whether Si facilitated the excessive segregation of Hf and/or Y was obtained so far, no conclusion can be given.

Figure 4.10 shows the cyclic oxidation kinetics of Ni-20Al-5Cr-0.05Hf-0.05Y and Ni-20Al-5Cr-0.05Hf-0.05Y-1Si during 1 hour cycles at 1150°C and Figure 4.11 (a) and (b) are the corresponding cross-sectional SEM images after 1000 one hour cycles at 1150°C. It is clearly seen that the addition of Si significantly decreased the overall weight gain after 1000 one hour cycles. The final weight gain of the Si-free alloy was 0.98 mg/cm<sup>2</sup>, but it was only 0.6 mg/cm<sup>2</sup> for the Si-containing alloy. Moreover, it is noted that the Si-free alloy began to show weight loss after around 850 cycles, indicating the occurrence of spallation, while the Si-containing alloy showed a gradual weight gain through the entire 1000 one hour cycles. Cross-sectional SEM images show that the Si-containing alloy formed a thin, continuous and adherent Al<sub>2</sub>O<sub>3</sub> scale with only very few HfO<sub>2</sub> particles (<1 μm) embedded inside the scale. By contrast, the Si-free alloy formed a relatively thicker and non-planar Al<sub>2</sub>O<sub>3</sub> scale with a few protrusions to the alloy substrate and some isolated internal oxidation areas. The occurrence of internal oxidation means that the inward flux of oxygen exceeded the outward flux of aluminum. In this case, adding silicon made the aluminum outward diffusion more predominant.

The cyclic oxidation results of Ni-20Al-5Cr-0.05Hf-0.05Y and Ni-20Al-5Cr-0.05Hf-0.05Y-1Si (Figure 4.10) are in agreement with that of modified-René N5 alloys (Figure 4.5), and the addition of silicon should decrease the overall weight gain by the same mechanism, because they all formed exclusive Al<sub>2</sub>O<sub>3</sub> scale. As discussed in Section 4.3.1, a possible mechanism is that the addition of silicon helped reactive elements (Hf and Y) to distribute along Al<sub>2</sub>O<sub>3</sub> grain boundaries in a more efficient manner and significantly decrease the Al and O grain boundary diffusion that dominates the growth of Al<sub>2</sub>O<sub>3</sub> scale. As will be discussed in the later chapters, one way that silicon can modify the distribution of reactive elements is through decreasing the activities of reactive elements in Al<sub>2</sub>O<sub>3</sub> scales and/or alloys.

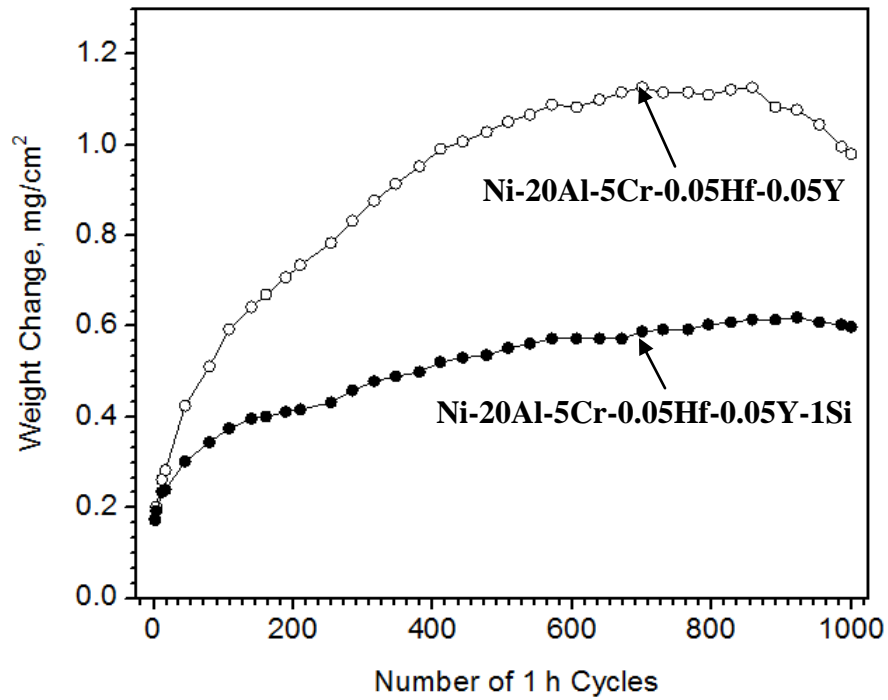


Figure 4.10 Cyclic oxidation kinetics of Ni-20Al-5Cr-0.05Hf-0.05Y and Ni-20Al-5Cr-0.05Hf-0.05Y-1Si during 1000 one hour cycles at 1150°C

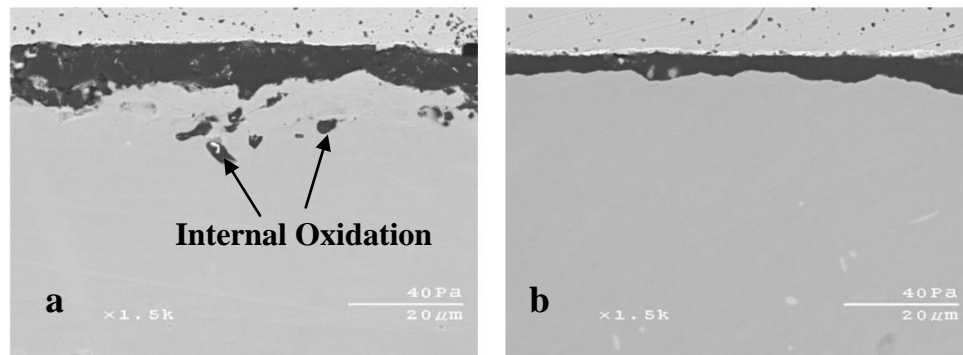


Figure 4.11 Cross-sectional SEM images of (a) Ni-20Al-5Cr-0.05Hf-0.05Y and (b) Ni-20Al-5Cr-0.05Hf-0.05Y-1Si after 1000 one hour cycles of oxidation at 1150°C

### 4.3.3 Ni-7.5Cr-13Al-1Ta-1Re-0.12C-0.05Hf-0.05Y alloys (Group #3)

Figure 4.12 presents the isothermal oxidation kinetics of Ni-7.5Cr-13Al-1Ta-1Re-0.12C-0.05Hf-0.05Y-0.5Si and Ni-7.5Cr-13Al-1Ta-1Re-0.12C-0.05Hf-0.05Y-1Si at 1150°C. The overall oxidation weight gain of the alloy containing 1 at. % Si is slightly lower than that of the alloy containing 0.5 at. % Si. Parabolic plots of weight gain as a function of square root of time for both alloys are shown in Figure 4.13. Similar as the results presented in the last section for Ni-20Al-5Cr-0.05Hf-0.05Y and Ni-20Al-5Cr-0.05Hf-0.05Y-1Si alloys, the oxidation rate for both alloys also experienced an initial fast-growing stage followed by a slow-growing stage, and the kinetic curves also showed a crossover. The appearance of the kinetics crossover indicates that the silicon level affected the initial oxidation behavior of these two alloys, possibly through affecting the meta-stable  $\rightarrow \alpha$ -Al<sub>2</sub>O<sub>3</sub> transformation kinetics. Fitting the lines on the parabolic plots after ~10 hours gave the parabolic rate constant,  $k_p$ , of  $8.9 \times 10^{-13} \text{ g}^2/\text{cm}^4 \cdot \text{s}$  for the alloy containing 0.5 at. % Si and  $7.1 \times 10^{-13} \text{ g}^2/\text{cm}^4 \cdot \text{s}$  for the alloy containing 1 at. % Si. Figure 4.14 (a) and (b) are the cross-sectional SEM images of Ni-7.5Cr-13Al-1Ta-1Re-0.12C-0.05Hf-0.05Y alloys with 1 at. % Si (a) and 0.5 at. % Si (b). Both alloys formed an exclusive Al<sub>2</sub>O<sub>3</sub> scale with a few scattered HfO<sub>2</sub> particles dispersed inside the scale. More significantly, the increase in Si content from 0.5 at. % to 1 at. % markedly decreased the size of the HfO<sub>2</sub> particles. The diameter of most HfO<sub>2</sub> particles in the alumina scale of the alloy containing 1 at. % Si is smaller than 0.5  $\mu\text{m}$ , while a great majority of HfO<sub>2</sub> particles in the alumina scale of alloy containing 0.5 at. % Si is larger than 1  $\mu\text{m}$ . Moreover, the increase in silicon level from 0.5 at. % to 1 at. % reduced the amount of the scale protrusions to alloy substrate and improved the flatness of the scale/metal interface.

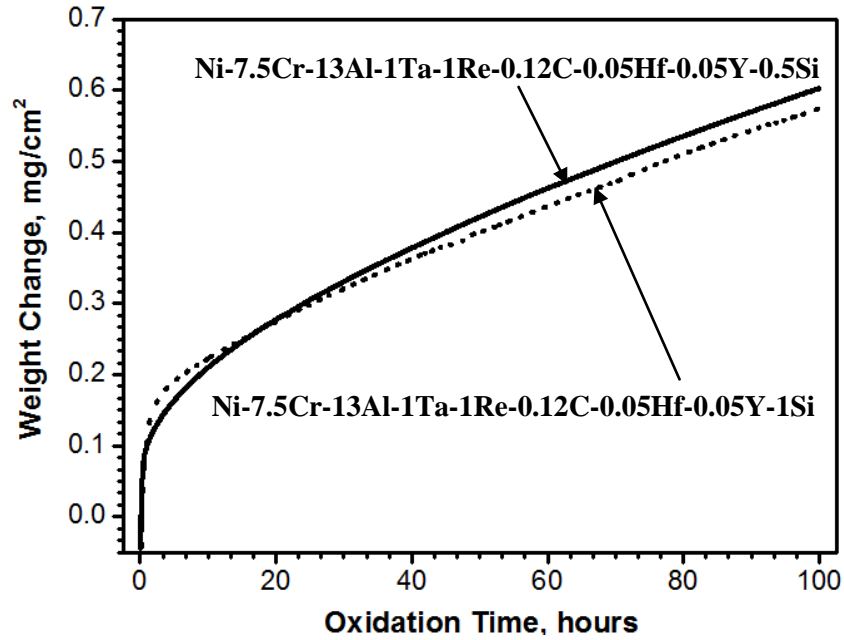


Figure 4.12 Isothermal oxidation kinetics of Ni-7.5Cr-13Al-1Ta-1Re-0.12C-0.05Hf-0.05Y-0.5Si and Ni-7.5Cr-13Al-1Ta-1Re-0.12C-0.05Hf-0.05Y-1Si at 1150°C

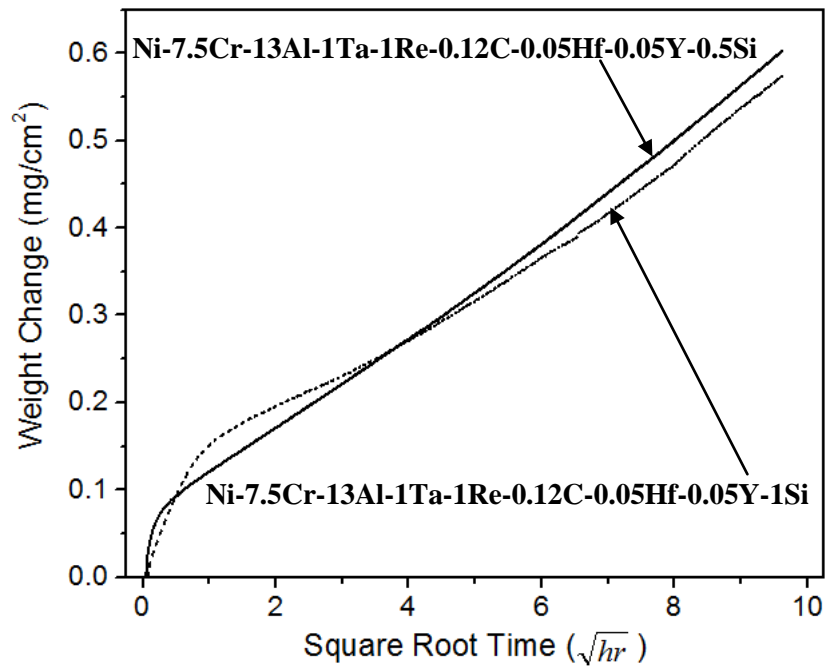


Figure 4.13 Parabolic plots of weight gain as a function of square root of time for Ni-7.5Cr-13Al-1Ta-1Re-0.12C-0.05Hf-0.05Y-0.5Si and Ni-7.5Cr-13Al-0.12C-0.05Hf-0.05Y-1Si at 1150°C

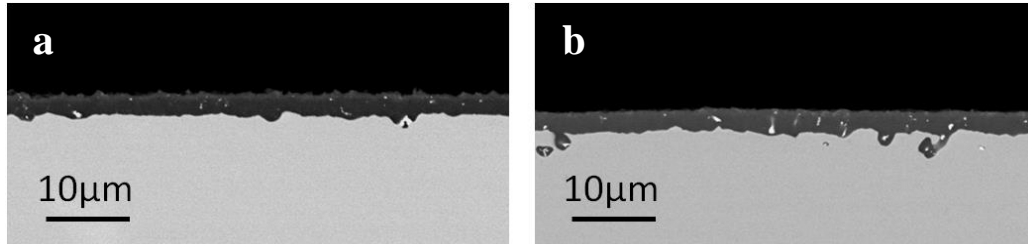


Figure 4.14 Cross-sectional SEM images of (a) Ni-7.5Cr-13Al-1Ta-1Re-0.12C-0.05Hf-0.05Y-1Si and (b) Ni-7.5Cr-13Al-1Ta-1Re-0.12C-0.05Hf-0.05Y-0.5Si after 100 hours of isothermal oxidation at 1150°C

A possible reason for the change of scale structure by increasing the silicon level is that the increment of silicon addition affected the behavior of Hf and/or Y compared to the cases in which reactive elements work by themselves. As discussed in Sections 4.3.1 and 4.3.2, the addition of Si may change the behavior that reactive elements segregating to  $\text{Al}_2\text{O}_3$  grain boundaries by changing the chemical activities of reactive elements in the alloy substrates. The SEM images in Figure 4.14 (a) and (b) showed in this section strongly support the speculation that increasing in silicon level decreased the activity of Hf because much less and smaller  $\text{HfO}_2$  particles were observed in the alumina scale of the alloy containing 1 at. % Si than its counterpart that containing 0.5 at. % Si. The mechanism by which Si addition could decrease the activity of reactive elements will be discussed in later chapters with more results.

Figure 4.15 shows the cyclic oxidation kinetics of Ni-7.5Cr-13Al-1Ta-1Re-0.12C-0.05Hf-0.05Y-0.5Si and Ni-7.5Cr-13Al-1Ta-1Re-0.12C-0.05Hf-0.05Y-1Si during one hour cycles at 1150°C. The cyclic oxidation kinetics of these two alloys is almost the same during the initial 500 one hour cycles. Thereafter, the weight gain of alloy containing 0.5 at. % Si became relatively slower than that of alloy containing 1 at. % Si. The final weight gain of the alloy

containing 0.5 at. % Si was  $1.03 \text{ mg/cm}^2$ , while it was  $1.16 \text{ mg/cm}^2$  for the alloy containing 1 at. % Si. Contrary to the trend during isothermal oxidation, the increase in silicon content slightly increased the overall weight gain after 1000 1 hour cycles of oxidation. The mechanism of the occurrence of this contrary phenomenon is not clear yet. More work needs to be done to elucidate a specific mechanism.

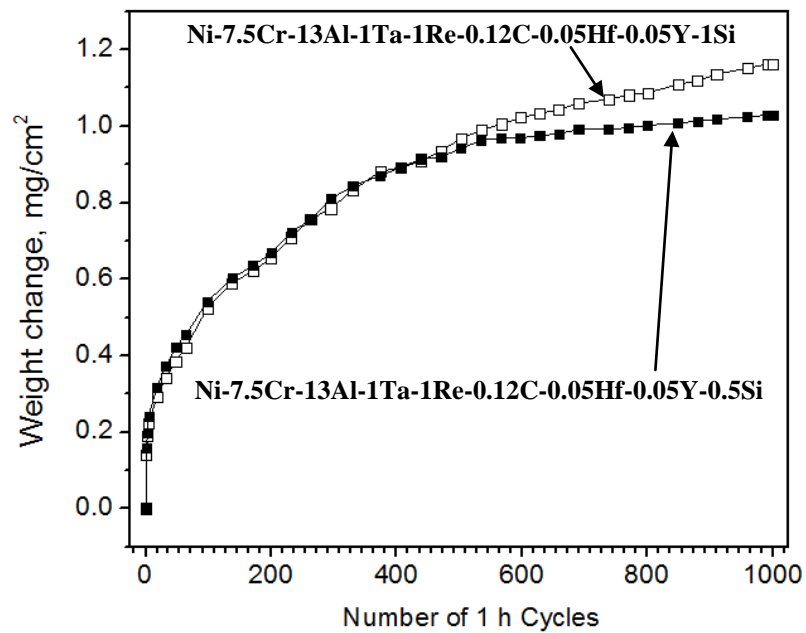


Figure 4.15 Cyclic oxidation kinetics of Ni-7.5Cr-13Al-1Ta-1Re-0.12C-0.05Hf-0.05Y-0.5Si and Ni-7.5Cr-13Al-1Ta-1Re-0.12C-0.05Hf-0.05Y-1Si during 1 hour cycles at 1150°C

#### 4.4 SUMMARY AND CONCLUSIONS

The effect of Si addition on the oxidation kinetics of  $\gamma + \gamma'$   $\text{Al}_2\text{O}_3$  scale forming alloys has been tested on modified-René N5 superalloys and two model alloys under both isothermal and cyclic oxidation conditions at 1150°C. The major results of this study are as follows:

1. The addition of silicon moderately decreased the overall weight gain of modified-René N5 superalloys and Ni-20Al-5Cr-0.05Hf-0.05Y group model alloys under isothermal oxidation condition up to 100 hours at 1150°C. For the modified-René N5 superalloys, the reason that the addition of silicon decreased the overall weight gain is likely because that silicon addition restrained the surface formation of NiO and/or  $\text{NiAl}_2\text{O}_4$ ; while for the Ni-20Al-5Cr-0.05Hf-0.05Y group model alloys, the speculated mechanism of silicon addition in reducing the overall weight gain is that silicon addition affected the initial oxidation kinetics, especially the metastable  $\theta\text{-Al}_2\text{O}_3 \rightarrow \alpha\text{-Al}_2\text{O}_3$  transformation process.
2. Silicon addition markedly decreased the overall weight gain of modified-René N5 superalloy and Ni-20Al-5Cr-0.05Hf-0.05Y model alloy under cyclic oxidation condition up to 1000 1 hour cycles at 1150°C. The speculated mechanism of this phenomenon is that the addition of silicon helped reactive elements (Hf and Y) to distribute along  $\text{Al}_2\text{O}_3$  grain boundaries in a more efficient manner and significantly decrease the Al and O grain boundary diffusion that dominates the growth of  $\text{Al}_2\text{O}_3$  scale. The possible way that silicon helped to improve the distribution behavior of reactive elements is through decreasing the activities of reactive elements in  $\text{Al}_2\text{O}_3$  scale or substrate alloys.
3. The increase of Si concentration from 0.5 at. % to 1 at. % slightly decreased the overall weight gain of Ni-7.5Cr-13Al-1Ta-1Re-0.12C-0.05Hf-0.05Y alloy under isothermal

oxidation condition up to 100 hours at 1150°C, but it slightly increased the overall weight gain under cyclic oxidation condition up to 1000 1 hour cycles at 1150°C; The results of isothermal oxidation strongly supported the speculation that increasing in silicon level decreased the chemical activity of reactive elements because much less and smaller HfO<sub>2</sub> particles were observed in the Al<sub>2</sub>O<sub>3</sub> scale of the alloy containing 1 at. % Si than its counterpart that containing 0.5 at. % Si. The reason why cyclic oxidation results were contrary to the isothermal oxidation results is not clear in this study.

4. Silicon addition or increasing of Si level affected the initial oxidation behavior of both Ni-20Al-5Cr-0.05Hf-0.05Y and Ni-7.5Cr-13Al-1Ta-1Re-0.12C-0.05Hf-0.05Y model alloys under isothermal oxidation condition at 1150°C. The addition of Si or the increasing of Si level should mainly affect the metastable  $\theta$ -Al<sub>2</sub>O<sub>3</sub> →  $\alpha$ -Al<sub>2</sub>O<sub>3</sub> transformation process.

Table 4.2 and Figure 4.16 summarize and compare the parabolic rate constants under isothermal oxidation condition at 1150°C of the three groups of alloys. Table 4.3 and Figure 4.17 summarize and compare the overall weight gain after 1000 1h cycles of oxidation at 1150°C for the three groups of alloys.

Table 4.2 Summary of parabolic rate constants (1150°C) of three groups of alloys studied in this chapter

Base Composition	Hf	Y	Si	$k_p$ ( $\text{g}^2/\text{cm}^4\cdot\text{s}$ )
<b>Ni-13.79Al-8.08Cr-7.64Co-0.95Mo-1.63W-0.97Re-2.16Ta (at. %)</b>	0.08	0.02	0.5	$7.8 \times 10^{-13}$
	0.08	0.02	0	$8.8 \times 10^{-13}$
<b>Ni-20Al-5Cr</b>	0.05	0.05	1	$5.0 \times 10^{-13}$
	0.05	0.05	0	$7.0 \times 10^{-13}$
<b>Ni-7.5Cr-13Al-1Ta-1Re-0.12C</b>	0.05	0.05	1	$7.1 \times 10^{-13}$
	0.05	0.05	0.5	$8.9 \times 10^{-13}$

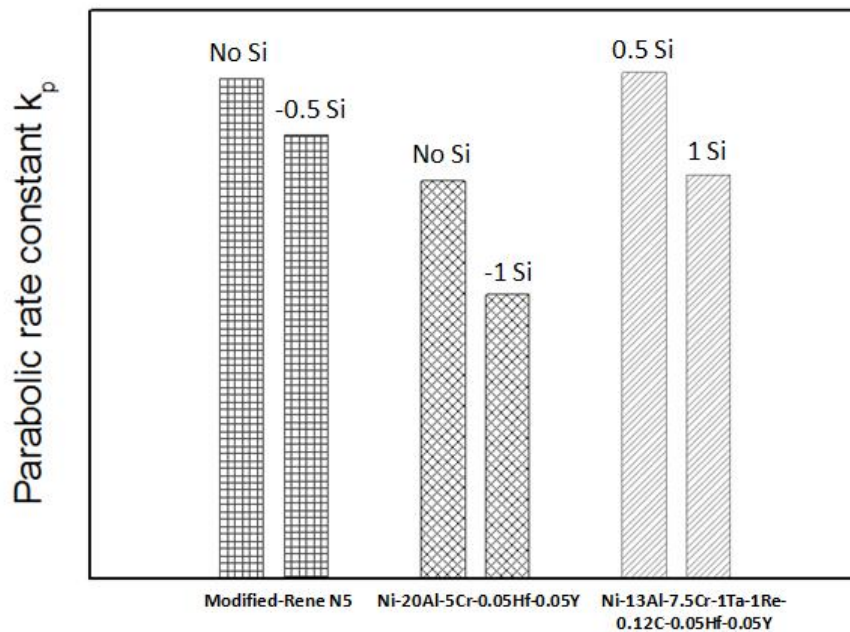


Figure 4.16 Comparison of parabolic rate constants (1150°C) of three groups of alloy studied in this chapter

Table 4.3 Summary of overall weight gain of three groups of alloys after 1000 one hour cycles of oxidation at 1150°C

Base Composition	Hf	Y	Si	$\Delta m$ (mg/cm <sup>2</sup> )
Ni-13.79Al-8.08Cr-7.64Co-0.95Mo-	0.08	0.02	0.5	0.99
1.63W-0.97Re-2.16Ta (at. %)	0.08	0.02	0	1.24
Ni-20Al-5Cr	0.05	0.05	1	0.6
	0.05	0.05	0	0.98
Ni-7.5Cr-13Al-1Ta-1Re-0.12C	0.05	0.05	1	1.16
	0.05	0.05	0.5	1.03

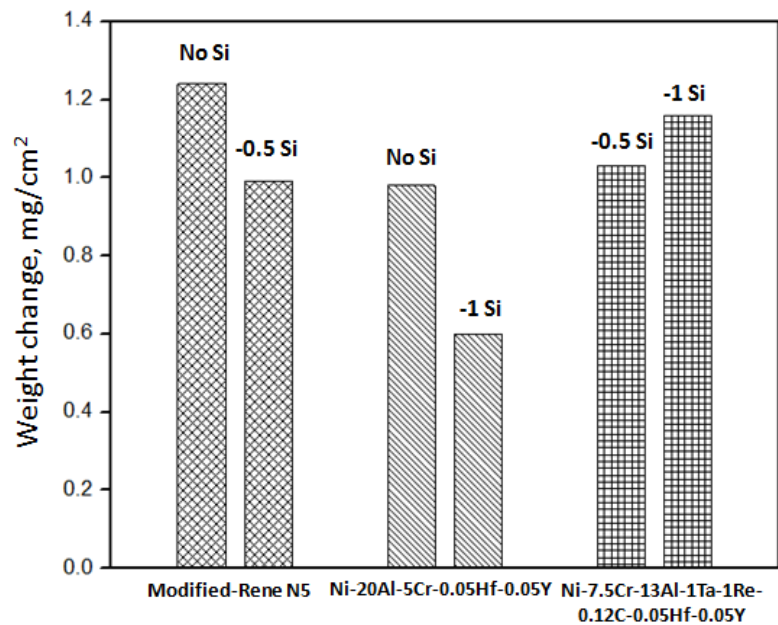


Figure 4.17 Comparison of overall weight gain of three groups of alloys after 1000 one hour cycles of oxidation at 1150°C

## 5.0 EFFECTS OF SILICON ADDITION ON THE EARLY STAGE OXIDATION BEHAVIOR OF $\gamma$ -Ni+ $\gamma'$ -Ni<sub>3</sub>Al ALUMINA SCALE FORMING MODEL ALLOYS

### 5.1 INTRODUCTION

The early oxidation stage, which usually involves a metastable aluminas (mainly  $\gamma$ -Al<sub>2</sub>O<sub>3</sub> and  $\theta$ -Al<sub>2</sub>O<sub>3</sub>)  $\rightarrow$   $\alpha$ -Al<sub>2</sub>O<sub>3</sub> transformation, plays a significant role in the Al<sub>2</sub>O<sub>3</sub>-scale growth behavior at temperatures above about 900°C and affects the scale performance from two important aspects. Firstly, the metastable  $\rightarrow$   $\alpha$ -Al<sub>2</sub>O<sub>3</sub> transformation is accompanied by large volume shrinkage (~10%)<sup>[127]</sup>, because the crystal structure of  $\alpha$ -Al<sub>2</sub>O<sub>3</sub> is more close-packed than that of the metastable aluminas<sup>[18, 30-32]</sup>. Thus, stresses developed by the volume contraction will cause cracking, which may subsequently deteriorate the scale protection against oxidation and limit the service life of the airfoils<sup>[128-131]</sup>. Secondly, the growth rate of metastable aluminas is much higher (1~2 orders of magnitude at the same temperature) than that of  $\alpha$ -Al<sub>2</sub>O<sub>3</sub><sup>[21, 35]</sup>, and the growth of metastable Al<sub>2</sub>O<sub>3</sub> is primarily dominated by outward diffusion of aluminum<sup>[14, 48, 132]</sup>. Consequently, the longer the metastable aluminas exist, the more aluminum will deplete from the subsurface region of the alloy substrate. Overconsumption of aluminum will cause breakaway oxidation when the aluminum concentration in the alloy substrate is too low to sustain a protective alumina scale<sup>[133]</sup>.

The influence of substrate compositions on the early-stage oxidation behavior of Al<sub>2</sub>O<sub>3</sub>-scale forming alloys has been frequently studied. Effects of both major (e. g. Cr) <sup>[21, 35, 134-135]</sup> and minor (e.g. Hf, Y, Pt) <sup>[9, 11, 136]</sup> alloying elements have been investigated. However, the role of Si in the early-stage oxidation behavior has been seldomly reported.

In Chapter 4, it was shown that the addition of Si moderately decreased the overall weight gain of Ni-20Al-5Cr-0.05Hf-0.05Y Al<sub>2</sub>O<sub>3</sub>-scale forming model alloy under isothermal oxidation conditions up to 100 hours at 1150°C. Moreover, detailed analysis of the kinetic data revealed that the addition of Si had a significant effect on the early stage of oxidation (Figure 4.7 and Figure 4.8), which is highly related to the metastable  $\theta \rightarrow \alpha$ -Al<sub>2</sub>O<sub>3</sub> transformation. Indeed, more attention is needed to assess the influence of Si on the early-stage oxidation behavior of Al<sub>2</sub>O<sub>3</sub>-scale forming alloys. Additionally, since the scale formed on the Ni-20Al-5Cr-0.05Hf-0.05Y and Ni-20Al-5Cr-0.05Hf-0.05Y-1Si model alloys are almost exclusive Al<sub>2</sub>O<sub>3</sub>, these two alloys become good candidates for studying the metastable  $\theta \rightarrow \alpha$ -Al<sub>2</sub>O<sub>3</sub> transformation kinetics.

Therefore, the objective of the study in this chapter was to investigate the effect of Si on the early-stage oxidation behavior of a model  $\gamma+\gamma'$  Al<sub>2</sub>O<sub>3</sub>-scale forming alloy, with particular focus on the  $\theta \rightarrow \alpha$ -Al<sub>2</sub>O<sub>3</sub> transformation kinetics. This investigation will help to gain a better understanding of the role of Si in affecting the scale performance.

## 5.2 MATERIALS AND EXPERIMENTAL PROCEDURES

Model alloys used in this particular study are  $\gamma+\gamma'$   $\text{Al}_2\text{O}_3$ -scale forming and either without and with 1 at. % Si. Drop-cast rods were homogenized at 1200°C for 6 hours followed by 1150°C for 48 hours in vacuum. The nominal composition of these alloys is given in Table 5.1.

Table 5.1 Nominal composition (at. %) of the two  $\gamma+\gamma'$  model alloys studied in this chapter

Ni	Al	Cr	Hf	Y	Si
Bal.	20	5	0.05	0.05	0
Bal.	20	5	0.05	0.05	1

Qualitative and semi-quantitative characterizations were carried out by confocal photo-stimulated microspectroscopy (CPSM) and glancing angle X-ray diffraction (GAXRD). More details of each characterization technique and associated experimental procedures will be introduced in the following sections.

## 5.3 RESULTS

### 5.3.1 Confocal photo-stimulated microspectroscopy (CPSM) characterization

Photo-stimulated luminescence spectroscopy (PSLS) is a reliable technique for characterizing the crystallographic forms of a thermally grown  $\text{Al}_2\text{O}_3$  scale<sup>[129,138-140]</sup>. Meta-stable or stable  $\text{Al}_2\text{O}_3$

formed by selective oxidation of Al usually contains a trace concentration of  $\text{Cr}^{3+}$  stemming from the metal substrate. The fluorescence of  $\text{Cr}^{3+}$ -doped  $\theta$  and  $\alpha\text{-Al}_2\text{O}_3$  has characteristic spectra peaks. At room temperature and stress-free conditions,  $\alpha\text{-Al}_2\text{O}_3$  is characterized by doublet peaks at wavenumbers of  $14,402\text{ cm}^{-1}$  and  $14,432\text{ cm}^{-1}$ , while  $\theta\text{-Al}_2\text{O}_3$  is characterized by doublet peaks at wavenumbers of  $14,575\text{ cm}^{-1}$  and  $14,675\text{ cm}^{-1}$  [140]. Characteristic luminescence spectra from  $\alpha\text{-Al}_2\text{O}_3$  and  $\theta\text{-Al}_2\text{O}_3$  are shown in Figure 5.1. The confocal photo-stimulated microspectroscopy (CPSM) method, as a refinement of the PSLS technique, is capable of obtaining high-resolution images with fluorescence information [139].

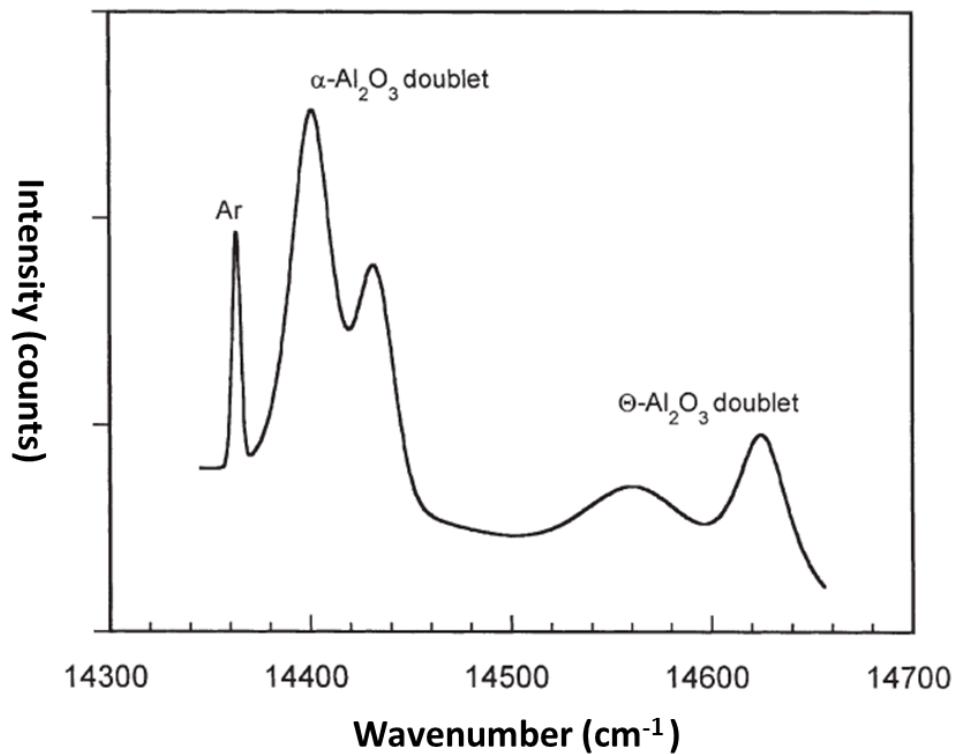


Figure 5.1 Characteristic luminescence spectrum of  $\text{Cr}^{3+}$ -doped  $\alpha\text{-Al}_2\text{O}_3$  and  $\theta\text{-Al}_2\text{O}_3$  [140]

The CPSM images of thermally grown  $\theta$ -Al<sub>2</sub>O<sub>3</sub> and  $\alpha$ -Al<sub>2</sub>O<sub>3</sub> formed on the Si-free and Si-containing model alloys at 1100°C in air are shown in Figure 5.2 and Figure 5.3, where  $\theta$ -Al<sub>2</sub>O<sub>3</sub> is represented by green and  $\alpha$ -Al<sub>2</sub>O<sub>3</sub> is represented by red. For each alloy, a series of images was taken at different oxidation time (0.5, 2, 6, 10, 20 and 50 hours) in order to track the evolution of Al<sub>2</sub>O<sub>3</sub> transformation. These dual color images are overlaps of the original individual  $\theta$ -Al<sub>2</sub>O<sub>3</sub> (green) and  $\alpha$ -Al<sub>2</sub>O<sub>3</sub> (red) intensity maps using 50% opacity. Images were processed using the public software Image J (<http://imagej.nih.gov/ij/>). For the Si-free alloy (Figure 5.2), the  $\theta \rightarrow \alpha$ -Al<sub>2</sub>O<sub>3</sub> transformation completed after around 10 hours of exposure at 1100°C. Compared to the Si-free alloy, the Si-containing alloy (Figure 5.3) took longer time, ~20 hours, for the  $\theta \rightarrow \alpha$ -Al<sub>2</sub>O<sub>3</sub> transformation to finish at the same temperature. This result suggests that the addition of Si appeared to delay the  $\theta \rightarrow \alpha$ -Al<sub>2</sub>O<sub>3</sub> phase transformation at 1100°C.

Significant morphological differences in the way  $\theta$ -Al<sub>2</sub>O<sub>3</sub> transformed to  $\alpha$ -Al<sub>2</sub>O<sub>3</sub> can also be seen when comparing Figure 5.2 and Figure 5.3. For the alumina scale formed on the Si-free alloy,  $\theta$ -Al<sub>2</sub>O<sub>3</sub> transformed to  $\alpha$ -Al<sub>2</sub>O<sub>3</sub> by forming  $\alpha$ -Al<sub>2</sub>O<sub>3</sub> patches (as circled on the image after 2 hours of oxidation in Figure 5.2). By contrast, for the Si-containing alloy, the  $\theta$ -Al<sub>2</sub>O<sub>3</sub> transformed to  $\alpha$ -Al<sub>2</sub>O<sub>3</sub> through a process similar to nucleation (see arrows on the image after 6 hours of oxidation in Figure 5.3) and lateral growth. Thus, the distribution of  $\theta$ -Al<sub>2</sub>O<sub>3</sub> and  $\alpha$ -Al<sub>2</sub>O<sub>3</sub> formed on the Si-containing alloy appeared to be more uniform than that formed on the Si-free alloy. It is generally believed that  $\theta$ -Al<sub>2</sub>O<sub>3</sub> transforms to  $\alpha$ -Al<sub>2</sub>O<sub>3</sub> through a nucleation and growth process<sup>[30]</sup>; however, the transformation behavior is also influenced by the orientation of alloy substrates<sup>[33-34]</sup>. Since the Si-containing and Si-free alloy substrates are not single crystal, the transformation behavior might be different from grain to grain. Thus, it is premature to make any conclusion in terms of the effect of silicon addition on the scale morphologies.

Attempts were also made to quantify the scale phase composition by comparing the surface-area fraction of  $\theta$ -Al<sub>2</sub>O<sub>3</sub> (green) and  $\alpha$ -Al<sub>2</sub>O<sub>3</sub> (red). For example, after 2 hours of oxidation at 1100°C, the area fraction of  $\alpha$ -Al<sub>2</sub>O<sub>3</sub> in the scales on the Si-free and Si-containing alloys are 54% and 8%, respectively. However, it is not possible to accurately correlate the area fraction with the actual weight fraction or volume fraction of  $\theta$ -Al<sub>2</sub>O<sub>3</sub> or  $\alpha$ -Al<sub>2</sub>O<sub>3</sub>, because the photoluminescence intensity is influenced by many factors, such as impurity and defect concentration, radiative efficiencies of materials, absorption and re-absorption of photoluminescence in medium, etc. <sup>[142-144, 150]</sup>. Since the impurity level of alloy substrates and oxidation processes are not precisely controlled, quantification of the intensity maps can vary from sample to sample. Moreover, these bi-color intensity maps only reflect mostly the phase composition in the region near the scale/gas interface <sup>[144]</sup>. The underlying structures and phase compositions may be different.

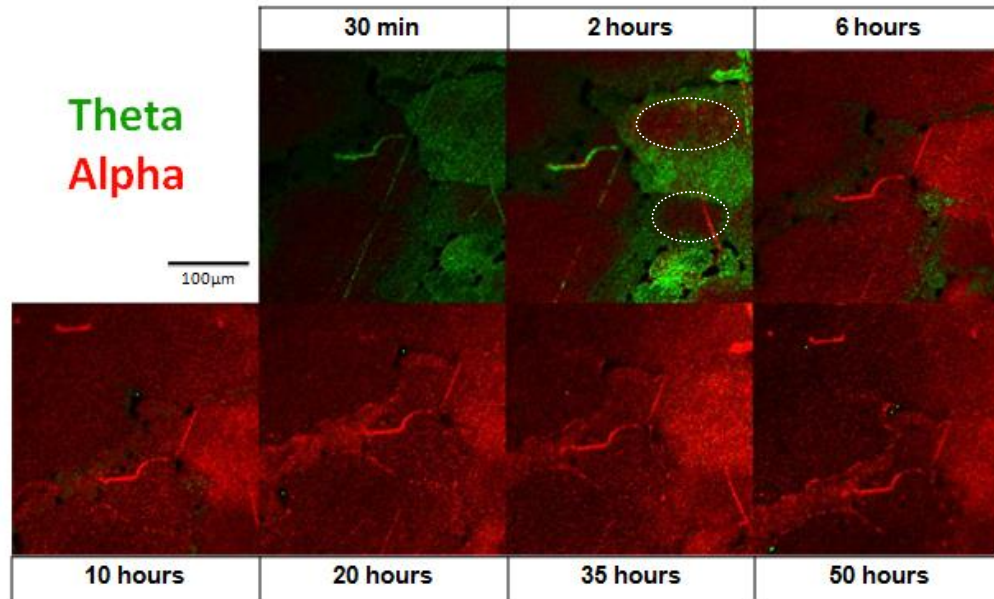


Figure 5.2 Confocal photo-stimulated microspectroscopy (CPSM) images of thermally grown  $\theta$ - $\text{Al}_2\text{O}_3$  and  $\alpha$ - $\text{Al}_2\text{O}_3$  formed on Ni-20Al-5Cr-0.05Hf-0.05Y.  $\theta$ - $\text{Al}_2\text{O}_3$  is represented by green color and  $\alpha$ - $\text{Al}_2\text{O}_3$  is represented by red color. Series images were taken after oxidized for 0.5h, 2h, 6h, 10h, 20h and 50h on Linkam TS1500 hot stage at 1100°C in air.

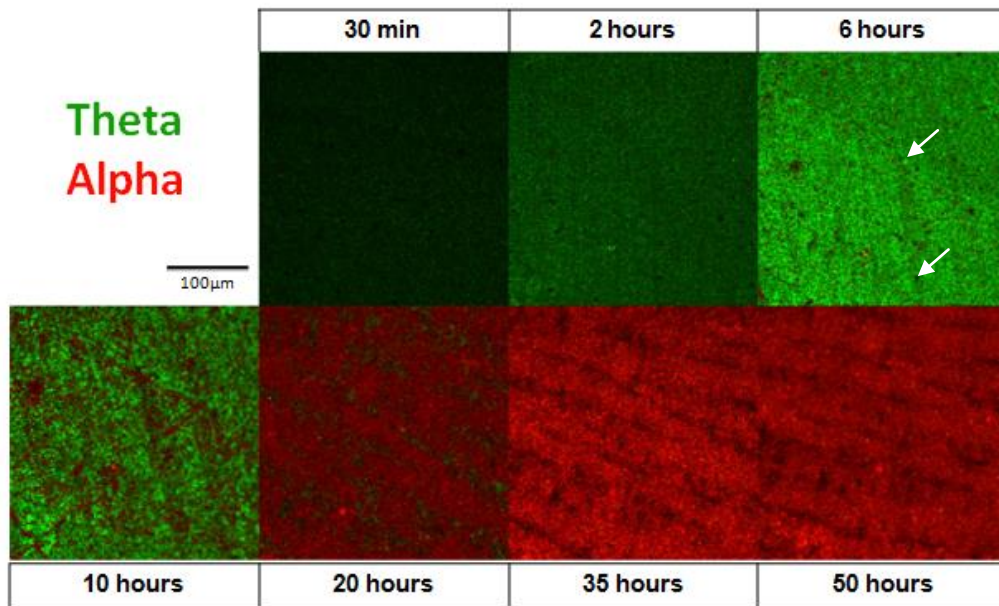


Figure 5.3 Confocal photo-stimulated microspectroscopy (CPSM) images of thermally grown  $\theta$ -Al<sub>2</sub>O<sub>3</sub> and  $\alpha$ -Al<sub>2</sub>O<sub>3</sub> formed on Ni-20Al-5Cr-0.05Hf-0.05Y-1Si.  $\theta$ -Al<sub>2</sub>O<sub>3</sub> is represented by green color and  $\alpha$ -Al<sub>2</sub>O<sub>3</sub> is represented by red color. Series images were taken after oxidized for 0.5h, 2h, 6h, 10h, 20h and 50h on Linkam TS1500 hot stage at 1100°C in air.

### 5.3.2 Semi-quantitative X-ray diffraction characterization

The confocal photo-stimulated images shown in Figure 5.2 and Figure 5.3 qualitatively showed the evolution of the Al<sub>2</sub>O<sub>3</sub> scale as a function of oxidation time at 1100°C for both Si-free and Si-containing alloys. However, quantitative characterization of the scale microstructure was not possible due to the limitation of this technique, as discussed in section 5.3.1. In order to further characterize the scale evolution in terms of the  $\theta \rightarrow \alpha$ -Al<sub>2</sub>O<sub>3</sub> transformation kinetics, glancing angle X-ray diffraction (GAXRD) was employed to quantitatively determine the scale phase composition.

Quantitative analysis by X-ray diffraction (XRD) technique is a standard method to measure the volume fraction of different phases in a multiphase sample <sup>[145-146]</sup>. It has been used to analyze the transformation of aluminas involved in the sintering processes of alumina powder <sup>[147]</sup>. Semi-quantitative approximation of the phase evaluation within a thermally-grown Al<sub>2</sub>O<sub>3</sub> scale has also been reported using GAXRD to minimize the interference from the alloy substrate <sup>[62, 148]</sup>.

The principle of semi-quantitative XRD analysis is that the volume fraction of a phase in a multi-phase sample is proportional to the integrated intensity of a diffraction peak associated with that phase <sup>[145]</sup>. In the case of  $\theta$ -Al<sub>2</sub>O<sub>3</sub> and  $\alpha$ -Al<sub>2</sub>O<sub>3</sub> analysis, this relationship is written as follows:

$$\frac{I_{\alpha i}}{I_{\theta j}} = \frac{K_{\alpha}}{K_{\theta}} \cdot \frac{v_{\alpha}}{v_{\theta}} \quad (5.1)$$

where  $I_{\alpha i}$  is the integrated intensity of the  $i^{\text{th}}$  peak of  $\alpha$ -Al<sub>2</sub>O<sub>3</sub>,  $I_{\theta j}$  is the integrated intensity of  $j^{\text{th}}$  peak of  $\theta$ -Al<sub>2</sub>O<sub>3</sub>;  $K_{\alpha}$  and  $K_{\theta}$  are constants which depend on the characteristics of the XRD

machine and the structure of  $\alpha$ -Al<sub>2</sub>O<sub>3</sub> and  $\theta$ -Al<sub>2</sub>O<sub>3</sub>;  $v_\alpha$  and  $v_\theta$  are the volume fractions of  $\alpha$ -Al<sub>2</sub>O<sub>3</sub> and  $\theta$ -Al<sub>2</sub>O<sub>3</sub>.

To simplify the present analysis,  $K_\alpha$  is taken to be approximately equal to  $K_\theta$  because the crystal structure of  $\theta$ -Al<sub>2</sub>O<sub>3</sub> resembles to some extent that of  $\alpha$ -Al<sub>2</sub>O<sub>3</sub> and all samples were prepared and tested using the same machine conditions. Such a simplified treatment will inevitably bring some error; however, it is almost impossible to estimate the error band because this is a non-standard quantitative analysis without calibration and corrections. Even so after referring to studies from other researchers, it is believed that this error will not heavily overshadow or diminish the actual data <sup>[62, 148]</sup>. Thus, equation 5.1 is reduced to:

$$\frac{I_{\alpha i}}{I_{\theta j}} \approx \frac{v_\alpha}{v_\theta} \quad (5.2)$$

In this study, another treatment was used to reduce the experimental errors. Since it is known that the thermally grown meta-stable aluminas are usually textured with some preferred orientations due to the nature of its diffusive growth <sup>[17, 37]</sup>, comparison of the integrated intensity of a single peak may cause excessive error. Thus, in order to alleviate the influence of texture, comparison of a sum integrated intensities of all diffracted peaks (from 15-80°) for each phase was used instead of a single peak intensity comparison <sup>[37, 141]</sup>, yielding equation 5.3:

$$\frac{\sum I_\alpha}{\sum I_\theta} \approx \frac{v_\alpha}{v_\theta} \quad (5.3)$$

where  $\sum I_\alpha$  is the sum intensity of all peaks from  $\alpha$ -Al<sub>2</sub>O<sub>3</sub> and  $\sum I_\theta$  is the sum intensities of all peaks from  $\theta$ -Al<sub>2</sub>O<sub>3</sub>.

A  $0.5^\circ$  incident beam angle was chosen in this study. Table 5.2 lists the semi-quantitative approximation of the volume contents of scale phases ( $\theta$ - $\text{Al}_2\text{O}_3$  % and  $\alpha$ - $\text{Al}_2\text{O}_3$  %) formed on the Si-containing and Si-free alloys after oxidation at  $1100^\circ\text{C}$  for different times (0.5, 2, 6, 10 and 20 hours) and Figure 5.4 plots these results as a function of oxidation time. Each percentage in Table 5.2 and Figure 5.4 was obtained from an individual sample. This is different from the CPSM images shown in Figure 5.2 and Figure 5.3, where a series of images was taken from the same area of the same sample for each alloy composition.

Table 5.2 Volume fraction of scale phases (% $\theta$ - $\text{Al}_2\text{O}_3$  and % $\alpha$ - $\text{Al}_2\text{O}_3$ ) of Ni-20Al-5Cr-0.05Hf-0.05Y and Ni-20Al-5Cr-0.05Hf-0.05Y-1Si after oxidized at  $1100^\circ\text{C}$  for different time

Oxidation Time	Ni-20Al-5Cr-0.05Hf-0.05Y		Ni-20Al-5Cr-0.05Hf-0.05Y-1Si	
	% $\theta$ - $\text{Al}_2\text{O}_3$	% $\alpha$ - $\text{Al}_2\text{O}_3$	% $\theta$ - $\text{Al}_2\text{O}_3$	% $\alpha$ - $\text{Al}_2\text{O}_3$
0.5h	23%	62%	47%	40%
2h	26%	74%	52%	48%
6h	2%	98%	18%	82%
10h	0%	100%	3%	97%
20h	0	100%	0	100%

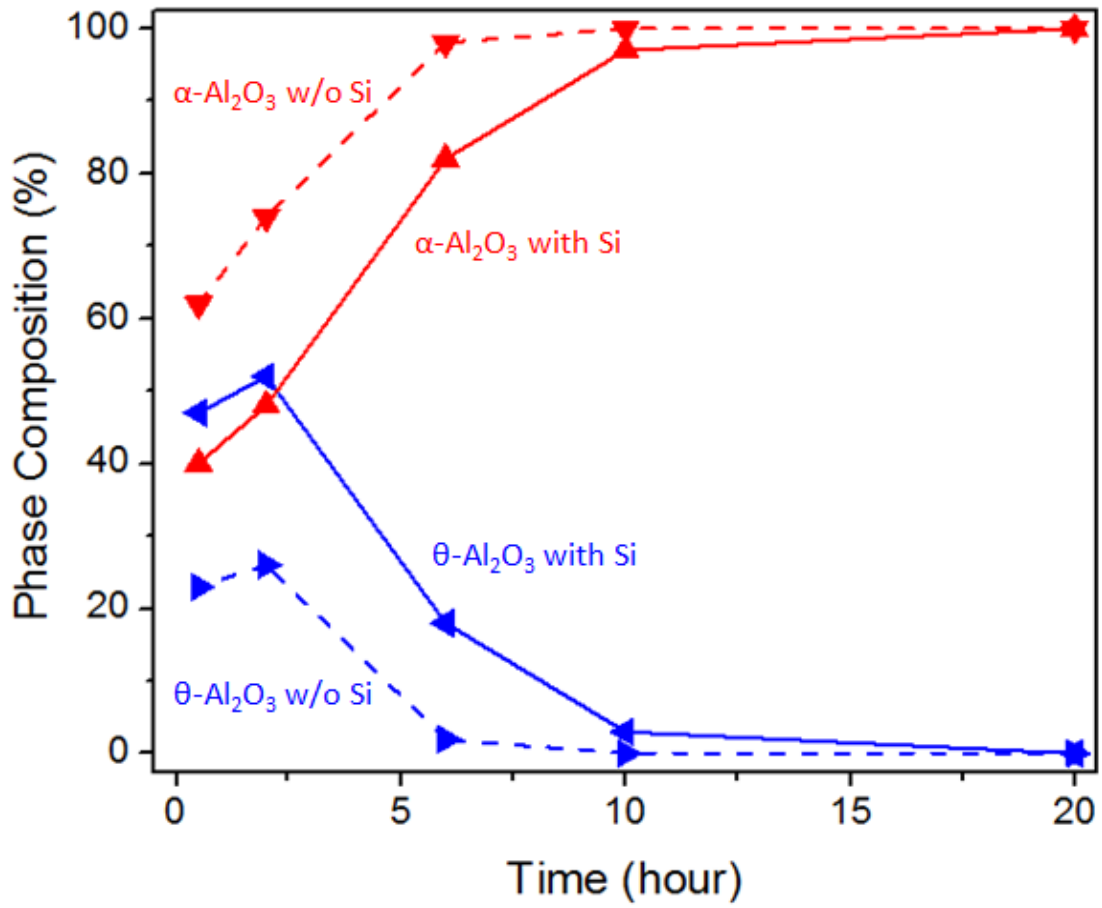


Figure 5.4 Semi-quantitative approximation of the phase composition of  $\theta$ -Al<sub>2</sub>O<sub>3</sub> and  $\alpha$ -Al<sub>2</sub>O<sub>3</sub> formed on Ni-20Al-5Cr-0.05Hf-0.05Y and Ni-20Al-5Cr-0.05Hf-0.05Y-1Si alloys as a function of oxidation time at 1100°C

The semi-quantitative approximation in Table 5.2 indicates that after 10 hours of oxidation the scale on the Si-free alloy was fully  $\alpha$ -Al<sub>2</sub>O<sub>3</sub>, while the scale on the Si-containing alloy still contained a small amount of  $\theta$ -Al<sub>2</sub>O<sub>3</sub>. After 20 hours of oxidation,  $\theta$ -Al<sub>2</sub>O<sub>3</sub> totally transformed to  $\alpha$ -Al<sub>2</sub>O<sub>3</sub> for the Si-containing alloy. The critical transformation time ( $\theta$ -Al<sub>2</sub>O<sub>3</sub> totally transformed to  $\alpha$ -Al<sub>2</sub>O<sub>3</sub>) determined by semi-quantitative GAXRD is in good agreement with that obtained from confocal photo-stimulated micro-spectroscopy. Moreover, the volume fraction of  $\theta$ -Al<sub>2</sub>O<sub>3</sub> and  $\alpha$ -Al<sub>2</sub>O<sub>3</sub> plotted as a function of oxidation time (Figure 5.4) shows clearly the extent to which the transformation kinetics are influenced by the addition of silicon. Therefore, these current results confirm that the Si addition delayed the  $\theta \rightarrow \alpha$ -Al<sub>2</sub>O<sub>3</sub> transformation on this model  $\gamma+\gamma'$  Ni-20Al-5Cr-0.05Hf-0.05Y Al<sub>2</sub>O<sub>3</sub>-scale forming alloy.

It is noteworthy that the volume fraction of  $\theta$ -Al<sub>2</sub>O<sub>3</sub> in the scale on both the Si-free and Si-containing alloys experienced a slight increase followed by a sharp decrease before complete transformation to  $\alpha$ -Al<sub>2</sub>O<sub>3</sub>. The transformation from  $\gamma$ -Al<sub>2</sub>O<sub>3</sub> to  $\theta$ -Al<sub>2</sub>O<sub>3</sub> is believed to account for this slight increase, which means that why early on the supply of  $\theta$ -Al<sub>2</sub>O<sub>3</sub> from  $\gamma \rightarrow \theta$ -Al<sub>2</sub>O<sub>3</sub> transformation is more than its consumption by  $\theta \rightarrow \alpha$ -Al<sub>2</sub>O<sub>3</sub> transformation. However, since  $\gamma$ -Al<sub>2</sub>O<sub>3</sub> only existed for a very short period at this oxidation temperature (1100°C), quantitative measurements of  $\gamma$ -Al<sub>2</sub>O<sub>3</sub> were not included in Table 5.2 and Figure 5.4. It is true though that  $\gamma$ -Al<sub>2</sub>O<sub>3</sub> does get involved in the early stage of oxidation, especially at relatively low temperatures (i. e.  $\leq 1000^\circ\text{C}$ ). This topic will be discussed in the next section.

Another noteworthy point is that that even though the critical transformation times determined by CPSM and GAXRD are consistent, there are some quantitative discrepancies between the two sets of results before the completion of transformation. For instance, after 6 hours of oxidation, the CPSM images indicate that the scale on the Si-containing alloy contains

88% (area fraction)  $\theta$ -Al<sub>2</sub>O<sub>3</sub>; whereas the GAXRD results show that the scale contains only 18% (volume fraction)  $\theta$ -Al<sub>2</sub>O<sub>3</sub>. As discussed in section 5.3.1, it is substantially meaningless to correlate the area fraction of  $\theta$ -Al<sub>2</sub>O<sub>3</sub> from the CPSM images to its actual volume or weight fraction; however, such a significant discrepancy must be addressed. The main reason for the existence of this discrepancy is the different reliabilities of these two techniques in terms of phase characterization. Generally speaking, the photoluminescence signals originate from the near surface region of the scale <sup>[144]</sup>, but the emission of photoluminescence is strongly influenced by interfaces <sup>[150]</sup>. It is known that the  $\theta \rightarrow \alpha$ -Al<sub>2</sub>O<sub>3</sub> transformation is accompanied by the lateral and vertical migration of  $\theta$ -Al<sub>2</sub>O<sub>3</sub>/ $\alpha$ -Al<sub>2</sub>O<sub>3</sub> interfaces; however, the influence of interfaces on the behavior of photoluminescence excitation is too difficult to estimate. In addition, the effects of impurity and defect concentrations on the yield efficiency of photoluminescence are hard to estimate based on the present experimental conditions. On the other hand, the data collected by X-ray diffraction are barely influenced in terms of phase characterization. Hence, the semi-quantitative approximation of the phase fraction obtained by GAXRD became much more reliable compared to that obtained by CPSM.

### 5.3.3 Construction of Time-Temperature-Transformation (T-T-T) type diagrams

The traditional time-temperature-transformation (T-T-T) diagram, which is also known as isothermal-transformation (I-T) diagram, was originally developed to illustrate the time dependence of microstructural transformation in steels <sup>[151]</sup>. It is also extensively used in other systems such as titanium alloys, aluminum alloys and ceramics <sup>[152-153]</sup>. Acting as a visual map, the T-T-T diagram allows one to determine or predict the transformation products as a function of time and temperature. T-T-T type diagrams for Al<sub>2</sub>O<sub>3</sub> formed on Fe-Cr-Al alloys have been constructed by Andoh *et al.* <sup>[154-155]</sup>. These T-T-T type diagrams have been characterized as having four regions: 1)  $\gamma$ -Al<sub>2</sub>O<sub>3</sub>, 2)  $\gamma$ -Al<sub>2</sub>O<sub>3</sub> +  $\theta$ -Al<sub>2</sub>O<sub>3</sub>, 3)  $\gamma$ -Al<sub>2</sub>O<sub>3</sub> +  $\theta$ -Al<sub>2</sub>O<sub>3</sub> +  $\alpha$ -Al<sub>2</sub>O<sub>3</sub> and 4)  $\alpha$ -Al<sub>2</sub>O<sub>3</sub> + Fe(Cr,Al)<sub>2</sub>O<sub>4</sub>, which are a function of the time and temperature. Pint *et al.* <sup>[14]</sup> have reported a T-T-T type diagram for Al<sub>2</sub>O<sub>3</sub> formed on  $\beta$ -NiAl alloy. A  $\theta$ -Al<sub>2</sub>O<sub>3</sub> +  $\alpha$ -Al<sub>2</sub>O<sub>3</sub> transformation zone was characterized on that diagram. In this study, effect of additives on the shift of the  $\theta$ -Al<sub>2</sub>O<sub>3</sub> +  $\alpha$ -Al<sub>2</sub>O<sub>3</sub> transformation zone has also been discussed <sup>[14]</sup>. Additives that facilitate the  $\theta \rightarrow \alpha$ -Al<sub>2</sub>O<sub>3</sub> transformation causes a shift in the transformation zone to the left; whereas, additives which inhibited the  $\theta \rightarrow \alpha$ -Al<sub>2</sub>O<sub>3</sub> transformation shifts and also broadens this zone to the right.

The self-consistent results obtained by CPSM and GAXRD presented in sections 5.3.1 and 5.3.2 give a clear conclusion that the addition of Si delays the transformation from  $\theta$ -Al<sub>2</sub>O<sub>3</sub> to  $\alpha$ -Al<sub>2</sub>O<sub>3</sub> during the early stage of oxidation for the  $\gamma+\gamma'$  Ni-20Al-5Cr-0.05Hf-0.05Y model alloy at 1100°C. In order to gain a more thorough understanding of the Si effect on the oxidation kinetics in a broader scope of temperature and time, T-T-T type diagrams of the thermally grown Al<sub>2</sub>O<sub>3</sub> scale were constructed for both Si-free and Si-containing alloys over the temperature range from 800°C to 1100°C for up to 100 hours exposure.

The T-T-T type diagrams for Ni-20Al-5Cr-0.05Hf-0.05Y and Ni-20Al-5Cr-0.05Hf-0.05Y-1Si alloys are shown in Figure 5.5 and Figure 5.6, where  $\gamma$ -Al<sub>2</sub>O<sub>3</sub> is represented by the green round symbols,  $\theta$ -Al<sub>2</sub>O<sub>3</sub> is represented by the blue triangle symbols and  $\alpha$ -Al<sub>2</sub>O<sub>3</sub> is represented by red diamond symbols. The size of symbols is not related to the relative ratio of each phase. At each oxidation temperature (800°C, 900°C, 1000°C and 1100°C), a series samples were oxidized for 0.5h, 1h, 2h, 4h, 20h and 100h to track the phase evolution of the scale. The data points on these diagrams were all obtained by GAXRD using 0.5° incident beam angle. Figure 5.7 and Figure 5.8 show the X-ray diffraction spectra of the scales formed on both of the Si-free and Si-containing alloys after 100 hours of oxidation at 800°C, 900°C, 1000°C and 1100°C.

Generally, over the oxidation temperature range 800°C and 1100°C the growth of any Al<sub>2</sub>O<sub>3</sub> scale is expected to experience five sequential stages:  $\gamma \rightarrow \gamma+\theta \rightarrow \gamma+\theta+\alpha \rightarrow \theta+\alpha \rightarrow \alpha$ . However, only the two or three later stages are present at each temperature in Figure 5.5 and Figure 5.6 due to the limited data collection in a relatively short time scale. Comparing with the  $\theta \rightarrow \alpha$ -Al<sub>2</sub>O<sub>3</sub> transformation, the  $\gamma \rightarrow \theta$ -Al<sub>2</sub>O<sub>3</sub> transformation has much less effect on the oxidation resistance of the alumina scale for two reasons: 1) the  $\gamma \rightarrow \theta$ -Al<sub>2</sub>O<sub>3</sub> transformation brings less volume contraction than the  $\theta \rightarrow \alpha$ -Al<sub>2</sub>O<sub>3</sub> transformation, because both  $\gamma$ -Al<sub>2</sub>O<sub>3</sub> and  $\theta$ -Al<sub>2</sub>O<sub>3</sub> have relatively open crystal structure and they belong to the same crystal group (ABCABC group) in terms of the stacking sequence of oxygen, while the crystal structure of  $\alpha$ -Al<sub>2</sub>O<sub>3</sub> is close-packed and it belongs to a different structure group (ABAB group) <sup>[20]</sup>; and 2) both of the  $\gamma$ -Al<sub>2</sub>O<sub>3</sub> and  $\theta$ -Al<sub>2</sub>O<sub>3</sub> are fast-growing meta-stable aluminas with less oxidation resistance, while only the slow-growing  $\alpha$ -Al<sub>2</sub>O<sub>3</sub> can act as diffusion barrier and provide enough protection to

oxidation<sup>[37]</sup>. Hence, more attention was directed to the  $\theta \rightarrow \alpha\text{-Al}_2\text{O}_3$  transformation kinetics on the T-T-T type diagrams.

The dashed lines in the T-T-T type diagram of Si-free alloy and solid lines in the T-T-T type diagram of the Si-containing alloy characterize the  $\alpha\text{-Al}_2\text{O}_3$  single-phase region and the  $\theta \rightarrow \alpha\text{-Al}_2\text{O}_3$  transformation zone. It is seen that the addition of Si broadened the  $\theta \rightarrow \alpha\text{-Al}_2\text{O}_3$  transformation zone, which means that the silicon addition stabilized the  $\theta\text{-Al}_2\text{O}_3$  and was able to delay the  $\theta \rightarrow \alpha\text{-Al}_2\text{O}_3$  transformation. This result is in good agreement with that obtained by CPSM and GAXRD at 1100°C. Accordingly, it further confirmed the effect of Si in delaying the  $\theta \rightarrow \alpha\text{-Al}_2\text{O}_3$  transformation over a broader temperature range.

The borderline between the  $\gamma\text{-Al}_2\text{O}_3$  single phase region and the  $\gamma \rightarrow \theta\text{-Al}_2\text{O}_3$  transformation zone was not characterized on these two T-T-T diagrams. Since several diffraction peaks of  $\gamma\text{-Al}_2\text{O}_3$  and  $\theta\text{-Al}_2\text{O}_3$  are very close or even overlap, identification of  $\gamma\text{-Al}_2\text{O}_3$  in a multiphase sample containing both  $\gamma\text{-Al}_2\text{O}_3$  and  $\theta\text{-Al}_2\text{O}_3$  is not straightforward, especially when for these samples oxidized at relatively low temperature (800°C ~ 900°C). Artificial separation of overlapped peaks by software (i.e., OriginPro) is sometimes subjective and makes the characterization of the borderline ambiguous. In contrast, identification of  $\alpha\text{-Al}_2\text{O}_3$  was more straightforward.

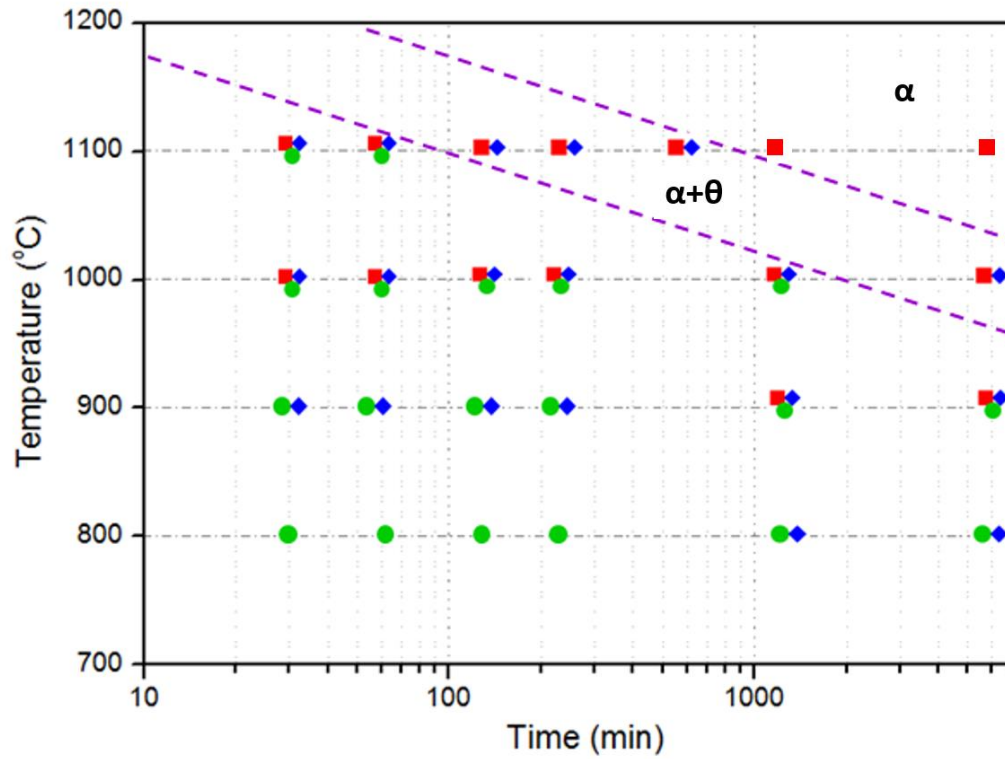


Figure 5.5 T-T-T type diagram of aluminum oxides formed on Ni-20Al-5Cr-0.05Hf-0.05Y over temperature range 800~1100°C

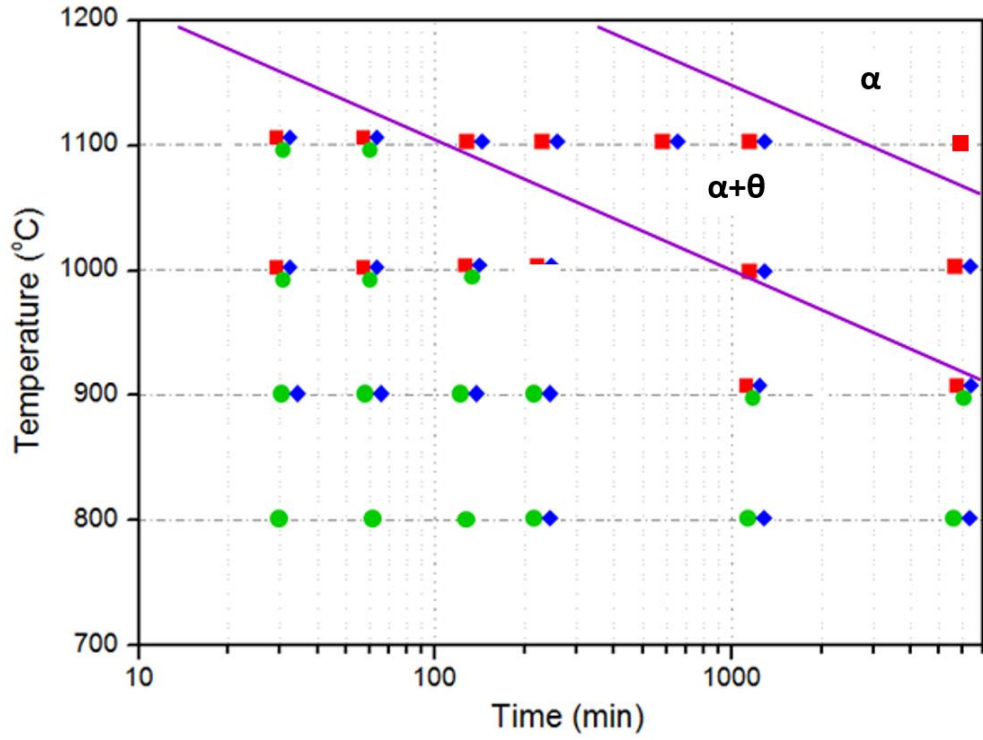


Figure 5.6 T-T-T type diagram of aluminum oxides formed on Ni-20Al-5Cr-0.05Hf-0.05Y-1Si over temperature range 800~1100°C

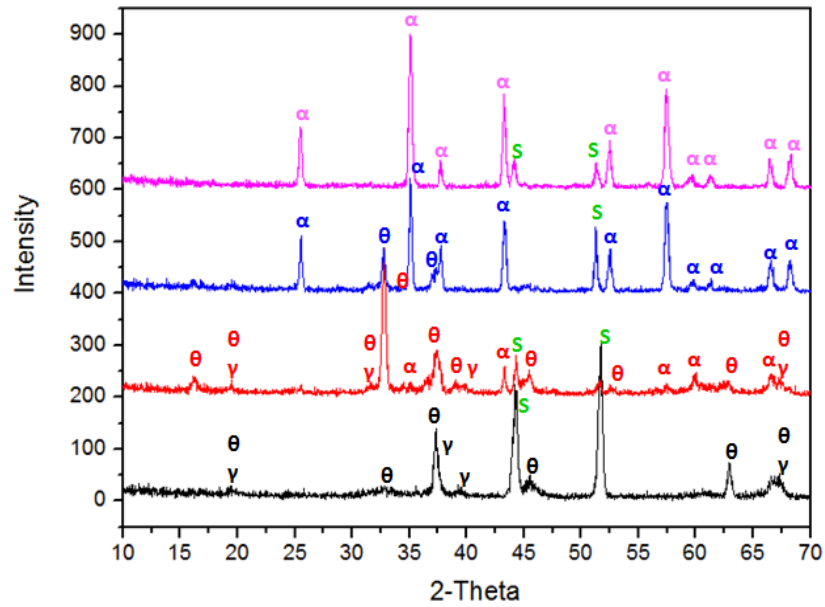


Figure 5.7 X-ray diffraction spectra of Ni-20Al-5Cr-0.05Hf-0.05Y after 100h oxidation at 800°C (black), 900°C (red), 1000°C (blue) and 1100°C (pink)

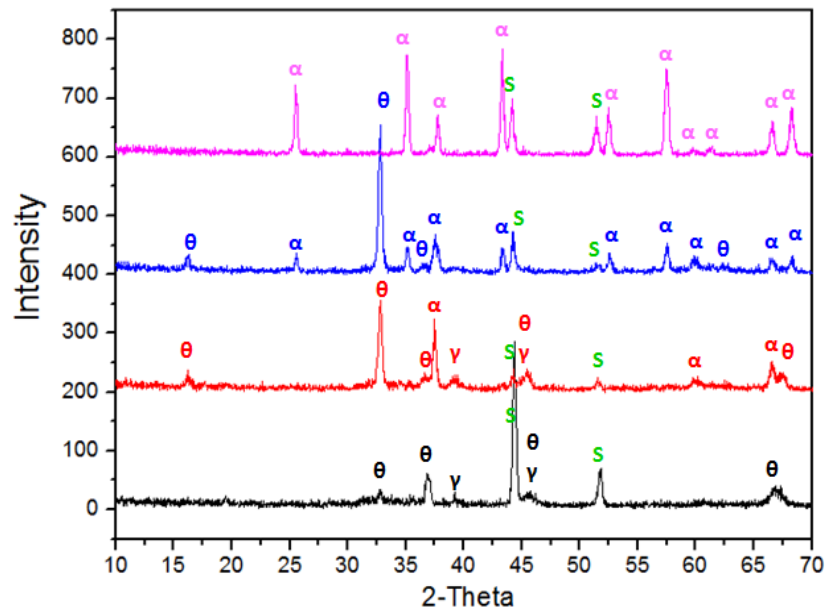


Figure 5.8 X-ray diffraction spectra of Ni-20Al-5Cr-0.05Hf-0.05Y-1Si after 100h oxidation at 800°C (red), 900°C (red), 1000°C (blue) and 1100°C (pink)

### 5.3.4 Mathematical analysis of $\theta \rightarrow \alpha\text{-Al}_2\text{O}_3$ phase transformation kinetics

In sections 5.3.1 and 5.3.2, results obtained by qualitative confocal photo-stimulated microspectroscopy measurements and semi-quantitative glancing angle X-ray diffraction measurement gave a clear conclusion that the addition of silicon significantly delays the  $\theta \rightarrow \alpha\text{-Al}_2\text{O}_3$  transformation. Indeed, it is known that quantitative measurements, regardless of the method, are able to give more detailed information about the extent of phase transformation kinetics; however, the time-consuming data collecting and analyzing processes limit their wide application. In a recently published paper by Zhao *et al.* <sup>[162]</sup>, an alternative mathematical method based on analyzing the thermogravimetric analysis (TGA) data was developed for quantifying the extent of  $\theta \rightarrow \alpha\text{-Al}_2\text{O}_3$  transformation. TGA is so far the most commonly used technique for measuring the oxidation kinetics of  $\text{Al}_2\text{O}_3$ -scale forming alloys. The main purpose of this mathematical treatment was to use the time dependence of the instantaneous time exponent  $n^i$  to describe the extent of  $\theta \rightarrow \alpha\text{-Al}_2\text{O}_3$  transformation for some model  $\text{Al}_2\text{O}_3$ -scale forming alloys.

Generally, the overall  $\text{Al}_2\text{O}_3$ -scale growth kinetics follows the basic rate law:

$$\Delta m = kt^n \quad (5.4)$$

where  $\Delta m$  is the measured weight gain per unit area at time  $t$ ,  $k$  is the rate constant and  $n$  is the time exponent. When  $n=1$ , 0.5 or  $1/3$ , equation 5.4 becomes the simplest linear, parabolic or cubic rate law.

However, during the transient oxidation stage, which is associated with the  $\theta \rightarrow \alpha\text{-Al}_2\text{O}_3$  transformation, the value of  $n$  is not fixed at a certain value and instead changes with exposure time. This is largely due to the fact that there is a significant difference in the intrinsic growth

rate of  $\theta\text{-Al}_2\text{O}_3$  and  $\alpha\text{-Al}_2\text{O}_3$  (~2 orders of magnitude <sup>[127]</sup>). Thus, the instantaneous time exponent  $n^i$  is employed and it is calculated by the following equation:

$$n^i = \frac{\partial(\log \Delta m)}{\partial(\log t)} \quad (5.5)$$

Figure 5.9 (a) and (b) gave a real example of a measured  $\Delta m$  vs.  $t$  curve and associated  $n^i$  vs.  $t$  curve according to equation 5.5. The alloy for this example is Ni-20Al-5Cr-0.05Hf-0.05Y and the oxidation was at 1100°C in air. In Figure 5.9 (b), it is seen that the instantaneous time exponent  $n^i$  firstly decreases from around 0.52 to a minimum of about 0.16 and then gradually increases toward 0.5.

The next question is how to use the  $n^i$  vs.  $t$  curve to describe the extent of  $\theta \rightarrow \alpha\text{-Al}_2\text{O}_3$  transformation. In order to answer this question, a kinetic model based on ideal  $\text{Al}_2\text{O}_3$ -scale formation was proposed <sup>[162]</sup>. This model mainly focuses on the  $\theta \rightarrow \alpha\text{-Al}_2\text{O}_3$  transformation process, which is further characterized as three stages encompassing the nucleation and growth of  $\alpha\text{-Al}_2\text{O}_3$ . Figure 5.10 schematically shows the three-stage model. In stage I,  $\alpha\text{-Al}_2\text{O}_3$  nuclei form along the  $\theta\text{-Al}_2\text{O}_3$ /alloy interface, and the lateral growth rate of the nuclei is assumed to be faster than its vertical growth rate; In stage II, the dominating lateral growth of  $\alpha\text{-Al}_2\text{O}_3$  nuclei results the formation of a continuous layer of  $\alpha\text{-Al}_2\text{O}_3$  underneath the outer layer of primary  $\theta\text{-Al}_2\text{O}_3$ , and the vertical growth of  $\alpha\text{-Al}_2\text{O}_3$  become dominating after the continuous layer of  $\alpha\text{-Al}_2\text{O}_3$  formed; Finally in stage III, the inner layer of  $\alpha\text{-Al}_2\text{O}_3$  consumes the outer layer of  $\theta\text{-Al}_2\text{O}_3$  and eventually the whole scale becomes solely  $\alpha\text{-Al}_2\text{O}_3$ . In this proposed model, two important points should be noted: 1) the phase transformation from  $\theta\text{-Al}_2\text{O}_3$  to  $\alpha\text{-Al}_2\text{O}_3$  does not cause any weight change; and 2) the overall weight gain rate is controlled by the diffusion rate through  $\theta\text{-Al}_2\text{O}_3$  and  $\alpha\text{-Al}_2\text{O}_3$ . Therefore, since diffusion through  $\alpha\text{-Al}_2\text{O}_3$  is significantly slower

than through  $\theta\text{-Al}_2\text{O}_3$  due to the close-packed crystal structure of  $\alpha\text{-Al}_2\text{O}_3$ , the overall weight gain significantly slows down once the continuous layer of  $\alpha\text{-Al}_2\text{O}_3$  formed.

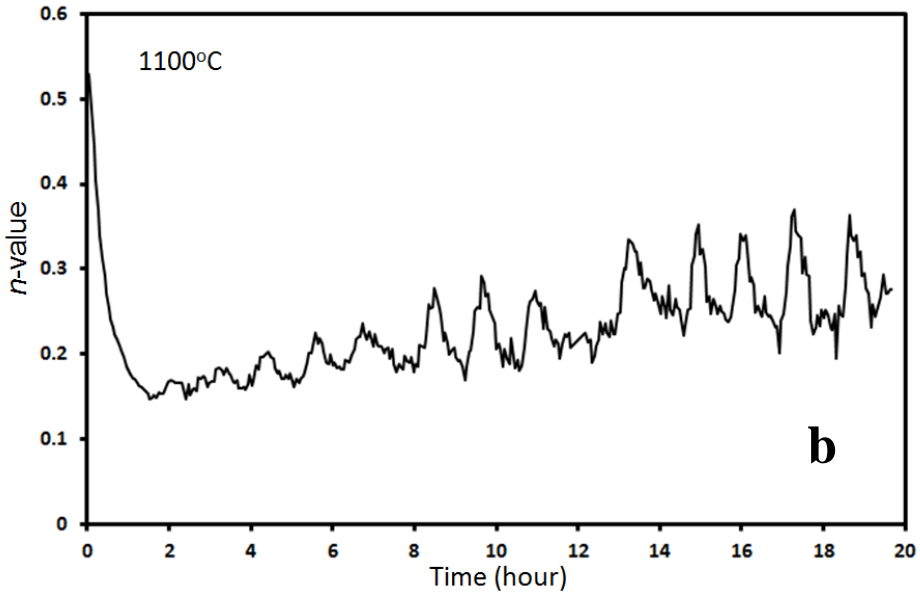
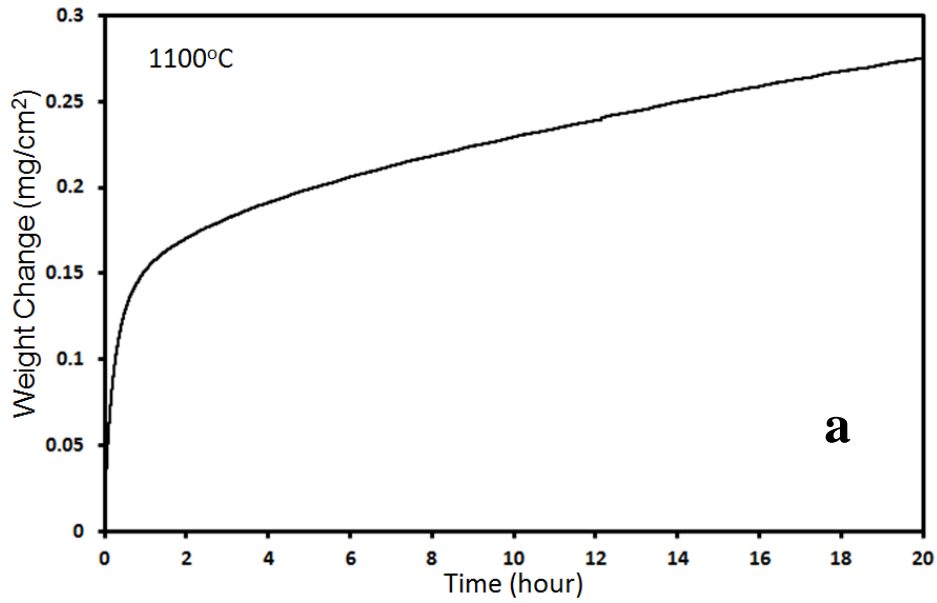


Figure 5.9 (a)  $\Delta m$  vs.  $t$  curve of Ni-20Al-5Cr-0.05Hf-0.05Y alloy at  $1100^\circ\text{C}$  in air (b)

Corresponding  $n^i$  vs.  $t$  curve of the  $\Delta m$  vs.  $t$  curve <sup>[162]</sup>

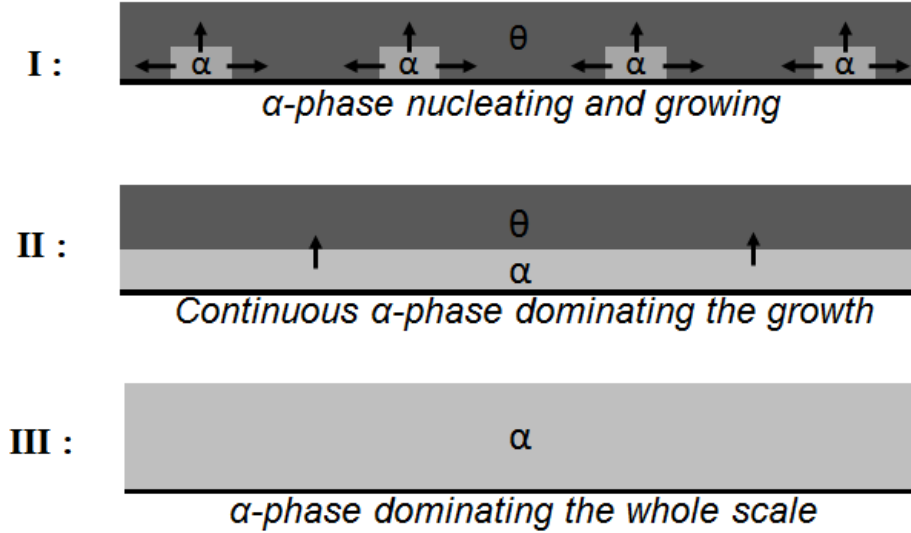


Figure 5.10 Schematic of the proposed three-stage  $\theta \rightarrow \alpha\text{-Al}_2\text{O}_3$  transformation model during  $\text{Al}_2\text{O}_3$ -scale growth <sup>[162]</sup>

Base on the proposed three-stage model, a mathematical treatment is carried out as follows <sup>[162]</sup>.

Firstly, the growth of both  $\theta\text{-Al}_2\text{O}_3$  and  $\alpha\text{-Al}_2\text{O}_3$  are assumed to follow the parabolic rate law:

$$\Delta m_i = (k_i t)^{\frac{1}{2}} \quad (5.6)$$

where  $\Delta m_i$  is the weight gain per unit area for phase i (either  $\theta\text{-Al}_2\text{O}_3$  or  $\alpha\text{-Al}_2\text{O}_3$ ) and  $k_i$  is the parabolic rate constant for phase i.

Secondly, the differential form of the weight gain is introduced in order to describe the transient weight gain for each phase:

$$dm_i = k_i^{\frac{1}{2}} \cdot dt^{\frac{1}{2}} \quad (5.7)$$

Thirdly, assuming the surface area covered by  $\alpha$ -Al<sub>2</sub>O<sub>3</sub> and  $\theta$ -Al<sub>2</sub>O<sub>3</sub> are A <sub>$\alpha$</sub>  and A <sub>$\theta$</sub> , the total transient weight gain is written as:

$$dm \cdot A_{total} = dm_{\alpha} \cdot A_{\alpha} + dm_{\theta} \cdot A_{\theta} \quad (5.8)$$

Then, the area fractions of  $\theta$ -Al<sub>2</sub>O<sub>3</sub> ( $f_{\theta}$ ) and  $\alpha$ -Al<sub>2</sub>O<sub>3</sub> ( $f_{\alpha}$ ) are introduced by dividing both side of equation 5.8 by total area A<sub>total</sub>:

$$dm = dm_{\alpha} \frac{A_{\alpha}}{A_{total}} + dm_{\theta} \frac{A_{\theta}}{A_{total}} \quad (5.9)$$

$$dm = dm_{\alpha} \cdot f_{\alpha} + dm_{\theta} \cdot f_{\theta} \quad (5.10)$$

and here

$$f_{\alpha} + f_{\theta} = 1 \quad (5.11)$$

Substituting equations 5.7 and 5.11 into equation 5.10 gives:

$$dm = f_{\alpha} k_{\alpha}^{\frac{1}{2}} dt^{\frac{1}{2}} + (1 - f_{\alpha}) k_{\theta}^{\frac{1}{2}} dt^{\frac{1}{2}} \quad (5.12)$$

Integrating both sides of equation 5.12 gives the total weight gain per unit area as:

$$\Delta m = \int_{t=0}^{t=t} [f_{\alpha} k_{\alpha}^{\frac{1}{2}} dt^{\frac{1}{2}} + (1 - f_{\alpha}) k_{\theta}^{\frac{1}{2}} dt^{\frac{1}{2}}] \quad (5.13)$$

Noting that  $f_{\alpha}$  is a function of time, equation 5.13 can be rewritten as:

$$\Delta m = \left( k_{\theta}^{\frac{1}{2}} - k_{\alpha}^{\frac{1}{2}} \right) \int_0^t (1 - f_{\alpha}) \cdot d \left( t^{\frac{1}{2}} \right) + k_{\alpha}^{\frac{1}{2}} \cdot t^{\frac{1}{2}} \quad (5.14)$$

In this treatment, we use the Johnson-Mehl-Avrami (JMA) model <sup>[164-166]</sup> to describe the change of  $f_\alpha$  as a function of time and it is expressed as:

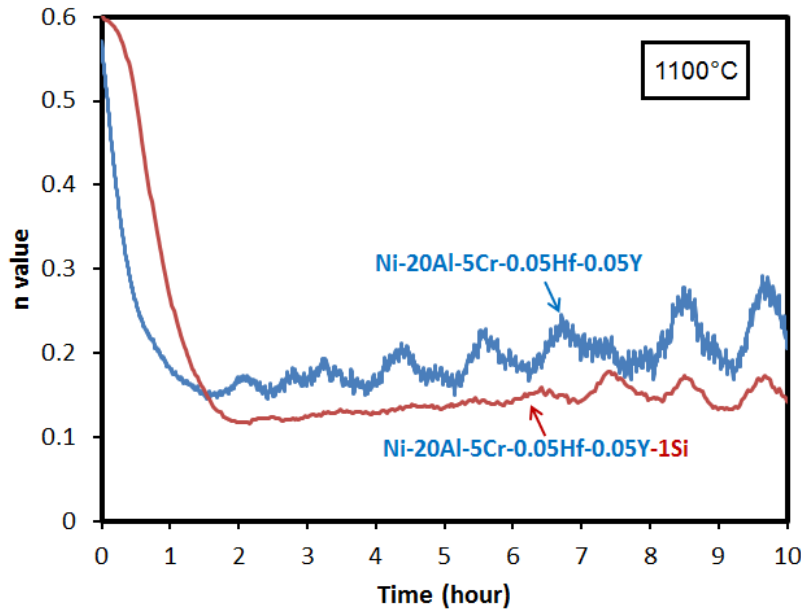
$$f_\alpha = 1 - \exp(-Kt^\omega) \quad (5.15)$$

Now, the relationship between  $f_\alpha$  and  $n^i$  is able to be connected via  $\Delta m$ , which is the measurable data by thermogravimetric analysis (TGA).

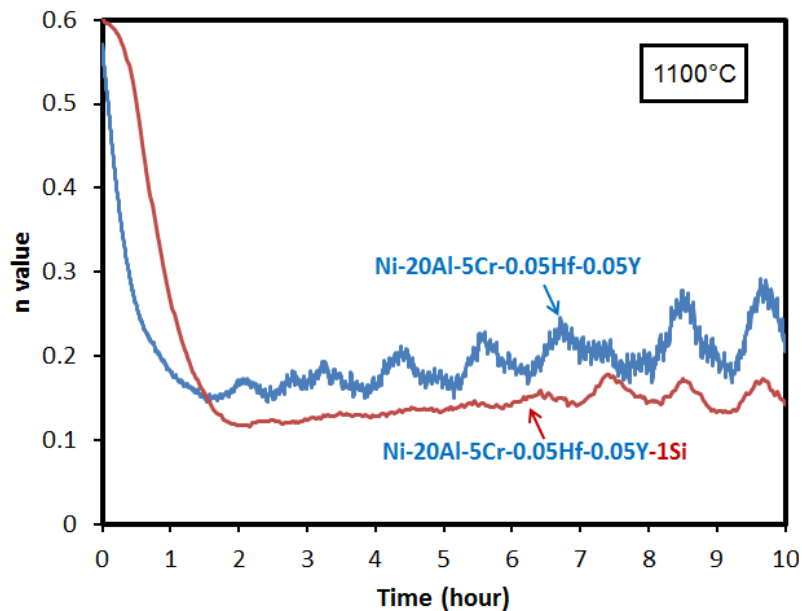
This mathematical treatment is now applied to the analysis of Si addition in affecting the  $\theta \rightarrow \alpha\text{-Al}_2\text{O}_3$  transformation for Ni-20Al-5Cr-0.05Hf-0.05Y model alloys. Figure 5.11 (a) and (b) are the measured  $\Delta m$  vs.  $t$  and calculated  $n^i$  vs.  $t$  curves for the Ni-20Al-5Cr-0.05Hf-0.05Y and Ni-20Al-5Cr-0.05Hf-0.05Y-1Si alloys oxidized at 1100<sup>o</sup>C in dry air (0-10h), and Figure 5.11 (c) is the associated bestfit of  $f_\alpha$  vs.  $t$  curves. It is seen that the time when  $n^i$  reaches minimum value shifts to the right when changing from a Si-free alloy to a Si-containing alloy, which is consistent with the trend in the  $f_\alpha$  vs.  $t$  curves, indicating that the addition of silicon delays the  $\theta \rightarrow \alpha\text{-Al}_2\text{O}_3$  transformation. This agreement suggests that the calculated  $n^i$  vs.  $t$  curves can be used to determine or predict the influence of additive on the transformation kinetics based solely on the measure  $\Delta m$  vs.  $t$  results.

A comparison of the  $f_\alpha$  vs.  $t$  curves obtained by semi-quantitative GAXRD measurement and by mathematical fitting based on the proposed three-stage model was carried out, and the results are summarized in Figure 5.12. It is noted that a quantitative deviation exists when using the fitted  $f_\alpha$  vs.  $t$  curve to determine the transition time (when  $f_\alpha \geq 90\%$ ) compared with using semi-quantitative GAXRD measurement. The transition time ( $t_{tr}^1$ ) determined by kinetic analysis is around 2 hours, while the transition time ( $t_{tr}^2$ ) determined by semi-quantitative GAXRD is around 6 hours. The existence of this difference can be explained by re-considering the proposed

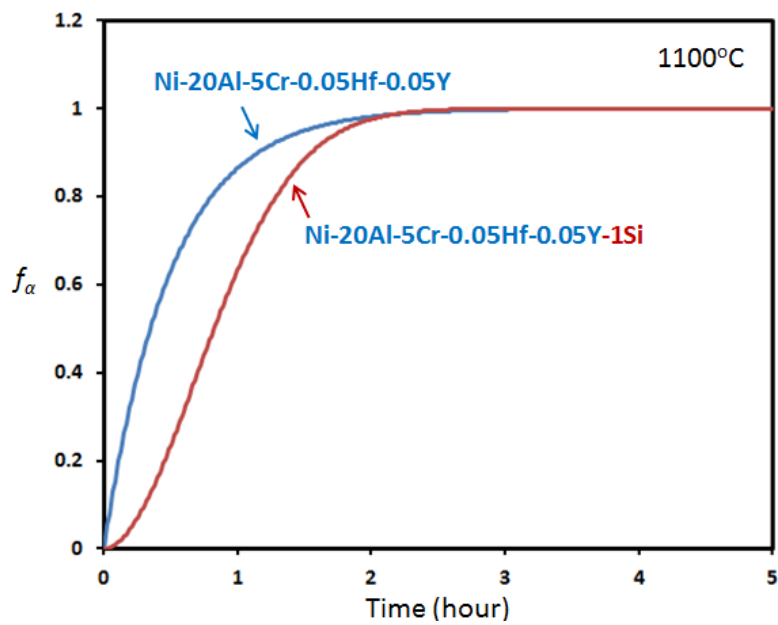
three-stage model. Noting that  $f_\alpha$  used in the mathematical treatment for kinetic analysis is the area fraction of  $\alpha$ -Al<sub>2</sub>O<sub>3</sub>, so that  $f_\alpha$  reaching corresponds to a continuous layer of  $\alpha$ -Al<sub>2</sub>O<sub>3</sub> and the overall oxidation rate significantly slows. At that point the second stage (II) in the proposed model has been finished. On the other hand, the  $f_\alpha$  used in the semi-quantitative GAXRD measurement represents the volume fraction of  $\alpha$ -Al<sub>2</sub>O<sub>3</sub>; hence the unity of  $f_\alpha$  corresponds to the whole scale being fully transformed to  $\alpha$ -Al<sub>2</sub>O<sub>3</sub>, meaning that the third stage (III) in the proposed model has been finished. Thus, it is seen that  $t_{tr}^1$  determined by kinetic analysis represents the transition time between stages I and II, while  $t_{tr}^2$  determined by semi-quantitative GAXRD represents the transition time between stages II and III.



(a)



(b)



(c)

Figure 5.11 (a)  $\Delta m$  vs.  $t$  curves of Ni-20Al-5Cr-0.05Hf-0.05Y and Ni-20Al-5Cr-0.05Hf-0.05Y-1Si oxidized at  $1100^{\circ}\text{C}$  in dry air; (b) Corresponding calculated  $n^i$  vs.  $t$  curves of data shown in (a); (c) Corresponding simulated  $f_{\alpha}$  vs.  $t$  curves of data shown in (a)

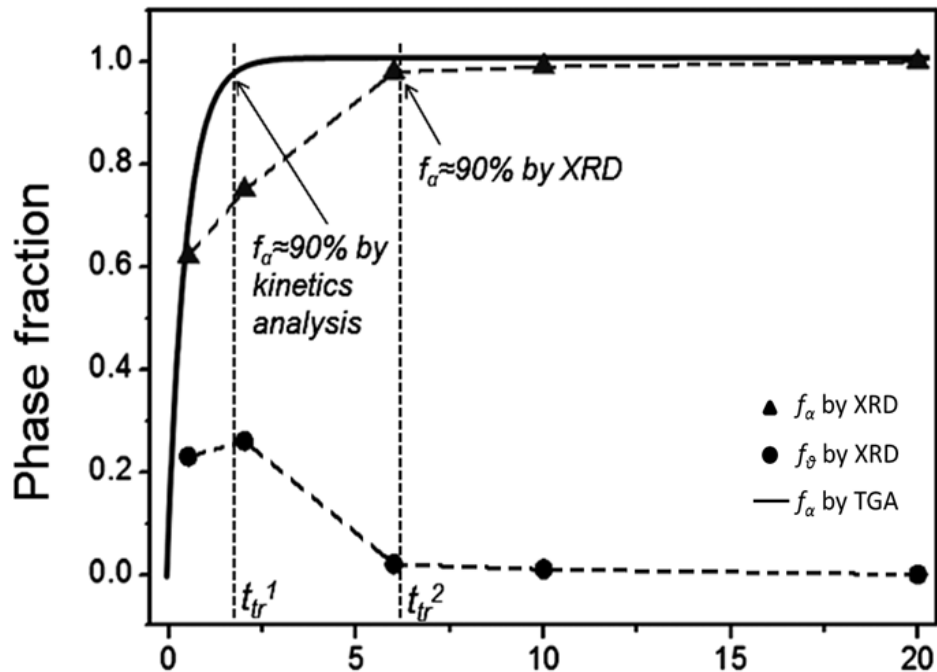


Figure 5.12 Comparison of  $f_\alpha$  vs.  $t$  curves determined by kinetic analysis and obtained by quantitative X-ray diffraction of Ni-20Al-5Cr-0.05Hf-0.05Y alloy oxidized at 1100<sup>o</sup>C in dry air

## 5.4 DISCUSSION

After presenting the experimental data obtained using CPSM and GAXRD in section 5.3, the key question is: How does silicon addition delay the  $\theta \rightarrow \alpha\text{-Al}_2\text{O}_3$  transformation? Previous studies on the influence of additives on the transformation from metastable aluminas to  $\alpha\text{-Al}_2\text{O}_3$  can be found in numerous papers in the areas of catalyst and ceramics <sup>[147, 156, 157]</sup>, but a limited number of reports can be found regarding the effect of silicon <sup>[162, 183]</sup>.

Chen *et al.* <sup>[147]</sup> investigated the influence of a variety of additives on the  $\gamma$  to  $\alpha$ -Al<sub>2</sub>O<sub>3</sub> transformation, and found that Si retards this transformation. The authors provided no speculation regarding the mechanism by which the Si retards the transformation, beyond suspecting suspected that it was associated with the formation of 3Al<sub>2</sub>O<sub>3</sub>•2SiO<sub>2</sub> (mullite). In the case of the influence of silicon on meta-stable  $\rightarrow$   $\alpha$ -Al<sub>2</sub>O<sub>3</sub> transformation during the early-stage oxidation of Ni-20Al-5Cr-0.05Hf-0.05Y alloy, SiO<sub>2</sub> or mullite is less likely to form because: 1) thermodynamically, silicon has less driving force to be oxidized compared to aluminum <sup>[2]</sup>, and 2) kinetically, the level of silicon content (1at. %) is not sufficient high to produce a significant amount of external SiO<sub>2</sub> to form mullite <sup>[2]</sup>. Experimental evidence supporting the speculation of forming mullite is also lacking, since energy-dispersive X-ray spectroscopy (EDX) analysis did not find significant existence of silicon inside the scale. Further characterization with finer resolution will be needed to clarify whether mullite does form or not.

Burtin *et al.* <sup>[156-157]</sup> systematically studied the influence of several additives on the transformation kinetics of powder Al<sub>2</sub>O<sub>3</sub> used extensively as catalyst supports. It was found that additives with larger ionic radius, such as La<sup>3+</sup> (1.15 Å), Th<sup>4+</sup> (0.95 Å), Ca<sup>2+</sup> (0.99 Å), inhibit the transformation from metastable Al<sub>2</sub>O<sub>3</sub> to stable  $\alpha$ -Al<sub>2</sub>O<sub>3</sub>. A theoretical model based on the annihilation of vacancies as the rate-determining step was proposed to interpret this result. Larger ions were believed to occupy the divalent vacancy sites and decrease the vacancy concentration required for the occurrence of phase transformation. Burtin *et al.*'s model found success in explaining the effect of Y<sup>3+</sup> (0.93 Å) on inhibiting the transformation from  $\theta$  to  $\alpha$ -Al<sub>2</sub>O<sub>3</sub>. However, it does not explain the retarding effect of Si because the ionic radius of Si<sup>4+</sup> (0.41 Å) is much smaller than La<sup>3+</sup>, Y<sup>3+</sup> and even smaller than Al<sup>3+</sup> (0.5 Å) <sup>[158]</sup>.

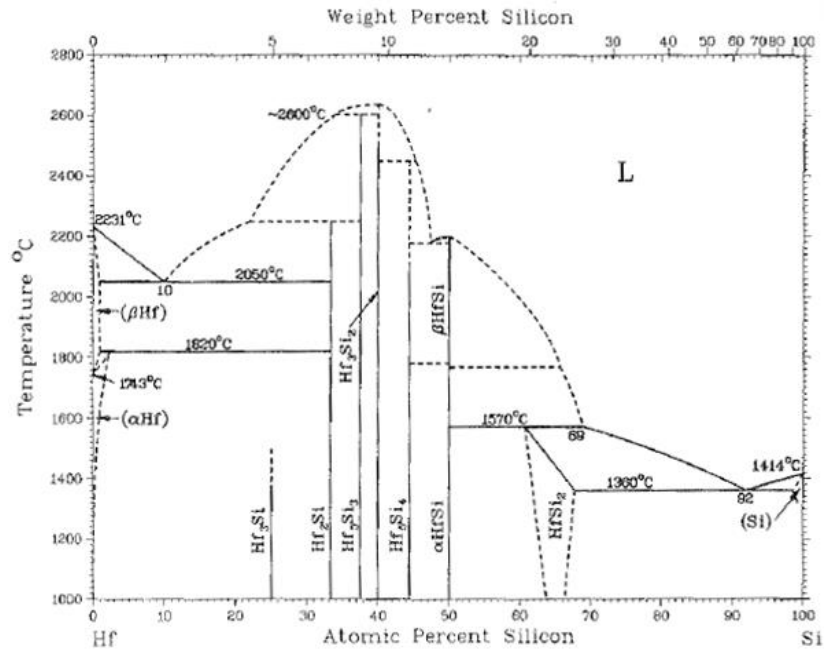
Clarke <sup>[161]</sup> used an interfacial dislocation model to describe the epitaxial  $\gamma \rightarrow \alpha\text{-Al}_2\text{O}_3$  transformation and the effect of dopants on the transformation. Since the  $\gamma \rightarrow \alpha\text{-Al}_2\text{O}_3$  transformation is associated with a rearrangement of the oxygen sublattice from ABCABC stacking in  $\gamma\text{-Al}_2\text{O}_3$  to ABAB stacking in  $\alpha\text{-Al}_2\text{O}_3$ , it was postulated that dislocations and stacking faults are introduced to accommodate the alteration of stacking sequence. Moreover, the growth of  $\alpha\text{-Al}_2\text{O}_3$  is under tension because the space of oxygen planes in the close-packed direction in  $\alpha\text{-Al}_2\text{O}_3$  (0.21655 nm) is smaller than that in  $\gamma\text{-Al}_2\text{O}_3$  (0.2285 nm). Dopant ions with relative larger ionic radius, such as  $\text{Fe}^{3+}$ , are favorable to segregate around dislocations and lower the overall elastic energy of the new grown  $\alpha\text{-Al}_2\text{O}_3$  islands, thereby accelerating the transformation. In the case of  $\theta \rightarrow \alpha\text{-Al}_2\text{O}_3$  transformation, around 10% volume shrinkage is accompanied with the occurrence of transformation, so it is rational to use this model to explain the present results of the silicon effect. If dopants with relatively larger ionic radius tend to accelerate the transformation, Si, whose ionic radius is smaller than  $\text{Al}^{3+}$ , would be expected to inhibit the transformation.

In above discussion, the role of silicon in affecting the metastable  $\rightarrow \alpha\text{-Al}_2\text{O}_3$  transformation is only considered from the standpoint of the incorporation of silicon, into the crystal lattice of the aluminas. However, it should be noted that the model alloys (Ni-20Al-5Cr-0.05Hf-0.05Y and Ni-20Al-5Cr-0.05Hf-0.0Y-1Si) used in this study were also co-doped. Since reactive elements can also play a significant role in affecting the metastable  $\rightarrow \alpha\text{-Al}_2\text{O}_3$  transformation kinetics <sup>[4, 9, 10, 12]</sup>, their effects must be taken into account when discussing the effect of silicon. It is speculated here that there is a synergistic effect between silicon and reactive elements (Hf and Y).

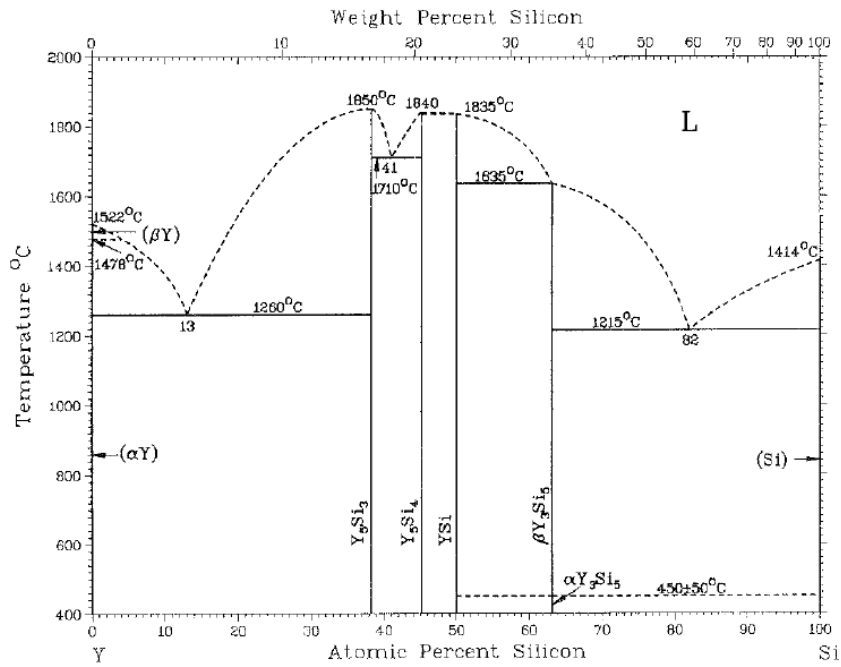
It was reported that the effectiveness of reactive elements is highly related to their chemical activities [59, 78]. In the present study, it is postulated that the addition of silicon affects the activities of Hf and Y in the alloy substrates. Figure 5.13 (a) and (b) [185] are the phase diagrams of Hf-Si and Y-Si. High melting point compounds of Hf-Si ( $\text{Hf}_2\text{Si}$ ,  $\text{Hf}_5\text{Si}_3$ ,  $\text{Hf}_5\text{Si}_4$  and  $\text{HfSi}$ ) can be found on the phase diagram of Hf-Si, showing that Hf and Si form a very strong bond which, in turn, suggests that Si decreases the chemical activity of Hf. Silicon should also be able to decrease the activity of Y, but may not as effective as with Hf, because the melting points of Y-Si compounds ( $\text{Y}_5\text{Si}_3$ ,  $\text{Y}_5\text{Si}_4$  and  $\text{YSi}$ ) are much lower ( $\sim 800^\circ\text{C}$  lower) than those of Hf-Si compounds. Once the chemical activities of Hf and/or Y are decreased in alloy substrates, their tendencies to be oxidized during the initial stage of oxidation can be reduced. In Chapter 4, two examples were demonstrated that the addition of silicon could decrease the chemical activity of Hf. For the model alloys Ni-20Al-5Cr-0.05Hf-0.05Y and Ni-20Al-5Cr-0.05Hf-0.05Y-1Si (Figure 4.9), the addition of 1 at. % Si decreased the density of  $\text{HfO}_2$  fine particles in the  $\text{Al}_2\text{O}_3$  scale after 100 hours of oxidation at  $1150^\circ\text{C}$ . Similarly, for the model alloys Ni-7.5Cr-13Al-1Ta-1Re-0.12C-0.05Hf-0.05Y-0.5Si and Ni-7.5Cr-13Al-1Ta-1Re-0.12C-0.05Hf-0.05Y-1Si (Figure 4.14), increasing in silicon content from 0.5 at. % to 1 at. % significantly decreased size and density of  $\text{HfO}_2$  particles inside the  $\text{Al}_2\text{O}_3$  scale after 100 hours of oxidation at  $1150^\circ\text{C}$ .

If the postulation that silicon addition reduces the chemical activities of Hf and/or Y in alloy substrates is the case, a synergistic effect between Si and reactive elements (Hf and/or Y) on the  $\theta \rightarrow \alpha\text{-Al}_2\text{O}_3$  transformation kinetics during  $\text{Al}_2\text{O}_3$  growth at high temperatures can be elucidated. So far it is generally agreed that the way by which reactive elements affect the  $\theta \rightarrow \alpha\text{-Al}_2\text{O}_3$  transformation is by affecting the nucleation and growth processes of  $\alpha\text{-Al}_2\text{O}_3$  [4, 9, 10, 12]. Moreover, oxides of reactive elements are usually believed to be heterogeneous nucleation sites

that facilitate the  $\theta \rightarrow \alpha\text{-Al}_2\text{O}_3$  transformation <sup>[4, 9, 10, 12]</sup>. Therefore, in the present study, if silicon addition did decrease the chemical activities of Hf (and/or Y) in the alloy substrate and reduced the densities of the initially-formed  $\text{HfO}_2$  (and/or  $\text{Y}_2\text{O}_3$ ) nuclei in  $\text{Al}_2\text{O}_3$  scale, the  $\theta \rightarrow \alpha\text{-Al}_2\text{O}_3$  transformation on the Si-containing alloy would in turn be delayed compared with its Si-free counterpart because of the decreasing in heterogeneous nucleation sites.



(a)



(b)

Figure 5.13 (a) Hf-Si phase diagram; (b) Y-Si phase diagram <sup>[185]</sup>

## 5.5 SUMMARY AND CONCLUSIONS

The early-stage oxidation behavior of  $\gamma+\gamma'$   $\text{Al}_2\text{O}_3$ -scale forming model alloys Ni-20Al-5Cr-0.05Hf-0.05Y and Ni-20Al-5Cr-0.05Hf-0.05Y-1Si was qualitatively and semi-quantitatively studied by confocal photo-stimulated microscopy (CPSM) and glancing-angle X-ray diffraction (GAXRD). Inferences are as follows:

1. Qualitative results obtained by CPSM and semi-quantitative results obtained by GAXRD clearly show that the addition of Si delayed the  $\theta \rightarrow \alpha\text{-Al}_2\text{O}_3$  transformation at 1100°C.
2. T-T-T type diagrams for both of the Si-containing and Si-free alloys were constructed over the temperature range 800-1100°C and 0-100 hours exposure time. The  $(\theta + \alpha)\text{-Al}_2\text{O}_3$  transformation zone was characterized for both alloys. It was found that the  $(\theta + \alpha)\text{-Al}_2\text{O}_3$  transformation zone was broadened to longer exposure times for the Si-containing alloy, confirming that the addition of Si delayed the  $\theta \rightarrow \alpha\text{-Al}_2\text{O}_3$  transformation at temperature above 900°C
3. The mechanism by which silicon addition delayed the  $\theta \rightarrow \alpha\text{-Al}_2\text{O}_3$  transformation was speculated to be due to that silicon addition decreased the chemical activities of Hf (and/or Y) in the alloy substrates. Decreasing the chemical activities of Hf (and/or Y) reduced the density of the initially formed  $\text{HfO}_2$  (and/or  $\text{Y}_2\text{O}_3$ ) nuclei that act as heterogeneous nucleation sites for  $\theta \rightarrow \alpha\text{-Al}_2\text{O}_3$  transformation and in turn delayed the  $\theta \rightarrow \alpha\text{-Al}_2\text{O}_3$  transformation.
4. An alternative mathematical method was developed to determine the extent of  $\theta \rightarrow \alpha\text{-Al}_2\text{O}_3$  transformation based on analyzing the time dependence of instantaneous n-value,  $n_i$ . The time when instantaneous n-value reaches a minimum indicates the full establishment of a  $\alpha$ -

$\text{Al}_2\text{O}_3$  layer, and the left/right shift of the  $n^i$  vs.  $t$  curve suggests the acceleration/delay of  $\theta \rightarrow \alpha\text{-Al}_2\text{O}_3$  transformation. This method successfully described the effect Si addition on delaying the  $\theta \rightarrow \alpha\text{-Al}_2\text{O}_3$  transformation for the Ni-20Al-5Cr-0.05Hf-0.05Y-(1Si) model alloy.

## **6.0 TEM CHARACTERIZATION OF THE SCALE/METAL INTERFACE EVOLUTION DURING THE INITIAL OXIDATION STAGE OF $\gamma$ -Ni+ $\gamma'$ -Ni<sub>3</sub>Al ALUMINA SCALE FORMING MODEL ALLOYS WITH AND WITHOUT SILICON ADDITION**

### **6.1 INTRODUCTION**

The mechanism of the effect of reactive elements on the oxidation behavior of Al<sub>2</sub>O<sub>3</sub>-scale forming alloys has been the subject of research for many decades <sup>[9-11]</sup>. Since it has been well known that the growth of an undoped alumina scale is dominated by simultaneous inward diffusion of O and outward diffusion of Al through scale grain boundaries <sup>[2, 4, 42, 49, 78, 171]</sup>, a large number of investigations have concentrated on the influence of reactive elements on the scale microstructure, particularly the segregation behavior to Al<sub>2</sub>O<sub>3</sub> scale grain boundaries <sup>[9, 11-13, 63, 64, 76, 78, 169, 170]</sup>.

Transmission electron microscopy (TEM), which has a significantly higher resolution than the more commonly used scanning electron microscopy (SEM), is an important and powerful technique for characterizing the microstructure of scale as well as scale/metal interface in an extremely small dimension. Reported TEM studies of the reactive element effect have focused on Zr and Y in  $\beta$ -NiAl <sup>[67]</sup>, Hf in  $\gamma'$ -Ni<sub>3</sub>Al <sup>[17, 149]</sup>, and Zr in PtAl <sup>[172]</sup>, etc. In addition, a derivative technique of TEM, the scanning electron microscopy (STEM) coupled with energy

dispersive spectroscopy (EDS), extends the capability of TEM in elemental characterization to high precision by providing nano-scale elemental contrast (Z-contrast). This makes the application of TEM more suitable for characterizing the scale microstructure and scale/metal interface structure, especially for the segregation behavior of reactive elements such as Hf and Y, which have higher atomic weight than Al.

Many of these previous studies on the effects of reactive elements simply compared the influence of one reactive element (RE) addition on the change of scale microstructure to the undoped counterpart. Fairly recently, it has been demonstrated that addition of two or more minor elements, such as “co-doping” or “tri-doping”, has a highly beneficial effect and further improves the performance of alumina scale <sup>[16, 137]</sup>. Pint <sup>[16]</sup> illustrated a strategy for optimizing the effects of reactive elements in FeCrAl alloys. It was shown that co-doping low levels of Hf (i. e., 0.018 at. %) and Y (i. e., 0.002 at. %) was very effective in decreasing the scale growth rate due to a reduction of RE-rich oxides in the scale. Moreover, Gupta and Duval <sup>[179]</sup> demonstrated that co-doping Hf (0.25 wt.%) + Si (0.4 wt. %) to a plasma sprayed NiCoCrAlY coating markedly improved alumina scale adherence and also improved its capability to reform alumina once spallation occurred during cyclic oxidation.

In Chapters 4 and 5, it was shown that the addition of 1 at. % Si not only decreased the overall weight gain of Hf+Y co-doped  $\gamma+\gamma'$  Ni-20Al-5Cr-0.05Hf-0.05Y model alloy under both isothermal and cyclic oxidation conditions at 1150°C, but it also delayed the  $\theta \rightarrow \alpha\text{-Al}_2\text{O}_3$  transformation at temperatures above 900°C. It was speculated that there is a synergistic effect between Si and Hf (and/or Y). The mechanism by which silicon addition delayed the  $\theta \rightarrow \alpha\text{-Al}_2\text{O}_3$  transformation was postulated to be due to that silicon addition decreasing the chemical activities of Hf (and/or Y) in alloys substrates. Decreasing the chemical activities of Hf (and/or

Y) reduced the density of very initially formed  $\text{HfO}_2$  (and/or  $\text{Y}_2\text{O}_3$ ) nuclei that act as heterogeneous nucleation sites for  $\theta \rightarrow \alpha\text{-Al}_2\text{O}_3$  transformation and in turn delayed the  $\theta \rightarrow \alpha\text{-Al}_2\text{O}_3$  transformation. In this chapter, TEM/STEM in conjunction with high resolution EDS analysis will be used to obtain more detailed information on the microstructures of the  $\text{Al}_2\text{O}_3$  scales as well as scale/metal interfaces. The complementary information provided by CPSM and XRD (in Chapter 5) and TEM/STEM (in this chapter) should lead to a better understanding of the synergistic effect of Si and reactive elements (Hf and Y).

## 6.2 MATERIALS AND EXPERIMENTAL PROCEDURES

The nominal compositions of the co-doped  $\gamma+\gamma'$  Ni-20Al-5Cr-0.05Hf-0.05Y and Ni-20Al-5Cr-0.05Hf-0.05Y-1Si model alloys are exactly the same as those used in Chapter 5 (see Table 5.1). Drop-cast ingots were homogenized at 1200°C for 6 hours followed by 1150°C for 48 hours in vacuum. Coupon samples ~10 mm in diameter and ~1 mm in thickness were ground to a 1200-grit finish using SiC abrasive paper. All samples were carefully cleaned in acetone followed by isopropanol in ultrasonic cleaner before oxidation.

Isothermal oxidation experiments were conducted using a tube furnace. Ni-20Al-5Cr-0.05Hf-0.05Y and Ni-20Al-5Cr-0.05Hf-0.05Y-1Si coupon samples were oxidized for 10 minutes, 0.5 hour and 2 hours at 1150°C in dry air. Surface morphologies of samples after oxidation were observed by SEM in the secondary-electron emission mode. Cross-sectional samples for TEM/STEM observation were prepared by state-of-the-art focused ion beam (FIB) lift-out technique. The microstructure and elemental composition of scale/metal interfaces were

observed and analyzed by scanning transmission electron microscopy (STEM), namely high-angle annular dark field (HAADF) imaging in conjunction with EDS.

## 6.3 RESULTS

### 6.3.1 Surface morphologies

Representative SEM images of the Si-free and Si-containing alloys after 10 min, 0.5h and 2h oxidation at 1150°C are shown in Figure 6.1 a-f. It should be noted that each SEM image was taken from different samples, so it is not an *in situ* observation of the surface morphology evolution from 10 min to 2 h oxidation.

After 10 minutes exposure at 1150°C, the surface of the Si-containing and Si-free alloys were covered by a thin layer of Al<sub>2</sub>O<sub>3</sub> with some regions of NiO on the Al<sub>2</sub>O<sub>3</sub> scale surface (see arrows). The grain boundaries of the alloy substrates were decorated by Al<sub>2</sub>O<sub>3</sub> and/or NiO. The as-ground morphologies of the substrates were still visible. The diameter of the NiO on the surface of the Si-containing alloy ranged from 1~2 μm (Figure 6.1 b). Compared with the Si-containing alloy, it seems that the diameters of some NiO on the surface of the Si-free alloy (Figure 6.1 a) were comparatively larger (with some even larger than 5 μm). In Chapter 4, a similar result was shown that the addition of 0.5 at. % Si suppressed the surface formation of NiO and/or NiAl<sub>2</sub>O<sub>4</sub> modified-René N5 alloy (Figure 4.4) after 100 hours of oxidation at 1150°C. The role of Si in suppressing the formation of NiO and/or NiAl<sub>2</sub>O<sub>4</sub> is so far not conclusive, but it may be related to the speculation (in Chapter 5) that the addition of silicon decreased the chemical activities of reactive elements Hf (and/or Y). It is known that reactive elements have

high affinity to oxygen, so they are driven to oxidize first once the alloy is exposed to the oxidation environment. The oxides of reactive elements may subsequently act as heterogeneous nucleation sites that facilitate the formation of NiO particles. Thus, if the speculation that the addition of silicon decreased the chemical activities of Hf (and/or Y) is the case, it is reasonable to believe that less heterogeneous nucleation sites for NiO formation will be formed on the surface of the Si-containing alloy compared to its Si-free counterpart.

Figure 6.1 c and d show the surface morphologies of the Si-free and Si-containing alloy after 30 minutes of oxidation at 1150°C. Generally, ridged Al<sub>2</sub>O<sub>3</sub>-scale morphologies were found on both of the Si-containing and Si-free alloys, but the ridges seem to be slightly rougher on the Si-free alloy than on the Si-containing alloy. Nodules and whiskers, which are characteristic features of metastable aluminas, could also be observed on the surfaces of the Si-free and Si-containing alloys. However, the distribution of the nodules and whiskers appeared to be more uniform on the Si-containing alloy compared to that on the Si-free alloy. If the nodules and whiskers do represent metastable aluminas, the trend of their distribution influenced by the addition of Si is consistent with the CPSM images (Figure 5.2 and Figure 5.3) on which the distribution of  $\theta$ -Al<sub>2</sub>O<sub>3</sub> appears to become more uniform with the addition of Si.

Figure 6.1 e and f compare the surface morphologies of the Si-free and Si-containing alloys after 2 hours of oxidation at 1150°C. The ridged morphology on the Si-free alloy became more prominent and dense. A small amount of less apparent nodules, which are believed to be the remnant of untransformed metastable aluminas, were also observed on top of the ridges. By contrast, the surface of the Si-containing alloy is composed of circular regions containing radial cracks and nodule clusters. Doychak<sup>[180]</sup> described the formation of radial cracks in more detail. It is known that the processes of the nucleation and growth of  $\alpha$ -Al<sub>2</sub>O<sub>3</sub> within the transient

alumina scale is accompanied by a large volume contraction (~10%). However, since the fully transformed  $\alpha$ -Al<sub>2</sub>O<sub>3</sub> cells are not free-standing, a large biaxial stress state will build up to accommodate the fully transformed  $\alpha$ -Al<sub>2</sub>O<sub>3</sub> cells to the surrounded untransformed regions. When the magnitude of the circumferential stress component exceeds the fracture stress of the  $\alpha$ -Al<sub>2</sub>O<sub>3</sub>, radial cracks will form. The reason why more cracks were observed in the scale on the Si-containing alloy than on the Si-free alloy can be attributed to the incorporation of reactive elements Hf and Y to the Al<sub>2</sub>O<sub>3</sub> crystal lattice. The ionic radii of Hf and Y are much larger than Al and O. Thus, incorporation of Hf and Y to the crystal lattice of meta-stable alumina will slightly expand the space between lattice planes, like adding a small tensile stress to the untransformed aluminas. Thus, when the volume shrinkage occurs, this small pre-applied tensile stress will compensate the biaxial stress caused by transformation and make the total stress smaller than the fracture stress of  $\alpha$ -Al<sub>2</sub>O<sub>3</sub>, and in turn prevent the formation of radial cracks. It was postulated and discussed in Chapter 5 that the addition of silicon decreased the chemical activities of Hf (and/or Y) in alloy substrates. That means less Hf (and/or Y) will incorporate into the crystal lattice of Al<sub>2</sub>O<sub>3</sub> scale formed on the Si-containing alloy compared to its Si-free counterpart. In consequence, smaller pre-applied tensile stress will be generated to compensate the biaxial stress due to be metastable  $\rightarrow$   $\alpha$ -Al<sub>2</sub>O<sub>3</sub> transformation in the scale formed on the Si-containing alloy, and thus more cracks are expected to form. The limitation of this explanation is that it only considers the effect of Hf and Y solutes in the alumina crystal lattice. The role of the Hf and Y ions that segregate to the alumina grain boundaries are not estimated. Another possible explanation is that the cracks formed in the scale on the Si-free alloy were healed after 2 hours of oxidation at 1150°C, but the healing process in the scale on the Si-containing alloy was delayed at this stage. According to the mechanism proposed by Doychhak <sup>[180]</sup>, once the radial cracks

formed, the alloy substrate will be directly exposed to the oxidizing environment. The exposed alloy substrate will be quickly re-oxidized, and the vicinity of the healed cracks will become fast growing areas and results in the lacey morphology (see Figure 6.1 e). In Chapter 5, it was shown that the addition of Si delayed the  $\theta \rightarrow \alpha\text{-Al}_2\text{O}_3$  transformation. Once the  $\theta \rightarrow \alpha\text{-Al}_2\text{O}_3$  transformation process is delayed by the addition of Si, the subsequent forming and healing processes of the cracks will be in turn delayed. Thus, at the same observation point (after 2 hours of oxidation), healed morphology can be observed in the scale of the Si-free alloy, but a majority of cracks still exist in the scale of the Si-containing alloy due to the delayed  $\theta \rightarrow \alpha\text{-Al}_2\text{O}_3$  transformation process caused by the addition of silicon.

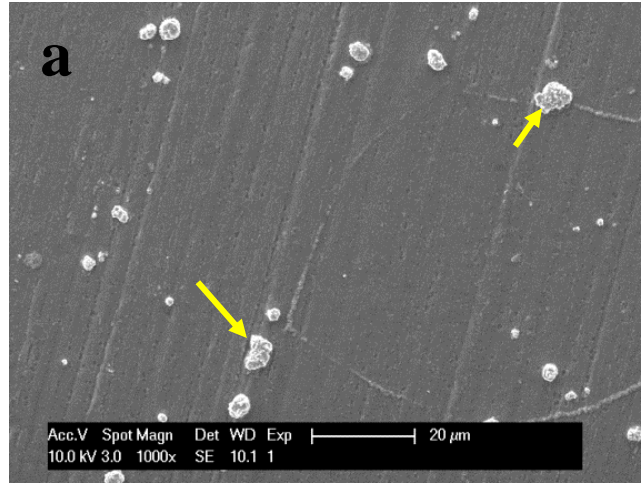


Figure 6.1 (a)

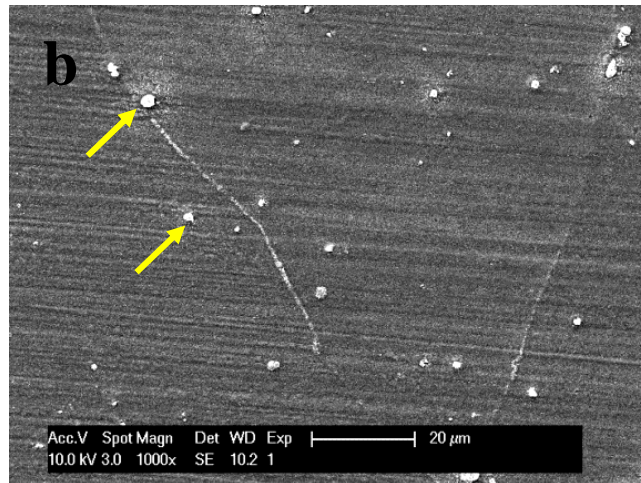


Figure 6.1 (b)

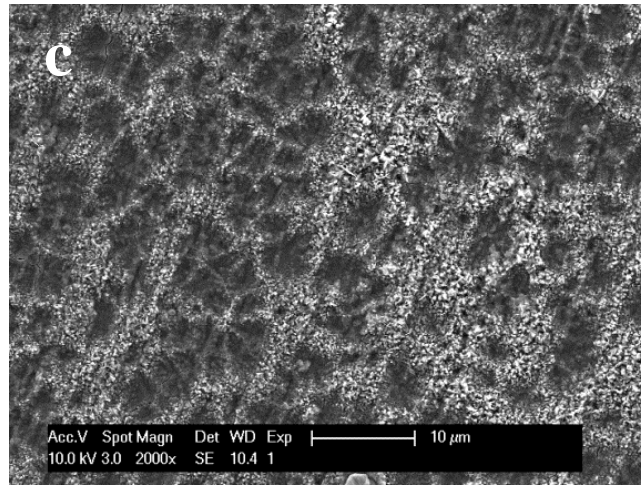


Figure 6.1 (c)

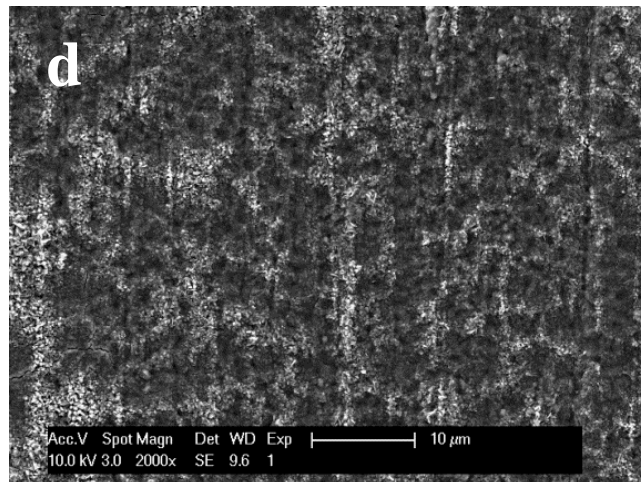


Figure 6.1 (d)

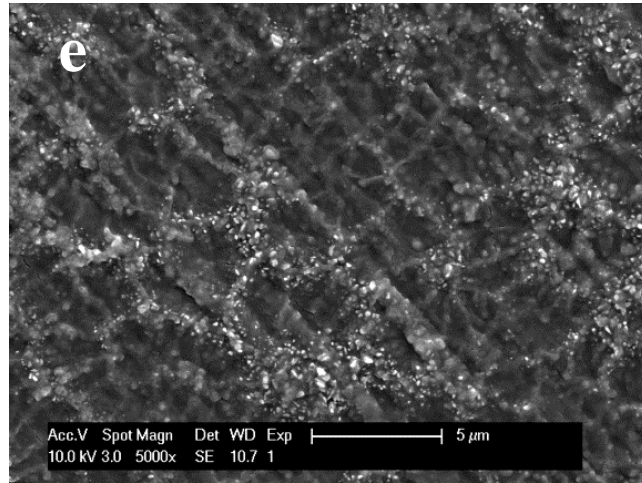


Figure 6.1 (e)

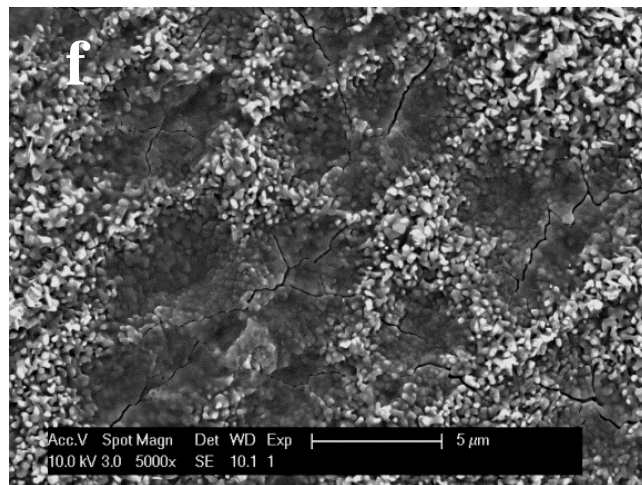


Figure 6.1 (f)

Figure 6.1 Surface morphologies of Ni-20Al-5Cr-0.05Hf-0.05Y (a, c, e) and Ni-20Al-5Cr-0.05Hf-0.05Y-1Si (b, d, f) after oxidation at 1150°C for 10 minutes (a – without Si and b – with Si), 0.5 hour (c – without Si and d – with Si) and 2 hours (e – without Si and f – with Si)

### 6.3.2 Cross-sectional STEM characterization of the scale/metal interfaces

Figure 6.2 (a) and Figure 6.3 (a) show the cross-sectional STEM images of Ni-20Al-5Cr-0.05Hf-0.05Y and Ni-20Al-5Cr-0.05Hf-0.05Y-1Si after 10 minutes of oxidation at 1150°C, respectively. According to the T-T-T type diagrams (Figure 5.5 and Figure 5.6) presented in Chapter 5, the alumina scale formed on the Si-free and Si-containing alloys after 10 minutes of oxidation at 1150°C should be a mixture of  $\gamma$ -Al<sub>2</sub>O<sub>3</sub>,  $\theta$ -Al<sub>2</sub>O<sub>3</sub> and  $\alpha$ -Al<sub>2</sub>O<sub>3</sub>.

The oxide scales, particularly the regions close to the scale/metal interface, have significantly different structures. For the Si-free alloy, as shown in Figure 6.2 (a), stringers perpendicular to the scale/metal interface and particles (2~10 nm in diameter) with a relatively brighter contrast are the main characteristics of the near-interface region. These stringers are believed to be the grain boundaries of the columnar Al<sub>2</sub>O<sub>3</sub> grains. The brighter contrast of the stringers might originate from the segregation of heavier elements (Hf and/or Y) to Al<sub>2</sub>O<sub>3</sub> grain boundaries; however, the detection limit of EDS used in this study made it not impossible to reveal the concentration profile of Hf and Y across the grain boundaries in such a small scale. Schumann *et al.* <sup>[67]</sup> examined the extent of Y segregation to the grain boundaries of alumina scale that formed on NiAl+1 wt. % Y after 24 hours of oxidation at 1200°C. The amount of segregated Y was quantified to be ~ 0.2 mono-layer. Figure 6.2 (b) shows the qualitative EDS point analysis spectra of the brighter particle (point 1) and the surrounding matrix (point 2). These spectra reveal that the bright particle is enriched with Ni.

For the Si-containing alloy (Figure 6.3 a), a clean layer (around 20 ~ 40 nm thick) of alumina without stringers and particles was observed in the near interface region. Ni-rich particles (2~10 nm in diameter) could also be observed but at places relatively further from the scale/metal interface. Qualitative EDS point analysis spectra, which compare the chemical

composition of the particle and its surrounding matrix, are shown in Figure 6.3 (b). The crystal structure of these Ni-rich particles was almost impossible to identify by selected area diffraction (SAD) at this particle size level. Suspected phases are metallic Ni, NiO, NiAl<sub>2</sub>O<sub>4</sub> or Ni-rich meta-stable Al<sub>2</sub>O<sub>3</sub>. Given that Ni is much nobler than Al, it is most likely that the phase is metallic Ni. The mechanism for the formation of the Ni-rich particles will be discussed later. Neither Hf nor Y were found within the scale for the Si-free and Si-containing alloy. Silicon was not found within the scale formed on the Si-containing alloy.

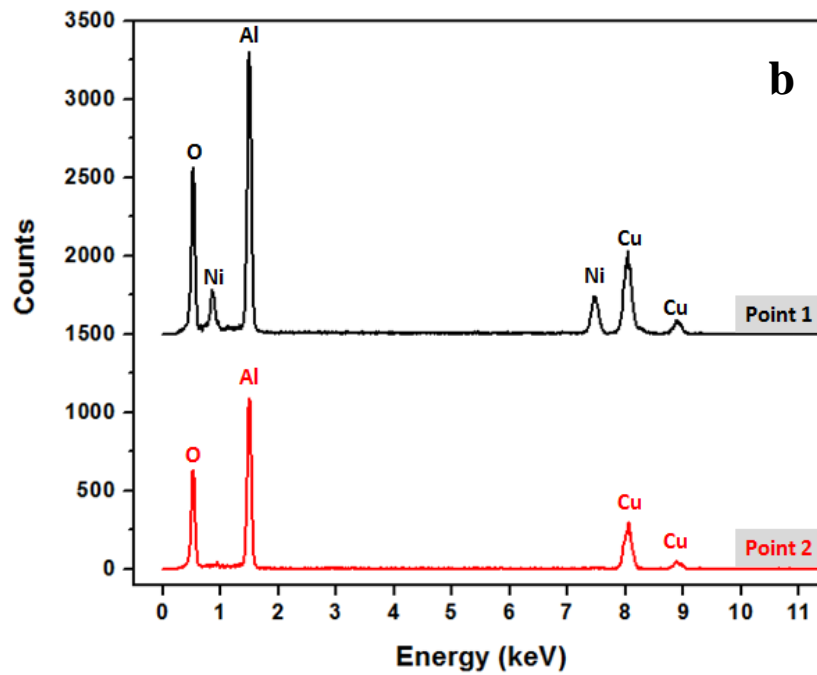
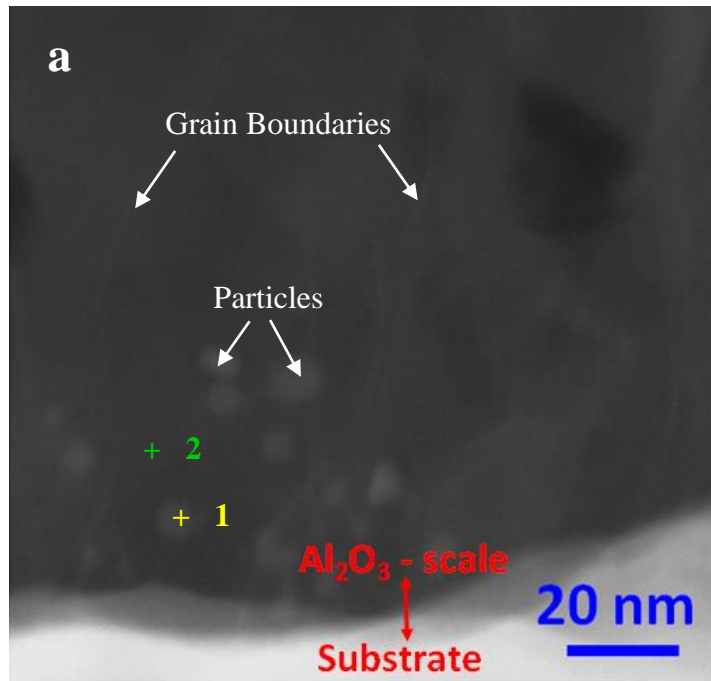


Figure 6.2 (a) Cross-sectional STEM images of Ni-20Al-5Cr-0.05Hf-0.05Y after 10 minutes of oxidation at 1150°C (b) Corresponding EDS analysis spectra of selected points

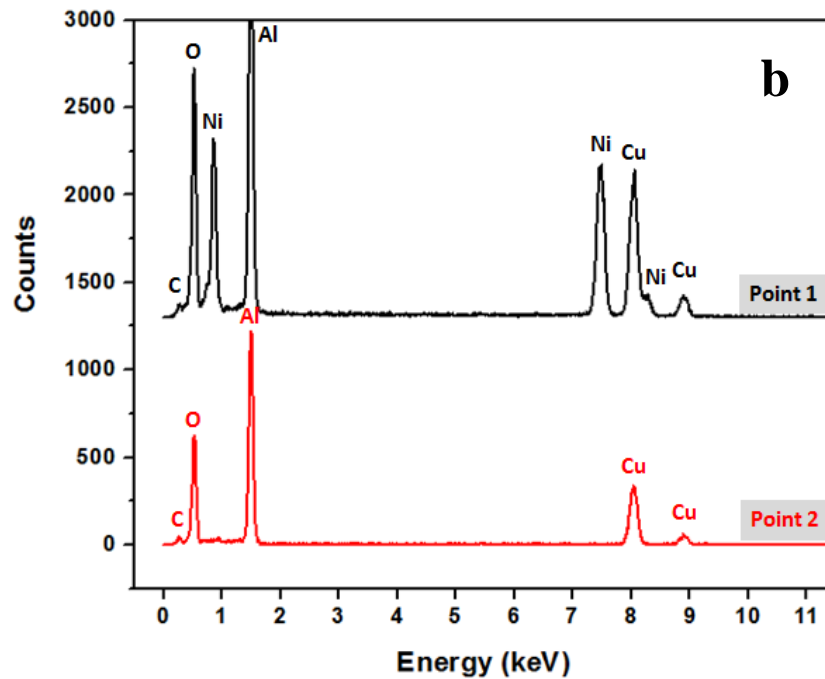
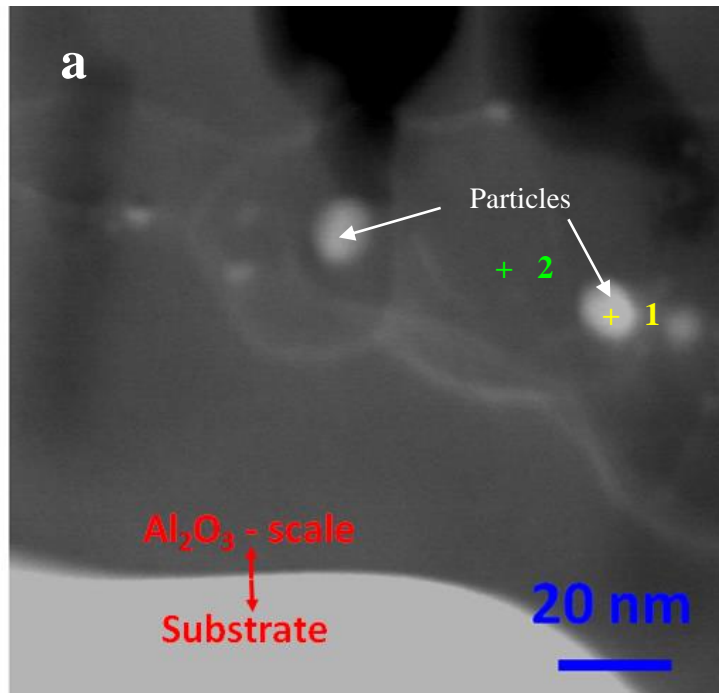


Figure 6.3 (a) Cross-sectional STEM image of Ni-20Al-5Cr-0.05Hf-0.05Y-1Si after 10 minutes of oxidation at 1150°C (b) Corresponding EDS analysis spectra of selected points

Figure 6.4 (a) and Figure 6.5 (a) show the cross-sectional STEM images of the alumina scale that formed on Ni-20Al-5Cr-0.05Hf-0.05Y and Ni-20Al-5Cr-0.05Hf-0.05Y-1Si alloys after 30 minutes of oxidation at 1150°C. According to the T-T-T type diagrams (Figure 5.5 and Figure 5.6) presented in Chapter 5, the alumina scales formed on the Si-free and Si-containing alloys after 30 minutes of oxidation at 1150°C should be composed of mainly  $\theta$ -Al<sub>2</sub>O<sub>3</sub> and  $\alpha$ -Al<sub>2</sub>O<sub>3</sub>, with only a very small amount of remnant  $\gamma$ -Al<sub>2</sub>O<sub>3</sub>.

The structure in the vicinity of the alumina scale/metal interface region of the Si-free alloy appears unchanged compared to the 10 minutes exposed sample. Alumina grain boundaries perpendicular to the scale/metal interface and Ni-rich particles (2~20 nm in diameter) with a relatively brighter contrast were still observable. In addition, the closer the Ni-rich particles are to the scale/metal interface, the smaller is the diameter of those particles. The average distance between the stringers is ~5 nm in the region close to the scale/metal interface and it increases to ~20 nm at distance 50~60 nm away from the scale/metal interface. Figure 6.4 (b) and (c) are the qualitative EDS spectra of three representative areas: Al<sub>2</sub>O<sub>3</sub> grain boundary (Area 1), Ni-rich particle (Area 2) and a matrix region away from grain boundaries and particles (Area 3). As shown in Figure 6.4 (b), both Hf and Y peaks were detected in the grain boundaries and Ni-rich particles, but neither Hf nor Y could be found in the matrix region away from grain boundaries and particles. Figure 6.4 (c) shows the enlarged portion of the EDS spectra that contains Hf and Y peaks. The appearance of Hf and Y in the grain boundary is a clear indication of grain-boundary segregation. Quantitative analysis of the Hf and Y contents was not made, because their intensities were too low. Quantification by the built-in software of the EDS cannot give a meaningful and reliable number for the purpose of quantitative analysis. These spectra can only answer if there is Hf/Y or not.

For the Si-containing alloy (Figure 6.5 a), the microstructure of the  $\text{Al}_2\text{O}_3$ -scale in the region of the scale/metal interface is quite different from that of the Si-free alloy (Figure 6.4 a). A clean and uniform layer (50~70 nm thick) of alumina was observed just above the scale/metal interface, but the alumina grain size in this layer is much larger. The space between the grain boundaries perpendicular to the scale/metal interface is greater than or equal to ~80 nm. Qualitative EDS spectra of two representative areas are shown in Figure 6.5 (b) and (c), where Area 1 was selected at an alumina grain boundary inside the clean alumina layer above the scale/metal interface; Area 2 was selected at a place relatively far away from the  $\text{Al}_2\text{O}_3$  scale/metal interface. An obvious Y peak was observed in the selected area across the grain boundary (Area 1), but no obvious Hf peak and Si peak were found in this area. The Ni and Cr peaks are believed to be from the alloy substrate, since Area 1 was selected close to the substrate. Compared with Area 1, Area 2 seems to be pure  $\text{Al}_2\text{O}_3$ .

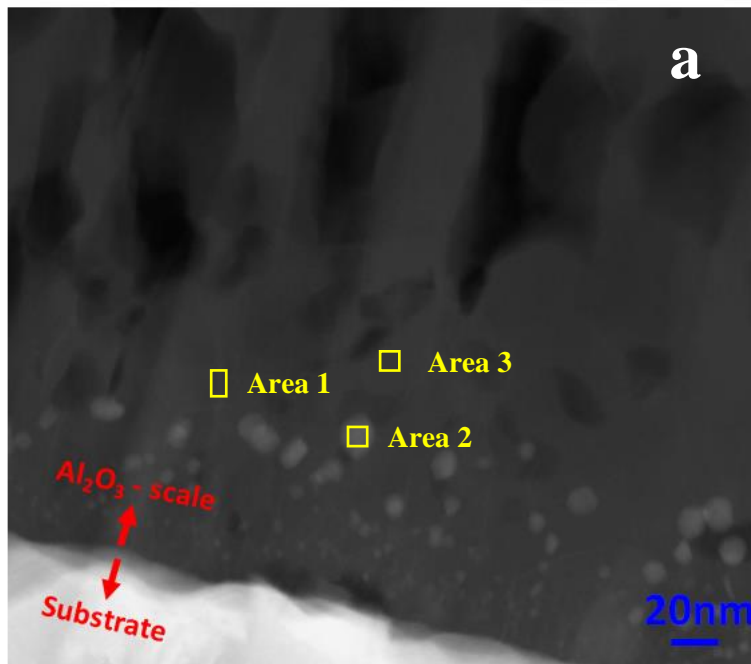


Figure 6.4 (a)

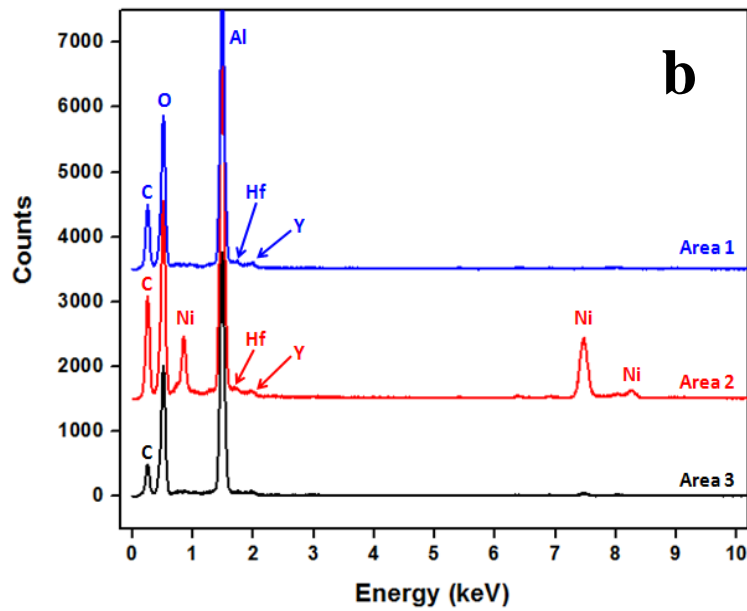


Figure 6.4 (b)

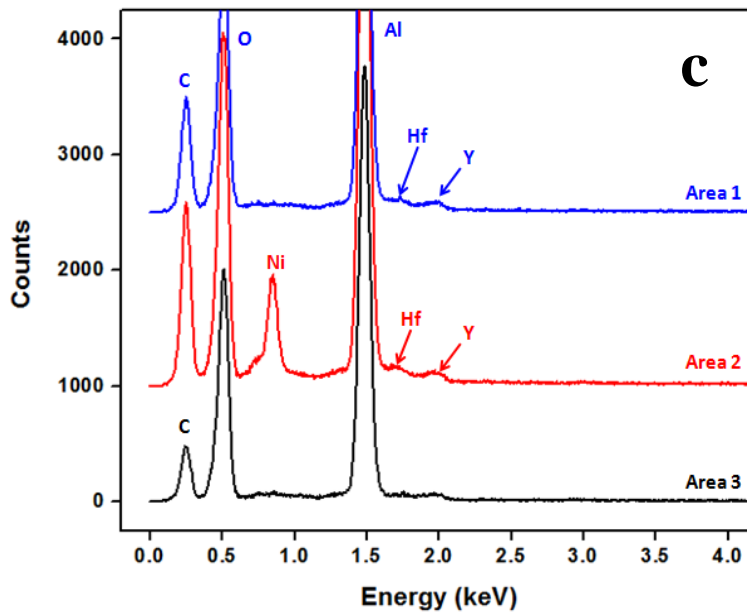


Figure 6.4 (c)

Figure 6.4 (a) Cross-sectional STEM image of Ni-20Al-5Cr-0.05Hf-0.05Y after 30 minutes of oxidation at 1150°C; (b) and (c) Corresponding EDS analysis spectra of three selected representative areas

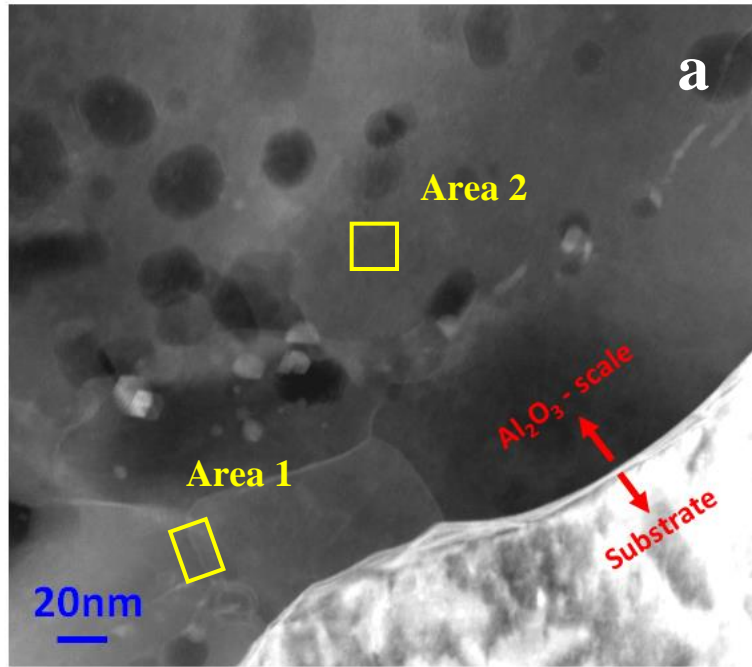


Figure 6.5 (a)

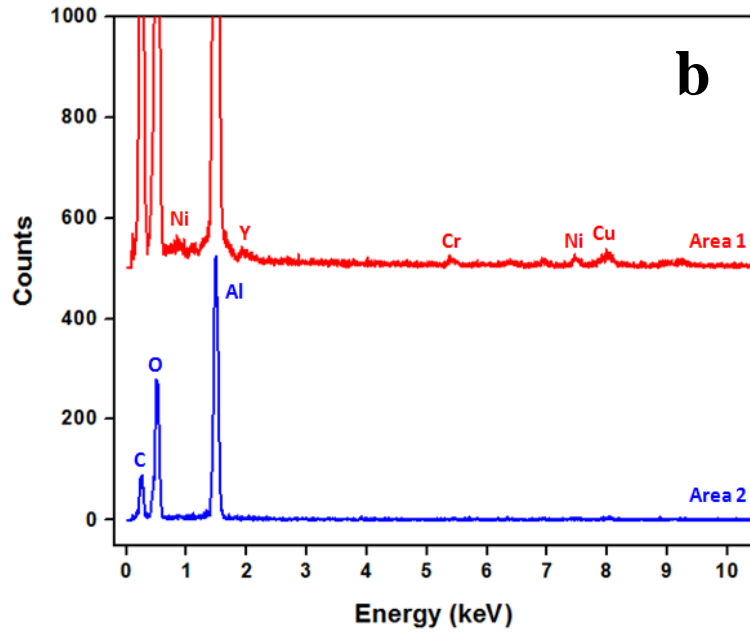


Figure 6.5 (b)

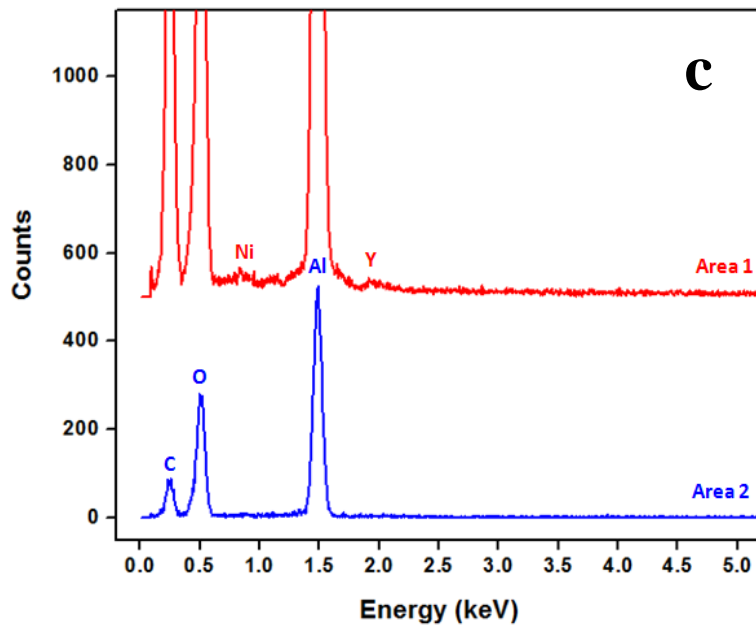


Figure 6.5 (c)

Figure 6.5 (a) Cross-sectional STEM images of Ni-20Al-5Cr-0.05Hf-0.05Y-1Si after 30 minutes of oxidation at 1150°C; (b) and (c) Corresponding EDS analysis spectra of two selected representative areas

Cross-sectional STEM images of the alumina scales formed on Ni-20Al-5Cr-0.05Hf-0.05Y and Ni-20Al-5Cr-0.05Hf-0.05Y-1Si alloys after 2 hours of oxidation at 1150°C are shown in Figure 6.6 (a) and (b), respectively. The Al<sub>2</sub>O<sub>3</sub> scales formed on the Si-free and Si-containing alloy could be characterized as two distinct layers: a dense inner layer and a porous outer layer. According to the T-T-T type diagrams (Figure 5.5 and Figure 5.6) presented in Chapter 5, the alumina scales formed on the Si-free and Si-containing alloys after 2 hours of oxidation at 1150°C should be a mixture of  $\theta$ -Al<sub>2</sub>O<sub>3</sub> and  $\alpha$ -Al<sub>2</sub>O<sub>3</sub>.

For the Si-free alloy, distinct excessive grain-boundary segregation, which is revealed by Z-contrast (see arrows in Figure 6.6 a), is observed in the dense inner layer. EDS line scan shown in Figure 6.7 further confirmed that both Hf and Y segregated to the alumina grain boundaries. By contrast, for the Si-containing alloy, the dense inner layer of the Al<sub>2</sub>O<sub>3</sub> scale is very uniform without obvious Z-contrast inside the alumina grains or on grain boundaries, suggesting that grain-boundary segregation is much less apparent. Selected area diffraction (SAD) of the dense inner layer showed that the crystal structure of Al<sub>2</sub>O<sub>3</sub> is  $\alpha$ -Al<sub>2</sub>O<sub>3</sub>, see Figure 6.8. In Figure 6.7 (b), it is seen that the counts of Hf is higher than that of Y. This is consistent with a study reported by Tatlock *et al.* <sup>[181]</sup>. In that study, the Hf (1.5 wt. %) level in the grain-boundary regions was five times higher than that of Y (0.3 wt. %). However, one should be very careful when interpreting these results. Since the FIB prepared TEM/STEM sample was mounted to a copper grid, it is inevitable that the EDS spectra contain some yield from copper. There is a significant overlap of the Cu K $\alpha$  (K $\alpha$ <sub>1</sub> – 8047.78, K $\alpha$ <sub>2</sub> – 8027.83) peaks and Hf L $\alpha$  (L $\alpha$ <sub>1</sub> – 7899.0, L $\alpha$ <sub>2</sub> – 7844.6) peaks. Thus, the amount of the counts in Figure 6.7 (b) may not reflect the actual concentration of each element.

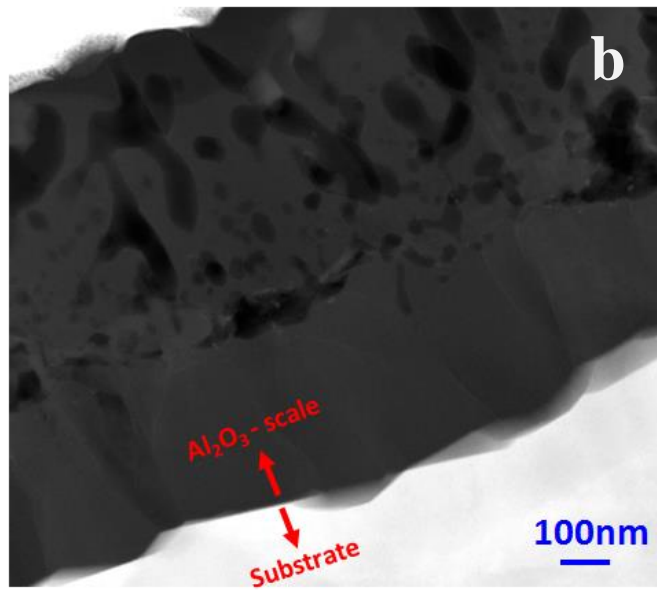
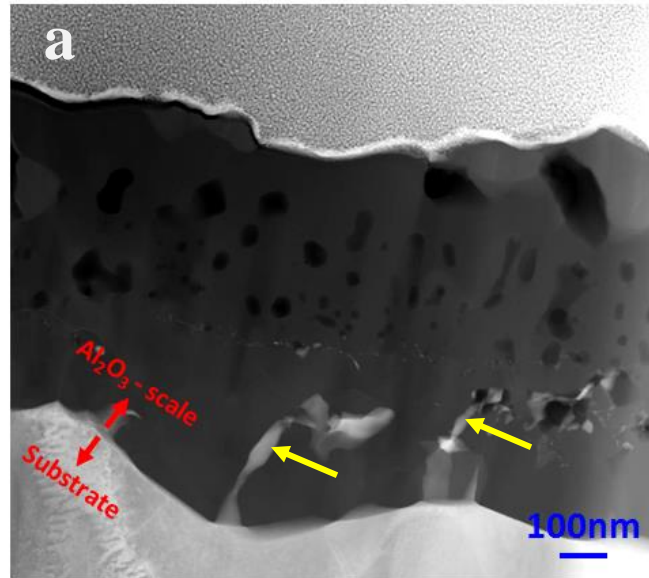


Figure 6.6 Cross-sectional images (a) Ni-20Al-5Cr-0.05Hf-0.05Y and (b) Ni-20Al-5Cr-0.05Hf-0.05Y-1Si after 2 hours of oxidation at 1150°C

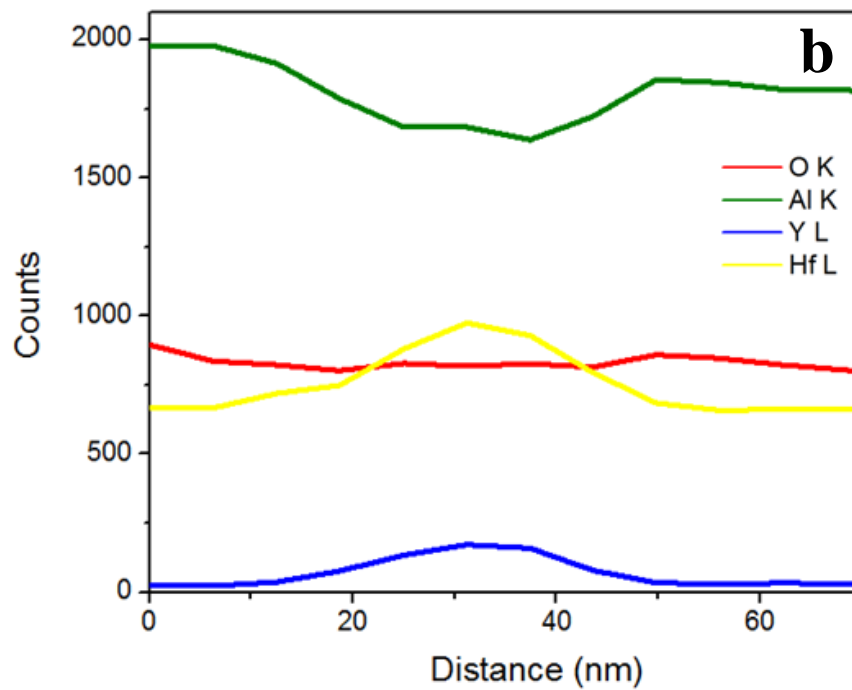
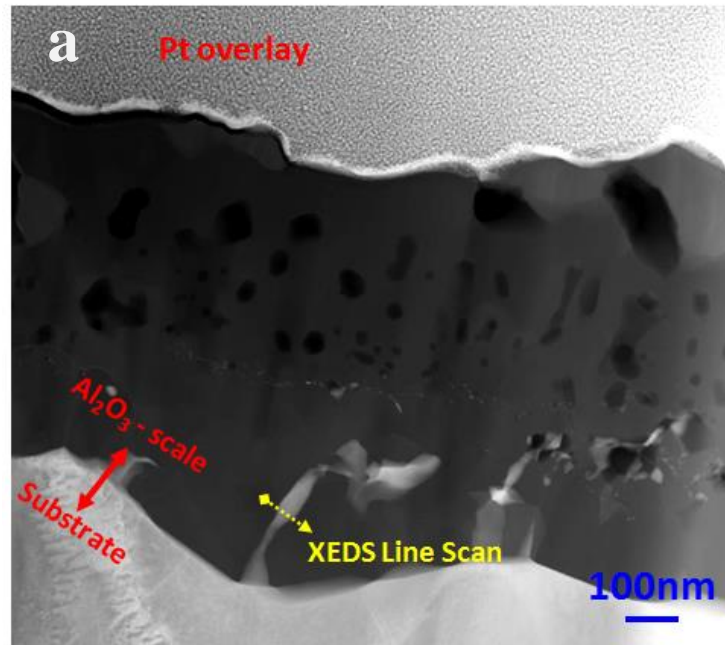


Figure 6.7 EDS line scan analysis of Hf and Y segregation to the grain boundary of  $\text{Al}_2\text{O}_3$  scale formed on Ni-20Al-5Cr-0.05Hf-0.05Y alloy after 2 hours of oxidation at 1150°C

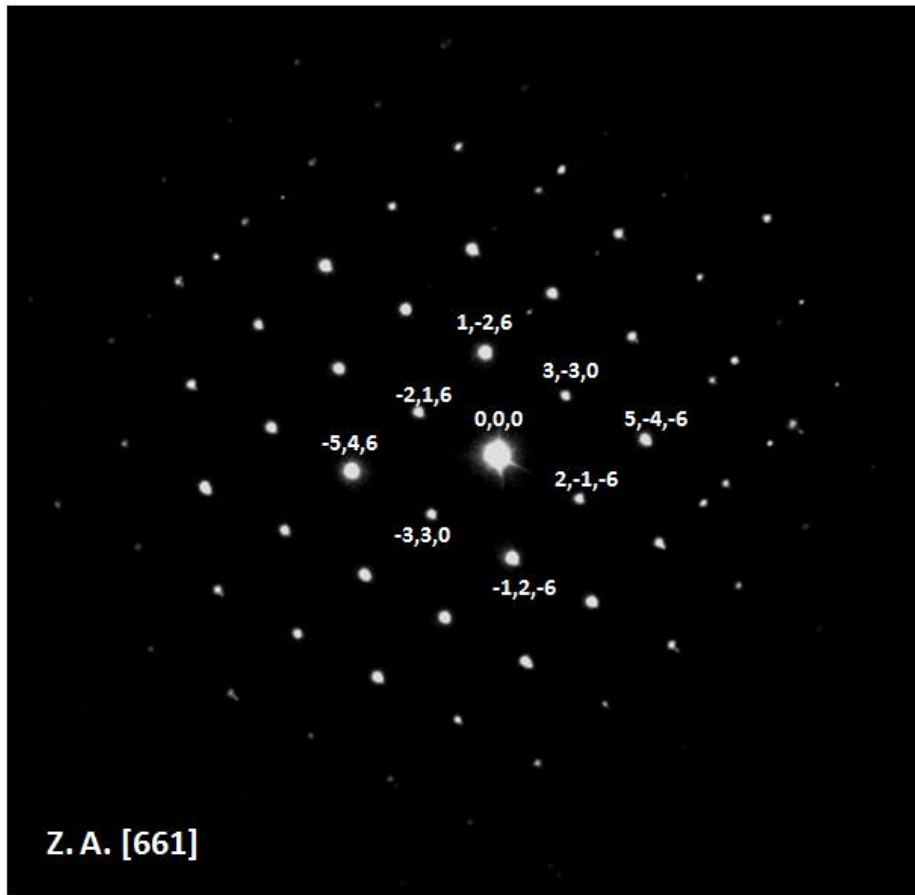


Figure 6.8 TEM selected area diffraction (SAE) pattern of  $\alpha$ - $\text{Al}_2\text{O}_3$  [661] taken from the inner layer of the  $\text{Al}_2\text{O}_3$  scale formed on Ni-20Al-5Cr-0.05Hf-0.05Y-1Si after 2 hours of oxidation at 1150°C

The outer layer of the  $\text{Al}_2\text{O}_3$  scale formed on the Si-containing alloy seems to be more porous compared to that formed on the Si-free alloy. This might be related to the delayed  $\theta \rightarrow \alpha$ - $\text{Al}_2\text{O}_3$  transformation, as discussed in Chapter 5. It is known that the meta-stable aluminas are usually shaped as needles or blades <sup>[26, 180]</sup>. Due to these characteristic morphologies, the alumina scale composed of a majority of metastable aluminas is usually loose packed and contains porosities. As the meta-stable  $\theta \rightarrow \alpha$ - $\text{Al}_2\text{O}_3$  transformation took place, the close-packed  $\alpha$ - $\text{Al}_2\text{O}_3$  consumed the loose-packed meta-stable aluminas and made the scale become denser. It was concluded in Chapter 5 that the addition of silicon delayed the  $\theta \rightarrow \alpha$ - $\text{Al}_2\text{O}_3$  transformation. That means the  $\text{Al}_2\text{O}_3$  scale formed on the Si-containing alloy should contain less  $\alpha$ - $\text{Al}_2\text{O}_3$  and more metastable  $\text{Al}_2\text{O}_3$  than the  $\text{Al}_2\text{O}_3$  scale formed on the Si-free alloy after oxidized for the same time period (2 hours). In addition, the selected area diffraction also confirmed that the inner dense layer is  $\alpha$ - $\text{Al}_2\text{O}_3$ . Thus, a more porous outer layer developed in the  $\text{Al}_2\text{O}_3$  scale formed on the Si-containing alloy.

For the Si-containing alloy, a semi-quantitative EDS analysis of the Si content was carried out across the alumina scale formed after 2 hours of oxidation at  $1150^\circ\text{C}$ , see Figure 6.9. Totally, eight points at approximately a 100 nm interval were selected from the gas/scale interface to the scale/metal interface and further to the alloy substrate. Points 1-5 were inside the  $\text{Al}_2\text{O}_3$  scale, point 6 was at the scale/metal interface and points 7-8 were selected inside the alloy substrate. Figure 6.9 (b) shows the resulting Si concentration (at. %) profile plotted with respect to relative position. It is seen that the Si concentration inside the  $\text{Al}_2\text{O}_3$  (point 1-5) is extremely low, even lower than 0.1 at. %, while the Si concentration inside the alloy substrate is close to its nominal concentration. It should be noted that even though this is a semi-quantitative analysis, the quantified concentration of Si is more reliable and meaningful than that of Hf and Y because:

1) the nominal concentration of Si is 20 times higher than that of Hf and Y; and 2) the detection limitation of the EDS used in this study makes it impossible to estimate the error for trace element like Hf and Y whose nominal concentration is lower than 0.1 at. %. Therefore, no measured concentrations of Hf and Y are presented in this study.

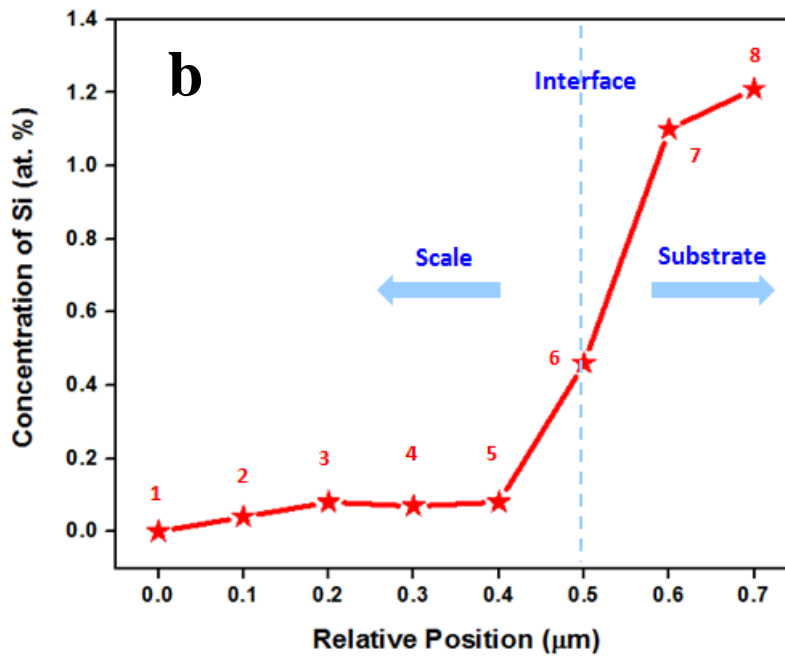
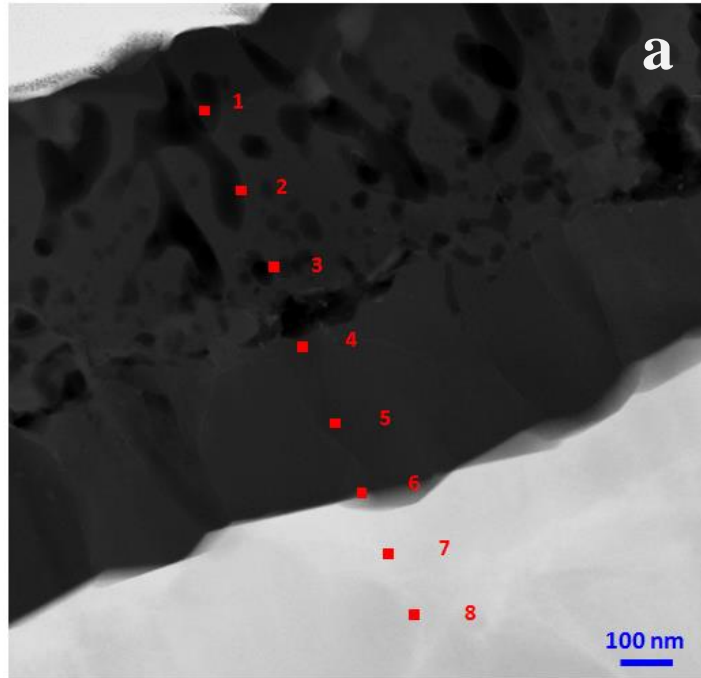


Figure 6.9 Semi-quantitative EDS analysis of the Si concentration across from the  $\text{Al}_2\text{O}_3$  scale to the alloy substrate for Ni-20Al-5Cr-0.05Hf-0.05Y-1Si after 2 hours of oxidation at 1150°C

Qualitative point EDS analysis of the alumina scale formed on the Si-containing alloy after 10 minutes (Figure 6.3 b) and after 30 minutes (Figure 6.5 b) of oxidation also did not reveal significant Si content inside the alumina scale. It was discussed in Chapter 5 that Chen *et al.* <sup>[147]</sup> ascribed the effect of Si in delaying the  $\theta \rightarrow \alpha\text{-Al}_2\text{O}_3$  transformation to the formation of  $3\text{Al}_2\text{O}_3 \cdot 2\text{SiO}_2$  (mullite). The current EDS results do not support that assertion.

Figure 6.10 is a summary of the cross-sectional STEM images of the  $\text{Al}_2\text{O}_3$  scale formed on the Si-free and Si-containing alloys after 10 minutes, 0.5 hour and 2 hours of oxidation at  $1150^\circ\text{C}$ , giving a full impression of the scale evolution.

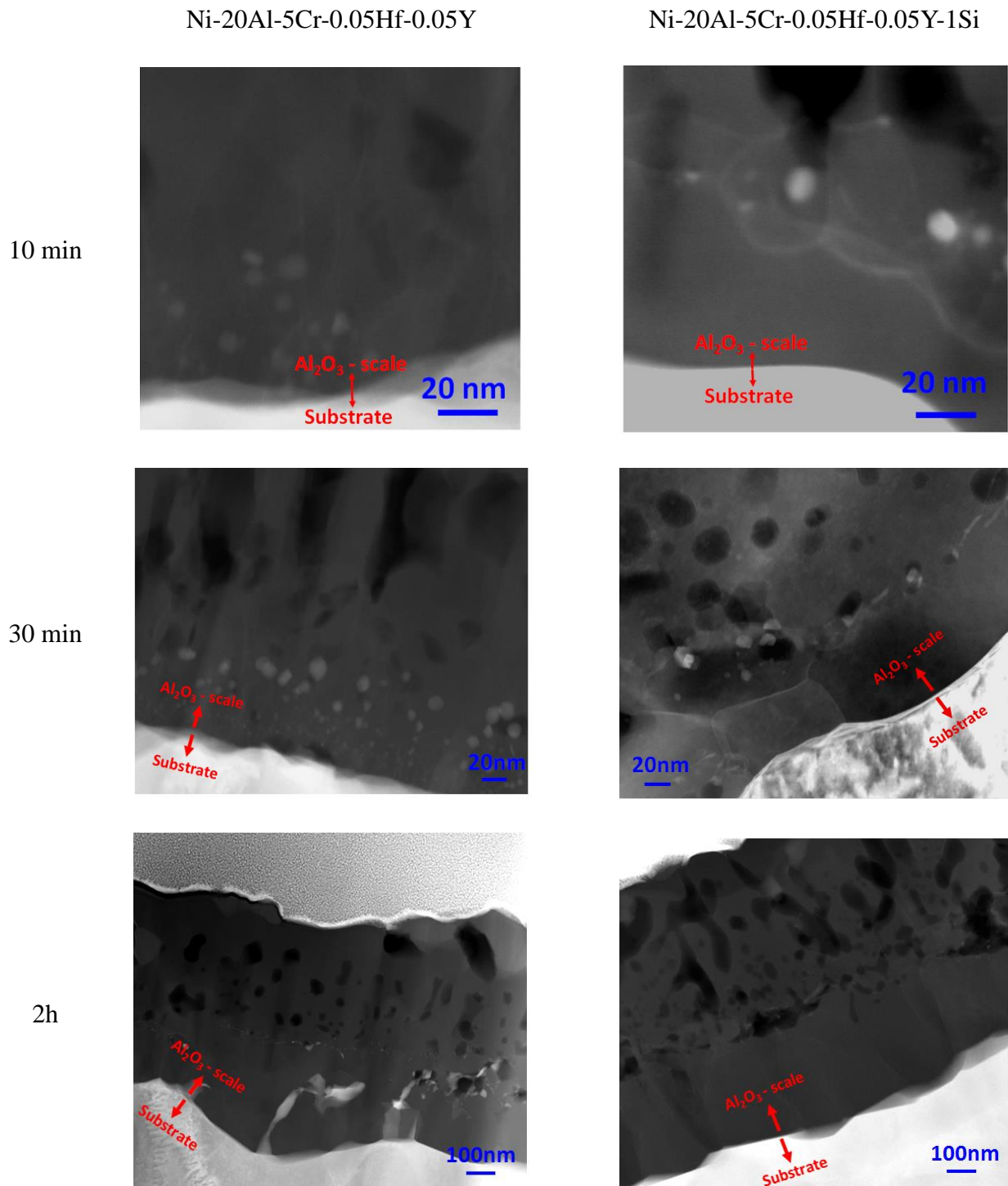


Figure 6.10 Summary of the cross-sectional STEM images of the  $\text{Al}_2\text{O}_3$  scale formed on Ni-20Al-5Cr-0.05Hf-0.05Y and Ni-20Al-5Cr-0.05Hf-0.05Y-1Si alloys after 10 minutes, 30 minutes and 2 hours of oxidation at 1150°C

## 6.4 DISCUSSION

The scale evolution during the very initial stages of oxidation at 1150°C has been presented for the  $\gamma + \gamma'$  Ni-20Al-5Cr-0.05Hf-0.05Y and Ni-20Al-5Cr-0.05Hf-0.05Y-1Si model alloys by using SEM, TEM/STEM and EDS. Combining the isothermal and cyclic oxidation data presented in Chapter 4 (Figure 4.7, Figure 4.8 and Figure 4.10) and the qualitative and semi-quantitative analysis of the  $\theta \rightarrow \alpha\text{-Al}_2\text{O}_3$  transformation kinetics presented in Chapter 5 (Figure 5.2, Figure 5.3 and Figure 5.4), there are several questions that need to be answered for the effect of Si on the oxidation behavior of the Hf+Y co-doped  $\gamma + \gamma'$  model alloys: 1) How do these Ni-rich particles form close to the scale/metal interface during the initial stage of oxidation; 2) Why does Si addition suppress the formation of Ni-rich particles; and 3) Why does Si addition suppress excessive non-uniform Hf and Y segregation to  $\text{Al}_2\text{O}_3$  grain boundaries?

The appearance of Ni-rich particles was reported by Molins *et al.* <sup>[173]</sup> in the alumina scale formed on  $\beta\text{-Ni}_{40}\text{Al}_{60}$  alloy, by Hayashi *et al.* <sup>[17]</sup> in the alumina scale formed on Pt-doped  $\gamma'\text{-Ni}_3\text{Al}$  alloy and subsequently by Gao <sup>[167]</sup> in the alumina scale formed on  $\gamma + \gamma'$  alloy, during the early stage of oxidation. In Molins *et al.*'s study <sup>[173]</sup>, the Ni-rich particles distributed through the whole scale, without any preference in terms of location. These authors believed that the Ni-rich particles formed by supersaturation of Ni in the alumina scale during the cooling process. The distribution pattern of the Ni-rich particles reported by Hayashi *et al.* <sup>[17]</sup> is similar to that presented in this study. The Ni-rich particles were only observed in the inner part of the alumina scale close to the scale/metal interface. Hayashi *et al.* <sup>[17]</sup> proposed that the formation of Ni-rich particles is due to a progressive decrease in the local oxygen partial pressure (it was assumed that chemical activity of  $\text{O}_2$  is equal to its partial pressure), in part owing to the  $\theta \rightarrow \alpha\text{-Al}_2\text{O}_3$  transformation. It is known that with the growth of alumina scale, the local oxygen partial

pressure at the scale/metal interface decreases toward the establishment of local equilibrium [2]. According to the Ni-Al-O phase diagram (1000°C) proposed by Elrefaie *et al.* [174], the solubility of Ni in  $\alpha$ -Al<sub>2</sub>O<sub>3</sub> decreases with decreasing oxygen partial pressure, see Figure 6.11. The solubility of Ni in meta-stable aluminas should be higher than that in  $\alpha$ -Al<sub>2</sub>O<sub>3</sub>, since meta-stable aluminas have more open crystal structures than  $\alpha$ -Al<sub>2</sub>O<sub>3</sub> [20, 32-33]. Thus, with the oxidation reaction progressed, the decrease in local oxygen partial pressure will in turn result in supersaturation of Ni and lead to the precipitation of Ni-rich particles.

Hayashi *et al.* [17] used a series of schematics (Figure 6.12 a-d) to describe the formation of Ni-rich particles induced by the decrease of local oxygen partial pressure and Ni supersaturation. In Figure 6.12 (a), during the very first few minutes of oxidation, Ni-rich oxides (in the form of either particles or thin layer) quickly formed on the alloy surface, because the outward diffusion of Ni predominated in this stage even though aluminum oxides are thermodynamically more stable. As the oxidation proceeds, but still in the transient oxidation stage, the initially-formed Ni-rich oxides dissolved into the subsequently formed alumina scale, which is mostly composed of metastable aluminas and consequently has a relatively higher solubility of Ni at such high temperature, see Figure 6.12 (b). When the oxide scale becomes thicker with longer oxidation time (Figure 6.12 c), the local oxygen partial pressure at the scale/metal interface progressively decreases toward local equilibrium, and the solubility of Ni in Al<sub>2</sub>O<sub>3</sub> scale decreases accordingly based on the Ni-Al-O phase diagram shown in Figure 6.11. Eventually, Ni becomes supersaturated with continued growth of the alumina scale and precipitates in the form of Ni-rich metallic particles along the scale/metal interface, where the local oxygen partial pressure dropped to the lowest from the gas/scale interface.

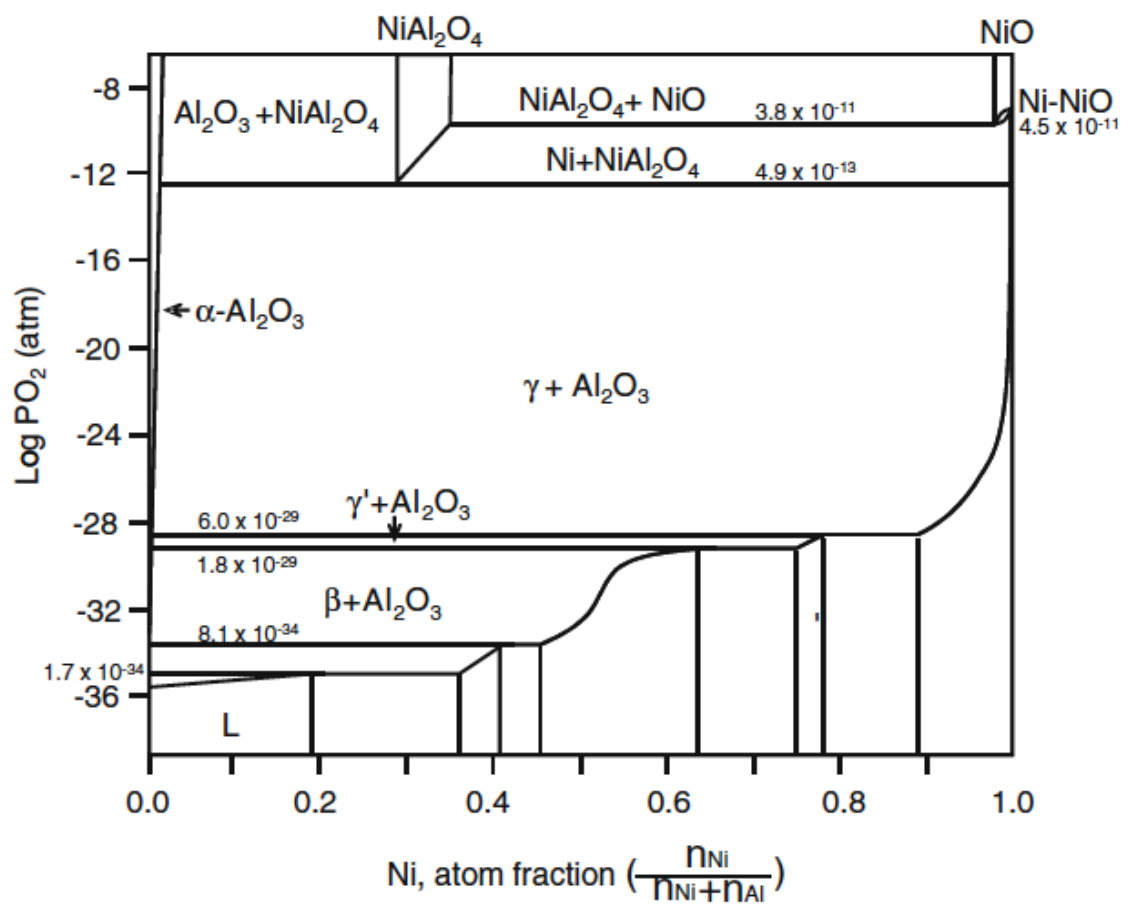


Figure 6.11 Ni-Al-O phase diagram <sup>[174]</sup>

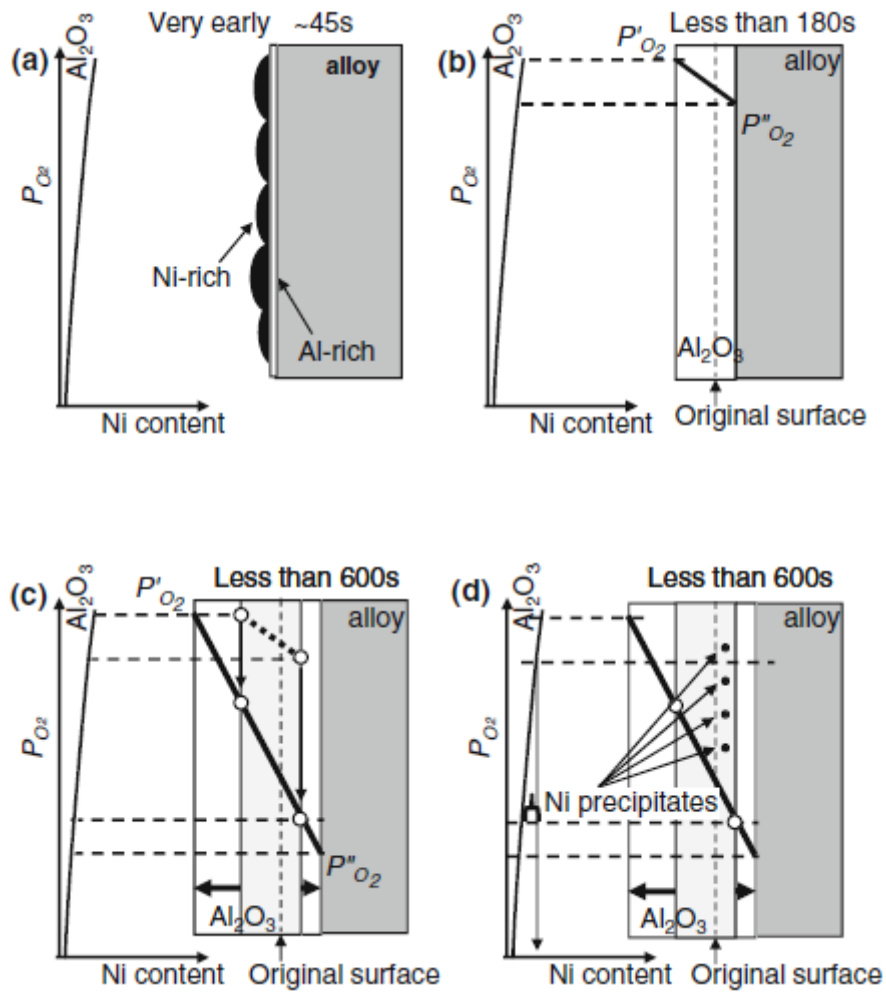


Figure 6.12 (a-d) Schematic of the formation of Ni-rich particles near the scale/metal interface during the early stage of oxidation <sup>[17]</sup>

The mechanism of the formation of Ni-rich particles proposed by Hayashi *et al.* <sup>[17]</sup> is also applicable to the present study, because the Ni-rich particles were also found near the scale/metal interface (see Figure 6.10) for both Si-free and Si-containing alloy in this study. Comparing the density of Ni-rich particles in the alumina scales (Figure 6.10), it is seen that the particle density of Ni-rich particles is higher in the scale on the Si-free alloy than in the scale on the Si-containing alloy. The reason why Si addition suppressed the formation of Ni-rich particles can be explained by comparing the surface morphologies of the two alloys after 10 minutes of oxidation. As shown in Figure 6.1 a and b, the average diameter of the NiO formed on the surface of Si-containing alloy is obviously smaller than that on the surface of Si-free alloy. Since these NiO will be dissolved into the alumina scale as the oxidation proceeds, larger Ni-rich oxides will supply more Ni to alumina scale and in turn cause more precipitation of Ni-rich particles close to the scale/metal interface. The reason why larger NiO formed on the Si-free alloy comparing to its Si-containing counterpart is not yet clear, but, as mentioned in Section 6.3.1, it may be linked to the synergistic effect between Hf and/or Y and Si. It was discussed in Chapter 5 that the addition of Si decreases the chemical activities of Hf and/or Y, since Si has great tendency to form high melting point compounds with Hf and Y according to the Hf-Si and Y-Si phase diagrams (Figure 5.13). The role that Hf and/or Y played during the formation of NiO is that they might form preferential heterogeneous nucleation sites through forming hafnium oxides or yttrium oxides prior to Ni-rich oxides. Therefore, if the chemical activities of Hf and/or Y were decreased by the addition of Si, then Hf and/or Y had less capability to form preferential heterogeneous nucleation sites for NiO, then less and smaller NiO formed on the surface of Si-containing alloy than on the Si-free alloy.

The different densities of Ni-rich particles in the alumina scales of the Si-free and Si-containing alloys might also be attributed to the different alumina scale microstructures. As shown in Figure 6.10, after 10 and 30 minutes of oxidation, the alumina scales of the two alloys have significantly different microstructures. The alumina scale on the Si-free alloy has more alumina grain boundaries perpendicular to the scale/metal interface. By contrast, for the Si-containing alloys, the scale/metal interface is covered by a layer of quickly established large grained  $\text{Al}_2\text{O}_3$ , which were further confirmed to be  $\alpha\text{-Al}_2\text{O}_3$  after 2 hours of oxidation (see Figure 6.8). The alumina grain boundaries might act as preferential nucleation sites for the precipitation of Ni-rich particles, because grain boundaries normally have higher surface energies. Therefore, the relatively higher alumina grain-boundary density on the Si-free alloy facilitated the formation of more Ni-rich particles. Figure 6.13 schematically compares the formation of Ni-rich particles during the very initial stage of oxidation of the Si-free and Si-containing alloy.

After answering the first two questions how do the Ni-rich particles form and why does Si addition suppress the formation of Ni-rich particles, the following discussion will focus on the effect of Si addition in suppressing the excessive Hf and Y segregation to  $\text{Al}_2\text{O}_3$  grain boundaries. EDS analysis of the  $\text{Al}_2\text{O}_3$  grain boundaries in the scales of both the Si-free and the Si-containing alloys after 10 and 30 minutes of oxidation (Figure 6.4 and Figure 6.5) revealed that Hf and/or Y were detected at the  $\text{Al}_2\text{O}_3$  grain boundaries for both alloys. However, after 2 hours of oxidation, excessive non-uniform Hf and Y segregation was only observed in the alumina scale of the Si-free alloy, see Figure 6.6 and Figure 6.7. This means that the addition of silicon made the Hf and Y distribute more uniformly inside the alumina scale. This phenomenon should also be linked to the synergistic effect between Hf and/or Y and Si. Considering the inference that the addition of Si decreases the chemical activities of Hf and/or Y, less Hf and/or Y would be tied up by oxygen

to form the oxides of reactive elements during the very initial stage of oxidation by the addition of silicon. For the Si-free alloy, having relatively higher Hf and/or Y chemical activities means that there is higher possibility for Hf and/or Y to form oxides during the very initial stage of oxidation. Once the oxides of reactive elements formed, these oxidized reactive elements will easily segregate to the closest  $\text{Al}_2\text{O}_3$  grain boundaries in the following stages of oxidation and reluctant to diffuse to  $\text{Al}_2\text{O}_3$  grain boundaries locating further from them. As a consequence, localized excessive non-uniform segregation of Hf and/or Y to  $\text{Al}_2\text{O}_3$  grain boundaries is expected to occur. By contrast, for the Si-containing alloy, since the chemical activities of Hf and/or Y were decreased by adding Si, oxides of reactive elements are less likely to form or form in larger size, thus chances for excessive Hf and/or Y grain boundary segregation to occur become smaller. Figure 6.13 e and f schematically show the different extent of Hf and/or Y segregation to the  $\text{Al}_2\text{O}_3$  grain boundaries for the Si-free and Si-containing alloys.

In a collaborative study with Case Western Reserve University<sup>[167]</sup>, ToF-SIMS elemental maps of Hf and Y (Figure 6.14 a-d) were provided for the alumina scales formed on both Ni-20Al-5Cr-0.05Hf-0.05Y and Ni-20Al-5Cr-0.05Hf-0.05Y-1Si alloys after 50 hours of oxidation at 1100°C. The intensities of Hf and Y shown on the maps are averaged intensities through the entire oxide scale. Compared to the distribution of Hf and Y in the scale on the Si-free alloy, the addition of silicon made the Hf and Y distribute more uniformly in the scale on the Si-containing alloy. This result strongly supports the speculation that the addition of silicon suppressed the excessive non-uniform segregation of Hf and/or Y to  $\text{Al}_2\text{O}_3$  grain boundaries.

The excessive non-uniform Hf and/or Y segregation to alumina grain boundaries might be detrimental to the cyclic oxidation resistance of alumina scale. Back to the cyclic oxidation results shown in Chapter 4 (see Figure 4.10), it was found that the Si-free alloy began to show

weight loss after around 850 1 hour cycles, indicating the appearance of spallation, while the Si-containing alloy only showed a gradual weight gain throughout 1000 1 hour cycles. As the ionic radii of Hf (0.71 Å) and Y (0.93 Å) are much larger than that of Al (0.5 Å), Hf and Y will tend to distort the crystal lattice of Al<sub>2</sub>O<sub>3</sub> when they incorporate into the alumina scale. Alumina grain boundaries excessively segregated with Hf and/or Y will cause a localized stress accumulation and make the grain boundaries areas not compatible with adjacent grains. This kind of incompatibility will initiate cracks at the heavily segregated grain boundaries during the rapid heating and cooling processes, and eventually cause spallation.

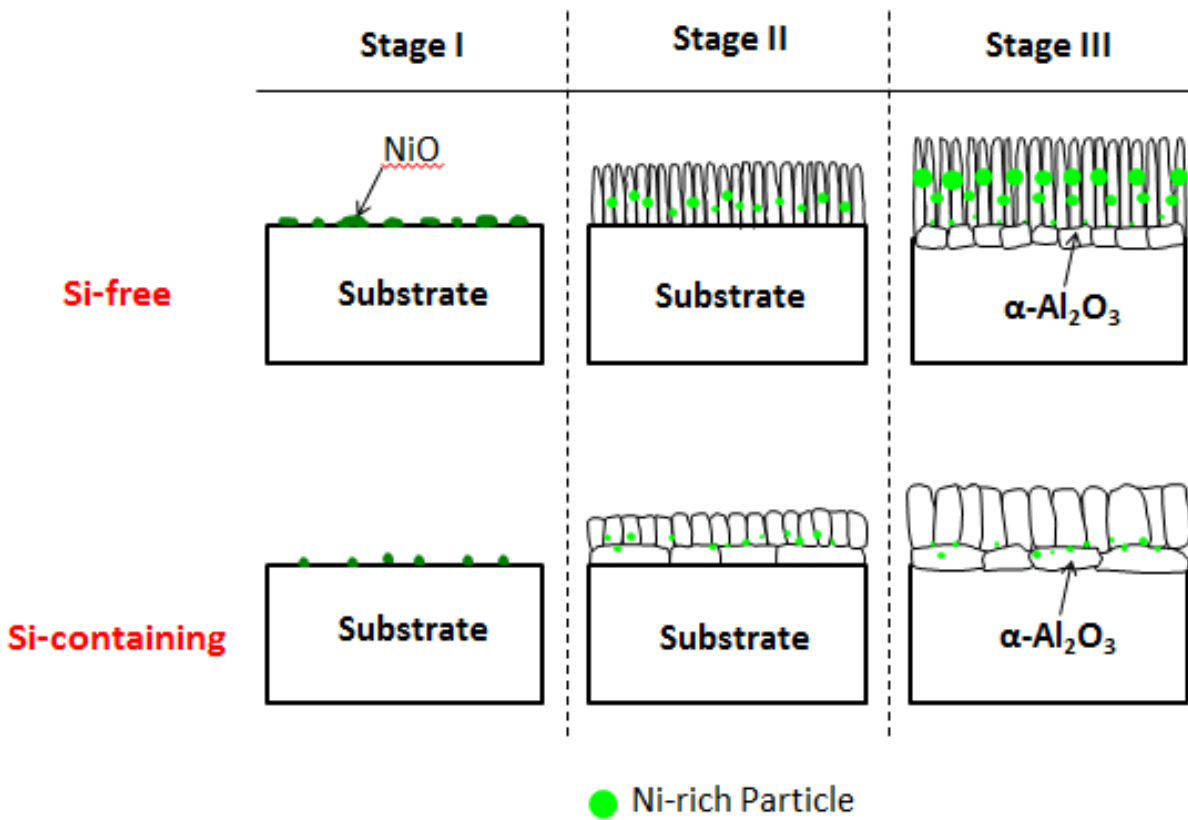


Figure 6.13 Schematics of the transient oxidation of Ni-20Al-5Cr-0.05Hf-0.05Y and Ni-20Al-5Cr-0.05Hf-0.05Y-1Si at 1100°C

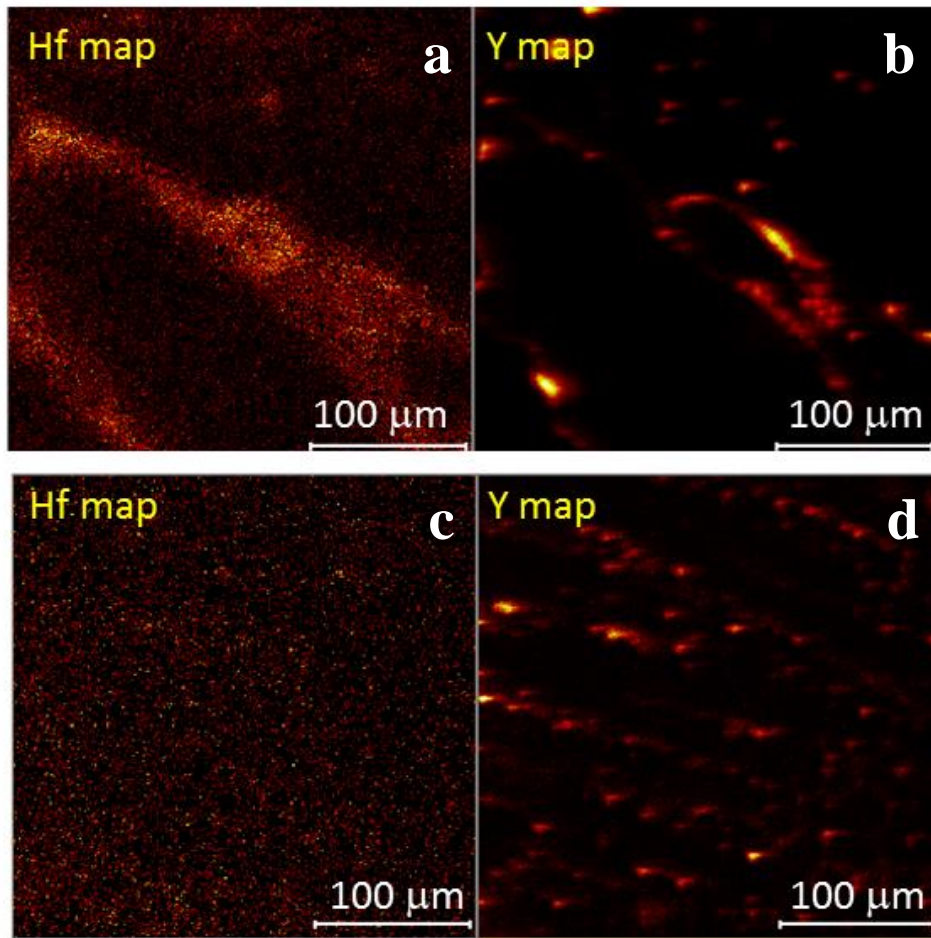


Figure 6.14 (a-d) Elemental maps of Hf and Y obtained by ToF-SIMS after 50 hours of oxidation at 1100°C (a and b) Hf and Y intensity maps in alumina scale formed on the Ni-20Al-5Cr-0.05Hf-0.05Y alloy (c and d) Hf and Y intensity maps in alumina scale formed on the Ni-20Al-5Cr-0.05Hf-0.05Y-1Si alloy

## 6.5 SUMMARY AND CONCLUSIONS

The effects of Si on the early stage of oxidation behavior of  $\gamma + \gamma'$  Ni-20Al-5Cr-0.05Hf-0.05Y and Ni-20Al-5Cr-0.05Hf-0.05Y-1Si model alloys were studied by SEM, TEM/STEM and EDS.

Major results are summarized as follows:

1. Significantly different microstructures of the alumina scales formed on the Si-free and Si-containing alloys were observed after 10 and 30 minutes of oxidation at 1150°C. The alumina scale formed on the Si-free alloy contained higher density of Ni-rich particles in the columnar-grained  $\text{Al}_2\text{O}_3$  region close to scale/metal interface. By contrast, for the Si-containing alloy, a layer of quickly established large-grained  $\text{Al}_2\text{O}_3$ , with much less Ni-rich particles, was observed in the region close to the scale/metal interface. The mechanism of the formation of Ni-rich particles is due to a decrease in local oxygen particle pressure in alumina scale, leading to supersaturation of Ni in  $\text{Al}_2\text{O}_3$  and precipitation of Ni-rich particles. The addition of silicon decreased the chemical activities of Hf and/or Y and as a consequence suppressed the surface formation of NiO during the very initial stage of oxidation. The suppression of NiO formation by the addition of silicon in turn caused less precipitation of Ni-rich particles because the reduced supply of Ni to alumina scale.
2. After 30 minutes of oxidation at 1150°C, both Hf and Y segregation were detected at the alumina grain boundaries in the scale formed on the Si-free alloy, while only Y segregation was found at the alumina grain boundaries in the scale formed on the Si-containing alloy. As the oxidation time prolonged to 2 hours, excessive non-uniform Hf and Y grain-boundary segregation was observed in the scale formed on the Si-free alloy, but no obvious non-uniform Hf and/or Y grain boundary segregation was found in the scale formed on the Si-

containing alloy. The addition of Si in decreasing the chemical activities of Hf and Y in the alloy substrates is believed to account for the suppression of non-uniform grain boundary segregation.

## 7.0 OVERALL CONCLUSIONS

The effects of Si both solely and in combination with reactive elements (Hf and Y) have been studied on both modified commercial and model  $\gamma + \gamma'$  alumina-scale forming alloys. Investigations encompassed long-term isothermal and cyclic oxidation kinetics, short-term metastable  $\rightarrow \alpha$ -Al<sub>2</sub>O<sub>3</sub> phase transformation kinetics, and nano to sub-micron scale microstructure and scale/metal interface evolution during the early stage of oxidation. Major findings in this dissertation are as follows:

1. The addition of Si moderately decreased the overall weight gain of modified-René N5 superalloy and Ni-20Al-5Cr-0.05Hf-0.05Y model alloy under isothermal oxidation condition up to 100 hours at 1150<sup>0</sup>C; Si addition markedly decreased the overall weight gain of modified-René N5 superalloy and Ni-20Al-5Cr-0.05Hf-0.05Y model alloy under cyclic oxidation condition up to 1000 1 hour cycles at 1150<sup>0</sup>C;
2. For the Ni-20Al-5Cr-0.05Hf-0.0Y and Ni-20Al-5Cr-0.05Hf-0.05Y-1Si model alloys, the addition of Si delayed the  $\theta \rightarrow \alpha$ -Al<sub>2</sub>O<sub>3</sub> transformation at temperatures above 900<sup>0</sup>C. The mechanism by which silicon addition delayed the  $\theta \rightarrow \alpha$ -Al<sub>2</sub>O<sub>3</sub> transformation was speculated to be due to that silicon addition decreased the chemical activities of Hf (and/or Y) in the alloy substrates. Decreasing the chemical activities of Hf (and/or Y) reduced the density of the initially formed HfO<sub>2</sub> (and/or Y<sub>2</sub>O<sub>3</sub>) nuclei that act as heterogeneous

nucleation sites for  $\theta \rightarrow \alpha\text{-Al}_2\text{O}_3$  transformation and in turn delayed the  $\theta \rightarrow \alpha\text{-Al}_2\text{O}_3$  transformation.

3. Significantly different microstructures of the alumina scales formed on the Ni-20Al-5Cr-0.05Hf-0.05Y and Ni-20Al-5Cr-0.05Hf-0.05Y-1Si alloys were observed after 10 and 30 minutes of oxidation at 1150°C. The alumina scale formed on the Si-free alloy contained higher density of Ni-rich particles in the columnar-grained Al<sub>2</sub>O<sub>3</sub> region close to scale/metal interface. By contrast, for the Si-containing alloy, a layer of quickly established large-grained Al<sub>2</sub>O<sub>3</sub>, with much less Ni-rich particles, was observed in the region close to the scale/metal interface. The mechanism of the formation of Ni-rich particles is due to a decrease in local oxygen partial pressure in alumina scale, leading to supersaturation of Ni in Al<sub>2</sub>O<sub>3</sub> and precipitation of Ni-rich particles. The addition of silicon decreased the chemical activities of Hf and/or Y and as a consequence suppressed the surface formation of NiO during the very initial stage of oxidation. The suppression of NiO formation by the addition of silicon in turn caused less precipitation of Ni-rich particles because of the reduced supply of Ni to alumina scale.
4. For the Ni-20Al-5Cr-0.05Hf-0.05Y and Ni-20Al-5Cr-0.05Hf-0.05Y-1Si model alloys, segregation behavior of reactive elements Hf and Y to Al<sub>2</sub>O<sub>3</sub> grain boundaries was significantly influenced by the addition of silicon during the early stage of oxidation. After 30 minutes of oxidation at 1150°C, both Hf and Y segregation were detected at the alumina grain boundaries in the scale formed on the Si-free alloy, while only Y segregation was found at the alumina grain boundaries in the scale formed on the Si-containing alloy. As the oxidation time continued to 2 hours, excessive non-uniform Hf and Y grain boundary segregation was observed in the scale formed on the Si-free alloy, but no obvious non-

uniform Hf and/or Y grain boundary segregation was found in the scale formed on the Si-containing alloy. The addition of Si in decreasing the chemical activities of Hf and Y in the alloy substrates is believed to account for the suppression of non-uniform grain boundary segregation.

## BIBLIOGRAPHY

1. M. J. Donachie and S. J. Donachie, "Superalloys: A Technical Guide (Second Edition)", ASM International, 2002
2. N. Birks, G. H. Meier and F. S. Pettit, "Introduction to the High Temperature Oxidation of Metals (Second Edition)", Cambridge University Press, 2009
3. D. Young, "High Temperature Oxidation and Corrosion of Metals", Elsevier Ltd, 2008
4. R. Prescott and M. J. Graham, "The Formation of Aluminum Oxide Scales on High-Temperature Alloys", *Oxidation of Metals*, 38 (1992) 233-254
5. M. P. Brady, B. Gleeson and I. G. Wright, "Alloy Design Strategies for Promoting Protective Oxide-Scale Formation (Overview)", *Journal of Minerals, Metals and Materials Society*, 52 (2000) 16-21
6. C. Wagner, "Reaktionstypen bei der Oxydation von Legierungen", *Z. Elektrochem*, 63 (1959) 772-782
7. F. S. Pettit, "Oxidation Mechanisms for Nickel-Aluminum Alloys at Temperatures between 900°C and 1300°C", *Transaction of Metallurgical Society AIME*, 239 (1967) 1296-1305
8. C. S. Giggins and F. S. Pettit, "Oxidation of Ni-Cr-Al Alloys between 900°C and 1300°C", *Journal of Electrochemical Society*, 118 (1971) 1782-1790
9. D. P. Whittle and J. Stringer, "Improvements in High Temperature Oxidation Resistance by Additions of Reactive Elements or Oxide Dispersions", *Philosophical Transactions of the Royal Society of London Series A, Mathematical and Physical Sciences* 295 (1980) 309-329
10. D. P. Moon, "Role of Reactive Elements in Alloy Protection", *Materials Science and Technology*, 5 (1989) 754-764
11. B. A. Pint, "Progress in Understanding the Reactive Element Effect Since the Whittle and Stringer Literature Review", ASM International, Materials Park, OH, (2003)9-19
12. T. A. Ramanarayanan, R. Ayer, R. Petkovic-Luton and D. P. Leta, "The Influence of Yttrium on Oxide Scale Growth and Adherence", *Oxidation of Metals*, 29 (1988) 445-472

13. F. H. Stott, G. C. Wood and J. Stringer, "The Influence of Alloying Elements on the Development and Maintenance of Protective Scales", *Oxidation of Metals*, 44 (1995) 113-145
14. B. A. Pint, J. R. Martin and L. W. Hobbs, "The Oxidation Mechanism of  $\theta$ -Al<sub>2</sub>O<sub>3</sub> Scales", *Solid State Ionics*, 78 (1995) 99-107
15. B. Gleeson, W. Wang, S. Hayashi and D. Sordélet, "Effects of Platinum on the Interdiffusion and Oxidation Behavior of Ni-Al-Based Alloys", *Materials Science Forum*, 461-464 (2004) 213-222
16. B. A. Pint, "Optimization of Reactive-Element Additions to Improve Oxidation Performance of Alumina-Forming Alloys", *Journal of the American Ceramic Society*, 86 (2003) 686-695
17. S. Hayashi and B. Gleeson, "Early-Stage Oxidation Behavior of Pt-Modified  $\gamma'$ -Ni<sub>3</sub>Al-Based Alloys with and without Hf Addition", *Oxidation of Metals*, 71 (2009) 5-19
18. K. Wefers and C. Misra, "Oxides and Hydroxides of Aluminum", Alcoa Laboratories, 1987
19. R. B. Heimann, "Classic and Advanced Ceramics: From Fundamentals to Applications" Publisher: Wiley-VCH, 2010
20. A. Vlad, A. Stierle, N. Kasper, H. Dosch and M. Ruhle, "In situ X-ray study of the  $\gamma$ - to  $\alpha$ -Al<sub>2</sub>O<sub>3</sub> Phase Transformation During Atmospheric Pressure Oxidation of NiAl(110)" *Journal of Materials Research*, 21 (2006) 3047-3057
21. H. J. Grabke, M. W. Brumm and B. Wagemann, "The Oxidation of NiAl", *Materials and Corrosion* 47 (1996) 675-677
22. S. Chevalier, A. Galerie, O. Heintz, R. Chassagnon and A. Crisci, "Thermal Alumina Scales on FeCrAl: Characterization and Growth Mechanism", *Materials Science Forum*, 595-598 (2008) 915-922
23. M. Pijolat, M. Dauzat and M. Soustelle, "Influence of Additives and Water Vapor on the Transformation of Transition Aluminas into Alpha Alumina" *Thermochimica Acta*, 122 (1987) 71-77
24. V. J. Vereshagin, V. Yu. Zelinskii, T. A. Khabas and N. N. Kolova, "Kinetics and Mechanism of Transformations of Low-Temperature Forms of Alumina in  $\alpha$ -Aluminum Oxide in the presence of Additives", *Zh. Prikl. Khim*, 55 (1982) 1946-1951
25. G. C. Bye and G. T. Simpkin, "Influence of Cr and Fe on Formation of  $\alpha$ -Al<sub>2</sub>O<sub>3</sub> from  $\gamma$ -Al<sub>2</sub>O<sub>3</sub>", *Journal of the American Ceramic Society*, 57 (1974) 367-371
26. J. C. Yang, E. Schumann, I. Levin and M. Ruhle, "Transient Oxidation of NiAl", *Acta Materialia*, 46 (1998) 2195-2201

27. E. Schumann and M. Ruhle, "Microstructural Observations on the Oxidation of  $\gamma'$ -Ni<sub>3</sub>Al at High Oxygen Partial Pressure", *Acta Metallurgica et Materialia*, 42 (1994) 1481-1487
28. J. Doychak, J. L. Smialek and T. E. Mitchell, "Transient Oxidation of Single-Crystal  $\beta$ -NiAl", *Metallurgical Transactions A*, 20A (1989) 499-518
29. J. R. Wynnyckyj and C. G. Morris, "A Shear-Type Allotropic Transformation in Alumina", *Metallurgical Transactions B*, 16B (1985) 345-353
30. Igor Levin and D. Brandon, "Metastable Alumina Polymorphs: Crystal Structures and Transition Sequences", *Journal of American Ceramic Society*, 81 (1998) 1995-2012
31. J. A. Kohn, G. Katz and J. D. Broder, "Characterization of  $\beta$ -Ga<sub>2</sub>O<sub>3</sub> and its Alumina Isomorph,  $\theta$ -Al<sub>2</sub>O<sub>3</sub>", *American Mineralogist*, 42 (1957) 398-470
32. H. Hosono, D. C. Paine and D. S. Ginley, "Handbook of Transparent Conductors", Springer, 1<sup>st</sup> Edition, (2010) 314
33. A. Stierle, F. Renner, R. Streitl, H. Dosch, W. Drube and B. C. Cowie, "X-ray Diffraction Study of the Ultrathin Al<sub>2</sub>O<sub>3</sub> Layer on NiAl(110)", *Science*, 303 (2004) 1652-1656
34. P. Gassmann, R. Franchy and H. Ibach, "Investigations on Phase Transitions within Thin Al<sub>2</sub>O<sub>3</sub> Layers on NiAl(001) – HREELS on Aluminum Oxide Films", *Surface Science* 319 (1994) 95-109
35. H. J. Grabke, "Oxidation of NiAl and FeAl", *Intermetallics* 7 (1999) 1153-1158
36. W. J. Quadackers and M. J. Bennett, "Oxidation Induced Lifetime Limits of Thin Walled, Iron Based, Alumina Forming, Oxide Dispersion Strengthened Alloy Components", *Materials Science and Technology*, 10 (1994) 126-131
37. G. C. Rybicki and J. L. Smialek, "Effect of the  $\theta$ - $\alpha$ -Al<sub>2</sub>O<sub>3</sub> Transformation on the Oxidation Behavior of  $\beta$ -NiAl + Zr", *Oxidation of Metals*, 31 (1989) 275-304
38. J. K. Doychak, Doctoral Thesis, Case Western Reserve University, Cleveland, Ohio, 1986
39. B. A. Pint, A. J. Garratt-Reed, and L. W. Hobbs, "The Effect of a Zr Alloy Addition on the Oxidation Behavior of  $\beta$ -NiAl: The Transition from Benefit to Breakdown", *Microscopy of Oxidation II, Proceedings of the 2<sup>nd</sup> International Conference on the Microscopy of Oxidation* (1993) 463-475. Edited S. B. Newcomb and M. J. Bennett. The Institute of Materials, London, U. K. 1993
40. B. A. Pint and L. W. Hobbs, "The Oxidation Behavior of Y<sub>2</sub>O<sub>3</sub> – Dispersed Ni<sub>3</sub>Al", *Proceedings of Oxide Films on Metals and Alloys* (1992) 92-100, The Electrochemical Society, Pennington, NJ
41. J. L. Smialek, "Oxide Morphology and Spalling Model for NiAl", *Metallurgical Transactions A*, 9A (1978) 309-320

42. J. Jedlinski and S. Mrowec, "The Influence of Implanted Yttrium on the Oxidation Behavior of  $\beta$ -NiAl", *Materials Science and Engineering*, 87 (1987) 281-287
43. C. Sarioglu, M. J. Stiger, J. R. Blachere, R. Janakiraman, E. Schumann, A. Ashary, F. S. Pettit and G. H. Meier, "The Adhesion of Alumina Films to Metallic Alloys and Coatings", *Materials and Corrosion*, 51 (2000) 358-372
44. J. D. Kuenzly and D. L. Douglass, "The Oxidation Mechanism of Ni<sub>3</sub>Al Containing Yttrium", *Oxidation of Metals*, 8 (1974) 139-178
45. A. Kumar, M. Nasrallah and D. L. Douglass, "The Effect of Yttrium and Thorium on the Oxidation Behavior of Ni-Cr-Al Alloys", *Oxidation of Metals*, 8 (1974) 227-263
46. A. S. Kahn, C. E. Lowell and C. A. Barrelet, "The Effect of Zirconium on the Isothermal Oxidation of Nominal Ni-14Cr-24Al Alloys", *Journal of Electrochemical Society*, 127 (1980) 670-679
47. R. Hutchings and M. H. Loretto, "Compositional Dependence of Oxidation Rates of NiAl and CoAl", *Metal Science*, 12 (1978) 503-510
48. E. W. A. Young and J. H. W. de Wit, "The Use of a <sup>18</sup>O Tracer and Rutherford Backscattering Spectrometry to Study the Oxidation Mechanism of NiAl", *Solid State Ionics*, 16 (1985) 39-46
49. J. Jedlinski and G. Borchardt, "On the Oxidation Mechanism of Alumina Formers", *Oxidation of Metals*, 36 (1991) 317-337
50. B. A. Pint, J. R. Martin and L. W. Hobbs, "<sup>18</sup>O/SIMS Characterization of the Growth Mechanism of Doped and Un-doped  $\alpha$ -Al<sub>2</sub>O<sub>3</sub>", *Oxidation of Metals*, 39 (1993) 167-195
51. M. J. Graham, J. I. Eldridge, D. F. Mitchell and R. J. Hussey, "Anion transport in growing Cr<sub>2</sub>O<sub>3</sub> and Al<sub>2</sub>O<sub>3</sub> scales", *Materials Science Forum*, 42 (1989) 207-242
52. D. J. Reed and B. J. Weunsch, "Ion Probe Measurement of Oxygen Self-diffusion in Single Crystal Aluminum Oxide", *Journal of the American Ceramic Society*, 63 (1980) 88-92
53. Y. Oishi, K. Ando and Y. Kubota, "Self-diffusion of Oxygen in Single Crystal Alumina", *Journal of Chemical Physics*, 73 (1980) 1410-1412
54. Y. Oishi and W. D. Kingery, "Self-diffusion of Oxygen in Single Crystal and Polycrystalline Aluminum Oxide", 33 (1960) 480-486
55. H. Hindam and D. P. Whittle, "Microstructure, Adhesion and Growth Kinetics of Protective Scales on Metals and Alloys", *Oxidation of Metals*, 18 (1982) 245-283
56. K. P. R. Reddy, J. L. Smialek and A. R. Cooper, "<sup>18</sup>O Tracer Studies of Al<sub>2</sub>O<sub>3</sub> Scale Formation on NiCrAl Alloys", *Oxidation of Metals*, 17 (1982) 429-449

57. J. Stringer, "The Reactive Element Effect in High-temperature Corrosion", *Materials Science and Engineering A*, 120 (1989) 129-137
58. A. M. Huntz, "Influence of Active Elements on the Oxidation of M-Cr-Al Alloys", *Materials Science and Engineering*, 87 (1987) 251-260
59. J. Stringer, I. M. Allam and D. P. Whittle, "The High Temperature Oxidation of Co-Cr-Al Alloys Containing Yttrium or Hafnium Additions", *Thin Solid Films*, 45 (1977) 377-384
60. J. L. Smialek, J. Doychak and D. J. Gaydosh, "Oxidation Behavior of FeAl + Hf, Zr, B", *Oxidation of Metals*, 34 (1990) 259-275
61. A. Rahmel and M. Schutze, "Mechanical Aspects of the Rare-Earth Effect", *Oxidation of Metals*, 38 (1992) 255-266
62. B. A. Pint, M. Treska and L. W. Hobbs, "The Effect of Various Oxide Dispersions on the Phase Composition and Morphology of Al<sub>2</sub>O<sub>3</sub> Scales Grown on  $\beta$ -NiAl" *Oxidation of Metals*, 47 (1997) 1-19
63. B. A. Pint, I. G. Wright, W. Y. Lee, Y. Zhang, K. Prubner and K. B. Alexander, "Substrate and Bond Coat Compositions: Factors Affecting Alumina Scale Adhesion", *Materials Science and Engineering*, A245 (1998) 201-211
64. B. A. Pint, "Experimental Observations in Support of the Dynamic-Segregation Theory to Explain the Reactive-Element Effect", *Oxidation of Metals*, 45 (1996) 1-37
65. J. Jedlinsk, "Comments on the Effect of Yttrium on the Early Stages of Oxidation of Alumina Formers", *Oxidation of Metals*, 39 (1993) 55-60
66. F. Riffard, H. Buscail, E. Caudron, R. Cueff, C. Issartel and S. Perrier, "Effect of Yttrium Addition by Sol-Gel Coating and Ion Implantation on the High Temperature Oxidation Behavior of the 304 Steel", *Applied Surface Science*, 199 (2002) 107-122
67. E. Schumann, J. C. Yang, M. Ruhle and M. J. Graham, "High-Resolution SIMS and Analytical TEM Evaluation of Alumina Scales on  $\beta$ -NiAl Containing Zr or Y", *Oxidation of Metals*, 46 (1996) 37-49
68. J. A. Haynes, B. A. Pint, K. L. More, Y. Zhang and I. G. Wright, "Influence of Sulfur, Platinum, and Hafnium on the Oxidation Behavior of CVD NiAl Bond Coatings", *Oxidation of Metals*, 58 (2002) 513-543
69. H. M. Tawancy and N. M. Abbas, "Role of Platinum on Aluminide Coatings", *Surface and Coatings Technology*, 49 (1991) 1-7
70. H. M. Tawancy, A. UI-Hamid, N. M. Abbas and M. O. Aboelfotoh, "Effect of Platinum on the Oxide-to-Metal Adhesion in Thermal Barrier Coating Systems", *Journal of Materials Science*, 43 (2008) 2978-2989

71. Y Zhang, W. Y. Lee, J. A. Haynes, I. G. Wright, B. A. Pint, K. M. Cooley and P. K. Liaw, "Synthesis and Cyclic Oxidation Behavior of (Ni, Pt)Al Coating on a Desulfurized Ni-Base Superalloy", *Metallurgical and Materials Transaction A*, 30A (1999) 2679-2687
72. G. J. Tatlock and T. J. Hurd, "Platinum and the Oxidation Behavior of a Nickel Based Superalloy", *Oxidation of Metals*, 22 (1984) 201-226
73. A. B. Anderson, C. Ravimohan and S. P. Mehandru, "Bonding at the  $\alpha$ -Al<sub>2</sub>O<sub>3</sub>(001)/Pt(111) Interface: Molecular Orbital Theory", *Surface Science* 183 (1987) 438-448
74. S. Hayashi, W. Wang, D. J. Sordelet and B. Gleeson, "Interdiffusion Behavior of Pt-Modified  $\gamma$ -Ni +  $\gamma'$ -Ni<sub>3</sub>Al Alloys Coupled to Ni-Al-Based Alloys", *Metallurgical and Materials Transactions A*, 36A (2005) 1769-1775
75. J. L. Smialek, "Effect of Sulfur Removal on Al<sub>2</sub>O<sub>3</sub> Scale Adhesion", *Metallurgical Transactions A*, 22A (1991) 739-752
76. P. Y. Hou, "Segregation Phenomena at Thermally Grown Al<sub>2</sub>O<sub>3</sub>/Alloy Interfaces", *Annual Reviews of Materials Research* (2008) 275-298
77. P. Y. Hou, T. Izumi and B. Gleeson, "Sulfur Segregation at Al<sub>2</sub>O<sub>3</sub>/ $\gamma$ -Ni+ $\gamma'$ -Ni<sub>3</sub>Al Interfaces: Effects of Pt, Cr and Hf additions", *Oxidation of Metals* 72 (2009) 109-124
78. P. Y. Hou, "Impurity Effects on Alumina Scale Growth", *Journal of the American Ceramic Society*, 86 (2003) 660-668
79. J. L. Smialek, D. T. Jayne, J. C. Schaeffer and W. H. Murphy, "Effects of Hydrogen Annealing, Sulfur Segregation and Diffusion on the Cyclic Oxidation Resistance of Superalloys: A Review", *Thin Solid Films* 253 (1994) 285-292
80. J. L. Smialek, "Maintaining Adhesion of Protective Al<sub>2</sub>O<sub>3</sub> Scales", *Journal of Minerals, Metals and Materials Society*, 52 (2000) 22-25
81. C. E. Lowell and G. J. Santoro, "The 1200<sup>o</sup>C Cyclic Oxidation Behavior of Two Nickel-Aluminum Alloys (Ni<sub>3</sub>Al and NiAl) with Additions of Chromium, Silicon, and Titanium", *NASA Technical Note TN D-6838*, June 1972, Lewis Research Center, Cleveland, OH
82. C. E. Lowell and R. V. Miner, "Improvement in Cyclic Oxidation on the Nickel-Base Superalloy B-1900 by Addition of One Percent Silicon", *NASA Technical Memorandum TM X-68191*, January 1973, Lewis Research Center, Cleveland, OH
83. R. V. Miner Jr. and C. E. Lowell, "Effects of Silicon Additions on Oxidation and Mechanical Behavior of the Nickel-Base Superalloy B-1900", *NASA Technical Note TN D-7989*, June 1975, Lewis Research Center, Cleveland, OH
84. J. L. Smialek, "Fused Silicon-Rich Coatings for Superalloys", *NASA Technical Memorandum TM X-3001*, March 1974, Lewis Research Center, Cleveland, OH

85. A. Paul, R. Sanchez, O. M. Montes and J. A. Odriozola, "The Role of Silicon in the Reactive-Elements Effect on the Oxidation of Conventional Austenitic Stainless Steel", *Oxidation of Metals*, 67 (2007) 87-105
86. H. E. Evans, D. A. Hilton, R. A. Holm, and S. J. Webster, "Influence of Silicon Additions on the Oxidation Resistance of a Stainless Steel" *Oxidation of Metals*, 19 (1983) 1-18
87. C. T. Sims, N. S. Stoloff and W. C. Hagel, "Superalloy II", Wiley-Interscience, 2<sup>nd</sup> Edition, (1987) 295
88. B. Pieraggi, "Calculations of Parabolic Rate Constants", *Oxidation of Metals*, 27 (1987) 177-185
89. P. Tomaszewicz and G. R. Wallwork, "Observations of Nodule Growth During the Oxidation of Pure Binary Iron-Aluminum Alloys", *Oxidation of Metals*, 19 (1983) 165-185
90. B. A. Pint, J. Leiowitz and J. H. Devan, "The Effect of an Oxide Dispersion on the Critical Al Content in Fe-Al Alloys", *Oxidation of Metals*, 15 (1999) 181-197
91. R. A. Rapp, "Hot Corrosion of Materials", *Pure & Applied Chemistry* 62 (1990) 113-122
92. J. K. Tien and F. S. Pettit, "Mechanism of Oxide Adherence on Fe-25Cr-4Al (Y or Sc) Alloys", *Metallurgical Transaction*, 3 (1972) 1588-1599
93. B. A. Pint, C. R. Roberts, P. F. Tortorelli and I. G. Wright, ORNL, unpublished research
94. D. R. Sigler, "Aluminum Oxide Adherence on Fe-Cr-Al Alloys Modified with Group IIIB, IVB, VB and VIB Elements", *Oxidation of Metals*, 32 (1989) 337-355
95. M. Landkopf, A. V. Levy, D. H. Boone, R. Gray and E. Yaniv, "The Effect of Surface Additives on the Oxidation of Chromia-Forming Alloys", *Corrosion NACE*, 41 (1985) 344-357
96. M. R. Jackson and J. R. Rairden, "The Aluminization of Platinum and Platinum-Coated In-738", *Metallurgical Transactions A*, 8A (1977) 1697-1707
97. F. Qin, C. Jiang, J. W. Andereg, C. J. Jenks, B. Gleeson, D. J. Sordelet and P. A. Thiel, "Segregation of Pt at Clean Surfaces of (Pt, Ni)<sub>3</sub>Al", *Surface Science*, 601 (2007) 376-380
98. C. Jiang, M. F. Besser, D. J. Sordelet and B. Gleeson, "A Combined First-principles and Experimental Study of the Lattice Site Preference of Pt in B2 NiAl" *Acta Materialia* 53 (2005) 2101-2109
99. B. A. Pint, "On the Formation of Interfacial and Internal Voids in  $\alpha$ -Al<sub>2</sub>O<sub>3</sub> Scales", *Oxidation of Metals*, 48 (1997) 303-328

100. K. M. N. Prasanna, A. S. Khanna, Ramesh Chandra and W. J. Quadackers, "Effect of  $\theta$ -Alumina Formation on the Growth Kinetics of Alumina Forming Superalloys", *Oxidation of Metals*, 46 (1996) 465-480
101. H. M. Tawancy, Luai M. Al-Hadhrami, "Influence of Titanium in Nickel-Base Superalloys on the Performance of Thermal Barrier Coatings Utilizing  $\gamma$ - $\gamma'$  Platinum Bond Coats", *Journal of Engineering for Gas Turbines and Power*, 133 (2011) 042101, 1-6
102. R. A. Versaci, D. Clemens, W. J. Quadackers, "Distribution and Transport of Yttrium in Alumina Scales on Iron-base ODS Alloys", *Solid State Ionics*, 59 (1993) 2359242
103. D. R. Sigler, "The Oxidation Behavior of Fe-20Cr Alloy Foils in a Synthetic Exhaust-gas Atmosphere", *Oxidation of Metals*, 46 (1996) 335-364
104. Y. Tamarin, "Protective Coatings for Turbine Blades", ASM International, ISBN: 0-87170-759-4, pp 55-78
105. G. W. Goward, "Progress in Coatings for Gas Turbine Airfoils", *Surface and Coatings Technology*, 108-109 (1998) 73-79
106. J. R. Nicholls, "Designing Oxidation-Resistant Coatings (Overview)", *Journal of Minerals, Metals and Materials Society*, 52 (2000) 28-35
107. Sudhangshu Bose, "High Temperature Coatings", Elsevier Inc. ISBN-13: 978-0-7506-8252-7, pp 71-149
108. G. W. Goward and D. H. Boone, "Mechanisms of Formation of Diffusion Aluminide Coatings on Nickel-Base Superalloys", *Oxidation of Metals*, 3 (1971) 475-495
109. R. Bianco, R. A. Rapp and J. L. Smialek, "Chromium and Reactive Element Modified Aluminide Diffusion Coatings on Superalloys: Environmental Testing", *Journal of the Electrochemical Society*, 140 (1993) 1191-1203
110. M. Yavorska and J. Sieniawski, "Oxidation Behavior of Platinum Modified Aluminide Coatings Deposited by CVD method on Nickel-based Superalloys under Air Atmosphere", *Journal of Achievements in Materials and Manufacturing Engineering*, 46 (2011) 204-210
111. G. M. Kim, G. H. Meier and F. S. Pettit, "Platinum-Modified Diffusion Aluminide Coatings on Nickel-Base Superalloys", Army Research Laboratory Report, AD-A263 597, under contract DAAG46-85-K-0008, March 1993
112. J. R. Davis, "ASM Specialty Handbook: Heat-Resistant Materials", ASM International, 1997, pp
113. J. R. Nicholls, N. J. Simms, W. Y. Chan and H. E. Evans, "Smart Overlay Coatings – Concept and Practice", *Surface and Coatings Technology*, 149 (2002) 236-244

114. G. W. Goward and L. W. Cannon, "Pack Cementation Coatings for Superalloys – A Review of History, Theory and Practice", ASME Paper 87-GT-50
115. R. V. Miner, Jr. "Effects of Silicon on the Oxidation, Hot-Corrosion, and Mechanical Behavior of Two Cast Nickel-Base Superalloys", Metallurgical Transaction A, 8A (1977) 1949-1954
116. K. A. Heck, D. F. Smith, J. S. Smith, D. A. Wells and M. A. Holderby, "The Physical Metallurgy of a Silicon-containing Low Expansion Superalloy", Superalloys (1988) 151-160
117. H. Arabi, S. Rastegari, Z. Salehpour and A. Bakhshi, "Formation Mechanism of Silicon Modified Aluminide Coating on a Ni-Base Superalloy", Journal of Engineering Science, 19 (2008) 39-44
118. Hecht Ralph Julius, "Superalloy Base Having a Coating Containing Silicon for Corrosion/Oxidation Protection", US Patent # 4034142, Publication Date 1977-07-05
119. T. A. Kircher, B. G. McMordie and A. McCarter, "Performance of a Silicon-modified Aluminide Coating in High Temperature Hot Corrosion Test Conditions", Surface and Coatings Technology, 68/69 (1994) 32-37
120. L. Swadzba, B. Formanek, and A. Maciejny, "Modified Heat Resistant Protective Coatings for Nickel Base Super Alloys", International Journal of Materials and Product Technology, 8 (1993) 155-169
121. M. K. Dinkel, P. Heinz, F. Pyczak, A. Volek, M. Ott, E. Affeldt, A. Vossberg, M. Goken, R. F. Singer, "New Boron and Silicon Free Single Crystal-Diffusion Brazing Alloys", Superalloys (2008) 211-220
122. M. Kutz, "Handbook of Materials Selection", John Wiley & Sons, Inc. 2002
123. J. S. Dunning, D. E. Alman, and J. C. Rawers, "Influence of Silicon and Aluminum Additions on the Oxidation Resistance of a Lean-Chromium Stainless Steel", Oxidation of Metals, 57 (2002) 409-425
124. H. M. Hindam and W. W. Smeltzer, "Growth and Microstructure of  $\alpha$ -Al<sub>2</sub>O<sub>3</sub> on Ni-Al Alloys: Internal Precipitation and Transition to External Scale", Journal of Electrochemical Society, 127 (1980) 1622-1630
125. H. M. Hindam and W. W. Smeltzer, "Application of Auger Electron Spectroscopy and Inert Metal Marker Techniques to Determine Metal and Oxygen Transport in Oxide Films on Metals", Oxidation of Metals, 14 (1980) 337-349
126. D. J. Young and M. Cohen, "Oxidation Behavior of Chromium Between 300°C and 600°C", Journal of the Electrochemical Society, 124 (1977) 769-774

127. H. C. Kao and W. C. Wei, "Kinetics and Microstructural Evolution of Heterogeneous Transformation of  $\theta$ -Alumina to  $\alpha$ -Alumina", *Journal of the American Ceramic Society*, 83 (2000) 362-368
128. J. Stringer, "Stress Generation and Relief in Growing Oxide Films", *Corrosion Science*, 10 (1970) 513-543
129. D. M. Lipkin, H. Schaffer, F. Adar and D. R. Clarke, "Lateral Growth Kinetics of  $\alpha$ -alumina Accompanying the Formation of a Protective Scale on (111) NiAl During Oxidation at 1100 °C", *Applied Physics Letters*, 70 (1997) 2550-2552
130. H. E. Evans and M. P. Taylor, "Creep Relaxation and the Spallation of Oxide Layers", *Surface and Coatings Technology*, 94-95 (1997) 27-33
131. P. Y. Hou, A. P. Paulikas and B. W. Veal, "Stress Development and Relaxation in  $\text{Al}_2\text{O}_3$  during Early Stage Oxidation of  $\beta$ -NiAl", 6<sup>th</sup> International Conference on the Microscopy of Oxidation, April 4-6, 2005
132. R. Prescott, D. F. Mitchell and M. J. Graham, "A Study of the Growth of  $\alpha$ - $\text{Al}_2\text{O}_3$  Scale Using High-Resolution Imaging Secondary Ion Mass Spectrometry", *Corrosion*, 50 (1994) 62-71
133. G. Y. Lai, "High-Temperature Corrosion and Materials Application", ASM International, 2007
134. M. N. Task, PhD Thesis, University of Pittsburgh, 2012
135. M. W. Brumm, H. J. Grabke, "The Oxidation Behavior of NiAl – I. Phase Transformation in the Alumina Scale During Oxidation of NiAl and NiAl-Cr Alloys", *Corrosion Science*, 33 (1992) 1677-1690
136. Y. Cadoret, D. Monceau, M. P. Bacos, P. Josso, V. Maurice and P. Marcus, "Effect of Platinum on the Growth Rate of the Oxide Scale Formed on Cast Nickel Aluminide Intermetallic Alloys", *Oxidation of Metals*, 64 (2005) 185-205
137. B. M. Gleeson MS&T Presentation, unpublished report, 2009
138. D. M. Lipkin and D. R. Clarke, "Measurement of the Stress in Oxide Scale Formed by Oxidation of Alumina-Forming Alloys", *Oxidation of Metals*, 45 (1996) 267-280
139. D. B. Hovis and A. H. Heuer, "Confocal Photo-Stimulated Microspectroscopy (CPSM) – Residual Stress Measurements in  $\text{Al}_2\text{O}_3$  Using Confocal Microscopy", *Scripta Materialia*, 53 (2005) 347-349
140. X. Peng, D. R. Clarke and F. Wang, "Transient-Alumina Transformation during the Oxidation of Magnetron-Sputtered CoCrAl Nanocrystalline Coatings", *Oxidation of Metals*, 60 (2003) 225-240F

141. B. Kampfe, P. Patzelt and C. G. Nestler, "Quantitative X-ray Diffraction Analysis of Textured Sheet Metals", *Kristall and Technik*, 14 (1979) 187-195
142. A. P. Voitovich, V. S. Kalinov, L. P. Runets and A. P. Stupak, "Quantitative Luminescent Analysis Methods", *Journal of Applied Spectroscopy*, 76 (2009) 727-737
143. B. Das, P. Kumar and C. N. R. Rao, "Factors Affecting Laser-Excited Photoluminescence from ZnO Nanostructures", *Journal of Cluster Science*, 23 (2012) 649-659
144. D. K. Schroder, "Semiconductor Material and Device Characterization", Wiley-IEEE (3<sup>rd</sup> Edition), 2006
145. L. E. Copeland and R. H. Bragg, "Quantitative X-ray Diffraction Analysis", *Analytical Chemistry*, 30 (1958) 196-201
146. C. Suryanarayana and M. Grant Norton, "X-ray Diffraction: A Practical Approach", Springer, 1998 edition, pp 223
147. L. A. Xue and I. -W. Chen, "Influence of Additives on the  $\gamma$ - to- $\alpha$  Transformation of Alumina", *Journal of Materials Science Letters* 11 (1992) 443-445
148. B. A. Pint and L. W. Hobbs, "Limitations on the Use of Ion Implantation for the Study of the Reactive Element Effect in  $\beta$ -NiAl", *Journal of the Electrochemical Society*, 141 (1994) 2443-2453
149. S. Hayashi and B. Gleeson, "Phase Transformation Behavior of Al<sub>2</sub>O<sub>3</sub> Scale Formed on Pt-Modified  $\gamma'$ -Ni<sub>3</sub>Al-Based Alloys with and without Hf Addition", *Oxidation of Metals*, 77 (2012) 237-251
150. T. H. Gfroerer, "Photoluminescence in Analysis of Surface and Interfaces", *Encyclopedia of Analytical Chemistry*, John Wiley & Sons Ltd, Chichester, 2000
151. G. Murray, C. V. White and W. Weise, "Introduction to Engineering Materials, 2<sup>nd</sup> Edition", CRC Press, 2007
152. E. W. Collings, "Materials Properties Handbook: Titanium Alloys", ASM International, 1995
153. G. E. Totten and D. S. MacKenzie, "Handbook of Aluminum - Volume 2 Alloy Production and Materials Manufacturing", CRC Press, 2003
154. A. Andoh, S. Taniguchi and T. Shibata, "TEM Observation of Phase Transformations of Alumina Scales Formed on Al-Deposited Fe-Cr-Al Foils", *Materials Science Forum*, 369-372 (2001) 303-310
155. S. Taniguchi and A. Andoh, "Improvement in the Oxidation Resistance of an Al-Deposited Fe-Cr-Al Foil by Preoxidation", *Oxidation of Metals*, 58 (2002) 545-562

156. P. Burtin, J. P. Brunelle, M. Pijolat and M. Soustelle, "Influence of Surface Area and Additives on the Thermal Stability of Transition Alumina Catalyst Supports. I: Kinetic Data", *Applied Catalysis*, 34 (1987) 225-238
157. P. Burtin, J. P. Brunelle, M. Pijolat and M. Soustelle, "Influence of Surface Area and Additives on the Thermal Stability of Transition Alumina Catalyst Supports. II: Kinetic Model and Interpretation", *Applied Catalysis*, 34 (1987) 239-254
158. L. Pauling, "The Nature of the Chemical Bond", Cornell University Press (1960) third edition, pp 514
159. F. W. Dynys and J. W. Halloran, "Alpha Alumina Formation in Alum-Derived Gamma Alumina", *Journal of American Ceramic Society*, 65 (1982) 442-448
160. P. Papon, J. Leblond and P. H. E. Meijer, "The Physics of Phase Transitions: Concepts and Applications", Springer, 2<sup>nd</sup> Edition, 2006, pp 51-55
161. D. R. Clarke, "Epitaxial Phase Transformation in Aluminum Oxide", *Physica Status Solidi (a)*, 166 (1999) 183-196
162. W. Zhao, Z. Li and B. Gleeson, "A New Kinetics-based Approach to Quantifying the Extent of Meta-stable  $\rightarrow$  Stable Phase Transformation in  $\text{Al}_2\text{O}_3$  scales formed during High-temperature Oxidation", submitted to *Oxidation of Metals*
163. W. Zhao, PhD Thesis, University of Pittsburgh, 2012
164. M. Avrami, "Kinetics of Phase Change. I General Theory", *Journal of Chemical Physics*, 7 (1939) 1103-1112
165. M. Avrami, "Kinetics of Phase Change. II Transformation-Time Relations for Random Distribution of Nuclei", *Journal of Chemical Physics*, 8 (1940) 212-224
166. M. Avrami, "Kinetics of Phase Change. III Granulation, Phase Change and Microstructure Kinetics of Phase Change", *Journal of Chemical Physics*, 9 (1941) 177-184
167. H. Gao, Master's Thesis, "The Effect of Silicon on the Oxidation of Dual Phase NiAlCrHfY(Si) Bond Coat Alloys", Case Western Reserve University, 2012
168. J. C. Yang, K. Nadarzynski, E. Shumann and M. Ruhle, "Electron Microscopy Studies of NiAl/ $\gamma$ - $\text{Al}_2\text{O}_3$  Interfaces", *Scripta Metallurgica et Materialia*, 33 (1995) 1043-1048
169. E. Schumann, J. C. Yang, M. Ruhle and M. J. Graham, "Segregation Studies of Oxidized Y and Zr Doped NiAl", *Materials and Corrosion*, 46 (1995) 218-222
170. T. A. Ramanarayanan, M. Raghavan and R. Petkovic-Luton, "Metallic Yttrium Additions to High Temperature Alloys: Influence on  $\text{Al}_2\text{O}_3$  Scale Properties", *Oxidation of Metals*, 22 (1984) 83-100

171. D. Naumenko, B. Gleeson, E. Wessel, L. Singheiser and W. J. Quadackers, "Correlation between the Microstructure, Growth Mechanism, and Growth Kinetics of Alumina Scales on a FeCrAlY Alloy", *Metallurgical and Materials Transaction A*, 38A (2007) 2974-2983
172. E. C. Dickey, B. A. Pint, K. B. Alexander and I. G. Wright, "Oxidation Behavior of Platinum-Aluminum Alloys and the Effect of Zr Doping", *Journal of Materials Research*, 14 (1999) 4531-4540
173. R. Molins, I. Rouzou and P. Hou, "A TEM Study of Sulfur Distribution in Oxidized Ni40Al and its Effect on Oxide Growth and Adherence", *Materials Science and Engineering A*, 454-455 (2007) 80-88
174. F. A. Elrefaie and W. W. Smeltzer, "Thermodynamics of Nickel-Aluminum-Oxygen System Between 900 and 1400 K", *Journal of the Electrochemical Society*, 128 (1981) 2237-2242
175. R. E. Mistler and R. L. Coble, "Rate-Determining Species in Diffusion-Controlled Processes in Al<sub>2</sub>O<sub>3</sub>", *Journal of the American Ceramic Society*, 54 (1971) 60-61
176. A. Atkinson, D. P. Moon, D. W. Smart and R. I. Taylor, "Tracer Diffusion Studies in NiO Bicrystal and Polycrystals", *Journal of Materials Science*, 21 (1986) 1747-1757
177. Monica C. Maris-Sida, "Effects of Water Vapor on the High Temperature Oxidation of Alumina-Forming Coatings and Ni Base Superalloys", *Doctoral Thesis, University of Pittsburgh, Pittsburgh, PA, 2004*
178. N. P. Padture, M. Gell and E. H. Jordan, "Thermal Barrier Coatings for Gas-Turbine Engine Applications", *Science*, 296 (2002) 280-284
179. D. K. Gupta and D. S. Duvall, "A Silicon and Hafnium Modified Plasma Sprayed MCrAlY Coating for Single Crystal Superalloys", pp. 711-720 in *Proceedings of the 5<sup>th</sup> International Symposium on Superalloys, Superalloys 1984*, Edited by M. Gell, *et al.* TMS-AIME, Warrendale, PA, 1984
180. J. K. Doychak, "The Evolution and Growth of Al<sub>2</sub>O<sub>3</sub> Scales on  $\beta$ -NiAl", *NASA Contractor Report 175097*, 1986
181. G. J. Tatlock, D. Ram and P. Wang, "High Spatial Resolution Imaging of the Segregation of Reactive Elements to Oxide Grain Boundaries in Alumina Scales", *Materials at High Temperature*, 26 (2009) 293-298
182. R. C. Novak, "Coatings Development and Use: Case Studies, Presentation to the Committee on Coatings for High-Temperature Structural Materials", *National Materials Advisory Board, National Research Council, Irvine, California, US*
183. P. C. Dai, Q. Wu, Y. Ma, S. S. Li and S. K. Gong, "The Effect of Silicon on the Oxidation Behavior of NiAlHf Coating System", *Applied Surface Science*, 271 (2013) 311-316

184. Materials Preparation Center, Ames Lab ([www.ameslab.gov/mpc](http://www.ameslab.gov/mpc))
185. W. G. Moffatt, "The Handbook of Binary Phase Diagram (Volume 4)", General Electric Company, Research Development Center, Genium Pub Corp